Phase change materials (PCMs), particularly salt hydrates, are thermally absorbent materials capable of storing large amounts of energy through latent heat. As global energy demand continues to rise, efficient thermoregulation has become both a technical and economic challenge, requiring innovative and sustainable solutions. Salt hydrate PCMs present a promising approach to passive thermal regulation in buildings. Their ability to store and release heat through phase transitions enables smart, responsive energy management and positions them as strong candidates for the next generation of thermal energy batteries. However, their widespread application is still hindered by key challenges, including phase separation, supercooling, high chemical reactivity, and limitations in sustainable sourcing. This thesis addresses these challenges by exploring sustainable sourcing routes, optimizing the performance of sustainably derived salts, evaluating the limitations of molecular simulation models, and examining the chemical interactions between salt hydrates and cementitious materials for potential implementation. The research combines extensive characterization techniques with quantitative analyses to deepen the understanding of how these materials behave and perform under real conditions. Overall, this work contributes to advancing salt hydrate PCMs as sustainable, high-performance materials for thermal energy storage. The findings offer both fundamental insights and practical pathways toward the development of smart, self-regulating energy storage systems designed for a more energy-efficient future.

Salt Hydrate Phase Change Materials: Material Behaviour and Thermal Energy Storage Applications

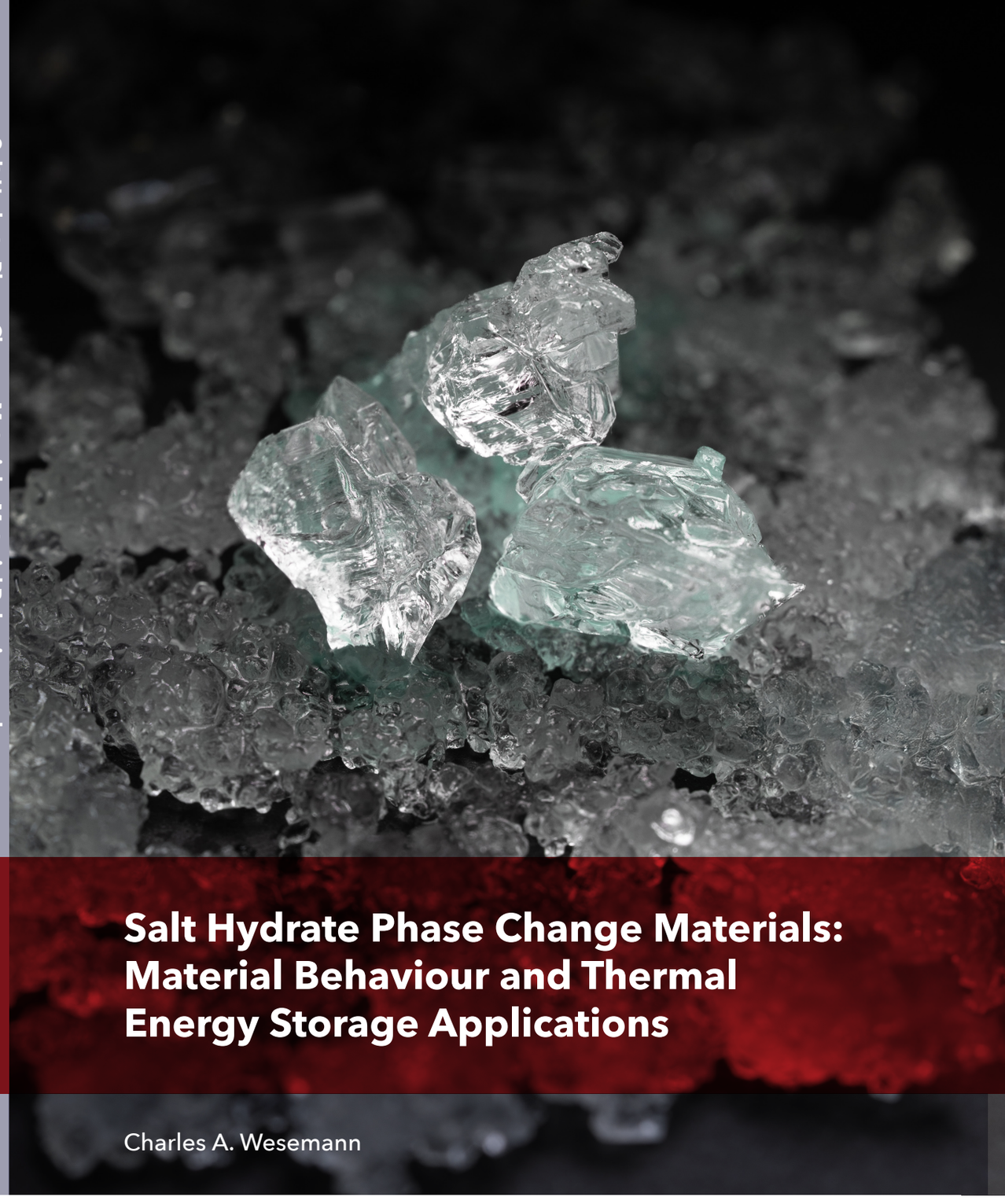

Salt Hydrate Phase Change Materials: Material Behaviour and Thermal Energy Storage Applications

Charles A. Wesemann

DEPARTMENT OF THE BUILT ENVIRONMENT

TU/e EINDHOVEN UNIVERSITY OF TECHNOLOGY

433

Bouwstenen 433

Salt Hydrate Phase Change Materials: Material Behaviour and Thermal Energy Storage Applications

Charles Alexander Wesemann

January 2026

CIP-DATA LIBRARY TECHNISCHE UNIVERSITEIT EINDHOVEN

Salt Hydrate Phase Change Materials: Material Behaviour and Thermal Energy Storage Applications / by Charles A. Wesemann

A catalogue record is available from the Eindhoven University of Technology Library

ISBN: 978-90-386-6608-2

Bouwstenen 433

NUR 971

Cover design: André Rijo Photography & Editing, -"Salt Crystals"

Ph.D. Thesis, Eindhoven University of Technology, the Netherlands

Salt Hydrate Phase Change Materials: Material Behaviour and Thermal Energy Storage Applications

PROEFSCHRIFT

ter verkrijging van de graad van doctor
aan de Technische Universiteit Eindhoven,
op gezag van de rector magnificus prof.dr.ir. S.K. Lenaerts,
voor een commissie aangewezen door het College voor Promoties,
in het openbaar te verdedigen op maandag 26 januari 2026 om 11:00 uur

door

Charles Alexander Wesemann
geboren te Bremen, Duitsland

Dit proefschrift is goedgekeurd door de promotoren en de samenstelling van de promotiecommissie is als volgt:

Voorzitter:	prof.dr.ir. A.S.J. Suiker
1e promotor:	prof.dr.ir. H.J.H Brouwers
2e promotor:	dr.dipl.min. K. Schollbach
Promotiecommissieleden:	prof.dr. E.M.J. Hensen
	prof.dr.ir. D.M.J. Smeulders
	prof.dr.ir. A.I. Fernández Renna (Universitat de Barcelona)
	prof.dr.ir. L.F. Cabeza (Universitat de Lleida)
	prof.dr.ir. M. Shahi (Universiteit Twente)
	prof.dr. E. Jewell BEng, PhD, FHEA (Swansea University)

Het onderzoek of ontwerp dat in dit proefschrift wordt beschreven is uitgevoerd in overeenstemming met de TU/e Gedragscode Wetenschapsbeoefening.

Dedicated to my family and friends

"No os haréis ricos estudiando aqui, pero se os dará una herramienta que no se puede comprar con dinero: la posibilidad de pensar, de saber: *Sapere Aude*[1]"

—Silvia Montolio, Merli: Sapere Aude

[1]Translation: Thou wont be rich with what you learn here, but you shall be given the tools that cannot be bought through money: the possibility to think, to know: *Sapere Aude*.

Preface

My Ph.D. has been an uphill and long journey for me to get here as many of you may know. I began my Ph.D. in September 2020 at the prestigious Eindhoven University of Technology. The bittersweet confusion of the pandemic had turned the world upside down with every day, week, month, and even years of uncertainty. Thankfully in 2022, things started to calm down. I had not expected how amazing and rewarding but also challenging this journey would become. After coming from the Caribbean and earning my master's degree at Maastricht University, and now my Ph.D. degree in Eindhoven, it has been an honor for me to get to this point in my life. Pursuing this degree has been a personal goal of mine for the longest time and one promoted by my family and my daily supervisor for my master's degree. I like to thank everyone who has been a part of this journey and allowed this thesis to come to fruition. I thank you all for your love and support.

I wish to begin by thanking the supervisor and promoter, Jos Brouwers, Ph.D. providing me with this opportunity and entrusted me with this Ph.D. project. Jos has been a key figure from day one, believing I can do anything and always open to great projects and collaborations, connecting me with amazing people providing me with feedback, and guiding my endless ideas into this publishable document. I always received new sources of information from the course he teaches or his connections. He was always available to provide me with valuable information about academia and industry, which I have learned to value deeply. I thank you for your support. It was invaluable for the next steps in my career. I would like to secondly thank my daily supervisor Katrin Schollbach, Ph.D., for her guidance in this project was critical for me to arrive at this final document. I could always count on her matchless skills in crystallography and knowledge of several building materials. Your door was always open to my insatiable questions and knowledge on the topics my brain would be running to find out. I would also like to thank my entire promotion committee. Without them, I would not be here today.

I want to thank the irreplaceable team of technicians who were always available and helpful in planning and fitting my experiments into the crazy scheduling while finding the equipment at Vertigo or elsewhere. Thank you, Anneke Delsing, Harrie Smulders, and Wout van Bommel.

I want to thank all the colleagues who have since gone on to do other work. They

favorably influenced my life at work, Kinga, Jawad, Johnathan, Winnie, Julien, and Marc. To my amazing colleagues and friends: Iris and Ricardo, whom I considered the best in their respective fields, could always be in awe of what they do. We were the 3 Musketeers, always the ones at the start of the pandemic. Thanks to Yari Foelen from the Chemistry department for helping me with chemical lab testing and setups. I would also like to thank Yuxuan for helping me at the start of this entire project. Without your knowledge, I would still be astray in how to manage olivine's reactions. I want to thank my friends outside the group, and my colleagues from the lighting group who always had a place for me when things got tough, thank you, Myrta, Verena, Maud, and Sietse. I thank the colleagues still here who give life to the department: Félix, Marina, Beatrice, Wei, Jia, Florent, Naomi, Zhihan, Daoru, Alex, Xuan, Zixing, Yan, Leila, Samuel, Helong, Yanjie, Zixiao, Samantha, Jinyang, Qingliang, Shashank, Ceren, Kingsley, Hoss, and the rest of my colleagues. I want to also thank the TCM team both friends and colleagues: Michaela Eberbach, Joey Aarts, Natalia Mazur, Martina Cotti, and Lisette Wijkhuijs. During my doctoral studies, I am glad to have had the experience and opportunity to supervise students Tessa, and Bram and co-supervise Michael, Bart, and Roeland. I am grateful for your help and contributions.

Now, I thank the people of my life, starting with my family in Puerto Rico, with whom I would not be here. Thank you, Sandra, for supporting me and being the amazing mother, you have been to me. I cannot thank you enough. My grandmother Lucy, for her courage, love, and motivation. To always believe in me without a doubt and for promising to witness this. You are both my rock and my core family. To my friends who have always been with me in the longest of distances and darkest of days. I thank you, Jorge Medina, Pablo Vega, Jorge "Jurian" Jimenez, Christian "Allen" Alvarez, Arturo Peralta, John Malvasia, Yanira Rivera, Claribel Pizarro, Glorivette Aguayo, Edgar Correa, Luis Ortiz, and Jose Abraham. My old supervisor Andrea Calore, thank you for putting me on this path. My local newfound friends have brought great hope and light into my life. I'd like to thank, Mart Smeets, Marty van Osch, Lode Comhair, Mathijs Vermeulen, Gabrielle Battaglia, Jurgen Boeren, Nazanin, Hector, Andre, Rita, Benjamin, Geert, Tom Franken, Owen, Athena, Rafaël, Jurgen, James, Martie, Kim, Sebastian, Sydney Dupasquier, May Sturman, Yassin, Steven, Alexander, Ludo, and Daniël Bolt. In memory of my late grandfather and his brother, who passed away during the years I have been overseas. I shall always remember these words: "Es mejor llegar segundo que primero en la carrera de la vida, ya que el segundo llega por su propio merito" [2] -Cervantes's excerpt from Don Quijote.

My journey and chapters of my Ph.D. show only a fraction of how amazing all these people have shaped and inspired me to grow and become the person I am today. I hope you can enjoy and appreciate the kindness and brilliance the effect of so many people can give to this work. This chapter of my life is one I shall never forget.

[2]This translates to "It is better to arrive second in the race of life because the person who does this, did so by their own merits".

Contents

List of Abbreviations

AUC Area Under the Curve.

CMC Carboxymethyl Cellulose.

CP Crystal Product.

CSA Calcium Sulphoaluminates.

DRM Dissolved Reference Mix.

DSC Differential Scanning Calorimetry.

DTG Differential Thermogravimetry.

Fe Iron.

FT-IR Fourier Transformed-Infrared Spectroscopy.

GS Glauber Salt/ Sodium Sulfate Decahydrate.

HEC Hydroxyethyl Cellulose.

IC Ion Chromatography.

ICP-OES Inductive Coupled Plasma Optical Emission Spectroscopy.

LOI Loss on Ignition.

Mg Magnesium.

MgO Magnesium Oxide.

MOS Magnesium Oxy-sulphate.

MRM Mechanical Reference Mix.

MTA Melting Temperature Apparatus.

Ni Nickel.

PCM Phase Change Materials.

TCM Thermochemical Material.

TES Thermal Energy Storage.

TGA Thermogravimetric Analysis.

XRD X-ray Diffraction.

XRF X-ray Fluorescence.

Chapter 1

Introduction

> "Sunlight will be used as a source of energy sooner or later anyway. Why wait?"
>
> —Maria Telkes, 1951

1.1 Background

The global pursuit of sustainable energy solutions has intensified interest in efficient Thermal Energy Storage (TES) technologies capable of balancing supply and demand in renewable-material driven systems. TES are divided into three categories based on their usage as presented on the following Table 1.1. Among these, phase change materials (PCMs) stand out for their exceptional energy density and ability to store and release heat at consistent temperatures. PCMs are a substance that undergoes a transformation in matter when reaching certain temperatures, leading to high amount of thermal energy storage. By harnessing heat mechanisms, PCMs offer compact, high-performance TES options for applications ranging from building climate regulation to industrial waste-heat recovery [1].

Table 1.1: Types of Thermal Energy storage.

TES	**Usage**
Sensible Heat Materials	Collect and store for later
Phase Change Materials	Active buffering system
Thermochemical Materials	On demand heating

PCMs undergo reversible phase transitions at predetermined temperatures—most commonly between solid and liquid states, although transitions such as solid-solid and hygroscopic (moisture induced) also exist. During melting, a PCMs absorbs its latent heat of fusion without a change in temperature; during solidification, that same energy is released [2]. Prior to any phase change, the material first experiences sensible heat

storage, where its temperature rises without altering its phase. In this regime, the stored energy is proportional to the specific heat capacity and temperature difference. Notably, latent-heat storage can exceed the energy stored by sensible heating by an order of magnitude per unit mass, providing efficient thermal management in constrained volumes [3]. While materials such as water or rock beds exhibit high thermal density and simplicity of implementation, they require significantly larger mass or volume to match the energy capacity of latent systems.

PCM's have a significant latent heat capacity (100-300 J/g) and have a large range of melting temperatures from -10 to 300°C [4]–[8]. The effectiveness of a PCM is governed by key thermophysical properties, including melting temperature, latent heat of fusion, specific heat capacities (in both solid and liquid states), density, and thermal conductivity. Disruption of some of these properties can lead to performance issues such as supercooling, a phenomenon in which the material fails to recrystallize below its crystallization temperature, thereby retaining the energy from the phase transition. Other common issues include volume expansion, which causes cracking due to repeated expansion and contraction during thermal cycles; low thermal conductivity, which slows down uniform melting; and phase segregation, where the material separates into distinct solid and liquid phases. Additionally, Yan et al. [9] defines salt hydrates to exhibit three melting behaviors—congruent, incongruent, and semi-congruent—where only congruent melting preserves full solubility, while incongruent melting irreversibly forms lower hydrates, reducing storage capacity. Optimization strategies—such as encapsulation to accommodate volume change, addition of nucleating agents to reduce supercooling, and incorporation of high-conductivity additives—address performance limitations and promote long-term cycling stability [10], [11].

PCMs are broadly classified into three categories—organic, inorganic, and eutectic—each offering a distinct balance of advantages and drawbacks [12]. Organic PCMs (e.g., paraffins, fatty acids) exhibit congruent melting and low corrosivity but relatively modest thermal conductivity and volumetric density. Additional information and details are provided on Chapter 3. Inorganic PCMs, such as salt hydrates and low-melting metals, deliver high latent heat and conductivity but can suffer from supercooling, phase segregation, and corrosivity without appropriate additives. Eutectic mixtures—binary or ternary blends of organic and/or inorganic constituents—offer tailored phase-change temperatures and often enhanced thermal cycling performance [13]. A table with advantages and disadvantages is presented in Table 1.2; the eutectic category is excluded, as it is typically a blend of existing PCM types.

Among these categories, salt hydrates stand out due to their unique phase-change dynamics and energy storage mechanisms. Alperts et al. [4] indicates that the mineralogic change of magnesium sulfate hydrates starts as an example, in Epsomite ($MgSO_4 \cdot 7H_2O$), and transforms into Hexahydrite ($MgSO_4 \cdot 6H_2O$), and finally ends in Kieserite($MgSO_4 \cdot H_2O$), as discussed extensively in Chapter 4. Each release of water from the crystal lattice represents stored energy that can potentially be recovered during cooling and recrystallization. These transformations involve multiple metastable states that are rarely stable under natural conditions, highlighting the need for a multidisciplinary approach to unravel the thermodynamics, kinetics, and

solid-state physics governing salt hydrate PCMs (Chapter 3).

When placed in the broader context of PCMs, the advantages of salt hydrates become even clearer through comparison with organic counterparts. Paraffin—one of the most widely used organic PCMs—has an energy density of 153 J/g and consists of long carbon-based alkane chains (waxes). While affordable and chemically stable, paraffin is more prone to flammability and degradation over time[6], [14]. Despite its widespread use, paraffin has a lower volumetric efficiency than salt hydrates, meaning that larger volumes are needed to achieve the same energy storage capacity. Salt hydrates, on the other hand, are safer, more abundant, and better suited for integration into building materials. An example of inorganic materials used in this research are Epsomite ($MgSO_4 \cdot 7H_2O$) which have a latent heat of 202 J/g and Glauber Salts ($Na_2SO_4 \cdot 10H_2O$) with a latent heat of 222J/g. Glauber salts are considered the standard inorganic PMC in building environments, as it is the most studied and examined PCM.

Despite their promise, practical deployment of PCMs in TES systems faces challenges including low intrinsic thermal conductivity, mechanical stresses from volume changes, and thermal cycling degradation. Recent advances in composite PCMs—incorporating metal foams, carbon-based nanomaterials, or other porous matrices—have demonstrated significant improvements in effective conductivity and structural integrity, moving PCMs closer to large-scale adoption in renewable energy and building-integration scenarios. However, their broader adoption is often hindered by issues such as phase separation, subcooling, and corrosion, which this thesis addresses in more detail in Chapters 4 and 5.

Table 1.2: Pros and Cons of Organic and Inorganic PCMs [8].

PCM	Pro	Con
Organic	- Long term use	- Supercooling
	- No phase separation	- High volume changes
	- Thermally stable	- Flammable
	- Low vapor pressure	- Low thermal conductivity
Inorganic	- High latent heat storage	- Corrosive
	- Non flammable	- Phase separation
	- High thermal conductivity	- Supercooling
	- Inexpensive	

1.2 Sensible Heat vs Latent Heat

Throughout this thesis the following two concepts are discussed repeatedly regarding PCMs: sensible and latent heat. Sensible heat is defined as the capacity of a material to store energy, increasing its temperature. The heat capacity and thermal flow/resistance

of the material play crucial parts concerning the material's behavior to store heat as temperature increases. Latent heat [15]–[19] is the energy stored for a material to change phases. During this point, the temperature of the material does not increase until the material has fully undergone phase change. This phase-changing point depends on the material's particular enthalpy of fusion, an interpretation of this can be seen on Figure 1.1.

The following equations represent the sensible heat:

$$Q_{SH} = \int_{T_i}^{T_f} mC_p \Delta T \tag{1.1}$$

and latent heat calculations [20]:

$$Q_{LH} = \int_{T_i}^{T_m} mC_{p(s)} \Delta T + mf\Delta H_L + \int_{T_m}^{T_f} mC_{p(l)} \Delta T \tag{1.2}$$

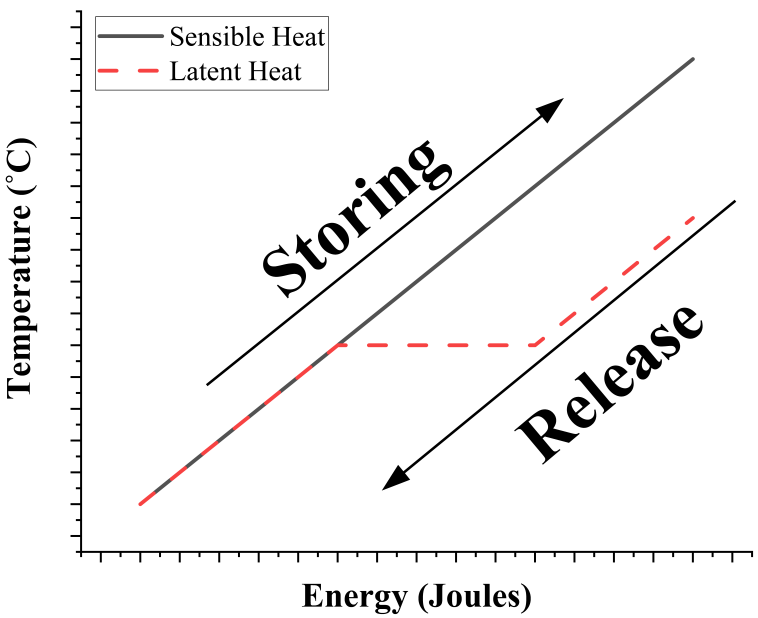

Figure 1.1: Simplified explanation on sensible and latent heat

T_i is the initial temperature in K, T_f is the final temperature in K, T_m is the melt temperature in K, m is the mass of material in kg, H_L is the latent heat of fusion in

J/kg, f is the melt fraction, c_p is the specific heat capacity of respective solids, liquids, or phases of the material in J/kg·K.

1.3 Applications

1.3.1 Thermal Batteries

As mentioned previously, salt hydrates can absorb significantly more energy per unit density than organic materials. This shows the true value of salt hydrates in storing thermal energy as thermal batteries. There are two common functions for thermal batteries: the initial definition is the storage of heat for the use of heat transfer for circulation, and the second is the transformation of heat energy into electrical energy.

Heat loss represents a major inefficiency in industrial and energy conversion systems, where approximately 40–60% of the total produced energy is released as waste heat instead of being converted into useful work [21]. Even with advanced recovery systems, a significant portion of this residual heat remains underutilized, underscoring the importance of efficient thermal management and storage strategies. As illustrated in Figure 1.2, various processes—ranging from electrical generation and hydrogen combustion to photovoltaic conversion—generate substantial amounts of recoverable heat that are often dissipated into the environment. Salt hydrate-based thermal batteries offer a means to capture and store this excess energy, transforming otherwise lost thermal output into a reusable resource for heating and energy balancing applications.

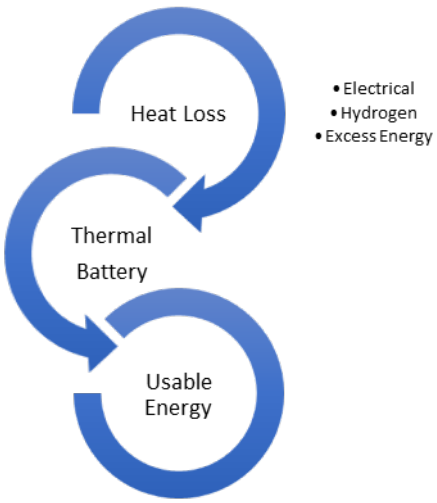

Figure 1.2: Circular heat energy overview.

As previously mentioned, thermal energy stored in salt hydrate systems can serve both heating and electricity generation purposes. At TU/e, a carbon-neutral battery concept was developed utilizing salt hydrates as a power source based on Thermochemical Material (TCM) mechanisms [22]. However, in most real-world applications, phase

change materials currently play a predominantly passive role, functioning as thermal buffers rather than active energy converters.

The passive performance of PCMs is where these materials have demonstrated the greatest practical benefit. By absorbing excess heat during periods of temperature rise through latent heat storage, PCMs help to prevent overheating and maintain indoor thermal comfort [23]–[27]. As the ambient temperature decreases, the stored energy is gradually released, providing a slow and consistent thermal output that reduces the need for external heating [7], [28]. In this way, salt hydrate PCMs act as smart, self-regulating thermal insulators that minimize energy fluctuations and lower the demand for mechanical heating and cooling systems.

This thermoregulatory capacity has significant implications for reducing peak energy loads in buildings and enhancing overall energy efficiency. When integrated into walls, floors, or ceilings, PCMs stabilize indoor temperatures, extend comfort periods without active HVAC intervention, and contribute to passive design strategies for low-energy or nearly zero-energy buildings.

In contrast, active PCM systems—such as those incorporating thermoelectric generators that convert temperature gradients into electricity via the Peltier effect [29]—remain largely theoretical for salt hydrate materials. Therefore, the focus of this thesis is on optimizing their passive performance for sustainable building applications, emphasizing how phase change processes can provide effective, low-maintenance, and environmentally responsible thermal regulation.

PCM batteries are implemented for seasonal thermal storage, offering a potentially sustainable solution for conserving heating and cooling energy and reducing costs [28], [30]. Currently, approximately 200 million households in the EU produce around 533 million tons of CO_2 emissions annually due to gas and oil heating [31], [32]. If each household could incorporate just 1 m^3 of inorganic salt hydrates PCMs with a storage capacity of 202 J/g [18], CO_2 emissions could be reduced by 3.05 million tons per year. If each EU household were to implement PCM-based thermal storage for approximately 150 cycles per year, an estimated reduction of up to 84% in heating-related CO_2 emissions could be achieved, highlighting the crucial role of salt hydrates in advancing climate goals [31], [33]. Given that the typical household requires 16 m^3 of thermal storage to cover its annual heating demand [34], illustrating the significant potential of salt hydrate PCMs in reducing both energy use and CO_2 emissions [33], [35].

The relevance of PCMs becomes even more critical when considering that, in the EU residential sector, approximately 77% of energy consumption is attributed to heating, compared to 21% is used for appliances and just 2% for cooling [36]. These percentages correspond to energy values of 2900.42 PJ for heating, 605.64 PJ for appliances, and 8.47 PJ for cooling. Notably, heating alone accounts for 25.9% of the total energy consumption across all sectors, underscoring its significant impact on overall energy demand.

Considering the disproportionate share of energy used for heating, it is essential to evaluate the thermal performance and practical applicability of materials suitable for

seasonal heat storage. Table 1.3 summarizes the key properties of selected phase change materials (PCMs) and sensible heat materials, allowing for a direct comparison of their thermal storage potential and associated economic benefits. The PCMs analyzed in this thesis include magnesium sulfate heptahydrate ($MgSO_4 \cdot 7H_2O$), magnesium chloride hexahydrate ($MgCl_2 \cdot 6H_2O$), sodium sulfate decahydrate ($Na_2SO_4 \cdot 10H_2O$), and paraffin wax, which are evaluated based on their energy storage density and cost-saving potential under typical heating conditions. For additional context, basalt and water—two common sensible heat storage materials used in construction—are also included to highlight the differences in storage mechanisms and capacities.

Table 1.3: Comparison of Some Thermal Storage Materials.

Phase Change Material	**Density**	**Latent Heat**	**Max Storage**	**Melting Temperature**	**Ref.**
	(g/ml)	(J/g)	(MJ/m^3)	(°C)	
$MgSO_4 \cdot 7H_2O$	1.68	202	339.36	48.5	[37]
$MgCl_2 \cdot 6H_2O$	1.47	170	249.90	117	[38]
$Na_2SO_4 \cdot 10H_2O$	1.57	222	348.54	32.4	[39]
Paraffin Wax	0.83	184	152.7	46-68	[40]
Sensible Heat Materials	**Density**	**Specific Heat Capacity**	**Max Storage @60°C**		**Ref.**
	(g/ml)	($J/g \cdot K$)	(MJ/m^3)		
Basalt	2.87	0.77	132.6	1450	[41]
Water	1.00	4.184	250.8	0	[42]

The comparison reveals several notable findings. First, in terms of volumetric energy storage capacity, salt hydrates generally outperform paraffin wax. Among the materials examined, sodium sulfate decahydrate exhibits the highest latent heat storage capacity at approximately 348.54 MJ/m^3, followed closely by magnesium sulfate heptahydrate with 339.36 MJ/m^3. These results clearly demonstrate the superior energy density of inorganic salt hydrates compared to organic PCMs such as paraffin wax, which offers a lower storage capacity of 152.7 MJ/m^3. When compared to sensible heat materials, the differences are even more pronounced. Basalt and water, despite their widespread use in thermal storage, offer much lower storage capacities of 132.6 MJ/m^3 and 250.8 MJ/m^3, respectively, based on a temperature difference of 60°C, a typical operational range for many applications [43].

Beyond their high energy storage capacity, salt hydrate PCMs offer significant environmental and economic advantages. In 2021, energy-related CO_2 emissions in the EU amounted to approximately 533 million tonnes, largely driven by residential heating [35]. If each of the 200 million EU households incorporated just 1 m^3 of inorganic salt hydrate PCMs with a storage capacity of 202 J/g [18], annual emissions could be reduced by 3.05 million tonnes. With an estimated 150 thermal cycles per year, this could translate to a reduction of up to 84% in heating-related CO_2 emissions [31], [33], underscoring the critical role of salt hydrates in achieving climate goals.

Economic considerations further reinforce the practicality of salt hydrates. Based on the average EU electricity price of €0.2889 per kWh [44], [45], the projected annual cost

savings per household are substantial. Magnesium sulfate heptahydrate and sodium sulfate decahydrate demonstrate the highest savings potential, estimated at €4084 and €4194 per year, respectively. While paraffin wax offers slightly lower savings, the superior energy density and lower environmental impact of salt hydrates make them more suitable for large-scale deployment.

Overall, the comparative analysis highlights the advantages of salt hydrates as high-performance, cost-effective, and environmentally beneficial materials for seasonal thermal energy storage in residential and building applications.

1.3.2 High Tech Applications of PCMs

TES is becoming increasingly important as energy demands for thermal regulation escalate, particularly in sectors with high computational intensity. A prominent example is the artificial intelligence (AI) industry, where energy consumption has surged due to the widespread deployment of GPU clusters and high-performance computing infrastructure. As of January 2023, the AI sector was responsible for approximately 539 tons of CO_2 emissions annually [46], largely driven by the substantial electricity required to power and cool data centers. The scale of energy use is significant: modern AI data centers can require up to 100 MW of continuous power, with 30–50% of that dedicated solely to cooling systems [47], [48]. As AI adoption expands, this thermal load is expected to grow even more rapidly.

In the EU, data centers have increased energy usage by 70%, and data transmission has seen a 64% increase in energy usage, accounting for 3% of all energy used in the EU. These figures are expected to increase by 1.5-2x in the next 5 to 10 years [49]. Google, for instance, admitted to using 21.2 billion liters of water for cooling in 2022, a 34% increase from the previous year, and this figure is estimated to increase by at least 3.79 billion liters of water per year [50]. Recent studies indicate that integrating PCMs into data center cooling systems can absorb excess heat during peak loads, thereby stabilizing thermal fluctuations and reducing the reliance on high-energy conventional cooling systems [15], [25], [26], [51], [52]. In this context, advanced cooling strategies already employed by tech leaders such as Google and Microsoft could be further enhanced by PCM-based solutions, utilizing salt hydrate phase change materials are particularly promising in this context due to their high energy density, non-flammability, and suitability for compact, modular designs.

Direct implementation mechanisms of PCM salt hydrates into these data centers, have three effective areas that can be applied into. The first and obvious implementation is replacing the already implemented organic PCM areas, this would extend the amount of energy stored/buffered that is available and reducing potential flammability. Second function would be to install in critical areas that require additional buffering such as GPU and CPU cores which require constant fanning and cooling. A third and most overlooked, is to store this excess heat and apply to other building functions that would require heat (i.e. thermal comfort, hot water, cleaning areas, food warmth, etc.)

These solutions described above are not merely theoretical; their practical effectiveness has already been demonstrated. For instance, Microsoft has reported that the imple-

mentation of thermal storage systems can reduce annual water consumption by 37.8 million liters per year, demonstrating that the industry is making strides towards more sustainable practices [53]. This success hints at the untapped potential of PCMs in both residential and industrial sectors. Currently organic PCMs are used in technology such as laptops in order to stabilize the heat of laptops with usage. The temperature range at which computer systems work are around 60-80°C [47]. However, for larger servers and data centers, the thermal energy provided greatly exceeds that of organics and provides higher risk of fire hazards. Water cooling and liquid cooling systems can be costly and required complex set ups and infrastructure redesigns. The use of salt hydrates as PCMs such as $Na_2P_2O_7 \cdot 10H_2O$ and $Ba(OH)_2 \cdot 8H_2O$ can manage the temperature range while having a higher thermal density to compensate.

Nonetheless, with the growing demand for energy due to sociopolitical factors and the limited supply of non-renewable sources, there is a need to reduce energy generation and focus on energy efficiency. The cost of energy rose by 25% in the last four years and continues to increase [44], [45], [54], highlighting the urgent need for more sustainable energy solutions [33], [55]. The use of salt hydrates as a material for thermal regulation and comfort could play a significant role in improving energy conservation and efficiency while helping the AI industry meet its growing energy demands more sustainably.

1.3.3 Building Applications

To fully appreciate the relevance of salt hydrates in contemporary energy systems, it is essential to consider their scientific and historical foundations, which laid the groundwork for current advancements in thermal storage. It is impossible to discuss salt hydrates PCMs without recognizing the significant scientific contributions of Telkes [56]. Her research on using solar energy led to the use of Glauber salts ($NaSO_4 \cdot 7H_2O$) as a heat storage battery in the mid-20th century, offering an alternative to traditional heating methods for homes. The idea was to remove the need to heat homes completely, from gas or other combustibles, and fully depend on solar heat to provide for thermal regulation year round. By storing solar heat and melting the Glauber salts that would provide heating long term. However, the initial design of the Telkes House in Massachusetts (Dover Sun/Solar House) faced sustainability and viability issues, as it required an exorbitant amount of salts, equivalent to a room's worth. Contemporary accounts report roughly 19–24 metric tons of material for a single residence and heavy reliance on powered fans to circulate heating, undercutting the net benefit [37]. Later models reduced the amount of material needed and improved design performance using the Trombe wall model [6]. This model works by circulating the heated air from the bottom-up using natural air density, through an opening above and below the wall, while the previous model required energy to move heat into the building using a housing attachment. A simple schematic overview is provided in Figure 1.3 for ease of understanding and comparing models.

While early studies required large quantities of salt—such as vats for solar heat storage—the development of refined processing techniques and innovative material formats has significantly improved efficiency [56]. For instance, modern PCM products

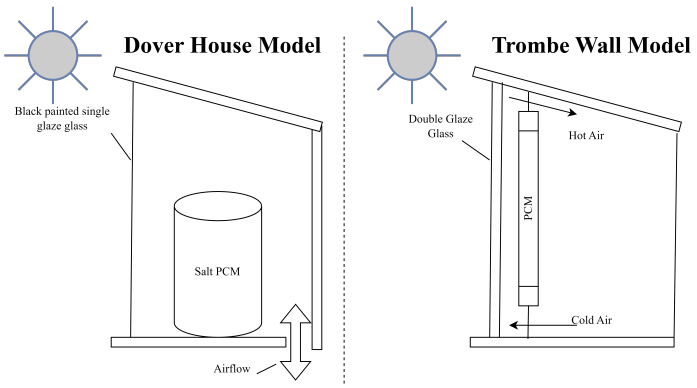

Figure 1.3: Visual schematic model comparison of Dover House vs Trombe Wall.

like microencapsulated beads, such as those developed by BASF in Germany [6], [57], require only a few hundred grams dispersed within building walls to achieve similar performance to the kilogram-scale installations used in early demonstrations like the Dover Sun House [6], [56]. This reduction in material volume, coupled with the salts' accessibility, highlights their practicality for integration into energy-efficient building systems using passive thermal energy storage and scalable heat exchanger technologies.

Passive thermal energy storage using PCMs involves embedding these materials into building components such as walls, ceilings, floors, or insulation layers. As indoor temperatures fluctuate, the PCM undergoes phase transitions—typically melting during heat absorption and solidifying during heat release—thereby regulating thermal conditions without active mechanical systems. This integration can be achieved through direct mixing with construction materials (e.g., plasters, mortars, wallboards), encapsulation within panels or pellets, or layering within composite structures. The effectiveness of passive PCM systems depends on factors such as thermal conductivity, phase change temperature, and compatibility with surrounding materials, all of which influence the material's ability to stabilize indoor temperatures and reduce energy demand.

Modern thermal energy storage technologies have increasingly favored wax materials as the primary PCMs [40], [58]–[60]. This shift is not due to wax having superior performance compared to salt hydrates but, rather, waxes are easier to work with and tend to avoid adverse effects on other building materials, which salt hydrates often cause. Although research consistently demonstrates that salt hydrates absorb significantly more energy per unit density than waxes, their broader adoption is limited by two main drawbacks. First, phase separation occurs when the salt dissociates into its base components (ions, water, and anhydrous salt) and does not fully re-mix into its original form, thereby reducing its overall energy storage efficiency. Second, salt hydrates promote metallic corrosion due to their ionic nature [61]. Although this limits their compatibility with metal-based heat transfer systems, the greater challenge remains addressing phase separation, which continues to hinder their broader application.

By addressing the key limitations described earlier—through material innovation and sustainable sourcing—salt hydrate-based PCMs could play a transformative role in lowering carbon emissions, reducing energy costs, and improving the thermal efficiency of built environments. As this thesis will demonstrate, their potential can be significantly enhanced when they are upcycled, stabilized, and adapted for scalable, real-world applications.

1.3.4 Other Applications

Salt hydrate PCMs offer versatile and practical solutions across a wide range of thermal-management applications that extend well beyond traditional building comfort or electronics cooling. Their melting temperatures, which typically range between 8°C and 120°C, align closely with the thermal requirements of several industrial and agricultural processes. For instance, salt hydrates with melting points near 27–30°C can be effectively used for greenhouse climate control, maintaining optimal conditions for crop growth during day–night temperature fluctuations. At slightly higher temperature ranges (55–60°C), they can serve as heat stabilizers for meat drying or curing, while compositions that melt between 60°C and 88°C are well suited for pasteurization and sterilization in food and pharmaceutical manufacturing [21]. Moreover, due to their inorganic composition and high salinity, salt hydrates naturally inhibit microbial growth—an intrinsic advantage in food and drug processing environments that demand strict thermal and hygienic stability. Recent studies have demonstrated their practical use in systems such as wall-integrated greenhouses and food-processing chambers, where encapsulated salt hydrate beads provide passive temperature regulation while simultaneously suppressing microbial proliferation [62].

Although this thesis focuses on building-integrated thermal storage, the broad temperature applicability and intrinsic antimicrobial nature of salt hydrate PCMs mean that they can be easily adapted to other thermal applications, such as controlled-environment agriculture, thermal food processing, and pharmaceutical storage. Their suitability in these sectors underscores their multifunctional potential beyond construction, opening avenues for future research and application.

1.4 Scope and Objective

The main objective of this PhD project lies in the generation of sustainable salt hydrates as well as in designing new methods for building applications. Under the current project design, the main objective was to establish seasonal heat storage—a battery of sorts that could store significant heat during summer and retain it until winter. In today's energy landscape, upcycling salt hydrates is essential not only for reducing the investment costs associated with raw materials but also for enhancing their practical application in thermal management systems. By repurposing waste or secondary salt materials into high-performance PCMs, production costs can be lowered and economic viability increased for large-scale deployment. Ideally, the project would use the recycled salt obtained through a silica extraction process described in the thesis of Lazaro Garcia [63]. As formerly outlined, sustainable sourcing is of vital

importance when applying seasonal thermal heat storage on such a large scale.

The project is divided into three main aspects. The first part of the project characterizes and develops methods to generate a recycled salt hydrate. As will be discussed in Chapter 3.1, the overall thermal capacity of a salt hydrate depends on the purity of the salt. The higher the purity, the greater the potential energy storage up to the material's enthalpy of fusion. Therefore, the material extracted from Lazaro's project would have to be purified via an optimized method. This purification will be discussed in detail in Chapter 4.

The second part of the project consists of identifying the best method to improve thermal energy storage performance. Using known approaches, the thermal behavior of recycled salts could be optimized to improve melting and crystallization stability while absorbing and releasing heat via multiple thermal cycles. This improvement is discussed in Chapter 5.

The third and final aspect of this thesis is the design of methods for applying salt hydrates in building components while maintaining both sustainability and the possibility of upcycling in case of renovation. This concept is key, as many current salt hydrate implementations rely on significant amounts of plastic [64], [65] or silica glass [66], which limits sustainability and recyclability. Furthermore, optimizing the integration of these upcycled materials into building components and cooling systems can improve thermal efficiency and durability, ultimately contributing to a more sustainable and cost-effective energy infrastructure. The proposed solution is discussed and tested in Chapter 7.

However, one critical question addressed in this thesis is the effect that salt hydrates have on cementitious materials. In particular, to examine the chemical reactions between salt hydrates and different cements—such as CEM I, CEM III, and CSA—especially when these systems are exposed to seawater. Salt hydrates can interact, similarly to seawater when melted, with cement phases to induce changes such as chemical degradation, which may compromise structural integrity over time. For example, seawater exposure can accelerate ionic exchanges and trigger unwanted reactions in the cement matrix, affecting both the strength and durability of the material [67]. This thesis discusses in Chapter 6 these reactions in detail, exploring how the presence of salt hydrates influences the hydration processes, and ultimately, the overall development and performance of cementitious systems. By understanding these interactions, the aim was to propose strategies for mitigating adverse effects and improving the long-term stability of cement-based structures exposed to salts and their ions, especially with regard to their phase separation.

Salt hydrates can also be considered inherently sustainable because they are often derived from abundant natural resources or produced as byproducts of existing industrial processes. Rather than focusing solely on sourcing virgin minerals, a more valuable approach is to recover and repurpose salts that would otherwise be treated as waste streams. For instance, salts precipitated from industrial brines or effluents can be purified and stabilized for direct use as phase change materials if they exhibit suitable hydration states. This approach reduces both the need for new extraction and the

environmental impact associated with disposal, while also providing a cost-effective feedstock for thermal energy storage applications. In contrast to organic PCMs, which often rely on resource-intensive synthesis, hydrated salts offer a pathway where material availability and circularity can be readily integrated into practical design strategies.

The practical value of hydrated salts lies in their widespread natural availability [68]–[71]. These salts are commonly found in various geological formations and industrial by-products, making them an abundant and accessible resource for thermal energy storage applications. Their prevalence reduces the need for costly or complex supply chains, enabling more sustainable and decentralized deployment of thermal regulation systems.

1.5 Outline of Thesis

Chapter 1: Introduction: In this chapter, the thesis provides an overview of its objectives and scope, outlining the significance of TES and addressing the research problem or gap. Basic definitions and concepts related to TES systems are introduced, including key terms and an overview of different TES technologies. The structure of the thesis is then outlined, detailing the organization of each chapter and briefly summarizing their respective contributions.

Chapter 2: Methodology and Characterization Methods: The chapter offers an overview of characterization methods employed in the thesis, elucidating the techniques used to analyze the thermal and structural properties of PCM and salt hydrates.

Chapter 3: Thermodynamics and Melting Mechanisms of Salt Hydrates: This chapter delves into the theoretical underpinnings of TES, focusing on the thermodynamic equations relevant to PCMs and salt hydrates. It provides an in-depth exploration of the principles governing heat transfer and storage in TES systems, offering perspective on the selection and performance of PCMs materials.

Chapter 4: Phase Change Behavior of Sulfate Salt Hydrates Extracted from Olivine Nano-Silica Side Stream: This chapter presents the results and analysis derived from published research on the extraction of epsomite from olivine. These findings offer valuable insights into the feasibility of developing a sustainable salt hydrate TES material. The chapter critically examines the experimental outcomes, discussing their implications for the advancement of salt hydrate TES technology and highlighting potential avenues for further research and development.

Chapter 5: Thermal Stability of Recycled Salt Hydrates for Seasonal Thermal Heat Storage: This chapter explores the thermal behavior of epsomite extracted from olivine, building upon the findings presented in Chapter 4. Through thermal cycling experiments, the study investigates the effectiveness of various thermostabilizers, including nucleating agents and gels, in enhancing the performance of salt hydrates. By analyzing the results of these experiments, the chapter aims to provide deeper insights into the potential mechanisms underlying thermal stabilization and to identify strategies for optimizing the performance of salt hydrate materials for thermal energy storage applications.

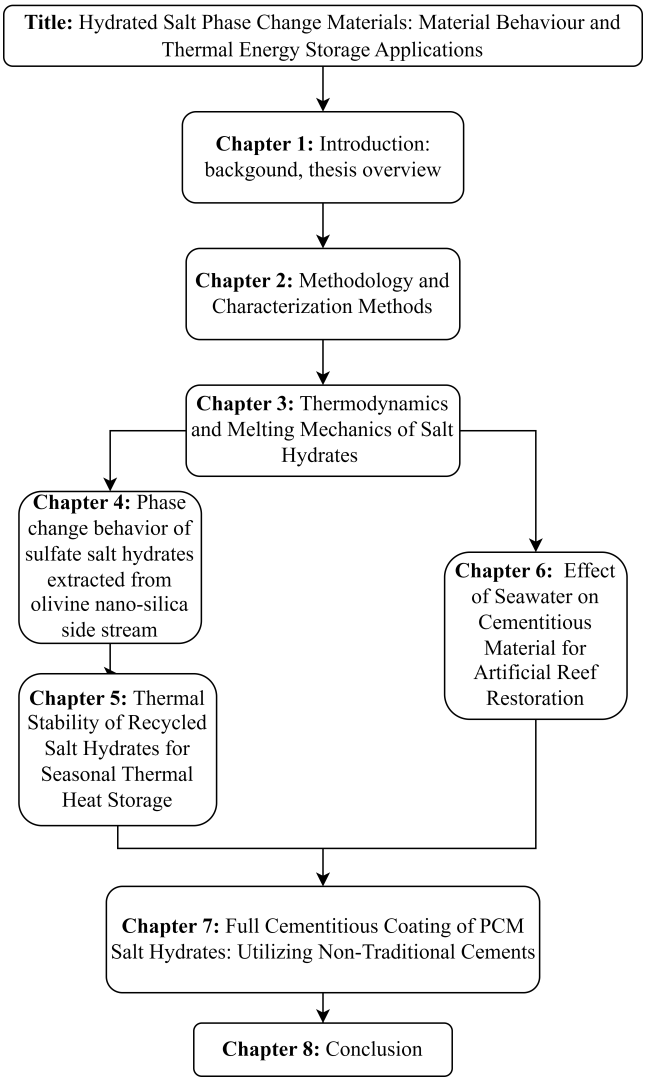

Figure 1.4: Thesis Outline.

Chapter 6: Effect of Seawater on Cementitious Material for Artificial Reef Restoration: This chapter investigates the potential use of carbonated cementitious materials, including CEM I, CEM III, and Calcium Sulphoaluminates (CSA), in the construction of artificial reefs. The study includes a viability assessment of the survival and growth of aquatic life within these structures. It also explores the chemical reactions that occur between salt solutions and cement, providing insight into the compatibility of these materials with salt solutions similar to those found in melted salt hydrates. Through experimental trials and ecological analyses, the chapter aims

to evaluate the suitability of carbonated cementitious materials for supporting marine ecosystems and enhancing biodiversity in underwater environments.

Chapter 7: Full Cementitious Coating of Salt Hydrates in a Vermiculite Matrix: Utilizing Non-Traditional Cements for Thermal Regulation: This chapter presents a proof-of-concept study involving Glauber salt as a PCM, encapsulated within expanded vermiculite cores and coated with cementitious material. The resulting pellets, measuring below 4mm in size, offer an alternative approach to PCMs encapsulation for building applications, facilitating thermal regulation. The efficacy of coatings, including CSA and Sorel Cement (Magnesium Oxy-sulphate (MOS)), is compared against an acrylate coating to assess their suitability for long-term performance and thermal stability.

Chapter 8: Conclusion: Combines all information from prior research to demonstrate the potential and impact of the research and its application methods for material research on recycled magnesium sulfate hydrate, and salt hydrates in general for modernized energy conservation and applications.

Chapter 2

Methodology and Characterization Methods

> "Every discourse, even a poetic or oracular sentence, carries with it a system of rules for producing analogous things and thus an outline of methodology."
>
> —Jacques Derrida

2.1 Introduction

This chapter outlines the suite of well-established material characterization techniques employed throughout the thesis. While these methods are commonly used in materials science, they have been carefully adapted to suit the specific properties and challenges presented by salt hydrates. Given the unique chemical and physical behavior of salt hydrates—including their hygroscopicity, solubility, electronegativity, and pronounced thermal responsiveness—standard protocols required thoughtful modification to ensure accurate and meaningful results.

These adaptations were essential not only to accommodate the general behavior of salt hydrates as a class of materials, but also to capture their performance as PCMs. The PCM functionality of salt hydrates introduces additional complexity, particularly in terms of thermal cycling, stability, and energy storage capacity. As such, the characterization techniques described in this chapter reflect both conventional best practices and targeted refinements tailored to the distinctive nature of salt hydrates.

By presenting these methodological adjustments in detail, this chapter provides a foundation for interpreting the experimental results that follow, and highlights the importance of context-specific approaches in materials research.

2.2 X-Ray Fluorescence

The use of X-ray Fluorescence (XRF) was for the identification of bulk chemical composition. The XRF determines the chemistry of a sample by measuring the fluorescent X-ray emitted from a sample when excited by a primary X-ray source. Samples were primarily prepared by performing a Loss on Ignition (LOI). This process required the crushing of material into powder using a mortar and pestle, ball mill, or disk mill. The required milling instrument depended on the toughness of the material to be crushed. Ideally, the material to be crushed into powder should be 0.5-1 mm in diameter. This powder was weighed and placed in a crucible and heated up to 1000°C for a minimum of 4 hours to ensure proper oxidation of the material using a high-temperature oven (Nabertherm P330). This released all volatiles of the material such as water, CO_2 and potential organics. The material was then weighed again to obtain the material's LOI. This oxidized sample was prepared in two ways. The first method comprised a pressed bead where 1-3 g of the material was mixed with 5 wt% of wax [84] and pressed into a pellet using up to 40N of force. This pressed pellet method is preferred for samples with high sulfate content because sulfate begins vaporizing at 800°C.

The second method, the fused bead method, where 1 g of the oxidized material was mixed in with 10 g of lithium tetraborate and a wetting agent of either 750μl lithium iodine (3-5 M), or 250 μl lithium bromide (5 M). The wetting agent was dependent on the presence of aluminum. If aluminum was present then iodine was used, as bromine interfered with the aluminum measurement. The mix was placed in the metal crucible. A predetermined program (slow heat-slow cool) is run on the PANalytical CLAISSE LeNEO to 1065°C for 13 min, rocked for 5 min 10 RPM at 10°, 6 min rocking at 30 RPM at 45°, 1 min rocking at 20 RPM at 30°, finalized with pouring and 5 min cooling at RT. The fused bead was measured using a caliper to determine its total volume (height and diameter). Then, the bead was placed and run on the PANalytical Epsilon3, where the material's was analyzed using the Epsilon 3 software. It gave the quantitative values of oxides and the composition of the material.

2.3 X-Ray Diffraction

To prepare a sample first the material was 0.4μ m powder, then 10wt% of crystalline silicone as internal standard was milled together (5ml max) in the X-ray Diffraction (XRD) mill (McCrone, Retsch). Then, the sample was placed in a D2 Phaser Bruker to measure from 5-90° (2θ) or in a D4 Phaser Bruker to measure for from 10-90° (2θ). Internal standard was not used for the salt hydrates. In order to not dehydrate the salt hydrate samples, scans were set to 0.5 seconds per step. This reduced measuring window was required for the salt hydrates being measured as they would melt due to the heat inside the machine. Both XRDs were performed using a Co-Anode (Kα1: 1.7901 Å and Kα2: 1.7929 Å) and a LynxEye detector. Samples were placed to rotate at 30 RPM, and measurement was 0.5 - 1 second per step, depending on sample. Qualitative analysis were conducted by X'pert HighScorePlus 2.2 (PANalytical), whilst quantitative x-ray diffraction analysis (QXDA) was performed using the software

TOPAS Academic 5.1. Primary cif data was obtained from the Crystallography Open Database.

2.4 Differential Scanning Calorimetry

Differential Scanning Calorimetry (DSC) was the analysis performed on a small amount of material and comparing absorbed or released energy (endo and exothermic) to an empty container, while the sample was heated or cooled. These measurements allowed to determine the glass transition temperature, where the material begins to soften, as well as the heat of fusion (melt), which quantifies the thermal energy stored or released during its phase transition or chemical transformation. DSC measured the release of heat when cooling where the crystallization of the material occurred. The measurement was conducted on the TA Instruments Q2000 on 2 mg of sample in a sealed aluminum cup, with a heating rate of 0.1-0.5°C/min from RT-120°C and cooling at 0.1-10°C/min back down to 0°C. Minor perforations were present at the lid in order to avoid steam buildup and possible explosion of the aluminum cup. The primary limitation of DSC analysis is that the small sample size is not representative of bulk material behavior, often resulting in discrepancies between laboratory measurements and real-world application performance. Analysis was performed using the program TRIOS from TA instruments. The DSC standards applied were based on the following protocols ISO 11357-1 [72], ASTM E793-06 [73], and ASTM E794-01 [74]. This method will be presented in more detail in Chapter 4.

2.5 Thermogravimetric Analysis

Thermogravimetric Analysis (TGA), a characterization technique, was used to estimate material decomposition by measuring the weight of material in an inert nitrogen environment while the temperature increased 10°C/min until reaching 1000°C. The weight of the material was tracked while the temperature increased. It helped to determine the general percentage of water and other components becoming volatile in the material. It was primarily used in this study to observe the thermal release of water in particular salt hydrates, determining whenever the material became anhydrous or decompoess into oxides. TGA was performed on a Netzch STA 449 F1 from RT to 1000°C at a rate of 10°C/min in Nitrogen flow of 20 ml/min and on a TA instruments TGA Q50 under the same parameters.

2.6 Fourier Transformed-Infrared Spectroscopy

Fourier Transformed-Infrared Spectroscopy (FT-IR) is the use of infrared wavelength to measure the covalent bonds of a material by exciting these bonds and measuring the remaining wavelength, resulting in a materials absorbency or transmittance. In this research, it was determined using reference measurements of sulfate salts for confirming the presence of sulfate [72]. FT-IR was measured using a Perkin Elmer Frontier with PIKE GladiATR attachment and 80 scans using wavelengths 4000 to

400 cm^{-1}. This method will be presented in more detail in Chapter 4.

2.7 Melting Temperature Apparatus

Melting Temperature Apparatus (MTA) was implemented to assess the melting of materials. This observation allows to track and verify a specific point at which a material would melt. The Buchi Melting Point M-565 with sample loader M-569 serves as MTA. The material was ground into a fine powder and subsequently packed into capillary tubes with a diameter of 1 mm, filling each to a height of approximately 1 cm. Then, the loader rocked the material to the bottom of the ampule without breaking it. Once the sample was loaded, it was placed in the M-565 apparatus. This device was capable of recording and evaluating the melting behavior of the material using visible light spectroscopy, by measuring the transmittance of light through the sample and correlating it with the degree of melting. The primary limitation of the apparatus was its lack of rapid cooling capacity; if the heating rate was too high, the system risked dehydrating the material before complete melting could occur. This device was employed in this research study to confirm the melting point of analytical and recycled materials.

2.8 Isothermal Calorimetry

The isothermal calorimetry measures the heat released in chemical reactions at a constant temperature. The Calmetrix I-Cal Ultra isothermal calorimeter was used to measure reaction heat released from the reaction of the setting of cementitious material. It was fully compliant with ASTM C1679 [75] and ASTM C1702 [76] standards. The amount of material added was based on a mathematical formula as seen in eq. (2.1). The dry material was added first into a 30 ml plastic vial, then mixed with the liquid portion determined by the upcoming equation. The mixture was vortex-mixed and immediately placed for measuring. The equation resumes the following relationship:

$$c_{pb} * m_b + c_{pw} * r * m_b = 20.8 J/g \tag{2.1}$$

Where c_{pb}, is the heat capacity of the binder, m_b is the mass of the binder, c_{pw} is the heat capacity of water, and r is the ratio of water to the binder. Based on this the amount of cementitious binder needed was calculated and combined with water to produce a capacity of 20.8J/g (heat capacity of reference). This methodology was used in the study of novel encapsulation of salt hydrates to assess the effect of these salts on the cementitious material.

2.9 Gas Pycnometer

The measurement of material density was performed using a gas pycnometer, specifically the Micromeritics AccuPyc II 1340. This instrument provides a highly accurate means of determining the volume and density of solid samples by applying the principles

of gas displacement. Helium gas is commonly used in such systems due to its small atomic size and inertness, allowing it to penetrate even the smallest accessible pores within a sample without reacting with the material.

The pycnometric method involves placing a known mass of the material into a sealed chamber. The instrument first records the pressure of helium gas in an empty reference chamber. The gas is then allowed to expand into the chamber containing the sample. By comparing the pressure differences between the filled and empty chambers, the volume of the solid (excluding open pores and voids inaccessible to gas) can be precisely calculated using the ideal gas law:

$$PV = nRT \tag{2.2}$$

where **P** is pressure, **V** is volume, **n** is the number of moles of gas, **R** is the universal gas constant, and **T** is the absolute temperature.

To estimate the rough porosity of the material, a second measurement was taken after crushing the sample into a fine powder. This approach increases the surface area and exposes previously closed pores. The difference in measured volume between the intact and powdered forms of the sample offers an approximation of the material's closed-pore volume, providing insight into its internal structure and compactness.

This method is particularly valuable in evaluating the structural characteristics of porous or composite materials, where conventional methods may fail to account for microstructural voids.

2.10 Manual Pycnometer

Manual pycnometers resemble the gas-based pycnometer with one difference, they determine the water absorption of the material as well. According to the C128-01 standard [77], glass pycnometers were employed to determine the water absorption of the material. This standard outlined the calculations and methods for performing the test.

Summarizing of standard ASTM C-128-01 of international standards is as follows. Approximately 500g of aggregate (adjusted to the pycnometer flask capacity, for instance, 250g for a 250ml flask) is measured out and mixed with 5% deionized water (dH_2O), then left overnight. The material is then dried using hot air to reach a saturated surface dry (SSD) condition, verified by shaping the material into a cone and lightly tapping it 25 times from a height of 5mm until it slumps. Next, 10g of water is added to the flask, followed by 500g of the SSD material, and the total weight is recorded [S]. The flask is filled with water to 90% capacity, agitated to remove bubbles, and then filled to the calibration line, with the weight noted [C]. The material is then removed from the pycnometer, dried in an oven at 110°C, and weighed again once fully dried [A]. The weight of the water at the calibration line (500ml = 500g) is denoted as [B].

2.11 Pelletization

Pelletization of materials comprises the ability to create small to large aggregates using a rotating drum while hydrating a dry material. The Eirich pelletizer TR04 (10L/12kg) was implemented to pelletize materials. The proper methodology is dependent on the material, the standard has a pre-weight amount of dry powder and a pre-weight spray bottle with water or reacting liquid. The powder rotated in the drum. It was sprayed with liquid until achieving the desired consistency. The size of the pellet depended on the speed and angle of the rotating drum. This method will be highlighted on Chapter 7 in more detail.

2.12 Strength Test

Automax5 Flexure and Compression machine was used to performed the testing. The EN196-1 standard [78], was applied to the testing of prisms of 40x40x160mm^3 for flexural and 40x40x40mm^3 for compressive testing. Concerning the nature of CSA, MOS testing time differed because of its rapid setting and curing. Therefore, timeline of testing for these materials happened on day 1,3,5,7, while all other materials were allowed 28 days to cure. Hydration was stopped using the standard RILEM TC-238 SCM [79], measuring hydration products through XRD.

2.13 Particle size distribution

glsPSD analysis was conducted for particles below 0.1 mm using the Fritsch Analysette 22 NeXT. The machine was filled with isopropanol as an inert dilution liquid. Background scans were performed to assess the impact of isopropanol (refractive index = 1.3902) on the beam. Solid powder was then added until 8-17% obscuration was achieved. The machine mixed the sample for 3 minutes with a constant flow and ultrasound to ensure even dispersion of powder particles.The sample was measured three times, and average values were reported.

2.14 IC / ICP-OES

The ICP-OES analysis was performed with the SPECTROBLUE ICP-OES, AMETEK. The samples were acidified using fuming nitric acid (1 ml per 30 ml of solution) to a pH of 2 and diluted 100 times to ensure that the ion concentrations fell within the margin of the standards.

IC chromatograms were obtained with a Thermo Scientific DIONEX ICS-1100 instrument. The concentration of cations sodium (Na^+), potassium (K^+) , magnesium (Mg^{2+}) and calcium (Ca^{2+}) were measured using ion exchange column CS12A (2 x 250mm) with eluent 20 mM Methasulfonic acid and an isocratic flow of 0.25 ml/min. Detection of ions was done by suppressed conductivity (Dionex DRS 600 2mm). This methodology is presented in more detail in Chapter 6.

2.15 Microscopy

The samples were analysed with an optical light microscope (Zeiss AxioImager Z2m) to study the microstructure of the samples. Initially, cross-sectional slices of the material were prepared for examination which were polished with a Struers Tegramin-30 machine using various grades of diamond based polishing paste and polishing cloth.

2.16 Thermal Testing

The ISOMET 2104 instrument, provided by Applied Precision, was used for this purpose. The measurements were taken using cylinders (h=2cm and r=3cm) as the measuring samples yielding values for thermal conductivity (λ), volumetric heat capacity (c_ρ), and thermal diffusivity (α). Measurements were conducted using surface probe 0.3-2.0W/m $\cdot$ K. The accuracy of the thermal conductivity measurement is 5% of the reading + 0.001W/m $\cdot$ K. For the volume heat capacity the accuracy is is 15% of reading + 1 J/m^3 $\cdot$ K. Thermal diffusivity is based on calculations from readings:

$$\alpha = \lambda / c_\rho \tag{2.3}$$

Chapter 3

Thermodynamics and Melting Mechanics of Salt Hydrates

"Theory without practice is just as incomplete as practice without theory"

—Assata Shakur

The material presented in this chapter is being developed into the following manuscript:
Wesemann, C.A., Schollbach, K., & Brouwers, H.J.H. Review on the Melting Mechanics of Salt Hydrate PCMs: from Fundamental Principles to Applications of Salt Hydrates in Thermal Energy Storage (in preparation).

3.1 Introduction

Salt hydrates have emerged as promising materials for thermal energy storage due to their ability to store and release significant amounts of latent heat during phase transitions, which distinguishes them from more conventional materials, such as paraffin waxes, anhydrates compounds or metals. However, the melting mechanisms of salt hydrates are far more intricate than those of conventional materials, involving the influence of water coordination, ionic strength, hydrogen bonding, and osmotic activity [80]. These complexities challenge traditional thermodynamic models and necessitate a deeper understanding of the underlying mechanisms [81], [82].

In addition, the role of water coordination in stabilizing or destabilizing the crystal lattice is discussed in detail, highlighting how kosmotropic and chaotropic ions influence thermal performance. The crystal lattice itself is defined as a regularly ordered, three-dimensional structure of atoms, ions, or molecules, composed of repeating units known as "unit cells" [83]. The discussion also considers the influence of crystal defects, such as Frenkel and Schottky defects on the thermal characteristics of salt hydrates, particularly in systems derived from waste sources and further observed in Chapter 4.

Building on this foundation, the following sections introduce theoretical frameworks for predicting the thermodynamic properties of salt hydrates, including lattice energy, enthalpy, entropy, and heat capacity. Models such as the Glasser–Jenkins approach, the Modified BET model, and the *slPCMlib* are examined for their roles in supporting the selection and optimization of salt hydrates for targeted thermal energy storage applications.

Several predictive models have been specifically developed for salt hydrates. For instance, the Glasser–Jenkins model offers a robust framework for estimating the thermodynamic properties of ionic solids and liquids, such as potential energy, heat capacity, and melting temperature [84]. Similarly, the modified BET model and *slPCMlib* contribute to understanding phase behavior and heat transfer characteristics across a range of hydrated salt systems. These tools enhance the predictive precision needed for selecting PCMs tailored to specific thermal performance requirements. A detailed discussion of these models is presented in Section 3.8.

A key conceptual insight connecting these models is the idea that the thermodynamic behavior of salt hydrates is fundamentally governed by the spatial arrangement of ions and associated water molecules. This concept parallels the role of the Madelung constant in solid-state physics, which quantifies the net electrostatic interactions within an ionic crystal lattice. Specifically, the Madelung constant represents the sum of attractive and repulsive Coulombic forces determined by the geometry and lattice parameters, and is crucial for explaining cohesive energy, melting point, and phase stability in crystalline systems.

By integrating theoretical predictions with empirical observations, this chapter aims to provide a comprehensive understanding of the thermal behavior of salt hydrates, thereby informing their development and implementation in next-generation thermal energy storage systems.

3.2 Thermodynamics of Salt Hydrates

Thermodynamics provides the framework to understand and predict the behavior of salt hydrates as PCMs. Central parameters such as temperature and pressure govern physical quantities including energy, enthalpy, and entropy—values that ultimately determine how a material responds during melting, freezing, condensation, or sublimation. For PCMs in particular, these transitions are not simply physical curiosities but the very mechanisms through which energy can be stored and released in a controlled and reversible manner.

The Gibbs free energy equation ($\Delta G = \Delta H - T\Delta S$) provides a baseline for the mechanism of phase transitions: a negative ΔG signals that melting or crystallization is thermodynamically favorable under given conditions. This interplay between enthalpy (ΔH), entropy (ΔS), and temperature (T) is central to PCM functionality, as the latent heat storage capacity (ΔH_f) is directly linked to the entropy change that accompanies a phase transition. The melting temperature (T_m) thus emerges as a defining threshold for salt hydrates, reflecting the delicate balance between lattice energy, hydration shell dynamics, and the surrounding thermodynamic environment.

Beyond the Gibbs formalism, other thermodynamic relations provide crucial insights into PCM performance. The mole fraction equation, derived from the Clausius–Clapeyron relation, illustrates the sensitivity of phase equilibria to solute concentration and explains melting point depression in non-ideal salt hydrate systems. Similarly, the Helmholtz free energy and grand potential (Ω) contextualize stability in confined or surface-active systems, where interfacial effects play a pronounced role.

Altogether, these thermodynamic parameters and equations form more than just a theoretical foundation—they directly shape the design and practical application of PCMs. By quantifying how salt hydrates absorb, store, and release energy, thermodynamics not only clarifies the fundamental mechanisms at play but also highlights the intrinsic challenges, such as entropy-driven disorder and structural instabilities, that limit the efficiency and reliability of these materials.

3.3 Melting Mechanics of Salt Hydrates

In general, melting refers to the excitation of atomic or molecular structures, resulting in the breakdown of a solid's ordered lattice into a disordered liquid phase [85], [86]. This behavior is typically observed in all materials, including metals and anhydrous salts, where increased thermal energy weakens intermolecular or ionic bonds, allowing for free molecular movement in the liquid state [87].

However, the melting behavior of salt hydrates deviates significantly from this classical view. In these systems, the term *molten hydrates* is often used to describe the intermediate phase formed during melting [88]. Rather than undergoing a straightforward phase change, hydrated salts exhibit a transition in which their crystal lattice adopts aqueous-like properties without fully dissolving. During this process, water molecules within the structure coordinate with both cations and anions, loosening the lattice while maintaining partial structural integrity. This unique change leads to properties

such as low water activity, high acidity, increased viscosity, and a marked tendency toward supercooling [89], [90].

Voigt et al. [89] described hydrated salts as maintaining solid-state behavior within a narrow water-to-salt ratio of roughly 4:1 to 7:1. Ratios below this range promote dehydration and lattice collapse, while excess water leads to deliquescence and solution formation. This defines the compositional window where salt hydrates function effectively as PCMs.

This phase transition represents a dynamic interplay between melting and dehydration processes. As illustrated in Figure 3.1, adapted from Voigt et al. [89], the behavior of salt hydrates spans a continuous spectrum from overhydration to complete dehydration [34], [91]–[93]. This overhydration disrupts ionic cohesion and water–cation coordination, leading to deliquescence, also referred to as the dissolution of the salt into an ionic solution [38], [71], [94], [95]. This excess water stems from the same crystal structure where dehydration from one unit is over hydrating others. Leading to multiple layers of different hydrates and a super saturated deliquescent solution [90]. In contrast, under controlled conditions such as: carefully managed temperature, heating rate, humidity, and pressure; salt hydrates can undergo a transition into a molten state, enabling thermal energy storage [93]. A good example of this is presented in the Figure 3.1 with magnesium sulfate salt. At standard temperature and pressure, only epsomite is thermodynamically stable, but in colder or even low pressure environments epsomite might hydrate into a 11 water form (Meridianiite) primarily seen in outer space [96]–[98], and extreme lab conditions. while melting of epsomite may also dehydrate as discussed in detail in Chapter 4, many lower hydrates can form until reaching full anhydrous state.

Yan et al. [9] described this melting behavior as a temperature–pressure equilibrium state, occurring just before the dehydration line. At this point, the vapor pressure of the coordinated water surpasses the thermal energy threshold required for dehydration, allowing the material to enter a semi-liquid or molten state. Crucially, this transition is not dependent solely on temperature, but also by the slow rate of heating as well as water vapor pressure.

This melting–dehydration mechanism can be schematically represented by the following reaction:

$$MX \cdot nH_2O_{(s)} \rightarrow MX \cdot mH_2O_{(s)} + (n-m)H_2O_{(l)} \tag{3.1}$$

In Equation (3.1), M represents the metal cation, X the anion, and n the initial number of water molecules. This equation illustrates that melting in salt hydrates is accompanied by partial dehydration, producing a lower hydrate ($MX \cdot mH_2O$) and releasing liquid water. This differs fundamentally from classical melting, such as that observed in metals, where the chemical composition remains unchanged through the phase transition [21], [99].

As demonstrated by Yan et al. [9], the phase-change behavior of salt hydrates is strongly dependent on external conditions such as heating rate and humidity. For

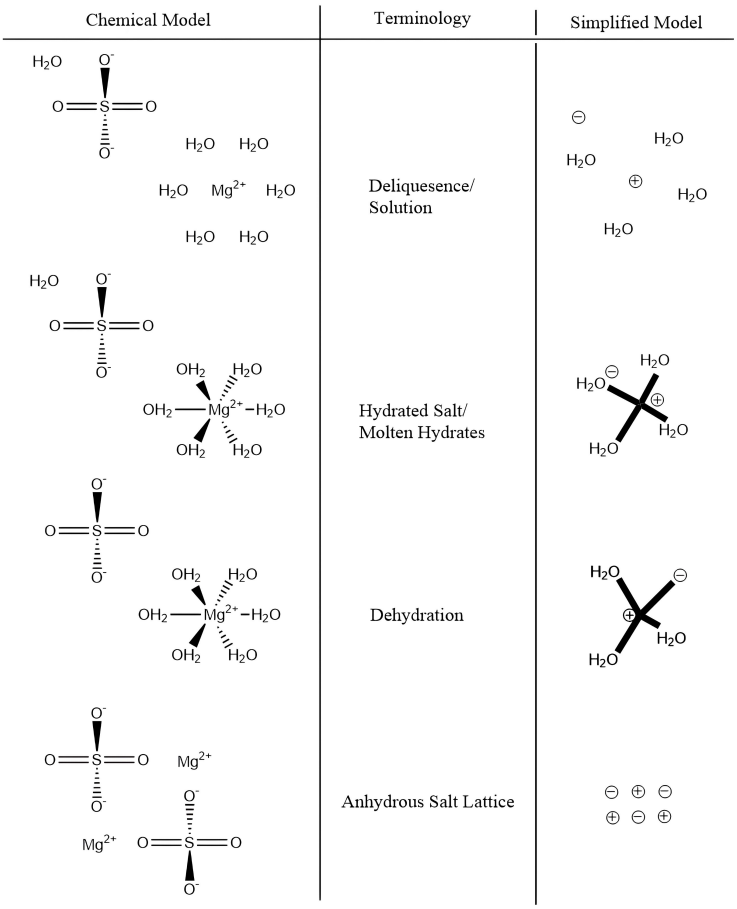

Figure 3.1: Melting mechanics overview, adapted from Voigt et al. 2002.

example, in epsomite ($MgSO_4 \cdot 7H_2O$), heating rates above 0.1 °C min $^{-1}$ induce incomplete dehydration, shifting the material's behavior toward a thermochemical mechanism rather than a reversible phase change. Maintaining low heating rates and sufficient vapor pressure enhances the stability of the hydrate phase, emphasizing the kinetic sensitivity of salt hydrate PCMs.

The release of water during this process involves chemical bond rearrangement, altering both the structure and properties of the material [87], [100], [101]. As a result, the thermal storage capacity and release behavior of salt hydrates are governed not only by latent heat but also by the kinetics of the dehydration reaction [34]. This distinction highlights the importance of understanding the dual role of phase change and chemical transformation in the design of salt hydrate-based thermal energy storage systems.

Yan et al. [9] further emphasized that this two-step mechanism, a partial dehydration followed by complete dissociation or release, defines how salt hydrates function in

TCMs. In one scenario, known as deliquescence [94], [102], the water released during dehydration acts as a solvent, fully dissociating the salt into its ionic components, as illustrated below:

$$MX \cdot mH_2O_{(s)} + (n-m)H_2O_{(l)} \rightarrow M^+_{aq} + X^-_{aq} + nH_2O_{(l)} \tag{3.2}$$

In this reaction, the liberated water facilitates complete dissolution, allowing the salt to exist in ionic form. However, more commonly, the dehydration process results in the formation of an anhydrous salt, with the water being released as vapor rather than forming a solution. This divergence between solution formation and vapor-phase water release is critical for determining the kinetics, energy storage density, and reversibility of salt hydrate systems. Understanding the interplay between physical phase change and chemical transformation is therefore essential for accurately modeling and optimizing the energy storage behavior of salt hydrates.

Despite the extensive interest in salt hydrates as PCMs, there remains a substantial knowledge gap regarding the fundamental mechanisms that govern their behavior. Specifically the question is: what is the molecular kinetic behaviour of melting for salt hydrates? This lack of understanding has led to repeated failures in accurately simulating and reliably analyzing the unique and often unpredictable properties of salt hydrates. Current models frequently oversimplify their melting behavior, neglecting the complex interplay of structural and chemical factors [103], [104]. In particular, water coordination within salt hydrate crystals, the kosmotropic/chaotropic nature of their ions, crystal lattice energy, and the presence of water pores and crystal defects all play critical roles [105]. These factors, examined in detail later in this chapter, are precisely what set salt hydrates apart from conventional PCMs and distinguish their behavior from purely thermochemical mechanisms. Without addressing these intricacies, the development of predictive models and practical applications of salt hydrates as PCMs will remain severely constrained.

3.4 Supercooling Mechanisms

The influence of lattice defects and hydration state extends directly to supercooling phenomena. Variations in crystal energy and the absence of ideal nucleation sites elevate the energy barrier for crystallization, explaining why many salt hydrates exhibit deep supercooling during repeated cycles. One of the most critical intrinsic behaviors of salt hydrates that affects their energy storage potential is supercooling. Supercooling or undercooling, refers to the phenomena where a liquid stays in a metastable state below its freezing temperature without turning into a solid. Although, in supercooling systems, nucleation is kinetically suppressed, so despite favorable thermodynamics, the phase change may not occur without external trigger [23]. This behaviour is prevalent in salt hydrate PCMs and presents both opportunities and challenges in TES systems. Multiple factors contribute to supercooling as shown in the following Table 3.1.

Supercooling is the difference between the melting temperature (T_m) and freezing onset temperature (T_F) as represented as follows:

Table 3.1: Factors that contribute to Supercooling.

Factor	Effect on Supercooling	Remarks	Ref
Purity of PCM	Increases supercooling	Fewer impurities = fewer nucleation sites	[23], [106]–[108]
Encapsulation Size	Increases supercooling (especially micro/nano)	Smaller volumes reduce probability of critical nucleus formation	[106]
Cooling Rate	Increases supercooling	Rapid cooling increases viscosity, prevents molecular rearrangement	[23]
Surface Roughness	Decreases supercooling	Rougher containers promote heterogeneous nucleation	[23]
Wettability (hydrophobicity)	Increases supercooling	Hydrophobic surfaces reduce contact and nucleation efficiency	[107]
Nucleating Agents	Decreases supercooling significantly	Additives like graphite, AgNPs, or carbon fibers enable controlled freezing	[23]
External Stimuli (active)	Eliminates supercooling on demand	Includes pressure pulses, or ultrasound	[23]

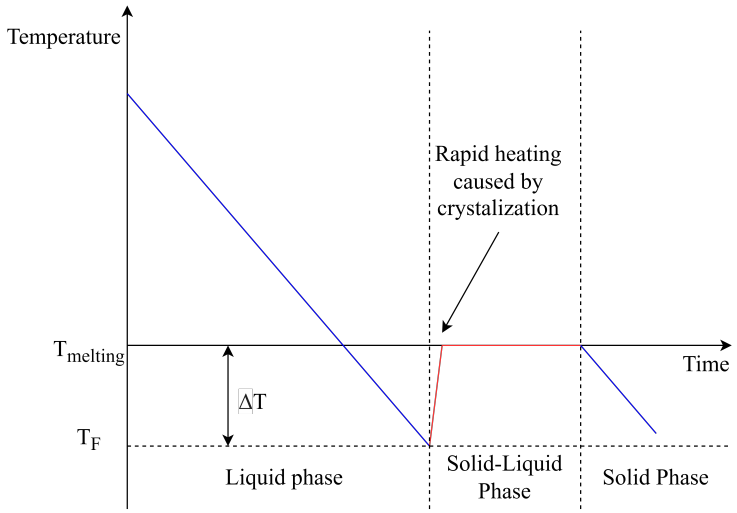

Figure 3.2: Visual presentation adapted from Samah et al. [107]

$$\Delta T = T_m - T_F \tag{3.3}$$

This is shown best on the Figure 3.2 adapted from Samah et al. [107].

In salt hydrate PCMs the degree of supercooling can range from a few degrees to just over 100K depending on composition and encapsulation methods [23]. While this allows the material store latent heat for extended periods, uncontrolled supercooling impedes predictable energy release and requires nucleation triggers to commence solidification [23]. In order to force a phase transition, it first requires the formation of a stable nucleus. According to classic nucleation theory, this process involves the balance between surface energy and volume energy contributions to the Gibbs free energy change ($\Delta G = \Delta H - T\Delta S$). The following equation expands on this as follows:

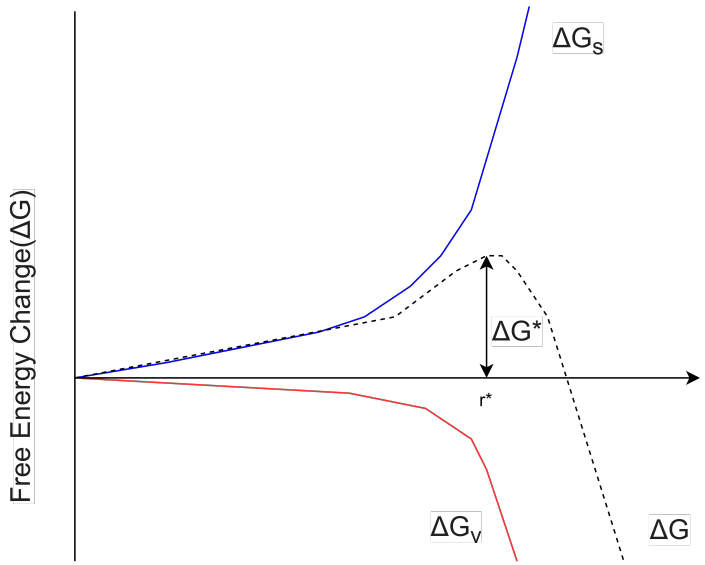

Figure 3.3: Energy competition in a nucleation even adapted from Beaupere et al.[23]

$$\Delta G = \Delta G_s + \Delta G_v = 4\pi r^2 \sigma_{SL} + \frac{4}{3}\pi r^3 \Delta g \tag{3.4}$$

In this equation r refers to the radius of the nucleus, σ_{SL} refers to the solid liquid interfacial energy, Δg refers to volumetric Gibbs free energy that has its own equation:

$$\Delta g = \frac{L\Delta T}{T_m} \tag{3.5}$$

Here the only new variable is L where it refers to latent heat per volume.

All this correlates to the critical radius r^* at which the nucleus becomes stable and is derived from minimizing ΔG with respect to the radius as per the following equation:

$$r^* = \frac{2\sigma_{SL} T_m}{L\Delta T} \tag{3.6}$$

This relationship highlights that a larger supercooling degree (ΔT) reduces the critical radius, thereby promoting nucleation. In fig. 3.3 , it demonstrates that the relationship of ΔG_v and ΔG_s is competitive showing that as surface effect increases, it reduces the particle size and stability, while volume effects leads to increase in size and stability.

There are two main methods to manage supercooling with PCMs the strategies that are commonly employed are passive and active methods. In passive methods involve adding nucleating agents such as nanoparticles, fibers, or surfaces with micro-texture. This decreases the ΔT up to 90% by providing heterogeneous nucleation sites [23]. In

active methods the use of external stimulu like ultrasonic waves, pressure pulses, or seed crystals induce nucleation on demand [23].

Supercooling in itself can be a beneficial tool for TES if controlled, however due to its unpredictable nature provides a significant deterrent of usage. Therefore understanding the mechanism of function and applications for corrections provide insight in PCM-TES systems design, especially for salt hydrates.

3.5 Water Coordination of Salt Hydrates

Ionic interactions with water molecules play a crucial role in the behavior of salt hydrates, and can be broadly categorized according to the kosmotropic–chaotropic classification system. *Kosmotropic ions* promote strong structural coordination with surrounding water molecules, enhancing hydration kinetics and reinforcing hydrogen bonding networks. In contrast, *chaotropic ions* disrupt water structure and hydrogen bonding, and typically exhibit slower hydration kinetics.

A common method for classifying these ions relies on the Jones–Dole viscosity coefficient, denoted as B, which appears in the following empirical relationship:

$$\frac{\eta}{\eta_0} = A\sqrt{c} + Bc \tag{3.7}$$

Here, η represents the viscosity of the electrolyte solution, η_0 the viscosity of pure water, c the concentration of the solution, A a coefficient accounting for ion–ion interactions (based on Debye–Hückel theory), and B the Jones–Dole coefficient [109]. A positive B value indicates kosmotropic behavior, whereas a negative B value corresponds to chaotropic behavior. While this classification originates from biochemical studies particularly in protein hydration contexts it has relevance for understanding water coordination in salt hydrates as discussed by Casimiro [110].

The kosmotropic–chaotropic classification of ions also shapes hydrate stability. Fully kosmotropic salts such as $Na_2SO_4 \cdot 10H_2O$ exhibit strong coordination and high latent heat, whereas mixed or chaotropic systems (e.g., $MgCl_2 \cdot 6H_2O$) display weaker binding and are prone to hydrolysis or decomposition to $Mg(OH)_2$ and HCl. These distinctions highlight the significance of ion–water interactions for PCM reliability.

According to Huynh et al. [111], the coordination behavior of water in salt hydrates is influenced by both the ionic radius and the number of valence electrons of the cation. As the ionic radius increases, it becomes more difficult to form water coordination, whereas higher electronegativity of the ion strengthens the coordination. These factors determine the minimum water-to-cation molar ratio required to form stable coordination structures. Their study also highlights that these hydrate structures store measurable free energy, indicating an enthalpic component associated with water coordination.

Thermal property measurements of selected salt hydrates further support this theory. For example, Iron(II) Nitrate Hexahydrate and Nickel(II) Nitrate Hexahydrate exhibit

melting temperatures (M_t) of 60.5°C and 57°C, and enthalpies of fusion (H_f) of 126 J/g and 169 J/g, respectively [112]. Similar trends are observed in Zinc Nitrate Tetrahydrate and Magnesium Nitrate Tetrahydrate, which have M_t values of 45°C and 47°C, and H_f values of 145 J/g and 142 J/g, respectively [112]. These values reflect not only the strength of water coordination but also the enthalpic rigidity of the hydrate structure.

The coordination environment can be further modulated by doping anions into the crystal lattice. This substitution disrupts the water–ion interactions, lowering the overall entropy of the system and altering its thermal response [111]. A tightly coordinated system stores more enthalpic energy, while loosely bound or free water contributes to greater entropic freedom. As such, systems with high entropy are more susceptible to destabilization, making dehydration more likely [87].

As Wells [87] observed, the stability of hydrated salts depends not only on ionic radius and charge but also on the number and spatial configuration of water molecules bound within the lattice. Even a single loosely coordinated water molecule can alter thermal behavior: for instance, in epsomite, the seventh water molecule is weakly bound, rendering the hexahydrate ($MgSO_4 \cdot 6H_2O$) more thermodynamically stable under thermal cycling.

These observations underscore that the role of water in salt hydrates extends beyond coordination—it also acts as a structural stabilizer and an energy carrier within the lattice. Theoretically, water molecules moving throughout the material can behave as either stabilizing agents or dynamic binding components. For example, the loosely and molecularly bound water found in opals behaves similarly to that in many salt hydrates [113]. The removal of these molecules typically requires temperatures exceeding 100°C, corresponding to the energy necessary to overcome both hydrogen bonding and partial ionic or covalent interactions. When water molecules are strongly coordinated, the total enthalpic energy of the system increases, but flexibility and reversibility may decrease. Conversely, weaker coordination allows higher molecular mobility but increases the likelihood of underhydration, overhydration, and lattice defects. Thus, the water within the crystal plays a critical role in determining both the energetic potential of the material and its structural integrity under repeated thermal cycling.

These combined thermodynamic and structural considerations highlight a key research gap in correlating kosmotropic–chaotropic behavior, water coordination strength, and long-term phase stability. Understanding these relationships is crucial for optimizing salt hydrates as phase change materials in thermal energy storage.

3.6 Crystal Lattice Energy: Implications for Phase Behavior of Salt Hydrates

Crystal lattices can adopt multiple structural arrangements, even when chemically identical. A classic example is calcium carbonate, which exists in polymorphs such as calcite, aragonite, and vaterite, each with a distinct lattice structure despite sharing the same chemical formula. These variations arise from differences in the spatial

arrangement and bonding strength of ions within the lattice, which directly affect its overall potential energy. In salt crystals, this lattice potential energy originates primarily from electrostatic interactions governed by Coulomb's law:

$$U = -\frac{kQ_1Q_2}{r_0} \tag{3.8}$$

Here, U is the lattice potential energy, Q_1 and Q_2 are the charges of the interacting ions, r_0 is the equilibrium distance between them, and k is the electrostatic constant (8.988×10^9 $\mathrm{Nm^2/C^2}$). This expression shows that lattice energy increases with ionic charge and decreases with interionic distance. However, to account for both attractive and repulsive interactions, the Born–Landé equation offers a more comprehensive model:

$$U = \frac{N_A M Z^2 e^2}{4\pi\epsilon_0 r}(1 - \frac{1}{n}) \tag{3.9}$$

In this equation, N_A is Avogadro's number (6.022×10^{23} $\mathrm{mol^{-1}}$), M is the Madelung constant, Z is the ionic charge, e is the elementary charge (1.6022×10^{-19} C), ϵ_0 is the vacuum permittivity (8.85418x10^{-12} $\mathrm{C^2/(J \cdot m)}$), r is the interionic distance, and n is the Born exponent, which accounts for repulsive forces and is determined empirically. Since most variables are constants, the interionic distance r and the Madelung constant M become the dominant factors in determining lattice energy.

An alternative expression derived from Coulombic principles, incorporating a repulsion term, gives the potential energy at equilibrium as:

$$U(r_0) = -(\frac{Mve^2}{4\pi\epsilon_0 r_0})[1 - \frac{\rho}{r_0}] \tag{3.10}$$

Here, v is the number of ion pairs per formula unit, and ρ is the repulsion coefficient. As ρ is typically small relative to r_0, the Madelung constant remains the most influential term.

The Madelung constant itself quantifies the net electrostatic interactions within a crystal lattice, accounting for the long-range periodic arrangement of ions. According to Banerjee, [114], if the disorder increases, Madelung's constant decreases. Hence, the true value of the energy concerning the lattice energy is $\leq$ M. When combining Banerjee, [114] and Baker 2010 [115], a simpler formulation where the Madelung's constant (α) is formed and is computed through summations over lattice coordinates:

$$M = \alpha = \sum_{i=1}^{N} \frac{\pm Z}{r_i} \Rightarrow r_i = \sqrt{x_i^2 + y_i^2 + z_i^2} \tag{3.11}$$

In this formulation, r_i represents the distance of the i^{th} ion from a reference ion at the origin (0,0,0), and Z is the ionic charge. In practice, this sum is computed

numerically using software such as Mathematica or Python, extending to many layers of neighboring ions in 3D space. The calculation is often illustrated using a 2D lattice as a simplified model: a central ion (full charge) is surrounded by ions along the x- and y-axes (each with half charge) and at diagonal positions (quarter charge), extended further along the z-axis in a 3D model. Such summations, when expanded to dozens or hundreds of layers, reveal the convergence behavior of the Madelung constant for a given crystal type.

Crystals such as NaCl, with their simple cubic symmetry and uniform charge distribution, are typically used for validating Madelung calculations. However, applying these models to salt hydrates introduces complexity. While water molecules within the hydrate are electrically neutral (i.e., $Z = 0$), they affect lattice parameters and modify the structural symmetry, indirectly influencing electrostatic stability and thermal behavior. As water is added or removed during hydration or dehydration, the effective interionic distances and lattice geometry change, which in turn alters the calculated Madelung constant and, therefore, the lattice potential energy.

Predictive models such as the Glasser–Jenkins method, the modified BET model, and *slPCMlib* extend the principles of ionic lattice theory into systems where water is not merely a space-filling species but an active participant in the structural and thermal dynamics of the material. These models incorporate both electrostatic interactions and the energetic consequences of water release or retention, enabling more accurate predictions of melting behavior, heat capacity, and enthalpy changes in salt hydrates.

While the Madelung constant offers a foundational measure of electrostatic cohesion in idealized crystalline solids, the tailored models for salt hydrates build upon this framework to account for the real-world complexities of hydration dynamics. By understanding both the geometric and energetic implications of lattice modifications, researchers can better design and optimize salt hydrate PCMs for specific energy storage applications.

In essence, this synthesis between classical lattice theory and modern hydrate modeling serves as a powerful tool for bridging theoretical and applied materials science. It enables a more nuanced prediction of how salt hydrates behave under thermal cycling, guiding the development of efficient and stable phase change materials.

3.7 Solid-State Defects of Salt Hydrate Crystals

Several factors can significantly affect the thermal performance and long-term stability of salt hydrates when used as PCMs. One of the most critical aspects is the crystallization method employed during material processing [116], [117]. Slow crystallization techniques, such as controlled cooling or annealing, generally produce superior results, as they relieve internal stresses, promote more ordered crystal lattices, and improve structural stability. In contrast, rapid solidification methods, such as quenching, tend to introduce structural defects that can compromise the thermal performance of the material. These defects may include inclusions, occlusions, and lattice disruptions, which reduce the effective storage capacity and lower the material's thermal reliability.

Interestingly, while such imperfections are often viewed negatively [118], [119], they can also provide specific advantages under certain conditions [120]. For instance, the presence of lattice defects can decrease the activation energy required for melting, potentially improving the reversibility of phase transitions. In some cases, these defects may also enhance the material's thermal conductivity. This dual role of crystallization-induced imperfections is discussed in greater detail in this section, with further experimental evidence presented in Chapter 5.

Crystal defects can be broadly classified into four types, each corresponding to a specific dimensional scale and structural effect. Type-0 defects, also known as point defects, occur at the atomic scale and include vacancies, interstitials, or substitutional impurities. Type-1 defects are one-dimensional dislocations, representing linear disruptions in the crystal lattice. Type-2 defects involve two-dimensional irregularities, such as slipped or faulted planes, which distort the lattice over a broader area. Finally, Type-3 defects are three-dimensional or volumetric defects, often referred to as granular irregularities or foreign particle inclusions.

Structural imperfections—such as point defects, ion substitutions, inclusions, and porosity—disrupt local bonding networks and reduce cohesive energy. These defects compromise the uniformity and integrity of the lattice, resulting in local voids, decreased packing density, and impeded phonon transport. Consequently, they diminish both the effective thermal conductivity and the latent heat storage capacity of the material, ultimately reducing its overall thermal performance. Furthermore, such irregularities can alter the latent heat and shift the melting behavior away from theoretical predictions based on idealized lattice energy models, such as those derived from Madelung potentials.

Single point defects, also referred to as Type-0 defects, can be broadly categorized as Frenkel or Schottky defects. Frenkel defects occur when an ion or atom vacates its lattice site and relocates to an interstitial position, disrupting local coordination but preserving the overall stoichiometry of the crystal. In contrast, Schottky defects involve the simultaneous absence of a cation–anion pair, maintaining ionic neutrality while reducing the crystal's density. In salt hydrates, Frenkel-type defects often manifest as cation substitutions or vacancies, while the associated anions remain distributed throughout the structure. These imperfections typically arise during crystallization, particularly under non-equilibrium conditions such as rapid cooling or incongruent melting. The resulting lattice distortions introduce gaps and internal stresses, which hinder molecular ordering and can contribute to phenomena such as incomplete rehydration or reduced thermal conductivity. Consequently, these point defects are often unavoidable in salt hydrates, as entropic effects inherent to melting and recrystallization promote local structural disorder.

Concerning Type-0 defects, substitutes of different-sized atoms have the same ionic values yet different atomic sizes and weights. For example, ferrous Iron and Nickel particles have an ionic valence of 2+ that is identical to Magnesium's ionic valence. The atomic weight of Magnesium is 24, while the atomic weight of Iron and Nickel is almost double ranging from 52-55. Additionally, the orbital size of the atoms is 3s orbitals in Magnesium while 4s orbitals in Iron and Nickel. Due to their ionic charge

the atomic radii are different from their neutral form, their size decreases as they have positive charges. Many references place the radii of the atom from the smallest to the largest based on the ionic charge from Mg, Ni, and Fe (Ranging from 65-90 picometers). The range depends on the configuration of atoms as they are bound to one another. The size difference in the atomic radii causes kinks or disruption in the uniformity of the orthorhombic nature of the epsomite crystals ($MgSO_4 \cdot 7H_2O$). According to Frenkel's and Schottky's defect definition, other effects are gaps or holes in the crystal, decreasing the potential energy of heat storage regarding crystal density.

The thermodynamics regarding these behaviors can be calculated from a theoretical standpoint using the following equation:

$$S^{config} = k_B ln \frac{N!}{n!(N-n)!} \tag{3.12}$$

This equation references the entropy of the configuration of a crystal S^{config}, relating to its atomic vacancies (n) versus the number of available known sites in a crystal (N) and combined with the Boltzmann constant (k_B) (1.38×10^{-23} J/K). The equation leads into determining the force that would be required to disrupt a crystal. The change in force from a perfect crystal adds to the factor of temperature by determining the energy required for removing an atom from the crystal structure. Although, it assumes that the entropic value of a perfect crystal is 0. Thus, a real crystal's entropic value will always be higher than 0 regarding its theoretical configuration.

These defects decreases the amount of potential energy of a material while increasing its entropic nature, allowing unique behaviors of the material. The Frenkel and Schottky defects must be accounted for regarding a crystal's behavior when evaluating a crystalline material. The material is constantly in motion and Frenkel's defects cause a concentration gradient throughout the crystal. It results in a more disruptive reconfiguration altogether. This calculation considers a concentration gradient (c), atomic planes (a), crystal frequency (v), and time of diffusion (dt), providing the probability of movement or jumps (P) of lattice unit cell spacing. The following equation resumes the relationship:

$$\frac{\delta n}{\delta t} = j \cong -va^2 P \frac{dc}{dx} \tag{3.13}$$

Where j is the material density as defined by Fick's first law as $j = -D\frac{dc}{dx}$ or in three dimensions as $j = -D\nabla c$. D represents the coefficient of diffusion, determined by the Arrhenius-type equation

$$D = D_0 e^{-\frac{E_D}{k_B T}}$$

where E_D is the activation energy (on the order of a few eV per atom) and D_0 is a constant ranging from 0.01 to $3\,cm^2/s$. If there is no change and the crystal maintains its impurities, then Fick's second law equation takes effect:

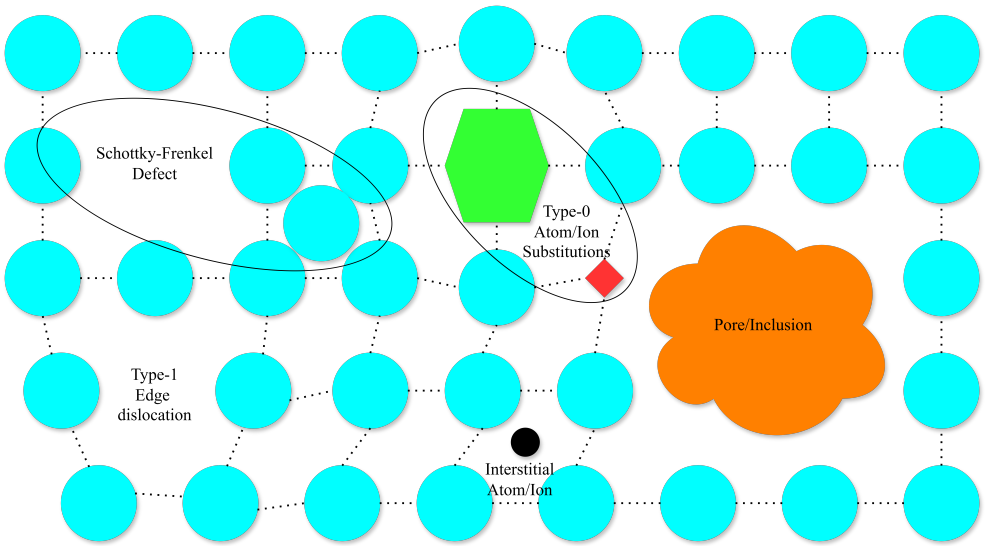

Figure 3.4: Simplified representation of common defects found in salt hydrates.

$$\frac{dc}{dt} = \nabla \cdot (D\nabla c) = D\nabla^2 c \tag{3.14}$$

This equation must have boundary conditions, which are defined through: $\langle x^2 \rangle = 2Dt$. The entire process requires energy to diffuse, which is considered both by atomic frequency and movement of alternative forces (e.g. electrostatic, Van der Waals, and nuclear).

The considered material of salt hydrates, has both Type-0 and Type-1 defects. Salt hydrates have both vacancies: an ionic plane gradient that shift their atomic configurations [121], [122]. The effects of defects must be evaluated both individually and collectively to understand their influence on the thermodynamic performance of salt hydrates in thermal batteries. These imperfections modify key parameters such as lattice energy, thermal conductivity, and phase transition kinetics. For instance, point defects can lower the lattice cohesion energy, thereby reducing the latent heat storage capacity, while planar or volumetric defects can create pathways for premature dehydration or hinder uniform heat transfer. As a result, the overall phase behavior of salt hydrates—particularly during repetitive melting and solidification cycles—remains in constant flux, influencing both energy efficiency and long-term material stability. In the following diagram (fig. 3.4) it presents a simplified version of crystal defects including pore inclusions that are found and discussed in Chapters 4 and 5.

Expanding on Type-1 defects, the discrepancy in electron density and ionic charge makes diffusion and energy loss a potential consequence of entropic disruption. Having the charge differential potential between planes of crystal structures causes the ions to jump from plane to plane.

3.8 Theoretical Thermodynamic Modeling of Salt Hydrates

3.8.1 Overview of Predictive Thermodynamic Approaches

After examining the diverse factors influencing salt hydrates—from water coordination and lattice energy to ionic interactions and defects—attention turns to predictive thermodynamic modeling. Predictive models allow for estimation of key properties such as lattice energy, enthalpy of fusion, and entropy, offering insights into both storage potential and stability. According to Beaupère et al. [23], the most critical parameters determining PCM performance are, in order of importance: solid density, latent heat of fusion (per volume), thermal conductivity, supercooling degree, specific heat, and melting temperature.

Three main approaches are particularly relevant to salt hydrates: (1) The Glasser–Jenkins (GJ) model, which estimates lattice and hydration energies from structural and volumetric parameters; (2) The Modified BET model, which introduces surface adsorption energetics to describe salt–water equilibria; and (3) The slPCMlib framework, which simulates real PCM behavior including hysteresis and non-isothermal transitions. Together, these models provide complementary insights into both the theoretical and practical thermodynamics of salt hydrates.

3.8.2 The Glasser–Jenkins Model

The Glasser–Jenkins model [84] provides a semi-empirical method for estimating the lattice and hydration energies of ionic solids based on structural parameters such as molar volume, density, and ionic strength. The model correlates these with macroscopic thermodynamic properties—enthalpy, entropy, and heat capacity—allowing for rapid property estimation of crystalline hydrates.

The lattice energy derived from volume is expressed as:

$$U_{\text{vol}} = 2I \left(\frac{\alpha}{V_m^{1/3}} + \beta \right) \tag{3.15}$$

where I is the ionic strength, V_m the molar volume, and α and β empirical constants (117 and 52 kJ/mol, respectively). A density-based equivalent form is:

$$U_{\text{den}} = \gamma \left(\frac{\rho}{M} \right)^{1/3} + \delta \tag{3.16}$$

with constants $\gamma = 1981.2$ kJ/(mol · cm) and $\delta = 103.8$ kJ/mol. From these, associated thermodynamic properties can be determined using empirical relationships for entropy ($S = kV_m + c$) and heat capacity ($C_p = k'V_m + c'$).

This model provides a compact, accessible framework for estimating fundamental thermodynamic quantities, though it is inherently limited to idealized ionic lattices

and assumes static hydration environments. As such, it forms a baseline reference for understanding energy relationships in salt hydrates, particularly where empirical data are scarce.

3.8.3 The Modified BET Predictive Model

Building on lattice-based frameworks, the Modified Brunauer–Emmett–Teller (BET) model [123] extends the analysis to include surface and adsorption effects—key for describing hydration and dehydration dynamics in salt hydrates. Originally developed for gas adsorption, the BET framework was adapted to represent the interaction between water molecules and salt surfaces, accounting for multilayer adsorption under varying humidity and temperature.

The general form is expressed as:

$$\ln a_s + n \ln a_w = \ln K_s \tag{3.17}$$

where a_s and a_w are the activities of the salt and water, respectively, and K_s is the solubility constant. Through Gibbs–Duhem integration, the model introduces two critical parameters: r, the maximum number of adsorbed water molecules on the first surface layer, and $c = \exp(-E/RT)$, the energetic ratio between adsorption and condensation energies.

The BET model thus captures how surface energetics affect phase behavior, enabling prediction of equilibrium states between solid, molten, and dissolved phases. Compared with G–J, it emphasizes the role of surface hydration and water activity rather than bulk lattice energy, making it particularly useful for multicomponent and eutectic systems. However, its reliance on accurate activity data limits its broader applicability without experimental validation.

3.8.4 Modeling Real PCM Behavior with slPCMlib

While the G–J and BET models provide theoretical and semi-theoretical perspectives, the *slPCMlib* model [124] focuses on simulating real, non-ideal PCM behavior, particularly for materials exhibiting supercooling, hysteresis, and non-isothermal melting—phenomena characteristic of salt hydrates. This framework defines effective thermophysical properties (enthalpy, density, heat capacity, conductivity) as continuous functions of temperature, using:

$$h(T) = (1 - \xi(T))h_s(T) + \xi(T)h_l(T) \tag{3.18}$$

where $\xi(T)$ is the liquid fraction. By differentiating between heating (ξ_H) and cooling (ξ_C) trajectories, the model captures hysteresis effects and incomplete transitions.

Compared to analytical approaches, *slPCMlib* provides a more realistic depiction of cyclic operation, though it assumes quasi-static behavior and depends on high-quality calorimetric data for parameterization.

3.8.5 Comparative Evaluation Using $CaCl_2 \cdot 6H_2O$

To evaluate and compare the applicability of the above models, Antarcticite ($CaCl_2 \cdot 6H_2O$) was analyzed as a representative hydrate. Using the Glasser–Jenkins model, the lattice energy was estimated as –5447 kJ/mol, corresponding to 24.86 kJ/g, while the first dehydration step yielded a theoretical enthalpy of 2130 J/g, an order of magnitude greater than the experimental latent heat of fusion (184 J/g). This discrepancy confirms that melting corresponds to partial structural reorganization rather than full dehydration.

The *slPCMlib* database reports a melting temperature of 31.1°C, a fusion enthalpy of 202.6 J/g, and pronounced hysteresis (supercooling to –21.7°C), closely aligning with empirical behavior. In contrast, the Modified BET model fails for this system due to water activity exceeding 0.5, a known limitation for highly hydrated salts [125].

Together, these models demonstrate complementary strengths: G–J provides foundational energy relationships, BET incorporates molecular-scale adsorption behavior, and *slPCMlib* captures real thermal dynamics. Their integration offers a comprehensive thermodynamic description spanning ideal, semi-ideal, and experimental representations of salt hydrate PCMs.

3.8.6 Advantages and Limitations of Modeling Salt Hydrate Systems

To consolidate the theoretical models discussed, namely the Glasser–Jenkins (GJ) model, the Modified Brunauer–Emmett–Teller (BET) model, and the *slPCMlib* phenomenological framework, a comparative overview is provided in Table 3.2. Each model offers a distinct approach to understanding the thermodynamic and kinetic behavior of salt hydrates, operating at different scales of description: from the ionic lattice (GJ), to surface-level adsorption phenomena (Modified BET), and finally to bulk phase transition dynamics (*slPCMlib*).

These three frameworks complement one another by addressing different thermodynamic aspects of salt hydrates. The Glasser–Jenkins model emphasizes fundamental lattice and hydration energetics; the Modified BET model provides molecular-level insight into water–ion interactions; and the *slPCMlib* framework translates these properties into macroscopic, system-level thermal performance. Together, they form a multiscale understanding—ranging from molecular coordination to real-world energy storage applications.

However, despite their collective strengths, modeling salt hydrate PCMs remains fundamentally constrained by the limited understanding of their melting and hydration–dehydration mechanisms. Experimental data are essential not only for validation but also for parameter estimation within these models. The molecular mechanisms of salt hydrate melting—whether they proceed through dissolution, incongruent melting, or metastable intermediates—remain poorly resolved. Consequently, even the most advanced predictive frameworks require extensive empirical input and cross-validation.

In conclusion, while theoretical and computational models such as the Glasser–Jenkins,

Table 3.2: Comparison of Thermodynamic Modeling Approaches for Salt Hydrate Systems

Model	Core Principle	Strengths	Limitations	Ideal Use Case
Glasser-Jenkins (GJ)	Predicts lattice and hydration energy from ionic strength, molar volume, and density (Volume-Based Thermodynamics).	Semi-empirical and straightforward; limited data input; enables estimation of lattice energy, entropy, and enthalpy; effective for screening material stability trends.	Assumes ideal ionic crystals; limited accuracy for multi-ionic or hydrated systems; excludes kinetic or phase-transition dynamics.	Preliminary screening and comparative assessment of ionic and hydrated salt stability.
Modified BET Model	Extends adsorption theory to model water–salt surface interactions through multilayer adsorption and activity coefficients.	Captures surface hydration/dehydration and equilibrium water activity; applicable to eutectic and concentrated systems.	Sensitive to input parameters; less valid when water activity > 0.5; neglects bulk lattice and kinetic effects.	Modeling equilibrium hydration, surface adsorption, and solubility dynamics of salt hydrates and eutectics.
slPCMlib Framework	Phenomenological model describing gradual phase transitions and hysteresis via temperature-dependent thermophysical properties.	Captures non-isothermal melting, hysteresis, and supercooling; adaptable to calorimetry data; reflects PCM behavior under real conditions.	Requires high-quality DSC or T-history data; assumes quasi-static processes; limited inclusion of nucleation or kinetic effects.	Modeling real PCM behavior, hysteresis, and system-level performance prediction for thermal storage materials.

Modified BET, and *slPCMlib* frameworks significantly enhance the capability to simulate salt hydrate behavior, they are not self-sufficient. Empirical characterization remains indispensable for bridging gaps in predictive accuracy. For research targeting the development of sustainable and high-performance salt hydrate PCMs, integrating modeling with experimental validation is both a scientific necessity and a practical challenge. Understanding the fundamental phase behavior and kinetics of salt hydrates will be pivotal in enabling robust modeling and, ultimately, reliable real-world energy storage systems.

3.9 Closing Remarks

The thermodynamics and melting mechanics of salt hydrates present a uniquely complex interplay between hydration, dehydration, and deliquescence processes. These mechanisms are governed by factors such as water coordination, ionic strength, and hydrogen bonding, which together define the structural and energetic landscape of the material. Understanding these phenomena remains essential for improving the predictability and performance of salt hydrates as phase change materials (PCMs) in thermal energy storage applications.

This chapter has explored the fundamental thermodynamic principles that dictate salt hydrate behavior, distinguishing between sensible and latent heat processes, and emphasizing the stabilizing or destabilizing influence of water coordination within the crystal lattice. Moreover, the discussion of crystal defects—particularly Frenkel and Schottky types [121]—highlighted how intrinsic lattice irregularities can significantly alter thermal conductivity, storage capacity, and cycling stability, especially in waste-derived or impurity-bearing materials.

Theoretical models, including the Glasser–Jenkins, Modified BET, and *slPCMlib* frameworks, were examined as predictive tools for interpreting key thermodynamic parameters such as lattice energy, enthalpy, entropy, and heat capacity. While these models provide valuable conceptual and computational insights, their dependence on empirical validation underscores the current limitations in fully capturing the coupled thermodynamic and kinetic behavior of salt hydrates.

Overall, this chapter underscores the need for a symbiotic approach between theory and experiment to fully elucidate the melting mechanics and energy-storage potential of salt hydrates. By bridging the gap between predictive modeling and empirical characterization, future research can better tailor salt hydrates to specific operational conditions, improving their stability, reversibility, and long-term performance in thermal energy storage systems.

The following chapter will therefore focus exclusively on empirical characterization, applying multiple analytical methods to evaluate and quantify the behavior of selected salt hydrates under controlled conditions. These experimental results will provide the necessary data foundation for validating and refining the theoretical frameworks discussed herein.

Chapter 4

Phase Change Behavior of Sulfate Salt Hydrates Extracted from Olivine Nano-Silica Side Stream

> "Often when you think you're at the end of something, you're at the beginning of something else."
>
> —Fred Rogers

Inorganic salt hydrates, known for their high thermal capacity, are promising materials for large-scale thermal energy storage. This chapter investigates the potential of salt solution, byproduct of green nano-silica extraction from olivine, as a sustainable source for crystallizing magnesium sulfate hydrates. The primary objectives include analyzing the composition and heat capacity of this salt, which contains minor amounts of iron and nickel. Through the use TGA and XRD, Hexahydrite was identified primarily as the recycled salt. The total heat capacity of these recycled salts was 247 J/g-267 J/g. The thermal behavior deviates from expected magnesium, iron, and nickel sulfate salt mix, challenging assumptions about the influence of iron and nickel on magnesium sulfate. Notably, the obtained recycled salts exhibit a comparable stored energy capacity to analytical grade sulfate salt mixtures.

The results of this chapter are published in the following article:
Wesemann, C.A., Schollbach, K., & Brouwers, H.J.H. (2024). Phase change behavior of sulfate salt hydrates extracted from olivine nano-silica side stream. Journal of Energy Storage, 80, Vol 80. https://doi.org/10.1016/j.est.2024.110730

4.1 Introduction

Continuing from the discussions in Chapter 1, this chapter delves into the development of sustainable salt hydrates sourced from side streams [28], [30]. PCM, renowned for their significant heat capacity and ability to store and release thermal energy during reversible phase changes, offer promising solutions for sustainable thermal energy storage [4]–[8], [37], [126]. Specifically, the focus shifts towards exploring the potential of salt hydrates, which have historically played a pivotal role in thermal energy storage due to their exceptional heat capacity[56].

The traditional methods of sourcing salt hydrates, primarily through chemical mining or extraction from salt flats, pose environmental and human health risks [127]–[129]. In light of this, there is a growing interest in exploring alternative, sustainable sources for salt hydrates[21], [24], [34], [38], [39], [130]–[132]. One such potential source is the waste streams generated during the nano-silica extraction process, as investigated by Lázaro García [63]. By dissolving olivine ($(Mg^{2+}, Fe^{2+}, Ni^{2+})\ SiO_4$) in sulfuric acid, a highly concentrated sulfate solution rich in magnesium sulfate can be obtained [14], [37], [133]. This magnesium sulfate hydrate exhibits a latent heat ranging from 189 to 220 J/g [18], [134], [135], with a known specific heat capacity between 1.205 J/(gK) and 1.599 J/(gK) [136], [137]. The olivine is a solid solution between forsterite ($MgSiO_4$) and fayalite ($FeSiO_4$), with high contents of Magnesium (Mg) and smaller amounts of Iron (Fe). Holds promise as a sustainable PCM for thermal energy storage. It may also contain trace amounts of Nickel (Ni). Most of this Fe and Ni is easily separated from the solution before crystallizing the magnesium sulfate, albeit trace amounts of Fe and Ni remain.

$$(Mg, Fe, Ni)_2SiO_{4(s)} + 2H_2SO_{4(l)} \rightarrow Si(OH)_{4(s)} + 2(Mg, Fe, Ni)SO_{4(aq)} \quad (4.1)$$

Understanding the influence of impurities, such as Fe and Ni, on the heat capacity of magnesium sulfate hydrates derived from waste streams is crucial for optimizing their performance. This chapter aims to assess the effect of Fe and Ni impurities on the heat capacity of magnesium sulfate hydrates, providing valuable insights into their potential as sustainable PCM [121], [138]. For this purpose, magnesium sulfate hydrate ($MgSO_4 \cdot xH_2O$) produced from the olivine nano-silica waste stream (furthermore referred to as Crystal Product (CP)) was investigated and compared with two distinct references. One was a Mechanical Reference Mix (MRM) of magnesium sulfate heptahydrate, iron sulfate heptahydrate, and nickel sulfate hexahydrate at the same proportions as the CP contains. The second reference was obtained by dissolving the mechanical reference mix and precipitating it again (Dissolved Reference Mix (DRM)) to see if any differences manifest to compare them to the CP sample. Through comprehensive characterization methods, including XRF, FT-IR, XRD, TGA [139], and DSC, this study evaluates the viability of utilizing magnesium sulfate hydrate from waste streams as a sustainable solution for thermal energy storage.

By pioneering an innovative approach to producing salt hydrates from sustainable

sources, this research contributes to the broader goal of sourcing inorganic materials for renewable thermal energy storage. Through experimentation and analysis, the chapter seeks to provide a deeper understanding of the properties and performance of salt hydrates derived from side streams, offering a pathway towards more sustainable energy storage solutions.

4.2 Materials and Methods

The magnesium sulfate hydrate ($MgSO_4 \cdot xH2O$) (Figure 1) was obtained using the process described by Lázaro García [63]. 110 g of olivine ($(Mg^{2+}, Fe^{2+}, Ni^{2+})_2SiO_4$) (Neg-70) were mixed with 500 mL of 3M Sulfuric Acid (VWR Chemicals, 50%). Using a sealed reaction chamber, the mix is stirred at 600 rpm for 72 h at 70°C. The mixture was centrifuged to separate the solution from the supernatant nano-silica and undissolved olivine (i.e., Residual Solid).

The clear liquid was neutralized using Magnesium Oxide (MgO) (VWR Chemicals, Ph.Eur.) to a pH between 6 and 7 as there was an excess of sulfuric acid (H_2SO_4). This also leads to a precipitate of Fe and Ni. To further remove the dissolved Fe and Ni, the air was bubbled through the solution for 30 min to promote oxidation and precipitation. Afterward, the precipitate was removed through centrifuging [140]. The excess water was evaporated to obtain the CP. Two steps for removing the excess water were used, slowly evaporating most excess water at 60°C for two hours, and evaporating the remainder of water at room temperature over 2 to 3 weeks. Alternatively, the use of ethanol was used to precipitate salt out of solution at a 1:2 ratio of EtOH: salt solution, as a faster method of generating salt. A general overview of this process is shown in Figure 4.2.

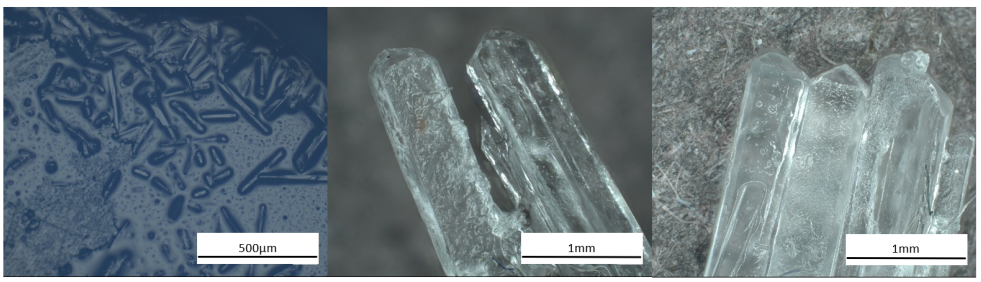

Figure 4.1: Crystal product (CP) optical microscopy images.

Additionally, two reference mixes were made: a MRM and a DRM. Both exemplified the expected outcome of impure recycled salt hydrate. MRM would be the mix by which separate sulfates would conjointly crystallize, without affecting the lattice structure, while DRM would be representative of a possible inclusion of Fe and Ni within the lattice of magnesium sulfate.

The MRM was produced from epsomite ($MgSO_4 \cdot 7H_2O$) (magnesium sulfate heptahydrate) (ACROS Organics, 99,5% pure), iron sulfate heptahydrate ($FeSO_4 \cdot 7H_2O$)

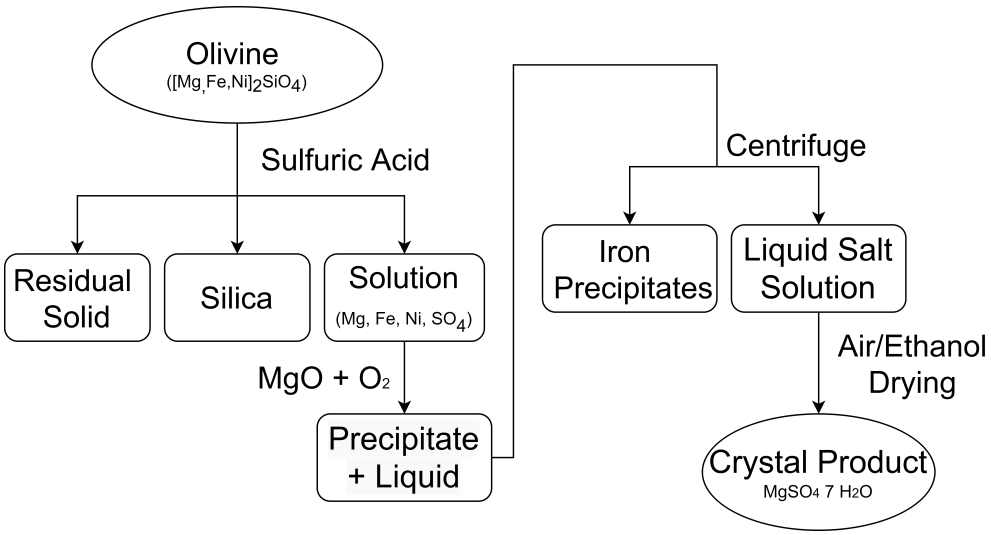

Figure 4.2: Flow Diagram of the olivine nano-silica process and the production of the magnesium sulfate hydrate from the waste solution process.

(Emsure, [ACS, ISO, Reag. Eur), and nickel sulfate hexahydrate ($NiSO_4{\cdot}6H_2O$) (ACROS Organics, 99% pure). Afterward, these three salts were mechanically mixed at a weight ratio of 85:14:01. This ratio was chosen as reported by Schollbach [141], and the liquid waste solution from the olivine nano-silica had the following composition: Mg = 22.1 g/L, Fe = 4.2 g/L, Ni = 188.67 mg/L, and S = 45.5 g/L, giving a ratio of 85:14:01.

The DRM was prepared by dissolving some of the MRM in water at a ratio of 2:1. Then, the excess water was removed to promote crystallization. The same method was implemented for CP. Figure 4.3 presents an overview of the salt mixtures with ratios and end references.

Figure 4.4 presents a phase diagram for Magnesium Sulfate Hydrates and the average experimental zone aimed towards during crystallization.

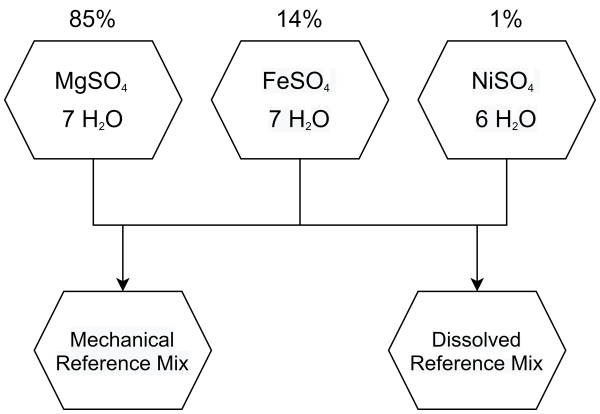

Figure 4.3: Composition of Reference Mix.

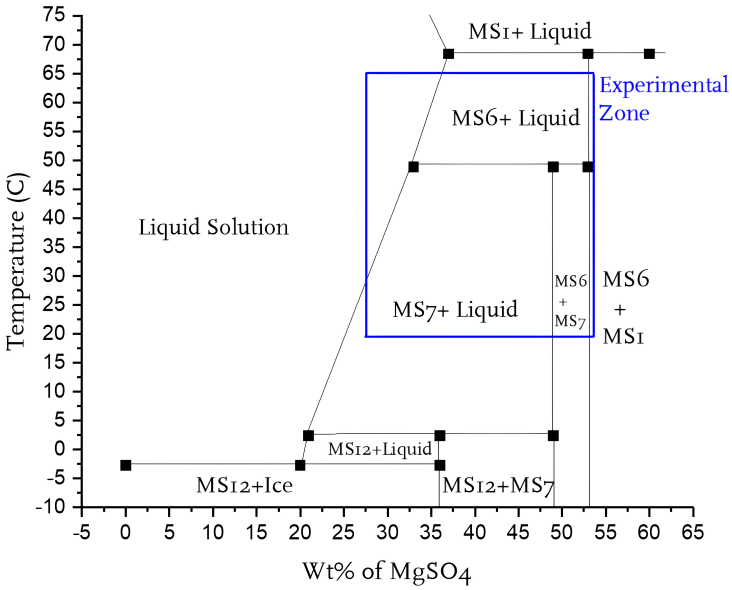

Figure 4.4: Phase diagram of magnesium sulfate, with experimental conditions identified in blue. MS is shorthand for magnesium sulfate and the number after indicates the moles of water. Adapted from conference abstract by Denson et al. 2009 [142].

4.3 Results and Discussion

4.3.1 Bulk Chemical Composition

As shown in Table 4.1, XRF measurements were performed to determine the bulk chemical composition of the olivine, the remaining undissolved olivine after sulfuric acid extraction, and the CP. The olivine is Mg-rich with a Fe_2O_3 content of 8 wt% and 0.4 wt% NiO. This composition was previously reported by Lázaro García [63]. The olivine residue contained significant amounts of sulfate from the solution it was removed from without washing. The CP is comprised of some Fe and Ni but was abundant in magnesium sulfate, as mentioned by Schollbach [141].

Table 4.1: XRF Results of Oxides found within olivine, Crystal Product, and unreacted olivine.

Wt%	**MgO**	**Al_2O_3**	**SiO_2**	**CaO**	**Cr_2O_3**	**MnO**	**Fe_2O_3**	**NiO**	**CuO**	**K_2O**	**SO_3**	**ZnO**	**LOI**
Olivine	50.14	2.3	38.4	0.08	0.22	0.1	7.99	0.41	0.003	—	—	—	0.36
Unreacted Olivine	16.91	0.14	6.28	0.02	0.15	0.03	3.31	0.22	—	0.005	33.31	0.002	39.63
Crystal Product	15.15	0.06	1.67	0.02	—	0.03	1.55	0.05	0.001	0.009	33.80	0.001	47.67

4.3.2 Fourier-Transform Infrared Spectroscopy

Figure 4.5 shows the results of the FT-IR analysis, with comparable outcomes. The peaks representing the water markers, such as the O-H Stretch at 3200 cm^{-1}, the combined OH- stretch and scissor at 2400 cm^{-1}, and the 1600 cm^{-1} OH scissor peak, were identified within all the samples. The samples also contained the identifiers for SO_4 since the S=O stretch at 1100 cm^{-1} and a unique O- umbrella bend, spanning from 400 cm^{-1} to 800 cm^{-1}. All salts belonged to the sulfate with metal ion variety, identified with a metal ion interaction and sulfate peak at 980 cm^{-1} (SO-M stretch) defined as a monodentate C_{3V} symmetry vibration of the sulfate. All pure sulfates, except the Nickel Sulfate Hexahydrate, exhibited this SO-M stretch [143], [144]. There was no observable difference between the two reference mixes (MRM & DRM) and CP.

Table 4.2: FT-IR Peak Data.

	Oxygen Bending	**Oxygen Bending**		**Metal-O-S**	**S=O Stretch**	**O-H Scissors**	**O-H Stretch**	
$MgSO_4$	420	604	—	982	1060	1686	3188	—
$FeSO_4$	448	595	—	976	1067	1640	3201	3296
$NiSO_4$	458	604	776	—	1080	1631	3184	3409
CP	424	568	882	982	1040	1653	3250	—
MRM	419	599	—	982	1058	1667	3197	—
DRM	411	587	—	981	1066	1661	3192	—

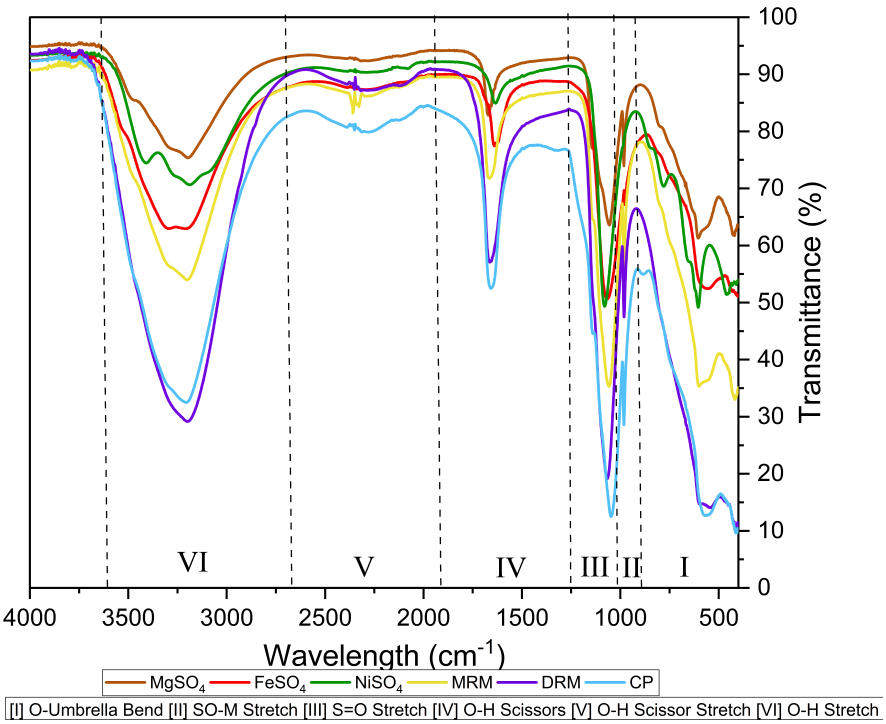

Figure 4.5: FT-IR spectra of CP, MRM, DRM, and all pure salts.

4.3.3 Mineralogical Composition

XRD was used to determine the phase composition of the samples (Figures 4.6 and 4.7). The literature shows that multiple magnesium sulfate hydrates exist, that can transform into each other [96], [98], [137], [144]–[146] (Figure 4.8). The CP mainly consisted of the mineral Hexahydrite ($MgSO_4{\cdot}6H_2O$) [ICSD 16546], the hexahydrate form of magnesium sulfate, followed by traces of iron sulfate and retgersite ($NiSO_4{\cdot}6H_2O$). The MRM showed a large amount of epsomite and smaller amounts of Hexahydrite. Minor traces of iron sulfate were also visible, as expected, considering the composition of the reference (85wt% epsomite, 14wt% iron sulfate heptahydrate, and 1wt% nickel sulfate hexahydrate). The nickel sulfate hexahydrate concentration was too low to be visible. The possible reason for the presence of Hexahydrite in the MRM sample was partial dehydration caused by the mechanical mixing/grinding of the material. In the DRM, only epsomite [ICSD 16595] was found with no indication of hexahydrite, and no newly formed iron or nickel sulfate was visible (Figure 4.7). The reason why the DRM sample contained epsomite and the CP samples contained Hexahydrite is not clear, since both samples were treated identically when crystallizing.

Figure 4.8 describes the dehydration and hydration processes of magnesium sulfate salts from Epsomite toward anhydrous magnesium sulfate. The metastable state, known as 2.4 or 2.5 H_2O magnesium sulfate was identified and characterized by Bish

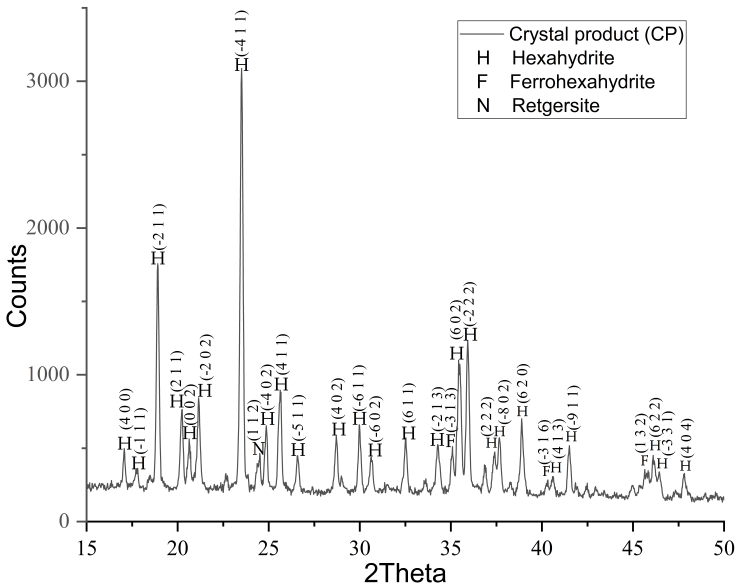

Figure 4.6: XRD diffractogram of CP (Crystal Product). Peaks identified with respective h k l values. All peaks with a relative intensity below 5% were not labeled for simplification.

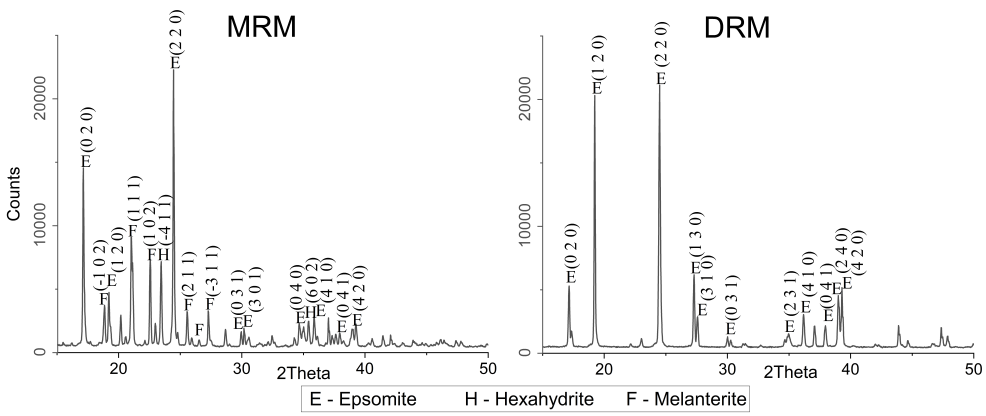

Figure 4.7: XRD diffractogram of the Reference Mix and Dissolved Reference Mix. Epsomite (E), Hexahydrite (H), and iron sulfate heptahydrate (Melanterite) (F) were identified in the samples.

et al. [145]. Wang et al. [147], discuss more d the complex nature of hydration and dehydration of the various magnesium sulfate hydrates counterparts. For example, Starkeyite ($MgSO_4{\cdot}4H_2O$) is very stable, and significant energy is required to add or remove water from this crystal structure. The conversion from Kieserite to Epsomite is also kinetically hampered due to all these stabilizing points in the hydration process,

requiring some additional forces to transform a hydrated polymorph into another.

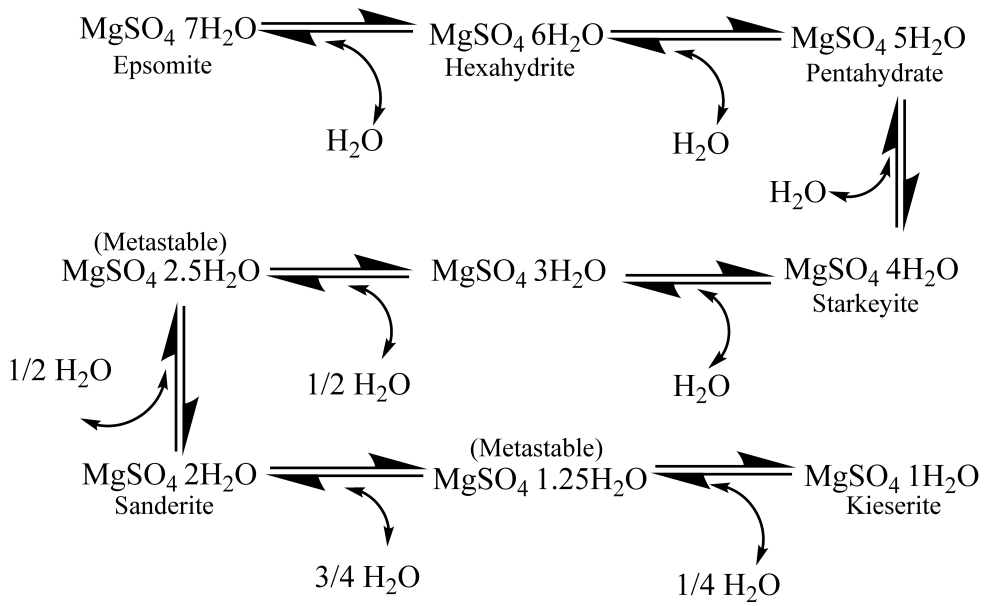

Figure 4.8: Simplified dehydration steps of magnesium sulfate salts. Description of the dehydration and hydration processes of magnesium sulfate salts from epsomite toward anhydrous magnesium sulfate [145], [147].

4.3.4 Thermogravimetric Analysis:

TGA and Differential Thermogravimetry (DTG) results are shown in Figure 4.9. TGA analysis is implemented to determine the ranges of interest for DSC analysis. The theoretical water content of each sample was calculated and compared to TGA results. Table 2 shows all the quantitative data.

The epsomite in Figure 4.9 (a) dehydrated in multiple small steps, that were not well-defined. The total weight loss was 44.45 wt%, after transforming into Kieserite ($MgSO_4 \cdot H_2O$) at 321.3°C. The theoretical weight loss of 6 molecules of water would be equivalent to 43.86 wt%, which is in good agreement. The removal of the seventh water molecule did not occur since Kieserite is stable within the temperature range of 320-920°C. It appeared to start losing its final water content at 960.3°C while the sulfate was removed as well [148]–[150]. Iron sulfate heptahydrate in Figure 4.9 (b) displayed two significant weight loss steps at 95-118°C and 580-670°C. The first step correlated with a loss of 1.5 water molecules, transforming it into a metastable state between ferrohexahydrite (iron sulfate hexahydrate) and siderotil (iron sulfate pentahydrate). According to the literature, iron sulfate occurs as a heptahydrate, a tetrahydrate, a monohydrate, and an anhydrous state [151]. Nickel sulfate hexahydrate in Figure 4.9 (c) became anhydrous at 114.4°C, followed by a significant weight loss,

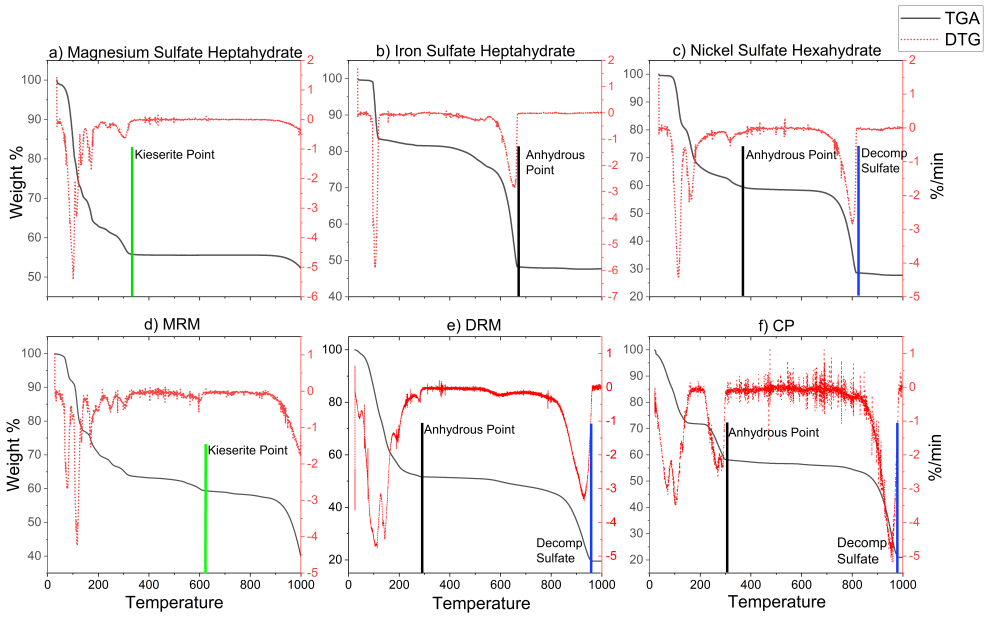

Figure 4.9: TG/DTG Curves.

attributable to sulfate's decomposition starting at 801°C [152]. This second weight loss of 28.59 wt% closely resembled the theoretical weight loss occurring through the decomposition of $NiSO_4$ to NiO, which is 28.41 wt%. MRM in Figure 4.9 (d) exhibited seven pronounced weight loss steps, correlating with the dehydration of pure epsomite (the main component of the salt mixtures).

At 620°C, MRM undergoes partial dehydration and forms Kieserite, exhibiting similar behavior to that of analytical epsomite. The DRM in Figure 4.9 (e) showed a noticeable weight loss in the range from 130 to 290°C because of dehydration, composed of multiple unresolved steps, visible in DTG. Starting at 963°C the weight loss caused by the decomposition of the sulfate occurred, which was observed in the MRM at a higher temperature. The CP in Figure 4.9 (f) presented two significant weight loss steps, the first from 25 to 160 °C (29 wt%), equating to 3.68 mol of H_2O. The second weight loss step occurred from 220 to 300°C (15 wt%) corresponding to 1.82 moles of H_2O. Finally, magnesium sulfate decomposed into MgO between 815 to 980°C. Overall the weight loss complied well with the ones reported for Hexahydrite [153].

The TGA measurements of MRM and analytical epsomite were similar suggesting that the thermal behavior of the MRM is highly influenced by the epsomite for it was the largest component of the sample. However, the behavior of CP was observably different. This difference in thermal behavior might correlate with differences in the crystallinity of the samples of MRM and DRM [154], [155]. MRM likely had a higher crystallinity, compared to DRM, as the different dehydration steps are clearer for the MRM sample when measured with TGA. Based on XRD, the CP sample was primarily Hexahydrite,

Table 4.3: Water loss measured with TGA compared to the theoretically calculated water loss of the pure mineral phase. Temperature Anhydrous refers to the point at which the sample has lost all water.

Name	**Measured water loss (wt%) +/-0.05%**	**Temperature Anhydrous (°C)**	**Theoretical Water loss (wt%)**
Magnesium Sulfate Heptahydrate	44.45	>1000	43.86 ($6\ H_2O$) 51.18 ($7\ H_2O$)
Iron Sulfate Heptahydrate	51.83	670	45.36
Nickel Sulfate Hexahydrate	42.06	380	41.12
MRM	42.89	620	43.72 ($6\ H_2O$) 50.12 ($7\ H_2O$)
DRM	48.37	290	50.12 ± 5
CP	43.30	300	47.31 ± 5

and the theoretical water loss of 47.31wt% matches the experimental value of 43.30 wt%, when considering that other phases were present as well. Additionally, the presence of other ions in CP could reduce the crystal size, increasing defects in the crystal structure. This could reduce the decomposition temperature, making the steps less prominent [156].

4.3.5 Phase Transitions and Heat Capacity:

DSC was implemented, determining the heat storage capacity of the samples. A complete heating and cooling cycle was measured. Figure 4.10-Figure 4.11 show the exothermic and endothermic reactions occurring during heating and cooling that were separated into two graphs for clarity. Stored energy was determined by integrating the area under the curve, starting from 0 W/g, as a baseline. During heating, the endothermic peaks show thermal energy absorbed by the material, through phase changes. During cooling, the exothermic peaks show the complete release of energy due to crystallization. The observed shift in the baseline towards higher heat flows at elevated temperatures can be attributed to the energy stored as sensible heat. Assigning specific phase transitions to the peaks measured with DSC can be complex because of the occurrence of numerous magnesium sulfate hydrates and the kinetically delayed transformation between them [133]. To determine whether the peaks observed in CP, MRM, and DRM data correspond to specific phase transitions, they are compared to the reference materials. Hysteresis behavior is visible when comparing the heating and cooling curves of all samples. This can have several causes: a) delayed phase transformation b) water loss during DSC measurement c) phase separation [6], [84], [133], [157]. Nevertheless, it is possible to evaluate heat capacity by integrating

the area under the curve in DSC measurements in the heating graph in Figure 4.10. The additional peaks of the different materials (depicted in Figure 4.10), correspond to a chemical transformation (epsomite to hexahydrite) caused by phase transitions (confirmed by TGA data Figure 4.9) [158].

The heating graphs (Figure 4.10) show the heating step from room temperature of 25°C to 120°C. Epsomite's reported phase transformation into hexahydrate and water was at 48-52°C [14], [37], confirmed with the melting temperature apparatus, and occurs similarly in MRM and DRM but was not present in CP. The second peak occurring in analytical epsomite (green box in Figure 4.10) at around 95°C does not match the phase diagram as seen in Figure 4.4, where the transformation from Hexahydrate into kieserite and water occurs at around 70°C demonstrating hysteresis by +30°C. In DRM and MRM the second peak occurs at around 80°C. The third peak (yellow box in Figure 4.10) seen in analytical epsomite indicates the transformation of kieserite into starkeyite, confirmed through DSC/TGA data of Yan et al. 2020 [9], that found similar temperature ranges. The most probable reason why the onset temperature for phase changes/transformation is different from reference data is due to differences in the crystallinity of the materials [156], [159]. As observed in Figure 4.10 MRM and DRM have an earlier onset than pure epsomite because of lower crystallinity as the materials were either ground (MRM) or dried out of solution (DRM). Additionally, it is possible that the perforated aluminium pans used for DSC measurements did not entirely prevent pressure buildup, which could have shifted the transformation temperatures. In Figure 4.10 bottom right, a distinctive peak at 100-105°C is observed in CP, indicating a phenomenon of cold crystallization [160] followed by melting. This process results in a transient decrease in the sample temperature before returning to the activation temperature, as evidenced by the graph plotted against time instead of temperature in the small plot highlighting the peak area. The dynamic behavior of cold crystallization, followed by melting, induces a loop in the graph because of the material's readjustment to absorb enough heat to cool the sample by a few degrees.

Figure 4.10, and Table 4.4 show the endothermic results. MRM, DRM, and Epsomite ($MgSO_4{\cdot}7H_2O$) have a phase change at around 48.5°C. Iron sulfate heptahydrate ($FeSO_4{\cdot}7H_2O$) changes at 65°C and nickel sulfate hexahydrate ($NiSO_4{\cdot}6H_2O$) manifests a change at 75°C followed by a secondary peak at 80°C. The phase change of CP as measured with the melting temperature apparatus is, similar to that of the DSC and correlates with the transformation of hexahydrite to starkeyite [161]. These measurements were confirmed with fresh material, using the MTA, where partial melting during the first phase transition was observed (Table 4.5).

The cooling graph (Figure 4.11) shows the cooling from 120°C to 0°C. Notice that in Figure 4.10 bottom right, the plot shows a large release of energy from (120-115°C) with a maximum average value of 0.4 W/g for all samples, with $MgSO_4{\cdot}7H_2O$ having a crystallization peak at 35°C, $FeSO_4{\cdot}7H_2O$ having no discernible crystallization peak, $NiSO_4{\cdot}\ 6H_2O$ has a crystallization peak at 30°C, and finally MRM shows an exothermic release starting at 15°C. The CP and DRM samples show no exothermic peaks indicating that no crystallization took place, likely due to supercooling [6], [30], [137], [162]. The positive heat flow indicates the release of energy, stored as

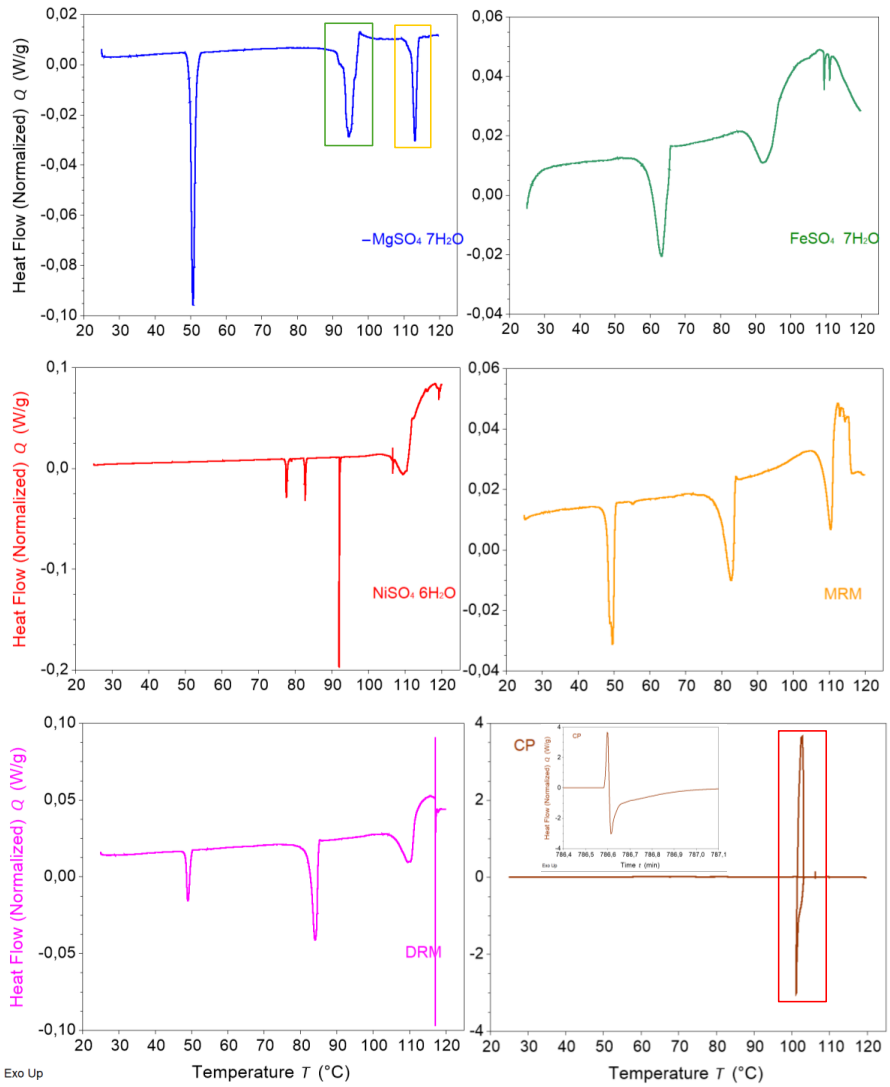

Figure 4.10: Endothermic Samples of DSC. From top epsomite (left), iron sulfate heptahydrate (right), in the center is nickel sulfate hexahydrate (left), followed by bottom samples MRM (right), finally in the bottom DRM (left), and CP (right). In the epsomite DSC, the green box indicates the phase transformation of hexahydrite, and the orange box indicates the transition of hexahydrite into starkeyite. The small graph in CP demonstrates the same peak in heat flow history to best visualize the effect in the red box.

both sensible and latent heat which can be used to obtain the total material heat capacity of the sample. Even so, the possible incorporation of foreign ions into the

Table 4.4: Endothermic DSC measurements.

Sample	Peak (Heating)	T_{onset} °C	T_{endset} °C	T_{peak} °C	ΔH, J/g
$MgSO_4$ $7H_2O$	1	49.8	51.6	50.7	74.9
	2	93.1	96.9	94.4	73.9
	3	112.1	113.8	113.0	32.1
$FeSO_4$ $7H_2O$	1	59.4	65.6	63.3	88.3
	2	86.6	95.8	92.7	89.9
$NiSO_4$ $6H_2O$	1	77.4	78.1	77.6	8.2
	2	82.6	83.0	82.7	6.9
	3	91.2	92.3	91.9	9.7
	4	106.6	111.5	110.4	113.5
MRM	1	47.9	50.2	49.6	47.3
	2	78.8	83.7	82.7	70.8
	3	107.4	111.3	110.4	66.6
DRM	1	48.4	49.8	48.9	19.9
	2	82.4	84.9	84.1	77.7
	3	105.3	111.4	110.1	86.0
CP	1	103.2	102.8	102.8	222.3

Table 4.5: Measured melting temperature of materials using MTA. Values were obtained from runs done at heating rates of 10, 5, 1, 0.5, and 0.1 °C/min.

Material	**Epsomite**	**$FeSO_4$·$7H_2O$**	**$NiSO_4$·$6H_2O$**	**MRM**	**DRM**	**CP**
Tm (°C)	49.3±0.4	65.3±0.2	75.1±0.1	47.7±0.3	48.5±0.2	102.1±1.2*

*Some visual changes observed at 49°C not sufficient to be considered melt.

magnesium sulfate was not the defining factor for the cooling behavior in CP and DRM, as the MRM displayed a similar cooling behavior to DRM (Figure 4.11). Similar data is attested when comparing DRM and CP samples, as detailed in Figure 4.11 and Table 4.6

Several factors may contribute to the supercooling phenomenon. The primary reason could be attributed to the testing methodology, specifically the rapid cooling at 10°C/min. Additionally, substance purity and the absence of nucleation sites might be influencing factors. Given the limited material in the DSC, there may not be enough to form nucleation sites. Finally, incongruent cooling, could also be a contributing factor, obscuring any clear exothermic signal of crystallization in curves that presented no clear definitive peaks, whilst cooling.

Table 4.7 presents the cumulative endothermic and exothermic energy from salt hydrates. The results indicate that the latent heat storage is approximately 183 J/g for DRM and 222 J/g for CP. This is comparable to other commonly used materials, such as paraffin wax (251 J/g), Glauber Salt/ Sodium Sulfate Decahydrate (GS) (238 J/g), and $CoSO_4$·$7H_2O$ (170 J/g) [18]. When considering the exothermic curve, the total heat capacity of both CP and DRM aligns at around 267 J/g.

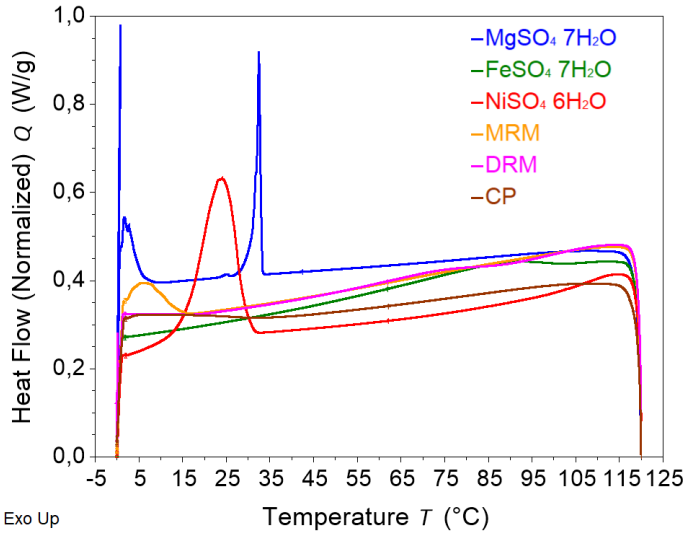

Figure 4.11: Exothermic Cooling DSC curves.

Table 4.6: Exothermic DSC measurements. Primarily determinable peaks from overall heat released.

Sample	Peak (Cooling)	T_{onset}°C	T_{endset}°C	T_{peak}°C	ΔH, J/g
$MgSO_4$ $7H_2O$	1	33.1	29.2	32.5	4.6
	2	4.6	0.6	1.7	4.3
$FeSO_4$ $7H_2O$	1	98.5	74.6	86.1	0.9
$NiSO_4$ $6H_2O$	1	29.4	14.7	24.0	21.5
MRM	1	13.1	2.9	7.3	2.4
DRM	1	97.7	76.6	72.9	0.8
CP	1	29.5	3.5	5.5	0.8

Table 4.7: DSC Overview Data of total thermal endo/exothermic energy.

Material	**Endothermic (J/g)**	**Exothermic (J/g)**
$MgSO_4$ $7H_2O$	180.95 +/- 2.58	336.87 +/- 5.05
$FeSO_4$ $7H_2O$	178.18 +/- 2.16	253.7 +/- 3.81
$NiSO_4$ $6H_2O$	138.31 +/- 2.47	211.1 +/- 3.17
MRM	184.67 +/- 2.88	274.7 +/- 4.12
DRM	183.62 +/- 2.50	267.38 +/- 4.01
CP	222.30 +/- 3.34	267.6 +/- 4.01

4.4 Closing Remarks:

The primary objective of this chapter was to explore the thermal heat capacity of recycled magnesium sulfate hydrates, particularly focusing on the “Crystal Product”,

in comparison to conventional analytical samples. Contrary to initial expectations, the CP was identified as hexahydrite rather than epsomite, a discovery made possible through detailed XRD analysis. This unexpected outcome revealed the CP's unique characteristics, showcasing its potential as a functional PCM. Notably, the CP exhibited favorable low-temperature interactions due to multiple inclusions without compromising its functionality.

In the analytical assessments, the FT-IR results, complemented by XRF and XRD analyses, provided valuable insights into the composition of the Crystal Product. However, a notable limitation emerged in the form of impurities, particularly 1.55% Fe and 0.05% Ni, which were present in the CP at a higher level compared to analytical-grade epsomite. Consequently, these impurities contributed to a reduced heating capacity, resulting in a lower thermal energy storage capacity (CP: 267.6 J/g versus Epsomite: 336.9 J/g). To propel this research forward, it is imperative to focus on refining the production process with the aim of minimizing impurities. Strategies such as minimizing air exposure during crystallization or exploring rehydration techniques could be employed to enhance the purity and, consequently, the thermal storage capacity of the CP.

Looking ahead, future research endeavors should prioritize optimizing the CP's production process to elevate its thermal heat storage capacity. Additionally, investigations into the optimal composition of the CP, understanding the role of various ions in its hydration and thermal properties, and addressing hysteresis properties are crucial avenues for further exploration. Despite the challenges posed by impurities, the CP demonstrates competitive latent heat storage (222 J/g) compared to established PCMs like Paraffin Wax, GS, $MgSO_4{\cdot}7H_2O$, and $CoSO_4{\cdot}7H_2O$. Furthermore, the environmentally friendly production process, generating near-zero waste from a chemical side stream, positions the CP as a promising alternative in the realm of salt hydrate materials. Suggesting applications in thermal batteries for both heating and energy purposes, emphasizing the need for continued research to unlock its full functionality and ascertain potential limitations. The future trajectory of this research envisages expanded applications of the CP in housing heating, envisioning its role as an external heat tank with the capacity to heat water for various domestic purposes. However, further investigations are warranted to explore nuances such as the number of heat cycles possible, water surplus requirements for sustained functionality as a hygroscopic PCM, and potential corrosiveness toward metallic containers. In the following chapter delves deeper in the application process of the stabilizing and details of the thermal performance of CP.

4.5 Appendix

Table 4.8: TGA weight percent changes in 200-300 degrees ranges.

TGA Temp (Celsius)	Magnesium Sulfate Heptahydrate (wt%)	Iron Sulfate Heptahydrate (wt%)	Nickel Sulfate Hexahydrate (wt%)	MRM (wt%)	DRM (wt%)	CP (wt%)
RT-100	100->84	100->96	100->96	100->91	100->84	100->82
100-300	84->58	96->81	96->62	91->65	84->51	82->58
300-500	58->55	81->78	62->58	65->62	51->50	58->56
500-700	55->55	78->48	58->57	62->58	50->48	56->55
700-1000	55->52	48->47	57->27	58->40	48->19	55->20

Chapter 5

Thermal Stability of Recycled Salt Hydrates for Seasonal Thermal Heat Storage

"There are no limits, only obstacles, and any obstacle can be overcome."

—David Belle

Recycled magnesium sulfate heptahydrate, byproducts in the nano-silica extraction from olivine, exhibits reduced purity compared to analytical-grade counterparts. This chapter investigates phase stabilizer usage, titania as a nucleating agent, and carboxymethyl cellulose (CMC) as a stabilizing gel, to enhance the functionality of recycled salt hydrates for thermal energy storage applications. Thermocouple measurements over ten heating and cooling cycles reveal distinct thermal characteristics, with observable latent heat manifesting as a critical indicator for melting-crystallization cycling. The addition of titania increases the number of functional cycles of recycled samples but diminishes performance in analytical samples. Suggesting it provides another function other than nucleation. Statistical analysis shows an exponential decay in thermal cycles ($R^2 > 0.84$) with increased cycles. While titania shows promise, gel stabilizers like CMC did not yield meaningful results. The average latent heat storage of the recycled epsomite was 285.4 ±37.1 J/g. This chapter addresses a previously unexplored area and highlights the potential of nucleating agents in improving the functionality of recycled salt hydrates for sustainable thermal energy storage.

The results of this chapter are published in the following article:
Wesemann, C.A., Junggeburth, T., & Brouwers, H.J.H. (2025). Thermal Performance Evaluation of Recycled Salt Hydrates through T-History. Case Studies in Thermal Engineering, Vol. 68. https://doi.org/10.1016/j.csite.2025.105961

5.1 Introduction

Thermal energy storage (TES) plays a critical role in improving energy efficiency and sustainability in the built environment, particularly through phase change materials (PCMs) that enable latent heat storage. Among these, salt hydrates offer high thermal energy density and superior thermal conductivity compared to organic PCMs, making them promising candidates for TES applications. However, challenges such as phase separation, supercooling, and hydration instability limit their long-term performance. While significant research has focused on analytical-grade salt hydrates, recycled alternatives remain underexplored, despite their potential for sustainable and cost-effective thermal storage solutions.

Heating is one of the major contributors to the energy demands of a building, motivating researchers to find ways to reduce, store, or substitute thermal energy [32]. One of the technologies that could enable TES is employing PCM [14], [130], [163]–[166]. These materials use latent heat storage, that occurs when the material undergoes a phase change [8], [10], [166]–[174]. The advantages of PCMs compared to sensible heat storage methods are 1) higher energy density (thus requiring a smaller volume), 2) minimal maintenance costs, and 3) they can be safer to manage [7], [34], [175]. PCMs may play a crucial role in regulating temperature fluctuations within buildings, offering a unique solution to thermal management [27] by strategically incorporating them into walls and ceilings within closed containers. Unlike traditional insulation materials, PCMs provide insulation, and absorb and release heat, effectively buffering indoor temperature fluctuations [176].

Inorganic PCMs, such as hydrated salts, are usually preferred over organic alternatives (e.g. paraffin waxes) in the build environment. These materials, on average, offer higher volumetric storage density (e.g. 367 MJ/m^3 for Glauber salt, compared to 180 MJ/m^3 for paraffin wax), increased thermal conductivity (1.02 W/mK for Glauber salt, compared to 0.3 W/mK for paraffin wax), and greater fire resistance, as documented in several studies [21], [34], [177]. Their superior thermal conductivity enables more efficient thermal discharging and charging, ensuring effective internal building temperature regulation.

However, salt hydrates present some practical challenges [178], particularly in maintaining their energy storage density (performance) over multiple heating and cooling cycles [95]. This can be caused by incongruent melting, which occurs when a salt hydrate phase does not melt directly but instead forms another phase containing less or no water, alongside a liquid phase [179]. Due to volumetric density differences, the remaining solid phase tends to settle at the bottom of its container causing clumps that are challenging to rehydrate completely [34]. This way incongruent melting can create a mixture that contains various hydrated material phases and reduce the overall efficiency of latent heat storage. Additionally, salt hydrates may encounter supercooling in practical environments. Supercooling occurs when the temperature of the salt drops below its solidification temperature, yet the salt remains in a liquid state due to a lack of nucleation. Understanding how phase separations and supercooling affect salt hydrate efficiency requires researching their behavior under various heating and cooling rates [9].

Heating and cooling rates significantly impact the thermal behavior of materials [72]–[74]. While current rates typically average between 5-10 °C/min [72]–[74], the standard heating rate for salt hydrates is generally lower, usually performed in the range of 1-5 °C/min [9]. Higher heating rates can accelerate detrimental processes in salt hydrates, potentially leading to phase separation or supercooling. The standard heating rate for salt hydrates differs however, it is usually performed around 1-5 K/min. At higher heating rates accelerate processes in salt hydrates, potentially causing phase separation or supercooling[167], [168], [180].

To improve thermal cycling for salt hydrates, various techniques are implemented to prevent phase separation and supercooling. A common solution for phase separation is the thickening agent usage such as Carboxymethyl Cellulose (CMC), Hydroxyethyl Cellulose (HEC), bentonite, or comparable viscous material. By increasing the viscosity of the salt hydrate, these agents hinder the solid crystals from settling at the bottom of the container and ensure they remain suspended in the liquid, facilitating the recrystallization process when the temperature is lowered again [177], [181], [182]. Supercooling prevention is more challenging. Dynamic solutions, such as ultrasonic vibrations, shockwaves, or electro-freezing, can help crystallization [108], [183]. However, they are non-practical when a salt hydrate is incorporated as a passive buffer in a building. In such a case passive nucleating agents such as copper, borax, or titanium oxide can be added to stimulate crystallization [102], [177], [182]. The function of nucleating agents is primarily to disrupt the effects of supercooling by providing a solid surface for crystallization to grow from, thereby reducing the surface energy required for crystallization [23], [184], [185].

Such an inorganic phase change material example is magnesium sulfate heptahydrate ($MgSO_4 \cdot 7H_2O$, epsomite). It has a thermal storage energy density of 287 kJ/kg if applied as a PCM [9], [137], [150], [175], [186]. Epsomite can be obtained through various methods such as mining, desalination from ocean regions, or as a byproduct from nano-silica production [63]. The magnesium sulfate from nano-silica production contains contaminants that can influence the thermal behaviour. However, despite its potential, epsomite poses challenges because its phase changes can be kinetically hindered, resulting in increased phase separation and diminished performance over repeated cycles [92]. The cyclability of magnesium sulfate heptahydrate can be evaluated by subjecting recycled epsomite to multiple cycles of heating and cooling of 40 to 55°C to investigate the phase change from epsomite to hexahydrate that occurs at 49.2±0.3°C [37], [187].

This chapter investigates the thermal performance and optimization of recycled magnesium sulfate heptahydrate (epsomite) sourced as a byproduct from nano-silica extraction from olivine. By employing the T-History method, the study evaluates the effects of titania (as a nucleating agent) and carboxymethyl cellulose (CMC) (as a stabilizing gel) on the phase change behavior and cyclability of recycled epsomite. While previous in the previous chapter explored salt hydrates as PCMs, the thermal behavior and cyclability of recycled magnesium sulfate heptahydrate remain largely unexplored [188].The goal is to determine whether recycled salt hydrates can achieve performance levels comparable to analytical-grade materials, thereby advancing sustainable PCM

development. This work contributes to the broader field of thermal energy storage materials by addressing material stability, phase transition mechanisms, and long-term thermal cycling behavior, providing insights into their feasibility for practical TES applications. Demonstrating that, with the appropriate stabilizing agents, it can achieve performance comparable to its virgin/analytical-grade counterpart. Unlike conventional approaches, which focus solely on analytical-grade materials, this work provides valuable insights into the viability of upcycled salt hydrates as a sustainable alternative for thermal energy storage. To our knowledge, this is the first study to systematically investigate and optimize the phase change behavior and long-term thermal cycling performance of recycled magnesium sulfate heptahydrate, using T-history analysis [177], [186], [189], paving the way for its practical implementation in sustainable thermal energy storage systems.

5.2 Materials and Methods

5.2.1 Materials

Recycled epsomite was obtained as a byproduct of the production of nano-silica from olivine as described in the work of Lazaro [63], [190], [191]:

$$(Mg, Fe, Ni)_2SiO_{4(s)} + 2H_2SO_{4(l)} \rightarrow Si(OH)_{4(aq)} + 2(Mg, Fe, Ni)^{2+}_{(aq)} + 2SO^{2-}_{(aq)} \quad (5.1)$$

$$Mg^{2+}_{(aq)} + SO^{2-}_{(aq)} + 7H_2O_{(l)} \rightarrow MgSO_4 \cdot 7H_2O_{(s)} \quad (5.2)$$

Initially, olivine undergoes dissolution through treatment with sulfuric acid (Equation (5.1)), followed by the oxidation process to remove iron and other heavy metals. Subsequently, the remaining liquid undergoes air drying for 24 hours (Equation (5.2)) and is further dried using a 1:2 ratio of ethanol to salt solution [188].

A comprehensive characterization of the recycled epsomite is discussed in Wesemann et al. [188]. It contained traces of Fe, Ni and Si and exhibited distinct thermal behavior compared to analytical grade epsomite, such as delayed melting and cold crystallization. Cold crystallization is a phenomenon in thermal testing where energy is released just before melting as the material is heated [192]. This generally occurs due to rapid improper crystallization, pollutants, and other effects that interfere with proper crystallization of material.

To investigate the thermal performance of the recycled epsomite, analytical magnesium sulfate heptahydrate (99.5% Acros Organics) was used as a reference material. CMC (Sigma-Aldrich) was used as a thickening agent and titanium (IV) oxide (Ph. Eur. BP USP 99-100.5% Sigma-Aldrich) was used as a nucleating agent.

The process for incorporating CMC began by dissolving it in distilled water at a ratio of 1:15 at 80°C. Once fully dissolved, the solution was cooled to 40°C. Mechanical mixing ensued until the PCM was thoroughly integrated with the CMC solution.

To determine the effect of the gel on the salt performance, additional CMC mixes containing 0.03%, 0.05%, and 0.25% by weight of the CMC powder into water were

evaluated (Table 5.1) [184], [193], [194]. Each mixture underwent the same process of dissolution and mechanical mixing as described. Similarly, 5 wt% of titanium oxide were added to the epsomite, which is a standard amount (0.5-5 wt%) commonly used for nucleating agents [185]. To comprehend the impact of these additives, mixtures without salts were also evaluated for their thermal performance. Furthermore, standalone experiments were conducted with individual additives, such as CMC and titania to discern their behavior in isolation. For a detailed breakdown of materials and sample sets, refer to Table 5.1.

Table 5.1: Overview of materials and samples.

Measurement Group	Sample ID	Analytical Epsomite (wt%)	Recycled Epsomite (wt%)	Water (wt%)	Titania (wt%)	CMC (wt%)
Control	CA	100	0	0	0	0
	CR	0	100	0	0	0
	C1	0	0	100	0	0
	C2	0	0	0	0	0
	C3	0	0	0	100	0
	C4	0	0	0	0	100
Nucleating Agent	NA	95	0	0	5	0
	NR	0	95	0	5	0
Thickening Agent	GA1	95	0	4.97	0	0.03
	GA2	95	0	4.95	0	0.05
	GA3	95	0	4.75	0	0.25
	GR1	0	95	4.97	0	0.03
	GR2	0	95	4.95	0	0.05
	GR3	0	95	4.75	0	0.25
Nucleating and Thickening Agent	NGA	85	0	9.9	5	0.1
	NGR	0	85	9.9	5	0.1

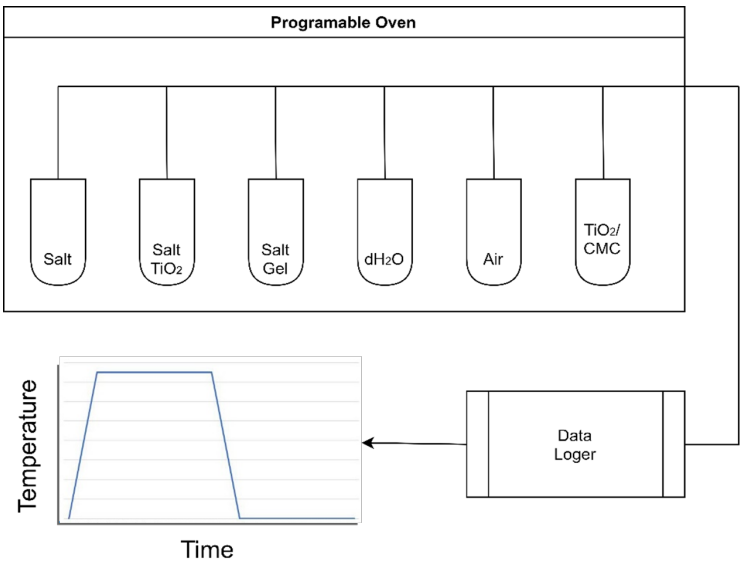

Figure 5.1: Experimental setup: Samples were placed in test tubes and subjected to controlled heating and cooling cycles in a programmable oven. Thermocouples were strategically positioned to measure and record temperature data inside an oven which a data logger then collected. This temperature data was utilized to plot the T-history of the experiment.

5.2.2 Methods

The experimental set-up consisted of a rack with six test tubes containing 15-30 mL of material, which were placed in a climate chamber (Memmert UF160 Plus) with an accuracy of $\pm 0.1\,^{\circ}$C and $\pm 0.5\%$ RH, as depicted in Figure 5.1. The tubes were closed off with parafilm, to prevent water escaping. Despite the sealing of the salt samples, dehydration was still observed. Consequently, all samples were tested at a relative humidity (RH) of 80% inside the climate chamber [195]. The material underwent 10 rounds of thermal cycling while maintaining constant humidity, resulting in a total of 11 heating and cooling cycles. The first cycle was excluded to avoid irregular values, and cycles 2 to 11 were analyzed. This is done to allow for proper alignment and crystallization as usually first melt cycle shows reduced temperature mainly caused due to stearic hindrances. The temperature range spanned between 40°C and 55°C and was selected to be slightly above the melting point of Epsomite (49.2±0.3°C) to ensure phase transformation, from solid to a liquid + solid (slurry).

The cycling procedure involved several steps: The temperature was raised from 40°C to 55°C at a heating rate of either 0.1°C/min or 0.5°C/min. Upon reaching the maximum temperature of 55°C, the material was held at that temperature for an additional two hours. Subsequently, the temperature decreased to 40°C using the same heating rate (0.1°C/min or 0.5°C/min). The material remained at 40°C for another two hours. This entire process was repeated ten times (as shown in Figure 5.1). The cooling curve

data is not included as the recrystallisation could not be observed with the chosen method.

Appendix 5.13 shows a slight temperature overshoot during heating in the control materials (air, dH_2O, and standalone additives). However, this is not considered to have any influence due to the 2-hour waiting time.

The temperature of the materials during the experiments was measured with six thermocouples that lay in the tubes enclosed by the material. The thermocouples Pt100 A, which have an accuracy of ±0.15°C, measured the temperature every 30 seconds using the Eltek Squirrel 1000 Series Data Logger, which has an accuracy reading of ±0.1%. XRD measurement determined the crystalline structure of the materials after cycling. After grinding the materials for 15 min using the XRD Mill McCrone, XRD was performed. The uncertainty in the enthalpy of fusion (J/g) measurements was primarily evaluated using standard deviation (S), as shown in Table 5.2, following the method described in [188].

5.3 Results and Discussion

5.3.1 Phase Change

In Figure 5.2, the plateau corresponds to the measured phase change of epsomite from solid to liquid slurry of hexahydrite with water, occurring around 49.5±0.4°C. The melting temperature was determined by identifying the intersection point of the tangential line drawn from the plateau of the measured curve and the tangential line of the heating curve. This value was then compared across multiple measurements and averaged to obtain the final melting temperature. This is the key feature of interest and outlines latent heat absorption during the phase transition. The plateau remains until the phase change ends, as depicted in Figure 5.2. The temperature then continues to increase. The mechanism of this phase change is presented in the subsequent chemical equation [161]:

$$MgSO_4 \cdot 7\,H_2O \xrightarrow{\Delta H} MgSO_4 \cdot 6\,H_2O + H_2O \tag{5.3}$$

However, it is important to note that the precise mechanism of salt hydrate melt is not comprehensively understood, and various scholarly sources present differing perspectives on its precise mechanism [89], [158], [196].

5.3.2 Heating Rates

The purpose of testing different heating rates, specifically 0.5°C/min and 0.1°C/min, using the T-History methodology in a programmable climate chamber is to evaluate how these rates influence the thermal behavior and phase change characteristics of the materials. As noted by Yan et al. [9] and Yang et al. [161], the phase change of epsomite is best observed at heating rates below 1°C/min. Therefore, a heating rate of 0.5°C/min and 0.1°C/min were tested to understand the effects of slower versus faster thermal transitions on material stability, energy storage capacity, and the accuracy of

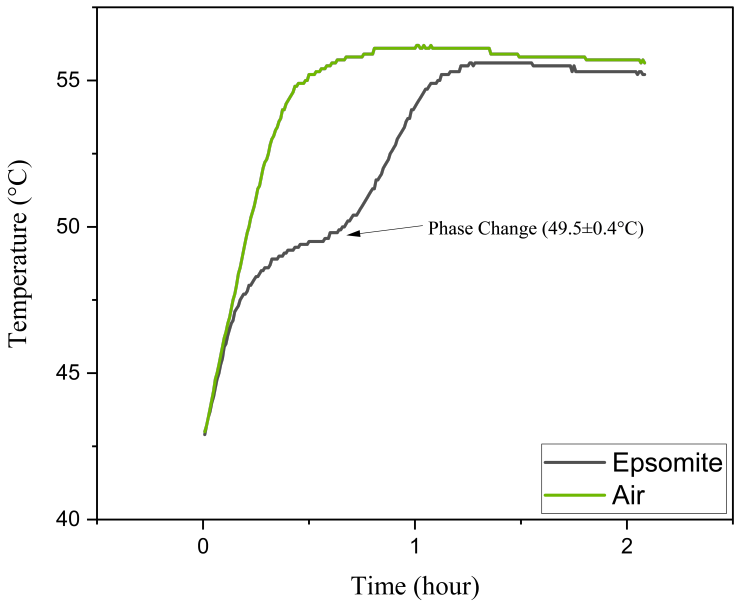

Figure 5.2: Measured sample of analytical quality epsomite, at a heating rate 0.5°C/min, compared to an empty test tube to highlight the phase change.

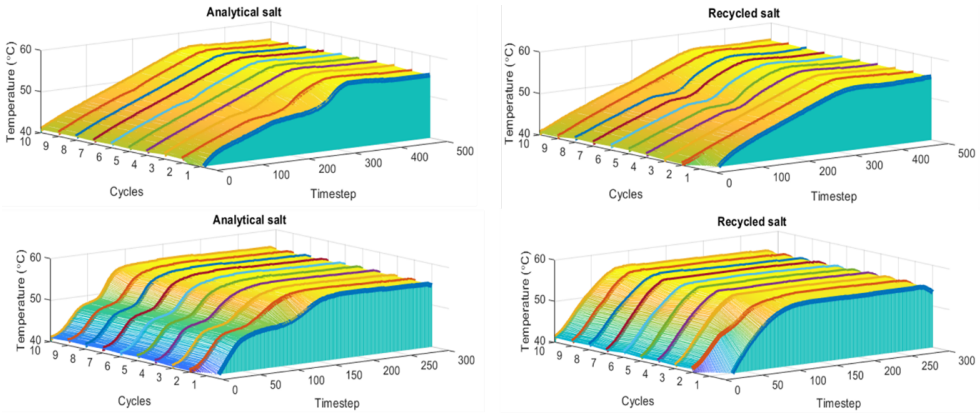

Figure 5.3: Comparison of heating rates of analytical epsomite (left) vs recycled epsomite (right) at 0.1°C/min (top) vs 0.5°C/min (bottom).

phase change measurements. This investigation is critical for optimizing the T-History method and ensuring that the selected heating rate accurately reflects the material's performance.

The results are shown in Figure 5.3, and make it evident that the phase change plateau obtained at 0.1°C/min heating rate (depicted as the top two graphs of Figure 5.3), is indistinct and challenging to interpret for both the CA and CR samples.

Conversely, when the heating rate was increased to 0.5°C/min, a clear plateauing was observed corresponding to the phase change discussed previously. Therefore all further experiments were conducted using the 0.5°C/min rate. The observed plateau appears to decrease over time, demonstrating an increasing lack of phase change taking place. In the recycled salt sample heated at 0.1°C/min, the phase change is evident for a few cycles but quickly disappears. Based on these raw material measurements, of the need for thermostabilizing agents is evident.

5.3.3 Performance of Nucleating Agent

Testing of the nucleating agent, titania, is crucial for enhancing the phase change performance of materials like CA and CR. By investigating how a nucleating agent affects the phase change stability and duration, improvements in material behavior are aimed to be identified. The goal is to determine how this agent can reduce inconsistencies, extend phase change cycles, and enhance the overall reliability of phase transitions. This approach is intended to optimize the performance of phase change materials, ensuring more predictable and effective thermal energy storage.

Figure 5.4 illustrates the influence of titania on the phase change behaviour of both NA and NR samples, which were tested in a programmable climate chamber. The NA sample exhibited a consistent phase change over 8 cycles, whereas the CA sample demonstrated a slightly longer duration with phase changes observed across 10 cycles. In contrast, the NR sample showed a significant improvement when titania was added, sustaining a clear phase change over 7 cycles. This is notably better than the CR sample, which only exhibited phase change for 2 cycles before the effect diminished.

The addition of titania to NR resulted in a more stable and predictable phase change behaviour, marked by a sustained plateau, compared to the erratic and short-lived phase changes seen in CR. Specifically, while CR showed considerable fluctuations and a rapid loss of phase change capability, NR with titania maintained a consistent performance throughout the testing period. This enhanced stability underscores the beneficial role of titania in improving the reliability and longevity of phase change behaviour in NR, in stark contrast to the performance observed with the untreated CR sample.

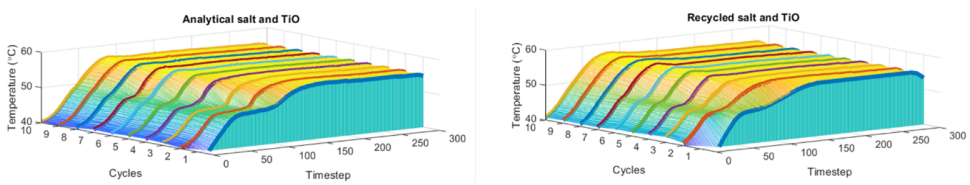

Figure 5.4: Analytical NA (left) and Recycled NR (right) epsomite salt with the titania mix at 0.5°C/min.

A continual and inconsistent decrease in performance was observed during the thermal cycling of the materials. To investigate this issue, the samples were weighed before and after a full test run of 10 cycles. A notable decrease in weight, amounting to 5.7wt%,

was observed, which was attributed to water loss corresponding to the dehydration of epsomite from 7 to 6 water molecules. XRD analysis confirmed that the material was no longer epsomite.

To address this problem, initial tests involved rehydrating the samples with the equivalent amount of water lost and then running them through 10 additional cycles. However, the results showed no significant improvement in performance. This lack of improvement may be due to the slow hydration kinetics of epsomite and possibly the formation of titanium hydroxide from the reaction of water with titania [197].

As a result, it was decided to conduct all subsequent tests at a relative humidity (RH) of 80% to prevent water loss. The effects of this adjustment are illustrated in Figure 5.5, showing the performance of fresh NA and NR samples.

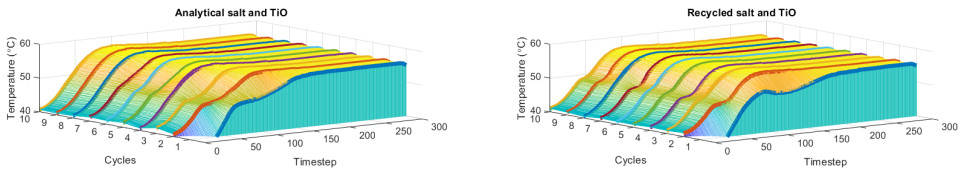

Figure 5.5: Thermal cycling of fresh analytical and recycled mixture with Titania in a humid environment.

Although maintaining a RH appeared to benefit the cycling of the material, the inability of the material to consistently achieve 10 full cycles prompted a closer examination of the nucleating agent. Figure 5.6 reveals that after several cycles, the salt mixture containing titania separated into two distinct layers: titania settled at the bottom, while the salt remained above.

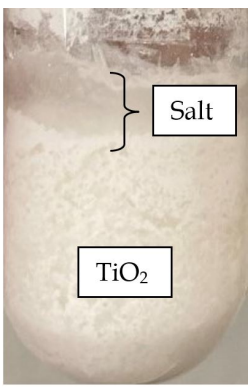

Figure 5.6: Overview of phase separation of titanium oxide and salt.

This separation into distinct phases can be explained by the difference in density between the epsomite (1.67 g/cm^3) and the titanium oxide (4.23 g/cm^3). To ascertain

whether the settling and therefore separation of the titania was the underlying cause of the observed phenomenon of decreasing performance after multiple phase changes, the separated analytical and recycled epsomite salt samples were subjected to mechanical remixing and retested. Figure 5.7 indicates that the density hypothesis alone can be ruled out, as the mechanical remixing of the material failed to induce thermal cycling for either the analytical or recycled salt.

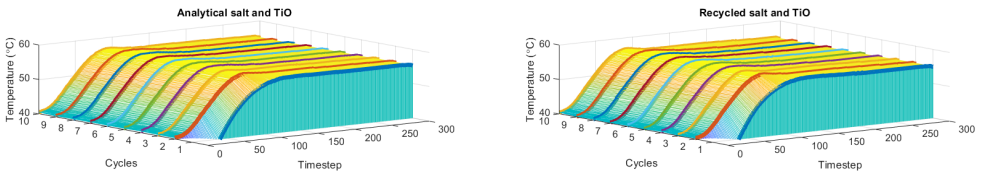

Figure 5.7: The figure illustrates the results of re-mixing NA and NR samples that had already undergone 10 cycles of thermal cycling. Both samples were subjected to 10 cycles of heating and cooling prior to re-mixing. The purpose of this experiment was to assess whether physically re-mixing the salt samples with titania would induce a phase change in the epsomite.

Despite remixing with titania, the material continued to exhibit a loss of performance, as verified by XRD analysis, which showed that dehydration persisted regardless of high (+80% RH) humidity. This indicates that while maintaining humidity helps, it does not fully prevent the dehydration of the samples. Further research into hydration mechanisms, as detailed by Clark et al. [92] and Rehman et al. [91], highlights the limitations of magnesium sulfate in rehydrating to its heptahydrate form regardless of humidity; they were only able to achieve the hexahydrate form. The likely explanation lies in the crystal structure of epsomite, where six water molecules are bound to the cation, with one unbound water molecule that is easily lost during heating. The most probable way for the hexahydrite to rehydrate into epsomite is through a process of deliquescence.

It can be concluded that titania likely did not serve effectively as a nucleating agent for epsomite. However, the marked improvement observed in NR samples suggests that titania may have functioned as a conductive agent, with a thermal conductivity of 7-10 $W/m \cdot K$. This conductivity likely enhanced the thermal performance of CR samples but had limited impact on CA samples. This can be explained by the presence of minor contaminants in the recycled epsomite, which disrupt the material's thermal conductivity. This issue can be mitigated by adding a conductive agent. However, in the case of CA, the addition of the conductive material appears to have disrupted the heating and cooling rates, causing the material to lose water and form hexahydrite more readily. The observed improvement in NR samples highlights the potential for enhancing the thermal performance of recycled salt hydrates by incorporating conductive materials. This suggests that further research into materials with high thermal conductivity and density compatibility could lead to more effective thermal energy storage solutions.

5.3.4 Performance of Thickening Agent

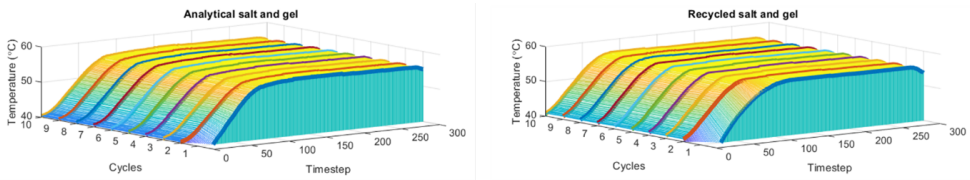

Figure 5.8: GA3 (left) and GR3 (right) epsomite salt mixtures of CMC gel with salt at 0.5°C/min.

Figure 5.8 presents the results of epsomite with CMC gel. As clearly observed neither analytical or GR3 show any phase change in the presence of CMC. There are two explanations for this observation: the salt dissolved entirely into the gel, preventing phase change, or the gel is significantly more hydrophilic than the hexahydrate. In the latter case, the gel could bind a substantial amount of water, which is released during phase change from heptahydrate to hexahydrate, making a rehydration impossible. As discussed in the previous section, the dehydration of epsomite to hexahydrate is notably easier than its rehydration. Consequently, if dehydration occurs, the likelihood of maintaining effective thermal cycling performance becomes negligible.

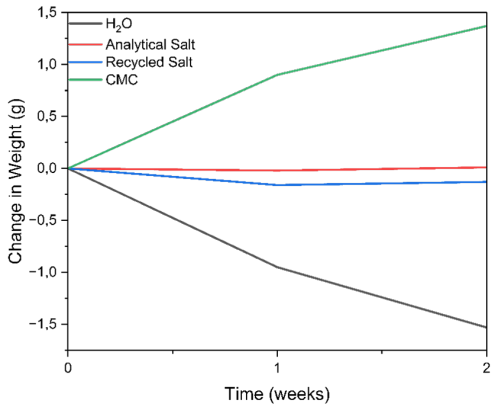

Figure 5.9: Weight change of CMC, recycled salt, analytical salt, and H_2O .

A short experiment was conducted to determine the relative hydrophilicity of the thickening agent (CMC 0.25 g) compared to the salts. A closed container with open bottles of H_2O, CR, CA, and CMC was weighed after one week. The results, presented in Figure 9, revealing a decrease in the weight of H_2O over time, while the weight of CMC increased. However, the weights of the salts remained relatively constant. This confirms the hydrophilic nature of CMC. However, the salt's minimal water absorption indicates a less hydrophilic nature than anticipated. It was initially expected that the salt hydrates would exhibit a level of hydrophilicity similar to that of CMC, ensuring that the two would not compete for moisture. Additional experimentation,

particularly including reducing gel concentrations, could provide additional insights into the interaction between CMC and CA/CR.

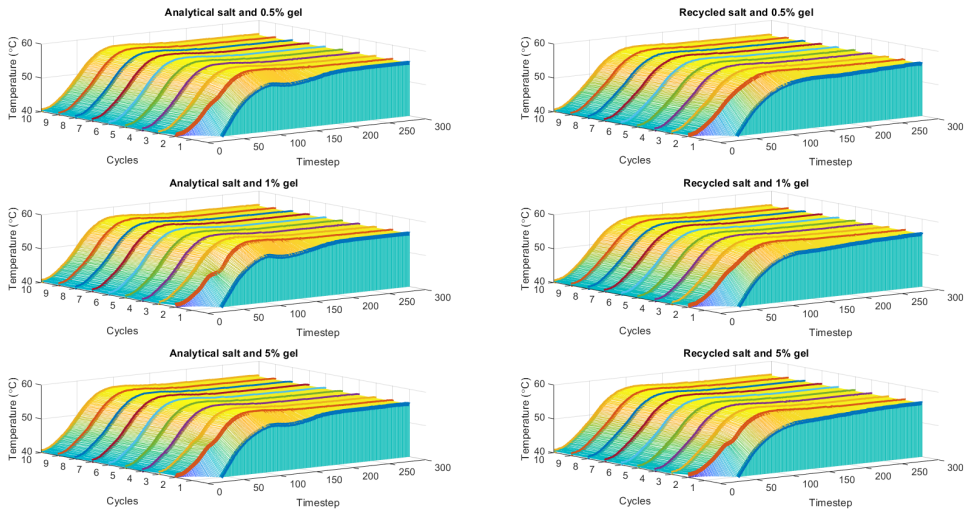

Figure 5.10: Analytical and recycled mixture with different gel ratios. 0.5% refers to the G1, 1% refers to the G2 and 5% refers to the G3 mixture all after combining with water.

To address this issue, the ratio of gel to salt in subsequent experiments was adjusted, resulting in different lesser ratios of GA1/GR1 (0.03g of CMC) and GA2/GR2 (0.05g of CMC). The hypothesis that epsomite might dissolve in the gel solutions was tested by experimenting with varying concentrations of CMC gel (G1, G2, and G3). The results, presented in Figure 10, revealed different levels of latent heat storage based on the CMC concentration. Samples with the lowest CMC concentration (G1) showed no PCM performance in both analytical and recycled salts. When the CMC concentration was increased to GA2, limited latent heat storage was observed. Further increasing the concentration to G3 led to some improvement in latent heat storage for both analytical and recycled materials, but performance remained suboptimal.

When comparing these results with those from samples that did not contain CMC gel, no phase transition was observed in the samples with CMC gel. For the GA samples, the phase change plateau is consistently visible throughout the 10 cycles without gel (as observed in samples CA, CR, NA, and NR). However, with the addition of gel, the plateau becomes barely discernible after the second cycle at the GA2 concentration and diminishes even further at GA3. In contrast, for GR, there is no significant performance improvement when comparing with samples without gel (as observed in samples CA, CR, NA, and NR). However, a sharper plateau is observed at the GR3 CMC gel concentration, although it only lasts for a shorter duration.

5.3.5 Combined Performance of Nucleating and Thickening Agent with PCM

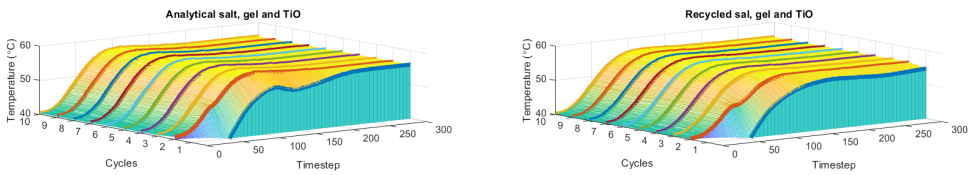

Figure 5.11: Analytical and recycled mixture with Titania and gel .

Ideally, both titania and thickening agents should work synergistically to enhance the properties of epsomite during thermal cycling. While the gels alone did not yield promising results when used with the salts, there was potential that their combination with titania as a conductivity agent could improve overall performance. In the final experiment, mixtures labeled NGA and NGR were prepared, consisting of 5 wt% titania and 10 wt% of the G2 gel. The results, presented in Figure 5.11, indicate no significant reaction, suggesting that the gel may have diminished the beneficial properties of titania rather than enhancing them.

5.3.6 Determining Heat of Fusion

An effective way to study the thermal properties of materials is primarily to determine the heat of fusion. To evaluate the effectiveness of the additive, it is crucial to quantify its impact. Area Under the Curve (AUC) was used to measure the salts mixed with titania to analyze their melting behavior. This analysis was conducted to determine the heat of fusion of the material, which is the amount of energy required to change the material from solid to liquid at its melting point. The AUC is used in this context as a way to quantify the thermal energy involved in the phase change during melting. The conventional approach involves performing DSC on samples; however, this method imposes a limitation on the total material quantity that can be used (typically <10 mg), which can make the result unrepresentative. Additionally, several challenges were encountered, particularly in maintaining proper humidity levels for the samples. The perforations in the hermetically sealed lid allowed steam to escape, resulting in the loss of water. Another observation when conducting DSC measurements on the samples, it was observed that the titania had settled to the bottom of the pan, interfering with the measurement.

The method utilizing the T-History of samples, as demonstrated in previous figures similar to Figure 5.3 and Figure 5.5, was evaluated and quantified. This methodology involved integrating the area difference between the control (ambient) and the measured samples. The resulting measurement was then compared to theoretical values. Subsequently, the AUC was determined and compared to literature standards to assess the validity of the approach. The reported heat of fusion (ΔH_f) for the transformation from epsomite to hexahydrate ranges between 54.3 kJ/mol [127] and 84.6 kJ/mol [150]. The wide range in these values is primarily due to the fact that they are estimations

based on simulations. These values are highly dependent on the specific variables and constraints applied in the modeling of such samples. Converting the average of these values to J/g, the heat of fusion is calculated to be approximately 287.85 J/g. The units of J/g are standard units for heat of fusion, commonly used in DSC, hence the conversion from kJ/mol to J/g for consistent values to be compared to literature.

Table 5.2 presents the values from five different runs of CA, which were used to obtain a robust dataset for statistical analysis. The values are based on the material's second cycle, aligning with the methodology used in DSC analysis. As previously noted, the first heating cycle was disregarded due to the significant noise associated with the initial cycle of the sample, similar to the observations made in DSC measurements. Similar values were observed in CR within normality of values of CA.

Table 5.2: Overview of the area under the curve of the first melt of five different samples of reference salts, the mean value of these five runs, standard deviation, and theoretical latent heat of fusion of epsomite.

Run	AUC ∫
1)	298
2)	253
3)	335
4)	244
5)	297

Mean $\bar{X}$	Standard Deviation S	Theoretical value μ (J/g)
285.4	37.14	287.85

A one-sample T-test was conducted to assess if the obtained values were statistically comparable to the theoretical ones. This analysis was performed under the assumption of normality, which was confirmed by the Shapiro-Wilk test ($p = 0.69$) and visual inspection of the Q-Q plot. Based on this T-test, the p-value equals 0.89, thus, there is no statistical difference ($\alpha = 0.05$), between the measured values and the theoretical one. The obtained values align well with theoretical measurements, indicating that the experimental setup manifests a valid alternative to DSC measurements for larger samples than those typically accommodated by DSC. However, like any rudimentary setup, it is not without limitations and potential sources of error. A significant limitation may be the sensitivity and accuracy of the thermocouples, which might not detect subtle changes effectively. Additionally, the data collection did not occur at every second. To address these issues, ensuring repeatability in testing is essential to minimize erroneous values.

After noting that the initial cycle's values were comparable to theoretically provided values, the analysis was extended to include 10 cycles to assess the overall behavior. Figure 5.12 illustrates the complete data comparison of CA and CR relative to NA and NR (left side of Figure 5.12). Additionally, further samples were tested at a lower maximum temperature, just above the melting point, adjusting the range from

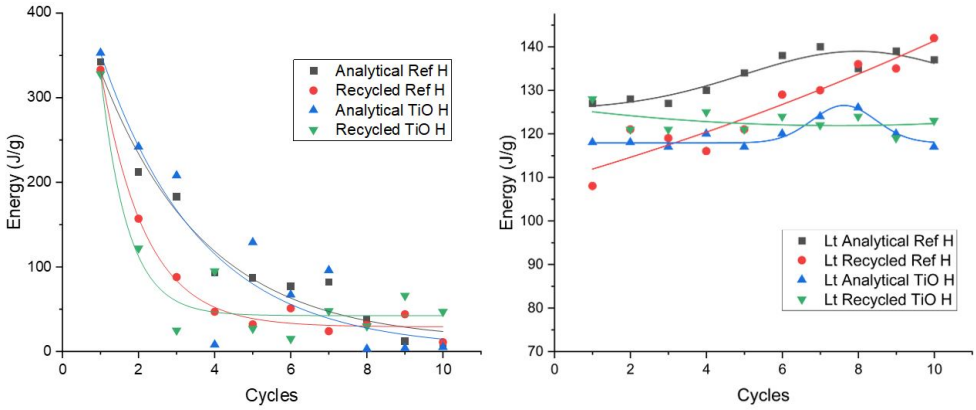

Figure 5.12: Non-Linear Regression [Exponential Decay], Non-Linear Regression of four samples for ten runs, heated to 55°C (Left), Non-Linear behavior of four samples for ten runs heated up to 50°C (Right).

55°C to 50°C (right side of Figure 5.12), while all other parameters were kept the same. The term used for identifying these samples was Lt, which stands for low temperature. This approach allowed for a more comprehensive understanding of the materials' performance across varying conditions.

Figure 5.12 compares non-linear regression behavior (Exponential Decay) applied to four samples over ten cycles. These models did not adequately capture latent heat storage behavior over time in the samples. However, the analysis revealed that the exponential decay model, $y = y_0 + A_1 e^{-x-x_0/t_1}$, provided the best fit for humid (H) climate chamber conditions. The equation components appear as follows: y_0 represents the offset, x_0 denotes the center of the curve, A_1 stands for the amplitude, and t_1 represents the decay constant. These parameters imply the existence of a consistent baseline energy level, y_0, which the material attains across different cycles.

A higher R-squared (R^2) value indicates a stronger correlation between the regression model and the data. Table 5.3 shows that most models had R^2 values around 0.85 or higher. The exception was the NR at a lower temperature, where the Exponential Decay had an R^2 of only 0.504.

Table 5.3: Statistical R^2 values of four samples.

	Analytical Ref	**Recycled Ref**	**Ana+TiO_2**	**Rec+TiO_2**
R^2 Exponential Decay	0.943	0.854	0.850	0.989

These findings suggest that when reaching 55°C, the samples exhibit the maximum energy output consistent with theoretical values of epsomite PCM behavior. However, the observed exponential decay at 55°C indicates the presence of multiple contributing factors, such as low discharge, phase separation, and a lack of nucleating agent sites, which impede an effective material's cycling. Conversely, heating the samples to

a lower temperature (50°C) resulted in greater stability in cycling behavior. This stability may be attributed to the material not being thermally fully charged at this temperature, allowing for a more consistent energy storage and release per cycle. The lower temperature likely enables the material to store more thermal energy per cycle, as it has not reached full latent heat storage capacity and facilitates easier charging and discharging over time.

Measuring and determining the heat of fusion of the samples using T-history methods allows for comparing the thermal energy storage capacity of both analytical and recycled salt hydrates. The results provide comparable numerical values that fall within statistical normalcy. Practically, this indicates that recycled salt hydrates, when used in this manner for thermal energy storage, can potentially be implemented in various beneficial TES applications.

5.4 Closing Remarks

This chapter demonstrated that recycled epsomite can achieve comparable thermal cycling performance to its analytical-grade counterpart when optimized with conductive additives. Despite containing minor impurities, such as brine (Appendix 5.16). The addition of titania improved performance in recycled samples by enhancing thermal conductivity, while CMC failed to prevent phase separation, emphasizing the need for alternative stabilizers. The measured heat of fusion (285.4 ± 37.1 J/g) closely aligned with theoretical values, validating the T-History method as a large-scale alternative to DSC for characterizing PCMs.

While heating samples to 55°C maximized energy storage, it also accelerated performance degradation, whereas heating to 50°C resulted in more stable long-term cycling. Statistical analysis ($R^2 > 0.84$) indicated an exponential decay in thermal performance, highlighting the challenges in rehydrating $MgSO_4 \cdot 6H_2O$ back to its heptahydrate form. The most likely cause for this difficulty is the melting of the epsomite, which reduces bed porosity and, in turn, hampers the vapor transport necessary for water reuptake, which is consistent with the findings reported by Zondag et al. [198].

Overall, this study confirms that recycled salt hydrates are viable alternatives to virgin PCMs for sustainable thermal energy storage applications. The findings contribute to the broader effort of reducing CO_2 emissions by integrating recycled materials into energy-efficient solutions, bridging the gap between material upcycling and TES technology advancements. Future research should explore alternative stabilizers, hydration mechanisms, and composite PCM systems to further improve cyclability and storage efficiency.

5.5 Appendix

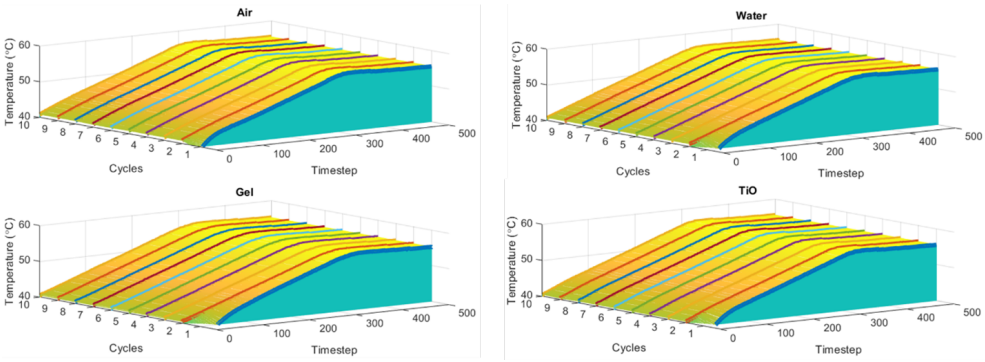

Figure 5.13: Standardized material mixtures at 0.1°C/min.

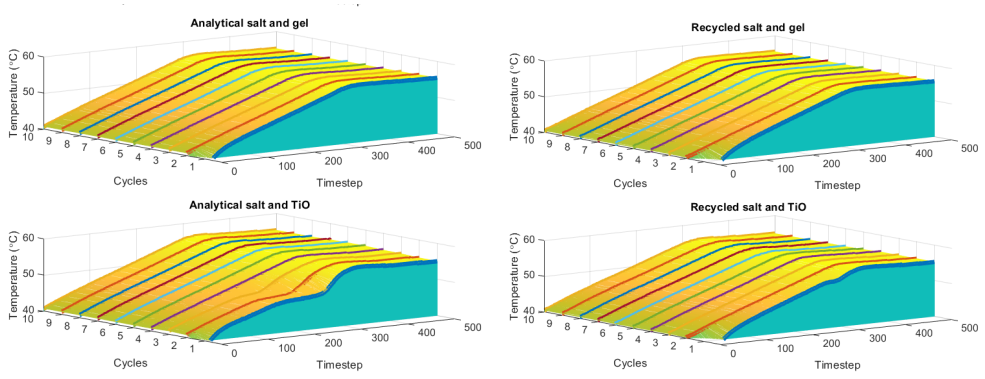

Figure 5.14: Analytical (left) and Recycled (right) epsomite salt mixtures of CMC gel with salt (top) and the titania mix (bottom) at 0.1°C/min.

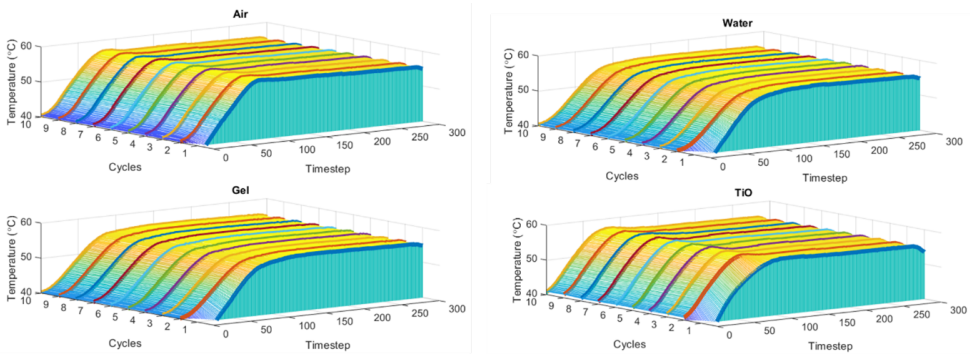

Figure 5.15: Standardized materials mixtures at 0.5° C/min .

Table 5.4: Uncertainty analysis results of the measured values

Uncertainty Parameter	Unit	Uncertainty (S)
Temperature	(°C)	±0.15
Rate of Heating	(°C/min)	±0.1
Enthalpy of Fusion	(J/g)	±1%

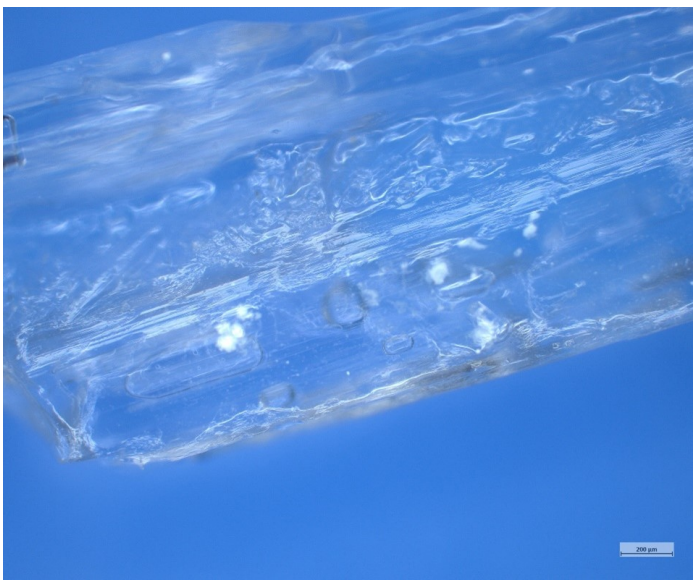

Figure 5.16: Microscopy of recycled Epsomite with observable water/brine bubbles trapped

Chapter 6

Effect of Seawater on Cementitious Material for Artificial Reef Restoration

"When it comes to marine life, our existence depends on their existence"

—June Stoyer

This chapter evaluates the carbonation behavior of sustainable cementitious bindersCEM I, CEM III (with 25% recycled concrete fines), and calcium sulfoaluminate (CSA) to assess their potential in artificial reef construction. Specimens were exposed to accelerated carbonation and artificial seawater for 91 days. Carbonation significantly reduced surface pH and promoted $CaCO_3$ formation via transformation of $Ca(OH)_2$, enhancing surface durability. Compressive strength tests revealed that CEM III achieved the highest strength (69.9 MPa), followed by CEM I (62.8 MPa) and CSA (42.5 MPa). Despite lower mechanical strength, CSA exhibited the highest oyster settlement density (0.0408 oysters/cm^2), attributed to ettringite decomposition and favorable mineral surface formation. CEM I and CEM III experienced calcium leaching, though surface carbonation mitigated degradation. These findings highlight the dual benefit of carbonated binders in structural performance and ecological integration. Moreover, this study provides insight and relevance of salt interactions with surface chemistry in cements, a critical factor in construction, demonstrating how ion exchange and phase transformations of salt hydrates could influence both cementitious composites.

The results of this chapter are published in the following article:
Wesemann, C.A., Antoun, M., Teune, I., Schollbach, K., Rippen, J., Hylkema, A., Oosterhoff, B., & Brouwers, H.J.H. (2025). Effect of Carbonation on Eco-Friendly Binders for Marine Infrastructures.Cement and Building Materials, Vol. 477. https://doi.org/10.1016/j.conbuildmat.2025.141293

6.1 Introduction

This chapter explores the interaction between saltwater solutions and cement-based materials, with a particular focus on artificial reef applications. Understanding the chemical cross-reactivity between cement and saline environments is crucial for evaluating long-term material stability, durability, and potential phase transformations. While salt hydrate PCMs are widely studied for thermal energy storage, their interaction with cementitious materials remains largely unexplored. Investigating these interactions provides valuable insights into the potential effects of PCM salt hydrates exposure on cement formulations, through the use of marine infrastructure, which is commonly exposed to salt water.

The interaction between salt solutions and cementitious binders is not only relevant for durability in marine environments but also reflects broader surface chemistry principles observed in salt hydrate PCMs. Just as phase change behavior in salt hydrates is partly governed by hydration dynamics and lattice stability, cement performance in saline conditions is shaped by ion exchange, surface carbonation, and the reactivity of dissolved salts. In particular, multivalent ions like Mg^{2+} and SO_4^{2-} (commonly present in PCM formulation in Chapters 4 and 5) can disrupt or stabilize hydration products in cements, altering both strength and biological compatibility. These insights reinforce the critical role of surface chemistry and salt interactions in both material design and long-term performance.

The primary objective of this chapter is to determine whether salt solutions influence the chemical composition, setting behavior, and structural integrity of cementitious materials. By analyzing the compatibility and reaction mechanisms between cement and salt solutions, this chapter aims to identify key factors affecting their performance, stability, and potential degradation. The findings will contribute to a broader understanding of cement durability in saline environments and offer practical considerations for designing artificial reefs and other marine-based cement applications.

Coral reefs provide an ecosystem that is recognized for its beauty and importance to marine biodiversity. These complex three-dimensional structures provide a habitat for diverse marine species such as fish, invertebrates, algae, and bacteria. Unfortunately, various direct and indirect human pressures severely burden these reefs continuously [199]. Since the 1970s, life on coral reefs has been critically diminished due to diseases [200], [201], intense fishing activities, water pollution, hurricanes, and an increase in average seawater temperature [202], [203]. As a result, coral reefs are considered one of the most endangered ecosystems on earth at present [204]. In temperate waters, oysters, mussels, and worms build biogenic reefs [205]. Similarly to coral reefs, temperate reefs provide a habitat for a large variety of other marine species and these reefs are under threat as well [206]. The loss of reef ecosystems would not only cause significant harm to other species and ecosystems outside the marine environment, but also to of the millions of people worldwide who rely on the ecosystem for food and a means of income [207].

Artificial reefs can be used to provide a habitat to support the settlement of reef-builders and promote the restoration of marine species in both tropical and temperate

environments [208]. They are manufactured underwater infrastructures that provide a home for various marine species and therefore generate significant economic and environmental benefits [209], [210]. Artificial reefs can vary in shape, material composition, and size, going from well-designed prefabricated structures to simple rubber tires lying at the bottom of the ocean [210]–[213].

Ordinary Portland cement (OPC) based concrete is one of the most used reef materials because it can easily be molded into the desired shape, is widely available, and relatively inexpensive [212], [214]–[216]. However, OPC creates a highly alkaline environment (pH ∼12-13), which hinders marine life from settling on the surface [211], [212], [214], [217], [218]. Marine species usually prefer a more neutral pH of seawater (∼8.3), and it takes OPC between six to eighteen months in the ocean before the pH of the surface reaches equilibrium with seawater [212], [215]. Some organisms are less affected by high pH and will attach to the surface earlier, which can obstruct the settlement of other desired species [219].

The high pH from OPC is primarily due to the leaching of the highly alkaline Ca(OH)2 found throughout the material. In addition to the high pH, concrete production is responsible for 8-9% of worldwide greenhouse gas emissions [220], [221]. The two main approaches to make OPC more sustainable is through the addition of supplementary cementitious material (SCM), such as coal fly ash, and blast-furnace slag, which contain amorphous silica and aluminium that can react with $Ca(OH)_2$ in the cement thereby reducing the cement content. Alternatively, different binders such as sulfoaluminate cements can substitute OPC altogether. Leading to the question: How do different binders influence the attachment and growth of marine organisms, and which materials offer the most optimal development for sustainable artificial reefs? [222]

The use of calcium sulfoaluminate cements (CSA) as an alternative binder has gained particular attention due to its lower CO_2 footprint [223], higher early strengths [224], lower pH [225], [226] and greater resistance to chlorides, sulfates, magnesium, and ammonium salts [227], [228]. Xu et al. demonstrated that the workability, mechanical properties, and surface pH of artificial reefs made with CSA were superior to those made with OPC, making it an attractive binder for their fabrication. CSA cements consist primarily of ye'elimite ($3CaO\ 3Al_2O_3{\cdot}CaSO_4$), C_2S, and sulfates such as gypsum and anhydrite used to regulate the setting. After hydration, the hydrated cement paste contains primarily ettringite ($Ca_4Al_6(SO_4)3(OH)_{12}{\cdot}26H_2O$), amorphous aluminium hydroxide ($Al(OH)_3$), and monosulfate ($Ca_4Al_2O_3(SO_4){\cdot}14H_2O$) and little to no $Ca(OH)_2$. OPC on the other had contains primarily C_3S and C_2S, which react with water to form amorphous C-S-H gel and $Ca(OH)_2$, which causes the high pH of the material. As a result, artificial reefs constructed with CSA has a lower pH which promotes faster marine life attachment, growth, and reproduction [215].

An alternative to using CSA, is the addition of SCMs such as ground granulated blast furnace slag (GGBFS), fly ash, and recycled concrete fines (RCF) to OPC. They can be used to lower the environmental impact of OPC-based structures. These SCMs are pozzolanic, meaning they contain amorphous silica which can react with the $Ca(OH)_2$ present in the hydrated OPC paste to form to form C-S-H gel, i.e. the binding phase, thereby allowing the reduction of OPC content in a mix. The addition of GGBFS

in cements (CEM III) is already widely applied in the Netherlands for marine and other applications [229]. The literature for mortar produced with CEM III show that initial bio-colonization as well as mechanical properties, were promising across various regions around the world [230]. With its lower pH and comparable strength to CEM I, CEM III is a strong candidate for such applications. However, when compared to other materials used in the fabrication of artificial reefs, CEM III alone is not a fully sustainable alternative to natural resources. Its efficiency can be enhanced through the addition of RCF, which reduce the reliance on virgin materials while maintaining overall performance. Recycled concrete fines are the by-product that forms during the crushing and recycling of aggregates from concrete and has been shown to, not only decrease the amount of $Ca(OH)_2$ when used as an SCM, but also improve the mechanical strength of mortar mixes [231], [232].

Since the addition of SCMs is usually associated with a decrease in $Ca(OH)_2$ content due to pozzolanic reactions, the pH of these cementitious mixtures decreases with respect to a their pure OPC analogue. However, previous research indicates that while the addition of SCMs can lower the bulk pH from 13.5 down to 11.7, although the actual magnitude of this decrease depends on the quantity added, fineness of the SCM and amount of amorphous silica [233].

Although alternative binders and the addition of SCMs might improve the sustainability of the structure, the pH might not be low enough to allow for proper settlement of reef-builders. Though there is marine life that is resistant to these higher pH values, there are usually non-desirable and can invade the structures before allowing the desired marine life to grow and populate the reefs [234]–[236]. To further lower the pH of the material's surface, treatments such as carbonation could be applied [208]. Carbonation describes the formation of calcium carbonate due to the reaction of (atmospheric) CO_2 with calcium containing phases in cement. During the carbonation, both calcium from the C-S-H gel and from $Ca(OH)_2$ is transformed to $CaCO_3$, causing a reduction in the pH. Natural carbonation is a relatively slow process due to the low CO_2 concentration and a high relative humidity which is required for the dissolution of calcium. Carbonation can be accelerated in a climate chamber by elevating the CO_2 concentration and relative humidity (RH). The speed of the carbonation, quantity of carbonated material and carbonation depth will depend on the material porosity in addition to the CO_2 and RH levels [237]–[239].

Although the mechanical and chemical performance of the mixtures described has been well documented, their respective suitability as materials for artificial reefs is still unclear. While previous studies have examined the chemical interactions between seawater and cement (e.g. precipitation, ion exchange), their relation to their ecological performance remains a gap in the literature. The role of material design in optimizing for both structural performance (against water currents and deep-water pressure) and ecological outcomes, particularly for promoting oyster settlement, thus remains underexplored [222]. Magallana gigas, the oyster species selected in this study, plays a critical role in temperate reef ecosystems as an ecosystem engineer, forming complex structures that enhance biodiversity and improve water quality through filtration [240]. Their settlement preferences are vital for reef restoration and management efforts,

as these preferences directly influence habitat stability, shoreline protection, and the overall health of marine ecosystems [241].

This research therefore aims to understand how different cementitious artificial reefs could be used for designing in a sustainable way, with the aim to achieve successful oyster settlement using sustainable cement alternatives. Combined with the wide array of available options to make a sustainable cement based artificial reef which is durable in salt water, it begs the question which material and possible treatment leads to the best ecological performance; taking into account the minerology and the pH of the materials.

This research aims to study the physical and ecological performance of three different binders before and after surface carbonation with the aim of utilizing them to produce artificial reefs. To assess which type of binder has the strongest impact on the pH, pure paste samples were used without the addition of aggregates. Three paste specimens were produced: 1) CEM I, 2) CEM III, where 25%vol was replaced by recycled concrete fines to reduce the cement content further, and 3) CSA. Half of the samples were subjected to accelerated surface carbonation to reduce the surface pH. The samples were then cured in artificial seawater in the lab for 91 days and assessed at specific intervals for pH, leaching in water (IC/ICP), chemical characterization (XRF and XRD), mechanical properties, microstructure (optical microscope). To assess the ecological performance of the binders for reef-builders, an oyster settlement experiment was conducted in a marine field environment.

6.2 Materials and Methods

6.2.1 Materials

For this study, pure paste samples were made since the focus is solely on the performance of the binders since they are responsible for the generation of the high pH in concrete. Moreover, the absence of added aggregates enables a more accurate assessment of the direct interaction between seawater and the cementitious binder, without interference from aggregates. The paste samples were produced using three different binders: CEM I 42.5 (Heidelberg Materials), CEM III B (Heidelberg Materials) + 25 vol% RCF (Circular Mineral), and CSA (Alpenat, VICAT). The CEM III + RCF samples will be referred to as SCM. The CEM I paste served as the reference sample (REF), the CEM III + RCF paste as a sustainable sample based on SCM addition (SCM), and the CSA paste as a sustainable alternative binder sample (CSA). Chemical composition, as well as the specific gravity of the raw materials, are given in Table 6.1 and Table 6.2.

The chemical composition was determined with XRF using the fused bead method as described in the methods section. In all Q-XRD analysis, C_2S includes Larnite and α'-C_2S; Carbonates are the sum of Aragonite, Calcite, and Vaterite; and Sulfates are the sum of Anhydrite, Bassanite, and Gypsum. Table 6.2 shows the mineralogical composition as determined with Q-XRD.

The artificial seawater batches were prepared in the lab, with a salinity of 3.5%, using distilled water and Tropic Marin REEFMIX Sea salt (Composition in annex). The

samples to seawater ratio was 1:10 volumetrically, and this remained constant as samples were removed over time.

Table 6.1: Chemical compositions of CEM I cement, CEM III cement, and CSA cement (% mass) and their Density (g/cm^3).

	CEM I	**CEM III**	**CSA**	**RCF**
MgO	2.28	5.17	1.27	1.25
Al_2O_3	5.14	7.96	18.2	4.39
SiO_2	19.39	28.25	9.04	58.62
SO_3	2.92	4.88	17.14	1.16
CaO	61.64	48.63	44.39	16.88
Fe_2O_3	3.25	1.43	8.43	1.3
Others	5.39	3.7	1.52	1.06
LOI	3.35	0.81	4.51	15.34
Density (g/cm^3)	3.15	2.8	2.98	2.6

Table 6.2: Mineralogical compositions of CEM I, CEM III, and CSA. All results are in wt%.

Name	**Chemical Formula**	**CEM I**	**CEM III**	**CSA**	**RCF**
Hatrurite	Ca_3SiO_5	49.24	21.48	-	-
C2S	Ca_2SiO_4	21.9	5.57	15.99	-
Brownmillerite	$Ca_2(Al,Fe)_2O_5$	10.66	3.02	-	-
Portlandite	$Ca(OH)_2$	-	-	-	0.81
Sulfates*	$CaSO_4 \cdot xH_2O$	2.05	3.42	13.16	3.04
Calcite	$CaCO_3$	-	-	3.77	12.34
Quartz	SiO_2	1.73	1.41	0.41	49.43
Feldspar	$NaAlSi_3O_8$	1.28	-	-	7.19
Dolomite	$MgCa(CO_3)_2$	-	-	1.27	1.04
Ye'elimite	$Ca_4Al_6O_{12}$	-	-	25.35	-
Perovskite	$CaTiO_3$	-	-	9.52	-
Magnetite	Fe_3O_4	-	-	1.86	-
Merwinite	$Ca_3Mg(SiO_4)_3$	-	2.17	-	-
Periclase	MgO	1.42	-	-	-
Amorphous	-	12.04	62.93	28.68	26.16

6.2.2 Methods

Sample Preparation and Testing

The three different pastes were mixed according to Table 6.3, where a constant water-to-cement ratio of 0.4 was used. For CEM I, the designation "REF" was used to indicate its role as the reference material, while CSA retained its standard naming. For the SCM mix, 25 vol% of the CEM-III was replaced with RCF (d_{50} 53.2 μm, span 4.7 μm -201.9 μm Appendix Figure 6.12). All the paste samples were thoroughly mixed according to EN 196-1 and cast in 40x40x160 mm^3 molds. The flowability of the paste was measured using the flow table spread test, and the flow was kept constant for all mixes at 22 cm by adding a superplasticizer (Sika ViscoFlow-37 con. 32% SPL).

Table 6.3: Cement mix designs.

	REF	**SCM**	**CSA**
Cement (g)	1393.81	1141.30	1359.49
Water (g)	557.52	456.52	543.80
Superplasticizer (g)	-	3.5	5.8
Recycled fines (g)	-	339.67	-

After casting, one set of samples was cured for a total of 28 days as shown in Figure 6.1 in a climatized room, while a separate set of samples was cured for 21 days and subsequently carbonated for 7 days so that the final age before exposure to sea water was the same. This is indicated by a C in the sample name. The samples were carbonated in a climate chamber (Memmert ICH 260 C) with 20% CO2 and 80% relative humidity (RH). After curing the samples were either placed in separate containers with artificial seawater at 20 $\pm$ 2°C (indicated by a W at the end of the sample name) or left to cure at 80% RH for the same amount of time and used as a reference. A schematic overview of the sample names and their respective treatment and conducted measurements is provided in Figure 6.1. Saltwater was refreshed at 7, 14, 28, 56, and 91 days to maintain consistent salt composition and pH levels, thereby preventing changes due to leaching. This approach also avoids equilibrium within the closed system and mimics the consistent composition of natural seawater as an open system. Before each water renewal, two liquid samples were taken from each container and used for IC and ICP analysis. Moreover, the pH value of the artificial sea water was measured by placing a pH-measuring electrode in the container where the samples were stored at 7, 14, 28, 56, and 91 days before the artificial sea water was renewed.

The samples were evaluated for their mechanical performance after placement in seawater at 28 and 91 days. For each sample, three prisms were used for compressive strength testing and one additional prism was used for chemical characterization. To characterize carbonation, the surface pH was measured by spraying phenolphthalein on the fresh surface of the cement prisms after flexural strength testing. The surface of the paste specimens was further analyzed using XRF and XRD to determine the chemical and mineralogical changes due to surface carbonation and seawater exposure.

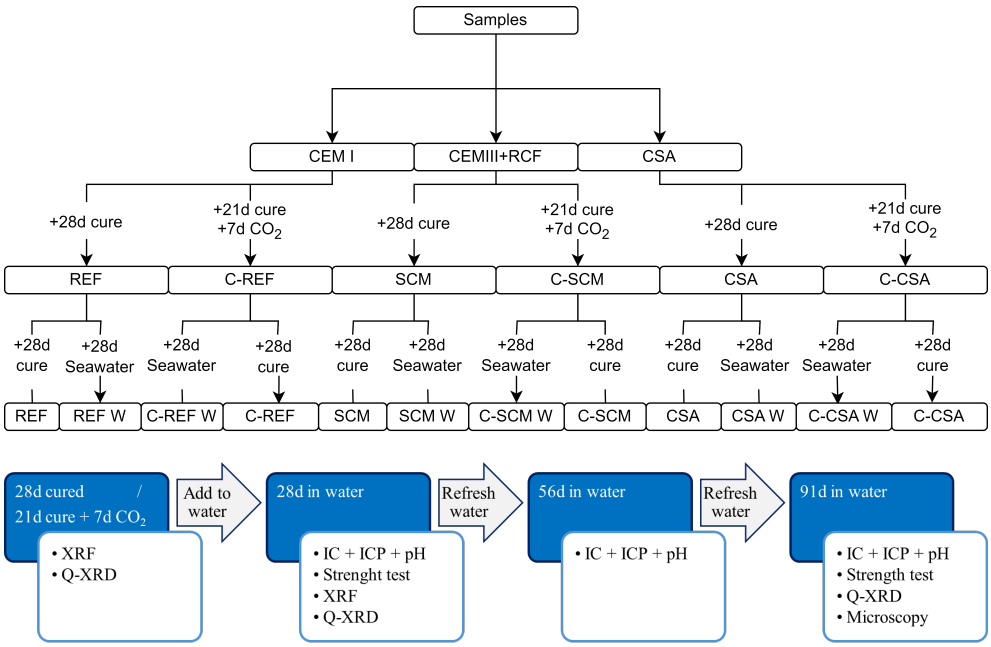

Figure 6.1: Schematic overview of sample naming according to preparation and aging and the respective measurements performed on the samples. The addition of "C" and "W" stand for the respective treatment by carbonation (C) and/or placement in artificial seawater (W).

For this purpose around three millimeters of the surface were cut, using a water-cooled saw and then dried at 60°C for 48 hours to evaporate the water and halt further hydration. The material was subsequently crushed manually, sieved below 500 microns, and used for further analysis.

ICP-OES and IC

The composition of the artificial seawater was also determined with ICP and IC as shown in Table 6.4.

Table 6.4: Artificial Seawater composition from IC/ICP-OES.

	Na^+ (g/L)	K^+ (g/L)	Mg^{2+} (g/L)	Ca^{2+} (g/L)	Si (mg/L)	Cl- (g/L)	SO_4^{2-} (g/L)
Artificial Seawater	10.25	0.41	1.35	0.41	0.71	19.67	2.72

The complete set of measured ion concentrations is reported in Tables 6.6 and 6.7 found in the Appendix section of this chapter.

Ecological Field Experiment

To test the ecological performance of the binders in the marine environment, an extra set of samples (80x80x20 mm) was produced using the cement mix design as described before (Table 6.3) with the same initial curing procedure until the samples were 28d old with half of them subjected to active carbonation for 7d after 21d of hydration. In total 18 tiles were divided over six settlement frames for each treatment (Figure 6.2), so 108 tiles in total were included. The frames were then placed in the Eastern Scheldt (51.45125° N, 4.116089° E), in June 2022. The Eastern Scheldt is a sea arm in the southwest of the Netherlands, where natural Pacific oyster reefs occur (Magallana gigas). After three months (90 days), the number of oyster recruits on each tile was counted in the field during low tide (Figure 6.2). A generalized linear mixed model (GLMM) was used to analyze factors influencing oyster recruitment, with material type (REF, SCM, CSA) and carbonation treatment (carbonated, uncarbonated) as fixed effects, position on the frame as a covariate, and random intercepts for frame (1|table) and row nested within frame (1|table:row). The dependent variable was oyster density (oysters/cm^2), modeled using a Poisson distribution with a log link function via the glmer function in the lme4 package (R). Pairwise comparisons were done with the "emmmeans" package [242].

Figure 6.2: Settlement frames were used to attach tiles of the different sample types (REF, SCM, CSA, C-REF, C-SCM, and C-CSA) in the marine environment to study their ecological performance. The six settlement frames were placed in the Eastern Scheldt (Netherlands).

6.3 Results and Discussion

6.3.1 Compressive Strength

The compressive strength of all samples was measured after 28 and 91d. The 0-day strength represents the compressive strength of the samples immediately after curing and prior to their exposure to seawater. The samples had, at this point, already been cured for a total of 28 days, or, in the case of carbonated samples, cured for 21 days followed by 7 days in a carbonation chamber. A set of dry samples (not exposed or immersed in seawater) were tested in parallel to the samples placed in artificial seawater to study the impact of seawater on the strength development as shown in Figure 6.1. The compressive strength was tested after 28 days and 91 days of seawater exposure as shown in Figure 6.3.

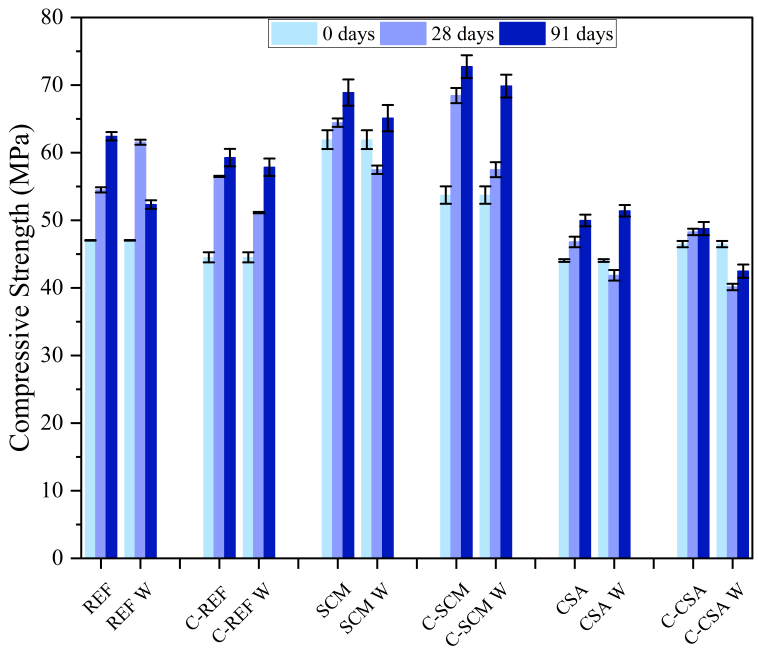

Figure 6.3: Compressive strength at 28 and 91 days with respective standard deviation based on three measurements. The zero days is added to indicate that these are the samples before placement in artificial seawater.

Both the dry REF sample and the dry carbonated C-REF sample show a consistent increase in strength during curing, which is associated with the continued hydration over time of OPC. The 28 day strength of the C-REF sample appears to be slightly higher than the REF sample, but has a lower final strength at 91 days (62.4 vs 59.3

MPa). After placement in seawater, the 91 day strength of both the carbonated C-REF W (57.9±1.3 MPa) and uncarbonated REF W (52.3±0.6 MPa) is lower than their dry counterparts. This may be attributed to the detrimental interaction of salt with hydration products, resulting in decreased strength [243]. Interestingly, the 91-day strength of REF W is not only lower than that of the REF sample but also decreases after 28 days. This shows that the strength of the REF sample is compromised upon prolonged exposure to seawater. The carbonated sample does not show this kind of behavior which suggests that surface carbonation does help to reduce the harmful effects of salts on the strength development of OPC.

The SCM (64.4 MPa) and C-SCM (68.5 MPa) samples show the highest strength development overall and even exceed the strength of the REF samples of the environment. After carbonation, the strength at 0 days is decreased, but after 28 days it exceeds the strength of the uncarbonated sample, both dry and when exposed to seawater. Curing in seawater does decrease the strength development. However, similar to the REF sample, surface carbonation seems to reduce this impact at 91 days, the C-SCM W sample (69.9 MPa) achieves similar strength of the SCM sample at 91 days (68.9 MPa). These effects of surface carbonation will be discussed later in more detail on under the minerology and cross-section imaging sections of this paper.

The CSA samples have the lowest strength development overall with an average strength of around 45 MPa. Surface carbonation of dry samples causes a slight increase in strength at 0 and 28 days, but at 91 days the strength development is similar to the uncarbonated dry samples. Exposure to seawater reduces the strength of the samples at 28 days. At 91 days the strength of the CSA W sample (51.4 MPa) increases significantly in strength, exceeding the strength of the dry counterpart. The C-CSA W sample (42.5 MPa) did, however, not show a significant increase in strength development at 91 days and has the lowest strength of all samples at 91 days.

Currently, there is no defined requirement for the compressive strength of cementitious artificial reefs [244]–[246]. However, an Atlantic regulation from 2004 suggests that the requirement for artificial reefs should be >24 MPa [247]. This regulation might be in consideration of strong water currents. Currently, the samples tested exceed such recommendations and meet the required 28 day curing strength building standards (BS EN 197).

6.3.2 Leaching Behaviour

Figures 6.4 and 6.5 show the change in cation and anion concentration respectively of the artificial sea water in contact with the samples after 28, 56 and 91d compared to the starting concentration of the artificial seawater (Table 6.4, Section 6.2.2). Changes in the concentration of other ions were below 0.5 mg/L and are shown in Appendix Table 6.10. Any negative change indicates an uptake of the respective ion, whereas an increase is due to leaching from the sample.

As shown in Figure 6.4, all samples take up sodium and magnesium from the seawater, with magnesium uptake showing a significant reduction over time from 40% down to 10% across all samples. The uptake of magnesium, sodium and potassium from the

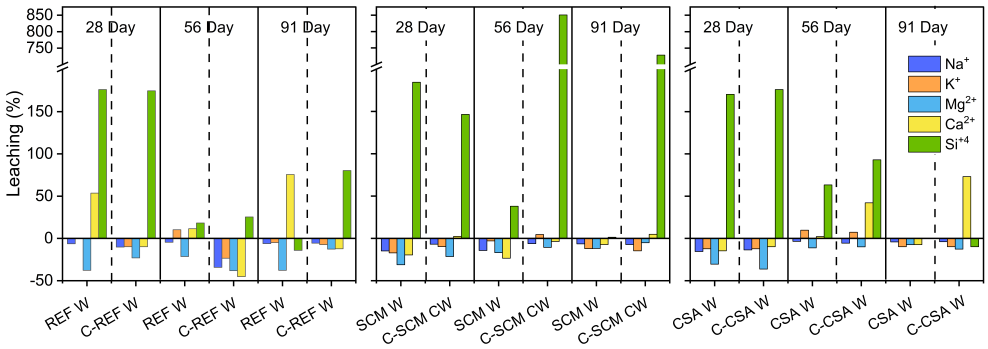

Figure 6.4: Respective change of ions measured with IC compared to artificial seawater.

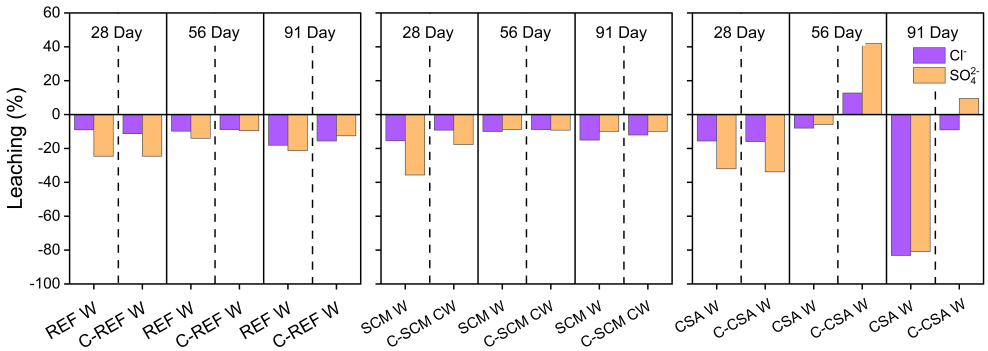

Figure 6.5: Respective change of ions measured with IC compared to artificial seawater.

seawater could be due to ion-exchange with the C-S-H gel or precipitation of salts, and gradually decreases as the sample ages. Moreover, nearly all the samples exhibit considerable leaching of silica, which is possibly due to the high pH of the samples (Figure 6.6) [248]. Lastly, with the exception of the surface carbonated CSA sample, all samples take up sulfates and chlorides. The uptake of sulfates by the sulfate-rich uncarbonated CSA is particularly remarkable given the high sulfate concentration of the sample. The leaching and uptake of these ions was further validated using XRF of surface (∼1cm) as shown in Appendix Table 6.8. Although the XRF analysis does not allow for a direct comparison with the measured sea water composition, any changes in elemental composition can be used as a secondary analysis to confirm the uptake or leaching of materials. For example, the uptake of magnesium in the REF sample according to the sea water composition was paired with an increase in MgO of approximately 1-4 wt%.

As shown in Figures 6.4 and 6.5, the leaching behavior of the REF and SCM sample is relatively similar. Both materials show significant silica leaching which increases upon carbonation of the sample, which could be due to an increase in porosity after carbonation which allows for more silica leaching from phases further below the surface

[249]. However, this behavior is not observed for the other samples, which suggests that the silica leaching is not solely due to a change in porosity after carbonation, but could also be due in part to the higher quantity of silica in the sample (28 wt%, Table 6.1). Additionally, it is known that carbonation of C-S-H leads to the formation of amorphous silica in addition to $CaCO_3$ [250]. Apart from the silica leaching, carbonation of the sample leads to little variation in leaching or uptake of other elements and appears to be reasonably comparable to the REF sample. Moreover, both materials have a very similar uptake of sulfates and chlorides, where carbonation leads to a slight decrease in sulfate uptake. However, the calcium leaching of the uncarbonated REF sample is significantly higher than for the SCM samples, where the latter shows an uptake of calcium rather than leaching. The only other sample which leaches calcium is the carbonated CSA sample at 56 and 91 days. This behavior is accompanied by a leaching of sulfates as shown in Figure 6.5 and is possibly due to an increased porosity of the sample after carbonation or the decomposition of ettringite [251].

The uncarbonated REF sample shows the highest pH of the leachate and the highest Ca concentration at all ages (Figure 6.6). The observed leaching is primarily due to the dissolution of $Ca(OH)_2$ and less likely, but still possible, ion-exchange of calcium in the C-S-H gel by magnesium or sodium from the seawater [252], [253]. The carbonated REF sample shows a calcium uptake throughout all the measured ages instead, which is likely due to the preferential precipitation of additional $CaCO_3$ on the layer formed during surface carbonation [254].

The uncarbonated REF sample further shows a significant uptake of magnesium from the seawater across all ages which is most likely due to the precipitation of salts like brucite which is further discussed in Section 5.3.3. As shown in Figure 6.6, the carbonated sample has a lower pH which could in part be responsible for the lower uptake of ions due to a decrease in pH which increases the solubility of metal hydroxides such as brucite. Similarly, a slight increase of potassium and sodium adsorption can be observed after carbonation of the reference sample which could be due to the uptake of these ions into the C-S-H gel [67].

It is clear that for all the samples the pH increases over time and carbonation lowers the pH of the solution, even though the water is replaced every 28 days. The most significant drop can be observed for the REF sample where the pH drops from 9.5 to 8.9. This can be explained by the reduction in leachable $Ca(OH)_2$ due to the carbonation as described in the following equation:

$$Ca(OH)_2 + CO_2 \rightarrow CaCO_3 + H_2O \tag{6.1}$$

Moreover, the pH continues to be lower for the carbonated samples after prolonged exposure to the artificial seawater, highlighting that the surface carbonation creates a leaching barrier. Of all the samples investigated, the CSA samples have the lowest leachate pH (8.6-7.9), which aligns with the pH reported in literature for CSA-based cement [255], [256].

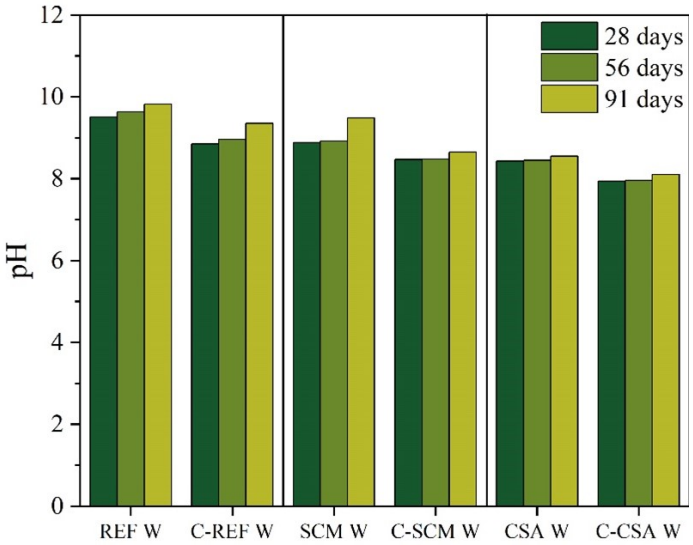

Figure 6.6: pH Measurements at 28, 56, and 91 days.

The pH of the samples can, to some extent, be associated with the concentration of leachable Ca^{+2}, however it cannot solely be explained by this since the increase in pH over time does not match the decrease in calcium leaching of the samples. When analyzing the data in Figure 6.4, REF and C-REF exhibit contrasting behaviors in calcium leaching. As previously mentioned, carbonation increases sample porosity, which enhances the diffusivity of components such as silica. However, for REF, silica leaching decreases as pH increases, while in C-REF, silica leaching remains constant. This behavior is contrary to expectations, as silica is typically more soluble at lower pH levels.

In the same figure, SCM and C-SCM samples consistently absorb calcium. This is expected for SCM due to its lower portlandite content, but the amount of silica leached from C-SCM at higher pH is unexpected. For CSA samples, the process differs significantly. Ettringite, which is water-soluble, breaks down during carbonation into calcium sulfates, alumina hydroxides, and carbonates. Interestingly, the carbonation layer appears to have a protective effect, as C-CSA behaves similarly to uncarbonated CSA, with the key difference being an increase in calcium leaching, likely from soluble gypsum, as indicated in Figure 6.5.

Interestingly, the change in pH may be attributed to the ion exchange of hydroxyl ions with chloride ions in solution. However, Figure 6.5 reveals that the CSA W sample exhibits a substantial uptake of chloride ions at 91 days, which does not correspond to the minor increase in pH observed. Furthermore, while the pH increases significantly between 56 and 91 days for all samples, the rate of chloride uptake remains relatively unchanged. The amount of Na^+ and Cl^- in the system does not change enough to suggest that the absorption of chlorides would lead to the formation of sodium

hydroxide. This discrepancy suggests that additional processes, beyond ion exchange, may be contributing to the observed changes in pH. These processes remain unclear and warrant further investigation.

6.3.3 Mineralogy of the Surface

To understand the change in pH and mineralogical composition, Q-XRD analysis was done of the surface of each cement sample as described in Paragraph 5.2.1. The results before and after 91 days of exposure to sea water are shown in Table 6.5, and the full analysis is provided in Tables 6.9 to 6.12 found in the Appendix section of this chapter. Since the Q-XRD analysis was conducted on the top layer of the sample, the resulting quantities may be influenced by the varying thickness of mineral precipitates. As a result, the measured quantities primarily reflect changes in the surface composition rather than the entire sample.

Table 6.5: Q-XRD analysis of the crystalline phases in wt% of samples both exposed and non-exposed to seawater conditions for 90d, both carbonated and uncarbonated samples.

Phases	REF	REF W 90	C-REF	C-REF W 90	SCM	SCM W 90	C-SCM	C-SCM W 90	CSA	CSA W 90	C-CSA	C-CSA W 90
Carbonates*	9.8	3.9	18.4	14.5	8.5	5.5	15.8	13.6	4.1	4.3	23.1	28.1
Ca Sulphates*	-	-	-	-	-	1.2	-	-	5	1.7	13.5	7.9
Ettringite	-	-	-	-	2.3	-	7.5	-	12.3	-	0.3	-
Brucite ($Mg(OH)_2$)	-	24.5	-	2.4	-	3.8	-	-	-	-	-	-
$Al(OH)_3$	-	-	-	-	-	-	-	-	2.4	3.3	2.8	2
Unreacted Clinker	23.3	12.8	21.1	18	3.7	3	2.9	2.3	14.5	11.6	5.5	3.8
Portlandite	5.6	0.8	0.6	0.5	0.9	0.1	0.1	-	-	-	-	-
Other	3.5	2.9	2.8	3.4	12	12	8.9	9.9	11.6	13.2	12	12
Amorphous	57.9	55.1	57.1	61.2	72	74.4	64.4	74	50	65.8	42.8	46.2

*includes the phases calcite, aragonite and vaterite

Table 6.5 summarizes the mineralogical phase composition of the samples. Here, the carbonate phases include the minerals aragonite, calcite, and vaterite. The sulfate phases are a summation of both gypsum and bassanite, while $Al(OH)_3$ is a summation of the mineral phases gibbsite, bayerite and nordstrandite. Finally, unreacted clinker phases include C_2S, C_3S (in REF and SCM), C_3A (REF), brownmillerite (SCM), and ye'elimite (CSA).

As shown in Table 6.5, the reference sample has the highest portlandite content (5.6%), followed by the SCM sample (0.9%), and no portlandite was detected in the CSA sample as is expected for the latter. The lower portlandite content in the SCM sample and complete absence of the portlandite in the CSA sample appears to be in line with the reduced pH of the respective samples as shown in in Figure 6.5 and previous literature [257]–[259]. After carbonation, the portlandite content decreases significantly for the reference sample (0.6%) and the SCM sample (0.1%). The carbonation of the SCM further caused the formation of small amounts of ettringite for reasons unclear. Carbonation of the CSA sample results in the formation of gypsum, paired with a decrease in ettringite content and a strong increase in carbonates (+19 wt%). This outcome aligns with previous research where carbonation-induced decomposition of

ettringite lead to the formation of calcium carbonate, gypsum, alumina gel, and water [260], [261]. Moreover, it has been reported that CSA cements generally have a higher porosity compared to OPC pastes with similar w/b ratios, which makes the CSA cement more prone to carbonation due to the increased diffusivity of CO_2 [262], [263]. This could, in part, explain the high carbonate content of the CSA samples (23.1%) compared to the REF (18.4%) and SCM samples (15.8%).

The formation of brucite ($Mg(OH)_2$) was detected for the REF and SCM sample, which is consistent with the uptake of Mg as shown in Table 6.5 [264]. As shown in Figures 6.3 and 6.4, there is significant calcium leaching for the REF sample and increase in pH over time, which is explain by the decrease in portlandite content. Interestingly no brucite formation was detected for CSA sample despite the magnesium uptake. The formation of brucite on cementitious materials has been well documented in various works [265], [266]. On these works there are two known chemical reaction that may occur for cementitious material to form brucite, one with CSH gel and another with portlandite. On Equation (6.2) the formation of brucite due to reaction of the C-S-H phase with magnesium sulfate is as follows:

$$3CaO{\cdot}2SiO_2{\cdot}nH_2O_{(s)} + Mg^{2+}_{(aq)} + SO^{2-}_{4(aq)} \rightarrow CaSO_4{\cdot}2H_2O_{(s)} + Mg(OH)_{2(s)} + SiO_2{\cdot}nH_2O_{(s)} \tag{6.2}$$

The other possible reaction that could explain the magnesium uptake is the reaction of magnesium sulfate with portlandite as shown in the following equation:

$$Ca^{2+}_{(aq)} + OH^{-}_{(aq)} + Mg^{2+}_{(aq)} + SO^{2-}_{4(aq)} \rightarrow CaSO_4 \cdot 2H_2O_{(s)} + Mg(OH)_{2(s)} \tag{6.3}$$

As with the C-S-H reaction, the reaction of magnesium sulfate with portlandite leads to the formation of gypsum which in turn forms brucite. Since there is less brucite formed in the SCM sample compared to the REF sample, it is more likely that the portlandite is primarily responsible for the precipitation of brucite, since the SCM sample contains less portlandite and more amorphous C-S-H.

Moreover, the high pH of the REF sample (Figure 6.6) would cause brucite to have a lower solubility, thus further promoting the precipitation of this phase on the material surface. Lastly, the formation of brucite in the REF sample could further explain the strong decrease in strength as observed in Figure 6.3, as the reaction of magnesium sulfate has been associated with a reduction in strength of cementitious materials [265], [267].

The decrease in brucite formation after carbonation can thus be explained by the decrease in C-S-H gel and portlandite content. Moreover, the absence of portlandite in the CSA sample thus prevents the formation of brucite. The formation of gypsum was not observed in either case, although sulfate uptake did occur (Figure 6.5). This could be due to the presence of only very small amounts or its amorphization during milling.

Placement of the uncarbonated CSA samples in seawater leads primarily to a reduction in ettringite and calcium sulfate phases such as gypsum. Since no calcium or sulfate leaching was observed, it could be that the ettringite transformed into an amorphous phase upon prolonged hydration. Since surface carbonation of CSA results in the decomposition of ettringite and the formation of gypsum, the strong decrease in calcium sulfates (13.5 versus 7.9 wt%) after placement in seawater could be due to the dissolution of the gypsum which is reflected by the leaching of calcium and sulfate.

Comparison of the residual clinker content of the samples shows that the samples continue to hydrate when placed in seawater, but carbonation appears to limits the hydration of residual clinker phases, which is particularly pronounced for the REF sample.

When further comparing the chloride leaching with the Q-XRD results, only one sample showed the precipitation of a chloride-containing salt: SCM-W at 91 days where a minor amount of Friedel's salts was detected (1.8%). The uptake of sodium and potassium did not lead to the formation of a XRD visible compound and could thus be due to ion-exchange or ion uptake of the C-S-H gel which is XRD amorphous. Moreover, the magnesium uptake of the CSA samples did not lead to brucite precipitation and thus remains unexplained.

Overall, the following relations were found between Q-XRD and the ions in solution: a reduction in portlandite content correlates with the leaching of calcium and increase in pH of the sample. The magnesium uptake observed in the REF and SCM samples corresponds to the formation of brucite on the sample surface. The leaching of calcium and sulfate content from the C-CSA sample was associated with the dissolution of gypsum.

6.3.4 Cross Section and Microscopy of Prisms

To further confirm the precipitation of new minerals on the surface of the material, cross sections of the prism after 91 days were studied with optical microscopy. Moreover, the species were sprayed with a phenolphthalein solution to study changes in the pH of the sample, as the solution turns pink when the pH exceeds 8.2. Since carbonation causes a lowering of the pH, the phenolphthalein solution will appear colorless on the areas which are carbonated and pink on the non-carbonated areas.

As shown in Figure 6.7, the microscopy image of the C-REF samples does not show a visible carbonation layer on the surface and looks identical to the uncarbonated sample. When tested with phenolphthalein, no visible color change was observed which shows that the carbonates are solely located on the very surface of the material and did not form deeper into the material.

In contrast, when examining samples exposed to seawater, a thick layer (around 315 μm) is observed on REF W. This layer was previously identified as containing brucite ($Mg(OH)_2$) which is discussed in Section 5.3.3. Interestingly, the carbonated REF samples exposed to seawater had a noticeably thinner layer (65 μm) of largely calcite with a small amount of brucite on the surface. This aligns with the decreased brucite content and decreased magnesium uptake of the material. The phenolphthalein tests

further indicate that there was no significant change in surface pH, which thus shows that there is no change in carbonation depth, highlighting the material's stability even after prolonged exposure to seawater.

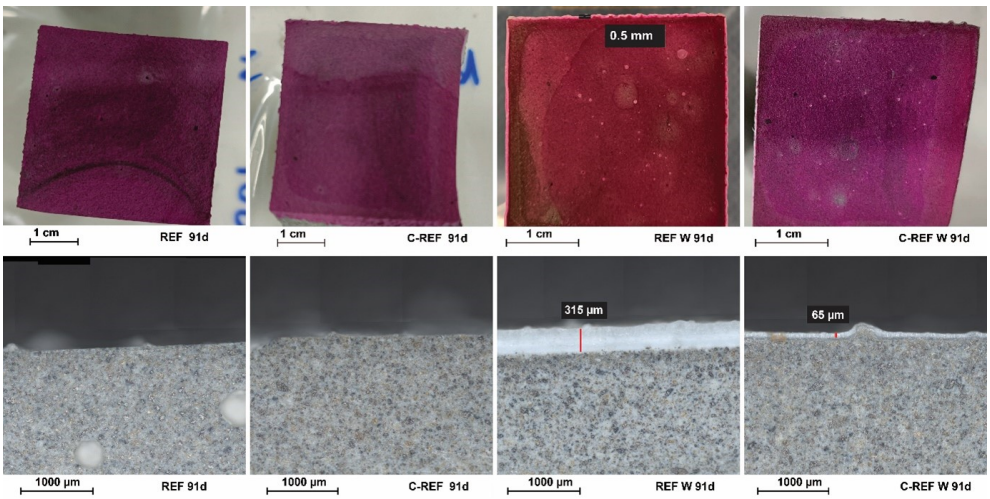

Figure 6.7: REF microscopy cross sections at 91 days, carbonated sample not exposed to seawater (left) in seawater uncarbonated (center) and carbonated in seawater (right).

In Figure 6.8, the microscopy results show no visible differences between SCM and C-SCM samples. In the C-SCM sample, the phenolphthalein test reveals a small colorless region, measuring around 0.9 mm, which likely corresponds to the depth of pH change due to carbonation.

After placement in seawater, the SCM W sample shows the formation of a 110 μm layer containing brucite on the surface which is absent in the C-SCM W sample and consistent with the Q-XRD results. The phenolphthalein test shows a stronger discoloration of surface with a thickness of approximately 0.9 mm, similar to the carbonation layer. The microscopy image further shows the formation of a dark layer in C-SCM W, which is located 670 μm below the surface, followed by a lighter layer (230 μm) running parallel to the dark layer. Together, these layers form a distinct internal demarcation, around 1.3 mm thick in total. The origin of this internal layer is likely due to a leaching front, which shows that the seawater was able to penetrate the material more compared to the REF sample. The increased leaching front could further explain the increased silica leaching values of the SCM sample.

In Figure 7.10, the phenolphthalein test shows a clear difference between the uncarbonated CSA and C-CSA sample, with a lack of color indicating a carbonation depth of around 3.9 mm. Additionally, a dark layer is visible on the surface of the cross-section measured with optical microscopy, measuring 1.3 mm. The origin of this discoloration is unknown.

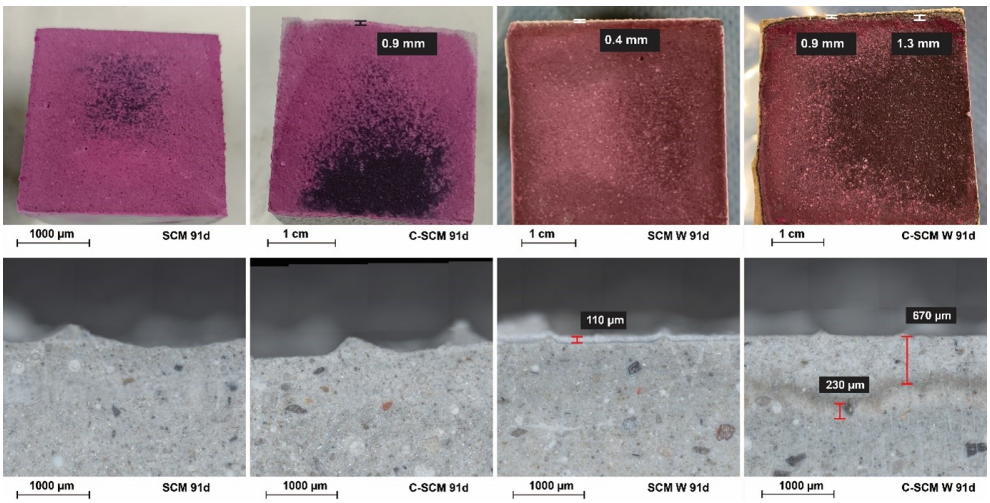

Figure 6.8: SCM microscopy cross sections at 91 days carbonated sample (left) in seawater uncarbonated (center) and carbonated in seawater (right).

After placement in seawater, the formation of a small dark layer (225 μm) is observed in the CSA sample, which likely indicates a leaching front that is not accompanied with a significant change in pH since no changes were observed in the phenolphthalein test. In the C-CSA W sample, the carbonation effect is evident, as the phenolphthalein test reveals a lack of color to a depth of 1.6 mm. A dark layer, most likely a leaching front similar to the one observed for C-SCM W, is visible in the cross-sectional microscopy, measuring 1.94 mm deep. Notably, the CSA samples exposed to seawater did not show any salt deposition, which aligns with the Q-XRD results.

6.3.5 Ecological Results

A total number of 203 oyster recruits settled on the tiles after 90 days, with the lowest number of oysters on REF (0.0295 oysters/cm^2 $\pm$ 0.009) and the highest number on the C-CSA (0.0408 oysters/cm^2 $\pm$ 0.007). Carbonation treatment significantly affected oyster recruitment ($\chi^2 = 5.88$, $p = 0.0153$), with carbonated samples showing on average 45% more oysters than uncarbonated samples, mainly driven by the difference between REF and C-REF. Oyster density was strongly correlated with row position on the frame ($\chi^2 = 18.58$, $p < 0.0001$), with a higher number of oysters on tiles closer to the seafloor. Material type did not have a significant effect on oyster settlement ($\chi^2 = 0.33$, $p = 0.8498$) and pairwise comparisons did not reveal any individual significant results.

An explanation of the higher number of oysters on carbonated samples could be associated with the decrease in pH where the pattern of oyster density matches the trend observed for the pH. However, the magnitude with which the pH values of the SCM and CSA samples differ does not cause a significant improvement in oyster settlement suggesting that the presence of the calcium carbonate further promotes

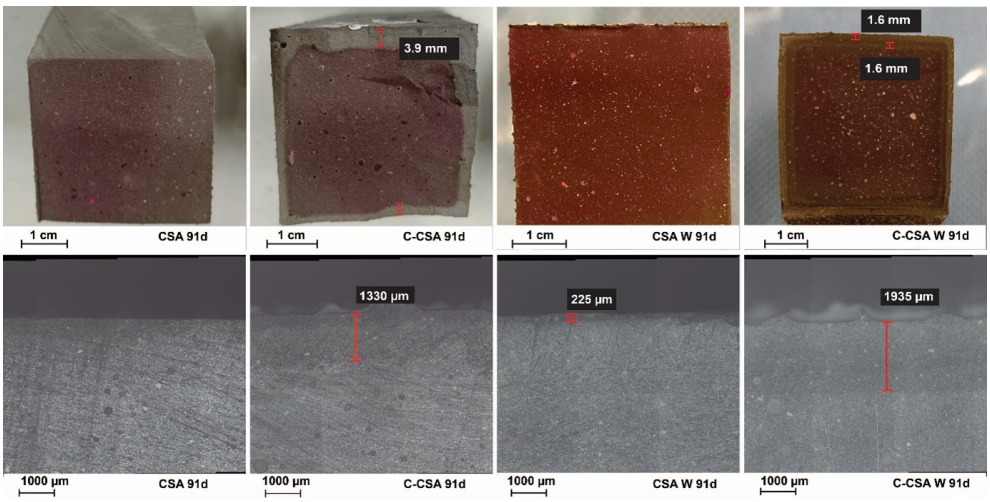

Figure 6.9: CSA microscopy cross sections at 91 days uncarbonated (left) carbonated sample (center left) in seawater uncarbonated (center right) and carbonated in seawater (right).

the settlement of oysters. This has previously been reported, where the presence of calcium carbonate provides a rich supplementary calcium for mollusks shells [268].

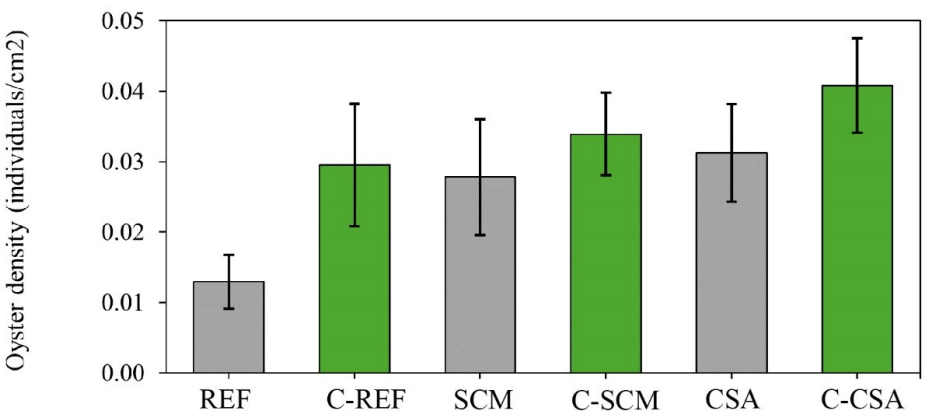

Figure 6.10: The density of oyster recruits (individuals per cm^2) for each of the tested materials after 90 days in the marine environment. Bars represent the average number of oyster recruits ± 1 S.E. (n=18) with the uncarbonated tiles in grey and carbonated tiles in green (C-REF, C-SCM, C-CSA).

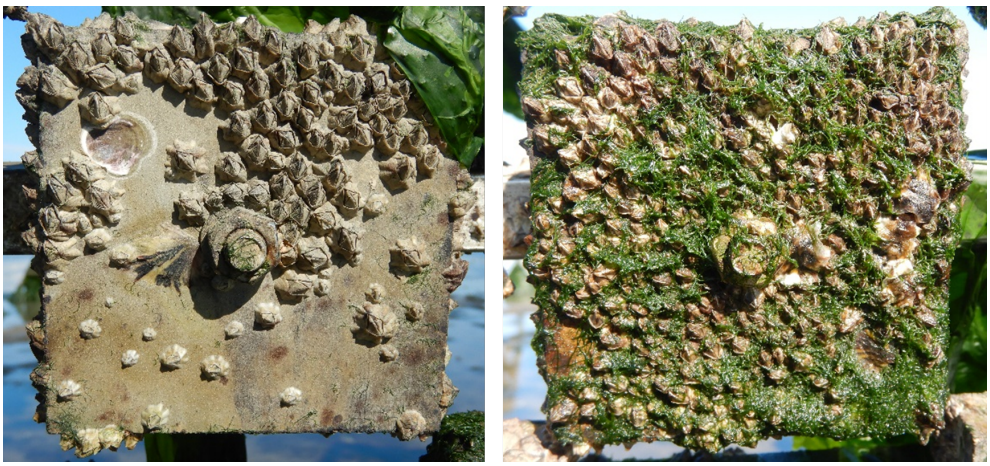

Figure 6.11: Marine life on settlement tiles, 90 days after deployment of the frames in the Eastern Scheldt (Netherlands). Left: Uncarbonated REF with low number of settled oysters (Magallana gigas). Right: Carbonated CSA with higher number of settled oysters and overall cover of marine organisms.

6.4 Closing Remarks

This chapter demonstrates the potential of sustainable cementitious materials in artificial reef applications, emphasizing the role of surface carbonation in enhancing both ecological and mechanical performance. The results highlight the importance of binder selection and carbonation treatments in optimizing marine material durability and oyster settlement rates. While each material exhibited distinct advantages, SCM-based binders (CEM III) emerged as the most promising option, balancing structural integrity and ecological benefits.

The goal of this research was to investigate how different cementitious artificial reefs can be designed in a sustainable way, with the aim to achieve successful oyster settlement using sustainable cement alternatives. Traditional OPC was compared to an SCM based mix and alternative CSA binder, both before and after carbonation. Both the mechanical, chemical, and ecological performance was studied to provide a complete overview of the respective performance of these materials.

Based on the ecological results, it was concluded that surface carbonation significantly improved the settlement of oysters. The carbonated CSA sample demonstrated the highest oyster density of 0.0408 oysters/cm^2 $\pm$ 0.007, compared to the carbonated CEM III (SCM) sample at 0.0342 oysters/cm^2 $\pm$ 0.005 and carbonated CEM I (REF) at 0.0295 oysters/cm^2 $\pm$ 0.009. The settlement followed a similar trend compared to the pH of the samples which was primarily associated with the content of $Ca(OH)_2$. Carbonation reduced the $Ca(OH)_2$ content, thus lowered the pH, and additionally provided a rich calcium supplementary for the oysters. This suggests that surface carbonation-induced pH reduction, along with the presence of calcium carbonate,

supports optimal settlement. The carbonated CSA sample was the best material in terms of oyster settlement, but the performance did not differ significantly from the carbonated SCM sample.

Mechanical durability was also evaluated through compression testing. Carbonated SCM samples achieved the highest compressive strength, reaching 69.9 MPa after 91 days, outperforming the REF samples (59.3 MPa) and CSA samples (45.8 MPa). The superior strength of the SCM samples can be attributed to the pozzolanic reaction, which reduces the $Ca(OH)_2$ content and enhances the material's microstructure. In contrast, carbonation of CSA cement resulted in the destruction of ettringite and the formation of gypsum, which dissolved upon seawater exposure, leading to a noticeable strength reduction.

Analysis with microscopy showed only minor change in the microstructure of the REF and SCM samples after placement in seawater for 91d, which suggests that they will provide a more durable support for the oysters for a longer period of time. However, combined with the strength results, visual inspection is not enough to assess the degradation of the material, as the REF sample showed a significant decrease in strength upon prolonged seawater exposure. The CSA samples showed the formation of a deep carbonation layer ($\sim$1.6 mm) which confirmed the high carbonate content of the sample and higher porosity which explains the lower strength development.

Based on the findings, carbonated SCM-based reefs are deemed the most suitable for artificial reef applications, offering a balance of superior mechanical performance and high oyster settlement rates. These results demonstrate the potential of sustainable binders, such as CEM III with recycled materials, to enhance marine biodiversity while maintaining structural integrity.

Beyond ecological performance, the long-term durability of cementitious materials in marine environments remains a critical factor in their viability for artificial reef applications. Exposure to seawater and saline solutions can lead to chemical degradation, phase transformations, and strength loss, which must be carefully evaluated to ensure material longevity. To further explore these effects, the following chapter investigates the interaction between salt hydrates and cementitious materials, examining potential cross-reactivity and durability concerns. This will provide deeper insights into material stability, degradation mechanisms, and strategies for improving cement resilience in saline environments.

6.5 Integration within the Thesis Framework

This chapter occupies a pivotal position within the thesis by explicitly linking the fundamental thermochemical behavior of salt hydrates to their long-term interaction with cementitious materials. While earlier chapters established the phase-change behavior, melting mechanisms, and stability challenges of salt hydrate PCMs, Chapter 6 addresses a critical and often overlooked aspect of their application: the chemical reactivity between salt solutions and cement matrices under realistic environmental conditions.

This chapter demonstrates that high-pH cementitious environment actively alters salt hydrate stability through ion precipitation and secondary mineral formation, compromising both mechanical integrity and thermal functionality. These findings complements earlier thermodynamic analyses, showing that PCM behavior is shaped not only by intrinsic properties but also by the chemical environment imposed by construction materials. Consequently, the durability challenges identified in salt hydrate–cement composites highlight the limitations of Portland cement for PCM integration and justify the exploration of low-pH binders as a mitigation strategy—an approach further developed in subsequent chapters to improve compatibility, reducing ionic driving forces, limiting undesired forced precipitation, and long-term thermal cyclability in the built environment.

As a conceptual bridge between material chemistry and application-driven design, Chapter 6 reframes salt hydrate PCM integration as a coupled chemical–thermodynamic problem rather than a purely thermal one, thereby informing the selection of compatible binders and encapsulation strategies discussed later in the thesis. Ultimately, this chapter strengthens the thesis narrative by demonstrating that durable and functional PCM systems require not only optimized salt hydrates, but also a cementitious environment specifically engineered to control ion mobility, precipitation, and long-term chemical stability.

6.6 Appendix

6.6.1 PSD of Recycled Concrete Fines

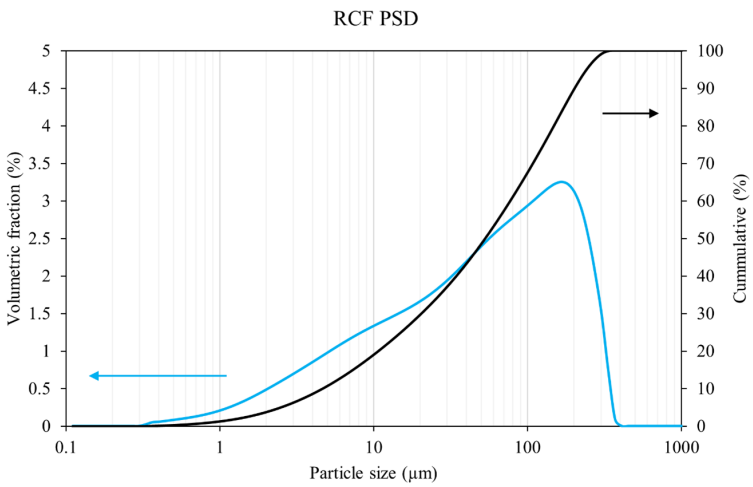

Figure 6.12: PSD curve of RCF.

Table 6.6: Complete ICP-OES of samples in water.

ICP(mg/L)	Al	B	Ba	Cr	Fe	Li	Mn	Sr	Zn	Si
Artificial Seawater	0.06	5.94	0.02	0.01	0.01	1.11	0.22	8.17	0.25	0.71
REF W 28	0.07	3.58	0.06	0.03	-	1.31	0.08	9.36	0.01	1.96
C-REF W 28	0.06	4.21	0.02	-	0.01	1.05	0.12	6.36	0.01	1.95
REF W 56	0.01	4.19	0.05	0.02	0.01	2.80	0.05	7.94	0.01	0.84
C-REF W 56	0.06	5.00	0.03	0.01	0.02	2.71	0.03	6.61	0.01	0.89
REF W 91	-	3.38	0.07	0.03	0.01	2.76	0.02	10.09	0.04	0.61
C-REF W 91	0.47	4.25	0.06	0.41	0.28	2.27	0.08	8.59	0.04	1.28
SCM W 28	0.06	3.49	0.01	-	0.01	1.03	0.12	5.94	0.01	2.02
C-SCM W 28	0.06	4.34	0.07	-	0.01	1.07	0.14	6.66	0.01	1.75
SCM W 56	-	4.79	0.04	0.01	0.01	2.73	0.03	6.73	-	0.98
C-SCM W 56	0.18	4.84	0.11	-	0.05	2.74	0.13	8.01	0.01	6.75
SCM W 91	-	4.86	0.03	0.08	0.05	2.32	0.05	6.82	0.02	0.72
C-SCM W 91	0.01	4.41	0.10	-	0.06	2.35	0.09	7.49	0.02	5.88
CSA W 28	0.05	3.94	0.02	0.08	0.03	1.05	0.13	6.41	0.01	1.92
C-CSA W 28	0.13	3.80	0.03	0.19	-	1.01	0.14	5.90	0.01	1.96
CSA W 56	-	4.99	0.04	0.19	0.01	2.76	0.09	8.15	0.98	1.16
C-CSA W 56	0.82	4.45	0.06	0.21	0.14	2.68	0.07	7.88	0.01	1.37
CSA W 91	0.03	4.58	0.03	-	0.15	2.41	0.04	6.90	0.03	0.71
C-CSA W 91	-	4.42	0.03	-	0.02	2.41	0.03	6.62	0.02	0.64

6.6.2 ICP of Cement Samples in Water

6.6.3 IC of Cement Samples in Water

Table 6.7: IC of samples in seawater.

ICP (g/L)	Na^+	K^+	Mg^{2+}	Ca^{2+}
Artificial Seawater	10.25	0.41	1.35	0.41
REF W 28	9.61	0.41	0.84	0.63
C-REF W 28	9.21	0.37	1.04	0.37
REF W 56	9.78	0.45	1.06	0.46
C-REF W 56	6.74	0.31	0.84	0.23
REF W 91	9.62	0.39	0.84	0.72
C-REF W 91	9.67	0.38	1.18	0.36
SCM W 28	8.73	0.34	0.93	0.33
C-SCM W 28	9.55	0.37	1.06	0.42
SCM W 56	8.78	0.40	1.12	0.31
C-SCM W 56	9.61	0.43	1.21	0.40
SCM W 91	9.59	0.36	1.19	0.38
C-SCM W 91	9.51	0.35	1.28	0.43
CSA W 28	8.66	0.36	0.94	0.35
C-CSA W 28	8.86	0.36	0.86	0.37
CSA W 56	9.90	0.45	1.20	0.42
C-CSA W 56	9.68	0.44	1.22	0.58
CSA W 91	9.82	0.37	1.25	0.38
C-CSA W 91	9.86	0.37	1.18	0.71

6.6.4 XRF of Cement Samples

Table 6.8: XRF results found within CEM I, CEM III, and CSA samples at 28 days (all results in wt%).

	MgO	**Al_2O_3**	**SiO_2**	**SO_3**	**CaO**	**TiO_2**	**Fe_2O_3**	**Others**	**LOI**
REF	1.80	4.40	15.87	2.45	52.30	0.37	2.94	0.93	18.94
REF W	5.95	3.99	14.43	3.52	45.34	0.34	2.73	1.65	22.05
C-REF	1.70	4.02	14.82	2.23	47.99	0.36	2.76	0.78	25.33
C-REF W	2.03	3.85	14.27	2.22	46.35	0.34	2.65	1.16	27.13
SCM	3.91	6.68	29.93	3.54	37.33	0.45	1.32	0.97	15.86
SCM W	4.28	6.44	28.98	2.99	36.22	0.48	1.27	1.43	17.92
C-SCM	3.68	6.25	28.23	3.48	35.52	0.48	1.28	0.94	20.13
C-SCM W	4.37	6.28	28.11	3.03	35.01	0.49	1.27	1.05	20.39
CSA	0.80	13.02	6.63	12.06	32.14	0.73	6.43	0.40	27.78
CSA W	1.12	12.47	6.43	11.50	31.01	0.70	6.26	0.43	30.08
C-CSA	0.75	12.87	7.13	11.76	32.03	0.73	6.33	0.47	27.93
C-CSA W	0.98	13.10	6.90	10.32	31.09	0.75	6.57	0.60	29.70

6.6.5 Q-XRD of Cements Samples at Different Ages and Conditions

Table 6.9: Quantified XRD results of REF samples (% by mass).

	Composition	REF	REF W 28	REF W 91	C-REF	C-REF 28	C-REF 91	REF Clinker
Albite	$NaAlSi_3O_8$	-	-	-	-	-	-	1.28±0.30
Anhydrite	$CaSO_4$	-	-	-	-	-	-	2.05±0.19
Brownmillerite	$Ca_2(AlFe)_2O_5$	6.89±0.29	6.79±0.29	3.05±0.41	5.03±0.31	5.18±0.34	4.75±0.39	10.66±0.31
Brucite	$Mg(OH)_2$	-	5.27±0.21	24.54±0.31	-	-	2.38±0.23	-
C_3A	$Ca_3Al_2O_6$	1.37±0.14	1.05±0.13	0.55±0.14	1.16±0.17	1.31±0.18	1.02±0.20	3.93±0.21
Calcite	$CaCO_3$	6.37±0.20	3.99±0.17	2.95±0.20	18.43±0.32	18.19±0.32	14.52±0.30	-
Dolomite	$CaMg(CO_3)_2$	0.93±0.23	1.50±0.20	1.38±0.24	0.29±0.19	0.37±0.22	0.55±0.24	-
Hatrurite	Ca_3SiO_5	12.04±0.28	11.08±0.24	5.79±0.32	11.52±0.31	9.78±0.34	9.84±0.32	49.24±0.42
Larnite	Ca_2SiO_4	2.96±0.30	3.22±0.29	3.46±0.40	3.38±0.43	3.67±0.43	2.43±0.53	17.96±0.41
Martensite	Fe_3C	-	-	-	-	-	-	0.43±0.07
Periclase	MgO	1.37±0.18	0.83±0.16	0.81±0.18	-	-	-	1.42±0.17
Portlandite	$Ca(OH)_2$	5.57±0.13	1.81±0.09	0.80±0.22	0.57±0.13	0.49±0.17	0.51±0.19	-
Quartz	SiO_4	1.22±0.07	2.56±0.06	0.62±0.07	2.54±0.07	0.70±0.06	2.82±0.08	1.73±0.09
Vaterite	$CaCO_3$	3.40±0.33	3.56±0.29	0.98±0.26	-	-	-	-
Amorphous		57.87±0.77	58.35±0.73	55.08±0.93	57.09±0.82	60.31±0.84	61.19±0.94	11.30±1.02

Table 6.10: Quantified XRD results of SCM samples (% by mass).

	Composition	SCM	SCM W 28	SCM W 91	C-SCM	C-SCM W 28	C-SCM W 91	SCM Clinker
Albite	$NaAlSi_3O_8$	0.66±0.16	1.76±0.15	0.87±0.16	0.39±0.11	-	-	-
Anhydrite	$CaSO_4$	-	-	1.22±0.64	-	-	-	3.42±0.18
Brownmillerite	$Ca_2(AlFe)_2O_5$	0.62±0.30	-	0.28±0.22	0.40±0.15	0.62±0.16	0.30±0.12	3.02±0.17
Brucite	$Mg(OH)_2$	-	1.16±0.24	3.84±0.25	-	-	-	-
α'- Belite	Ca_2SiO_4	0.93±0.23	0.86±0.20	0.51±0.15	0.47±0.15	0.58±0.15	0.45±0.19	-
Calcite	$CaCO_3$	7.52±0.25	7.25±0.35	5.42±0.25	12.53±0.28	12.59±0.28	11.43±0.28	-
Dolomite	$CaMg(CO_3)_2$	1.06±0.27	1.97±0.42	1.04±0.38	0.59±0.10	0.89±0.29	0.79±0.30	-
Ettringite	$Ca_6Al_2(SO_4)_3(OH)_{12}$ 26H2O	2.29±0.30	1.44±0.25	-	7.54±0.31	0.73±0.17	-	-
Friedel Salt	$Ca_2Al(OH)_6(Cl,OH)$ $2H_2O$	-	-	1.77±0.23	-	-	-	-
Hatrurite	Ca_3SiO_5	2.76±0.35	2.35±0.35	2.04±0.35	2.02±0.34	1.85±0.32	1.81±0.32	21.48±0.23
Larnite	Ca_2SiO_4	-	-	0.12±0.12	0.41±0.16	-	-	5.57±0.32
Merwinite	$Ca_3Mg(SiO_4)_2$	-	-	-	-	-	-	2.17±0.23
Portlandite	$Ca(OH)_2$	0.89±0.13	0.26±0.10	0.11±0.10	0.08±0.10	-	-	-
Quartz	SiO_4	10.27±0.13	9.47±0.13	8.29±0.12	7.96±0.12	9.54±0.13	9.09±0.13	1.41±0.05
Vaterite	$CaCO_3$	1.02±0.20	0.89±0.32	0.12±0.06	3.24±0.35	3.74±0.40	2.15±0.38	-
Amorphous		71.97±0.79	72.58±0.88	74.36±1.02	64.38±0.78	69.46±0.75	73.99±0.72	62.93±0.32

Table 6.11: Quantified XRD results of CSA samples (% by mass).

	Composition	CSA	CSA W 28	CSA W 91	C-CSA	C-CSA W 28	C-CSA W 91	CSA Clinker
Anhydrite	$CaSO_4$	5.02±0.16	5.20±0.17	1.74±0.12	5.59±0.13	5.36±0.14	3.58±0.16	13.16±0.25
Aragonite	$CaCO_3$	-	-	-	13.71±0.29	18.39±0.34	18.27±0.44	-
Bassanite	$2CaSO_4$ H_2O	-	-	-	0.04±0.11	0.76±0.14	3.65±0.18	-
Bayerite	$Al(OH)_3$	1.93±0.45	0.90±0.38	1.34±0.16	0.73±0.21	0.79±0.24	0.83±0.35	-
Calcite	$CaCO_3$	4.10±0.19	4.55±0.20	4.33±0.12	4.75±0.15	5.93±0.17	5.10±0.21	3.77±0.24
Dolomite	$CaMg(CO_3)_2$	0.70±0.21	0.32±0.17	0.74±0.13	0.83±0.17	0.46±0.19	0.22±0.14	1.27±0.31
Ettringite	$Ca_6Al_2(SO_4)_3(OH)_{12}$ 26H2O	12.35±0.39	12.00±0.42	-	0.25±0.17	0.89±0.25	-	-
Gibbsite	$Al(OH)_3$	0.48±0.10	1.11±0.29	1.06±0.12	1.23±0.29	1.80±0.35	0.97±0.25	-
Gypsum	$CaSO_4$ $2H_2O$	-	-	-	7.93±0.24	9.79±0.28	0.64±0.21	-
Larnite	Ca_2SiO_4	13.24±0.26	14.33±0.29	11.28±0.24	4.53±0.23	5.92±0.27	3.40±0.23	15.99±0.34
Lazurite	$Na_7Ca(Al_6Si_6O_{24})(SO_4)$ (S_3) H_2O	0.14±0.12	-	0.28±0.20	0.00±0.10	0.00±0.08	-	-
Magnetite	Fe_3O_4	1.64±0.14	1.76±0.15	2.12±0.40	2.11±0.13	2.64±0.19	2.01±0.14	1.86±0.18
Nordstrandite	$Al(OH)_3$	-	0.55±0.21	0.88±0.17	0.81±0.28	0.92±0.36	0.25±0.19	-
Perovskite	$CaTiO_3$	7.64±0.12	8.19±0.13	8.94±0.25	8.25±0.13	10.02±0.15	8.31±0.12	9.52±0.18
Quartz	SiO_4	1.51±0.13	1.27±0.15	1.13±0.16	0.81±0.09	0.89±0.10	1.42±0.15	0.41±0.16
Vaterite	$CaCO_3$	-	-	-	4.60±0.22	5.26±0.26	4.78±0.37	-
Ye'elimite	$Ca_4(AlO_2)_6SO_4$	1.24±0.18	1.47±0.18	0.34±0.15	1.00±0.11	0.53±0.10	0.39±0.17	25.35±0.34
Amorphous		50.03±0.93	48.38±0.90	65.84±0.97	42.85±0.85	29.65±1.04	46.19±1.15	28.68±1.00

Table 6.12: Quantified XRD results of RCF samples (% by mass).

	Composition	**RCF**
Albite	$NaAlSi_3O_8$	4.28±0.42
Anorthite	$CaAl_2SiO_3$	2.92±0.43
Brownmillerite	$Ca_2(AlFe)_2O_5$	-
Brucite	$Mg(OH)_2$	-
α'- Belite	Ca_2SiO_4	-
Calcite	$CaCO_3$	12.34 ± 0.25
Dolomite	$CaMg(CO_3)_2$	1.04 ± 0.15
Ettringite	$Ca_6Al_2(SO_4)_3(OH)_{12} \cdot 26H_2O$	3.04 ± 0.42
Friedel Salt	$Ca_2Al(OH)_6(Cl,OH) \cdot 2H_2O$	-
Hatrurite	Ca_3SiO_5	-
Larnite	Ca_2SiO_4	-
Merwinite	$Ca_3Mg(SiO_4)_2$	-
Portlandite	$Ca(OH)_2$	0.81 ± 0.10
Quartz	SiO_4	49.43 ± 0.50
Vaterite	$CaCO_3$	-
Amorphous		26.16 ± 1.10

Chapter 7

Full Cementitious Coating of PCM Salt Hydrates: Utilizing Non-Traditional Cements

> "Heat, like gravity, penetrates every substance of the universe, its rays occupy all parts of space."
>
> —Jean Baptiste Joseph Fourier

Phase change materials (PCMs) are promising for thermal energy storage in buildings; enhancing energy efficiency and indoor temperature regulation. This study presents a novel encapsulation method for PCM salt hydrates using expanded vermiculite, coated with calcium sulfoaluminate (CSA) and magnesium oxy-sulfate (MOS) cements. PCM composites were prepared by impregnating expanded vermiculite with sodium sulfate decahydrate. Thermal and mechanical properties were evaluated through calorimetry, compressive strength tests, X-ray diffraction (XRD), and heat transfer analysis. The encapsulated PCM composites demonstrated high thermal stability, with thermal diffusivity decreasing up to 70 %, compared to regular cement paste. The CSA and MOS coatings effectively prevented leakage and enhanced durability, with the coated vermiculite maintaining structural integrity under thermal cycling. This encapsulation method offers a promising approach for integrating PCMs into building materials, providing a solution for salt hydrate encapsulation and integration.

The results of this chapter are published in the following article:
Wesemann, C.A., Schollbach, K., & Brouwers, H.J.H. (2026). Novel encapsulation method for salt hydrates for building applications. (To be submitted)

7.1 Introduction

As previously discussed in Chapter 1, maintaining indoor temperatures is essential for comfort and productivity in buildings but often comes at a high energy cost. PCMs can absorb and release large amounts of heat at specific temperatures, thus stabilizing indoor temperatures and reducing the need for external energy sources [167], [269]. Integrating PCM into building structures presents an eco-friendly alternative, contributing to reduced carbon emissions when compared to traditional construction methods [92]. However, the integration of such systems using salt hydrates has its limitations [270].

One commonly applied method is the use of sleeves or envelopes, which are plastic containers filled with PCMs and placed in empty spaces where insulation would typically be installed, primarily within wall cavities. Another approach involves external vats, where HVAC systems extract heat from the building and transfer it to an external structure that absorbs the heat and can recycle it into cooled air; this process is usually reversible [61], [271]. Another approach suitable for new construction involves encapsulation, where the PCM is enclosed within a porous host material, such as foam or clay. This technique allows for the seamless integration of PCM into the building structure, effectively treating them as functional aggregates [272].

A common method of implementation is replacing aggregates in concrete, or render. The options of aggregates are coarse ones (>4 mm) or fine aggregates (<4 mm). Therefore, the objective for this research is to develop functional fine aggregates with a diameter of less than 4 mm. These aggregates will feature a coated layer of cementitious material, offering the possibility of seamless integration into mortar mixtures, providing a smart alternative to fine aggregates [273]–[276]. As explored in Chapter 6, the effects of salts on cementitious materials alter their chemistry as well as their strength. Therefore, it is critical to find suitable binders alternatives to integrate PCMs into buildings without negative effects. Figure 7.1 represents the schematic representation of the aggregate pellets.

Encapsulation techniques such as plastic coatings and glass bead methods introduce environmental and logistical challenges, including plastic pollution and energy-intensive processing [64], [66], [277]–[284]. Additionally, coating integrity often suffers from microleakage or fatigue after repeated thermal cycling, further complicating large-scale integration in buildings.

A potential alternative to polymeric coatings is the use of cement as encapsulation media. However, this approach introduces two primary causes of cracking. The first is volumetric expansion of the PCM during melting and solidification. When confined in a rigid matrix, this expansion generates internal stresses that can exceed the tensile strength of the cement, leading to cracking or delamination. The second mechanism is chemical reactivity between the salt hydrate and the cement matrix. Certain salts—such as Glauber's salt ($Na_2SO_4 \cdot 10H_2O$)—can react with calcium-bearing phases in cement, forming expansive minerals such as ettringite or gypsum [67]. This reaction-induced expansion can occur even without significant PCM volume change, ultimately compromising both the mechanical integrity of the composite and

the thermal reversibility of the PCM.

Therefore, there is a pressing need to explore alternative encapsulation approaches that minimize chemical incompatibility, accommodate PCM expansion, and ensure both cost-effectiveness and environmental sustainability [285], [286].

To address the prevention of leaking and volumetric expansion of the PCM from the cementitious coating, the use of an effective retention porous matrix is essential. A matrix should be able to expand , compatible with salt hydrates and cement, chemically inert, easily available and affordable. Expanded Vermiculite (EV) is a prominent contender for providing many of these requirements and has great retention for polar materials.

EV can be both a physical binding agent and a physical protective layer for the storage of PCM at room temperature [287]. Vermicullite, a naturally occurring mineral characterized by a layered structure with the general mineral formula $((Mg,Fe^{2+},Fe^{3+})_3(Al,Si)_4O_{10}(OH)_2{\cdot}XH_2O)$ and is expanded when heat is applied. EV has found applications in building construction as an insulator, as well as in various fields such as fireproofing, and soundproofing [135], [273], [274], [288]–[292]. EV possesses favorable thermal properties, including a low thermal conductivity of 0.06 $W/m \cdot K$ and a high specific heat capacity of 1.08 $kJ/(kg \cdot K)$,which allows it to effectively absorb and retain heat. Furthermore, its distinctive high liquid adsorption capacity enables the retention of melted PCM within the expanded vermiculite structure. This quality is important as it both reattains the salt within the pellet, reducing volumetric expansion, while also acting as a sponge that prevents leaking from any minor cracks. However with no encapsulation the pellet could still pose a risk to cement therefore the need of a special coating is needed. This leads to the next step: the coating of such pellets.

The PCM used for thermal energy storage in this study is Glauber Salt (GS), chemically known as $Na_2SO_4{\cdot}10H_2O$. As previously presented in Chapters 1, 3, and 4, GS has a phase change enthalpy of 250 kJ/kg and a melting temperature of 32°C, which enables substantial thermal energy storage and release during its phase transition. It demonstrates high reproducibility in thermal performance and exhibits stable melting behavior, making it an ideal model candidate for this research. However, a protective coating must be applied to the GS + EV pellets, as GS is known to react detrimentally with cementitious materials such as OPC and CEM III. This known detrimental interaction was further highlighted in Chapter 6, which examined the effects of salt solutions on the surfaces of OPC and CEM III pastes.

For the coating of the GS + EV core, calcium sulfoaluminate (CSA) [265], [293] and magnesium oxy-sulfate (MOS) were selected due to their resistance to sulfates [294]–[302]. In materials such as OPC and CEM III, exposure to sulfates can lead to the formation of gypsum, and retardation of cement setting [67]. In contrast to OPC, calcium CSA and MOS cements exhibit inherent sulfate tolerance [294], [297], [298]. Their lower alkalinity reduces the likelihood of deleterious reactions with GS, while their rapid setting and mechanical performance make them suitable as protective coatings. CSA offers fast curing and high early strength, and a relatively low pH compared to OPC. In contrast, MOS provides strong resistance to wear, reduced

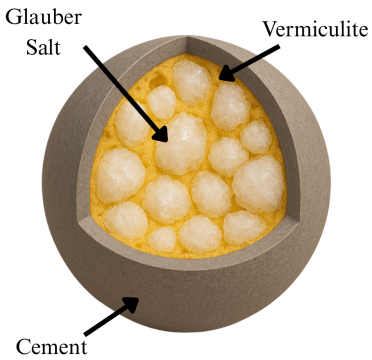

Figure 7.1: Schematic overview of pellets. The yelow matrix represents vermicullite, pores filled by the Glauber salt crystals, coated by a layer of cement in gray.

pH, and good resistance to sulfate-rich environments [303], [304]. The lower pH of these cements are a particular advantage, as it generally reduces the likelihood of detrimental chemical reactions with acidic compounds such as salt hydrates [233].

This chapter therefore investigates a cementitious encapsulation strategy for salt hydrate PCMs by using EV as the core carrier and CSA or MOS as protective coatings. The objective is to develop fine aggregate pellets (<4 mm) that are compatible with cementitious renders while preventing PCM leakage and minimizing chemical degradation. The study evaluates the physicochemical interaction between GS and CSA/MOS through isothermal calorimetry, compressive strength testing, and X-ray diffraction (XRD). Following coating and curing, EV-GS pellets are incorporated into MOS-based mortar, and their thermal behaviour is assessed to determine suitability for passive thermal regulation in building materials.

In line with these objectives, the following section outlines the materials, preparation procedures, and characterization methods used to develop and evaluate the EV–GS pellets coated with CSA and MOS cements. This includes material selection, mix design, pellet fabrication, and the experimental techniques employed to assess chemical compatibility, mechanical performance, and thermal behaviour. Together, these methods establish the framework for determining the feasibility of this encapsulation strategy for integration into cementitious building applications.

7.2 Materials and Methods

7.2.1 Materials

To form the core of the pellet, expanded vermiculite (EV) [Primaterra Grade 3 (0–5 mm) and Grade 2 (0–3 mm)] was impregnated with sodium sulfate decahydrate (Glauber's Salt, GS) [AnalaR NORMAPUR 99.6% from VWR]. EV has a bulk density of 0.9 g/mL, a low thermal conductivity of 0.0635 W/m · K, and a volumetric heat

capacity of 0.972 × 10^6 J/(m^3 · K) [305]. GS, the PCM, has an enthalpy of fusion of 251.2 kJ/kg, a melting point of 32.4°C, and a volumetric heat capacity between 3.06–4.91 × 10^6 J/(m^3 · K) [306].

For the cementitious coating, two materials were evaluated:

- Calcium Sulfoaluminate (CSA) cement [Alpenat UP from VICAT], with a thermal conductivity of 0.7 W/m · K, a volumetric heat capacity of 1.55 × 10^6 J/(m^3 · K) and thermal diffusivity of 1.03 mm^2/s [307].
- Magnesium Oxy-Sulfate (MOS) cement, formed by the reaction between magnesium oxide (MgO) [312/31212 Caustic burnt, Magnesia Co.] and magnesium sulfate heptahydrate ($MgSO_4 \cdot 7H_2O$) [99.5% Acros Organics] with water [298], [299], [301].

MOS generally exhibits a thermal conductivity of 1.68 W/m · K, a volumetric heat capacity of 0.898 × 10^6 J/(m^3 · K) and a thermal diffusivity of 1.05 mm^2/s [308].

7.2.2 Material Characterization

Particle Size Distribution (PSD)

The PSD of MgO and CSA powders was determined using an Analysette 22 NeXT (Fritsch). Isopropanol (refractive index = 1.39) was used as the dispersion medium. Samples were added until a beam obscuration of 10–18% was achieved. Each sample was measured three times and averaged. The solid refractive index for both cements was set at 1.73.

The median particle size (D_{50}) was 23.54 μm for MgO and 9.99 μm for CSA (Figure 7.2, Table 7.1).

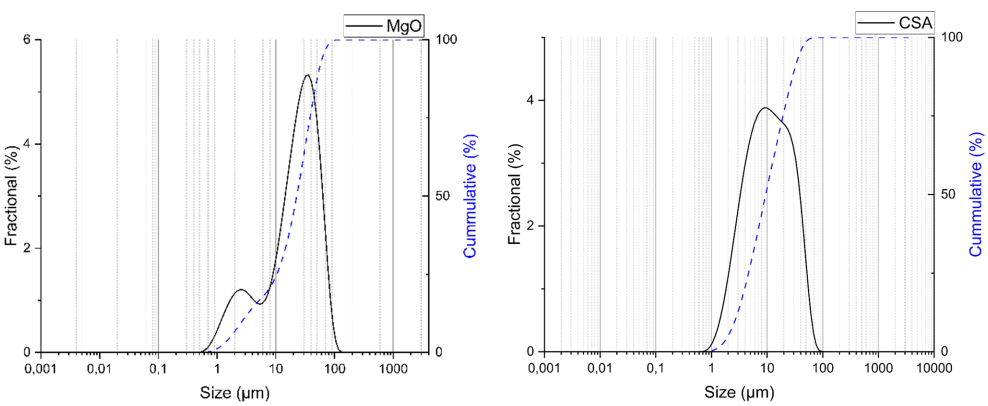

Figure 7.2: Particle size distribution (PSD) of MgO and CSA powders.

Table 7.1: Particle size distribution parameters (D_{10}, D_{50}, D_{90}) of MgO and CSA powders.

Material	**D_{10} (μm)**	**D_{50} (μm)**	**D_{90} (μm)**
MgO	2.76	23.54	55.43
CSA	2.77	9.99	32.45

X-ray Diffraction (XRD)

XRD analysis was performed using a D4 Phaser (Bruker) on powders sieved below 500 μm. For quantitative analysis, an internal standard of 10% silica was added to quantify the amorphous content.

The XRD results (Figure 7.3) revealed that vermiculite consisted of 59.9% vermiculite $[(Mg, Fe^{2+}, Fe^{3+})_3(Al, Si)_4O_{10}(OH)_2 \cdot xH_2O]$ and 40.1% phlogopite $[KMg_3(AlSi_3O_{10})(F,OH)_2]$, which are commonly coexisting minerals [309], [310]. The MgO sample exhibited high purity with trace carbonate impurities, while the CSA powder contained the expected mixture of calcium carbonates, sulfates, aluminates, and silicates [67].

X-ray diffraction (XRD) analysis was also performed on CSA and MOS samples at different stages of curing, following compression testing. To halt the hydration process, crushed samples were collected and immersed in either pure isopropanol or ethanol for 24 hours. The samples were subsequently dried in an oven at 40°C for two hours. Once dried, the samples were crushed further, and a silicone internal standard was added at 10wt%. This mixture was then ground in an XRD mill prior to measurement.

X-ray Fluorescence (XRF) and Loss on Ignition (LOI)

EV was placed in a porcelain crucible and heated to 1000°C for four hours. The weight loss was attributed to the LOI. Next, 1 g of EV residue was mixed with 10 g of lithium tetraborate and 750 μl of lithium iodide solution. The fused bead was produced using a PANalytical CLAISSE LeNEO at 1065°C. The results are summarized in Table 7.2.

Table 7.2: XRF quantified values of MgO, CSA, and EV.

Material	MgO	Al_2O_3	SiO_2	SO_3	CaO	K_2O	TiO_2	Fe_2O_3	Other	LOI
Vermiculite	21.40	8.87	39.05	–	–	7.75	1.97	13.98	0.29	7.17
CSA	0.86	15.18	7.79	13.29	48.86	0.28	1.05	9.67	0.32	2.78
MgO	91.52	–	1.16	–	2.90	–	–	0.92	0.04	3.51

7.2.3 Material Preparation

CSA Paste Preparation

The CSA paste was formulated using a water-to-binder (w/b) ratio of 0.4. This specific ratio was selected to balance optimal mechanical properties with minimal excess free water. W/b ratios greater than 0.4 can result in bleeding, where surplus water could dissolve the PCM salt hydrate, consequently diminishing its efficacy and compromising

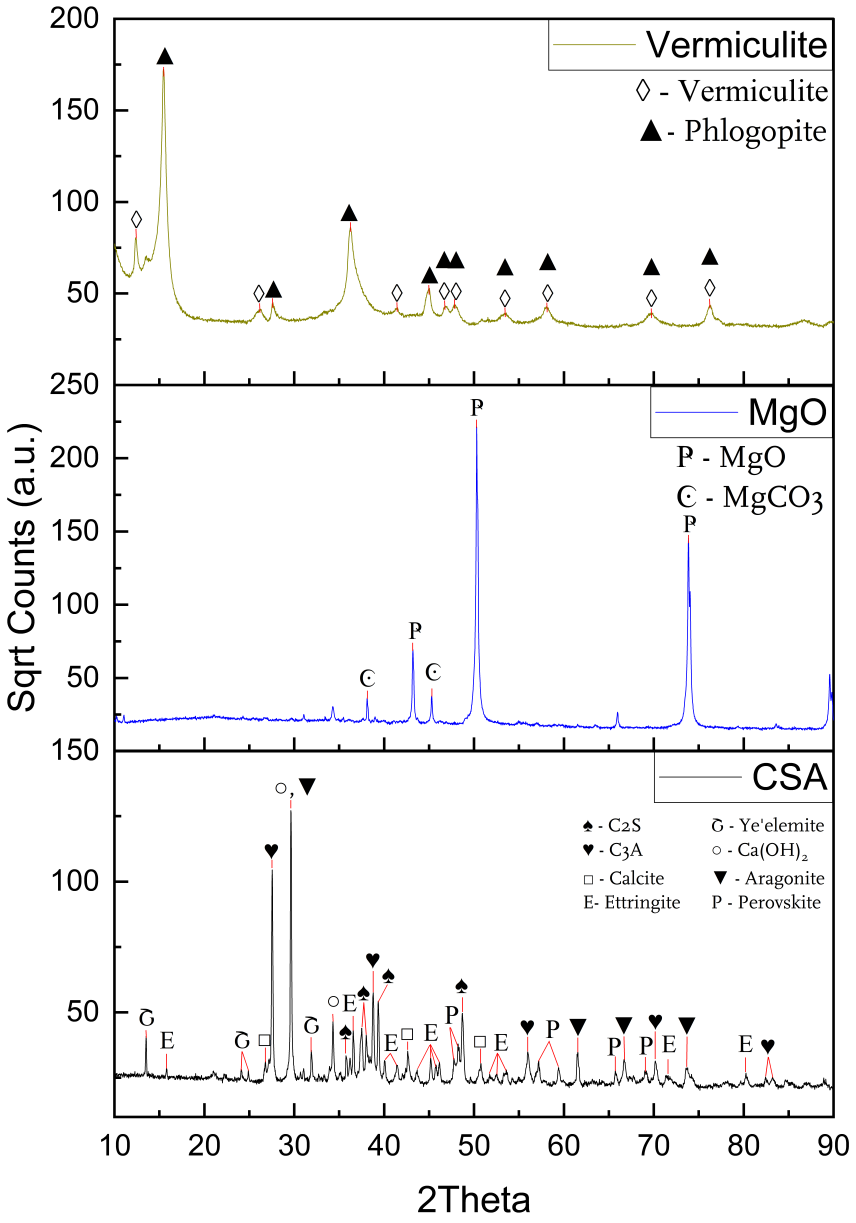

Figure 7.3: XRD patterns of expanded vermiculite (top), MgO (middle), and CSA clinker powder (bottom).

the paste's structural integrity. Furthermore, during curing, excess water promotes the surface formation of a deliquescent salt layer, which further degrades structural performance. The required addition of GS for reaction testing was calculated as a

wt% of the binder and subsequently pre-dissolved in the mixing water corresponding to the 0.4 w/b ratio. Samples made are shown in Table 7.3.

MOS Paste Preparation

MOS cement was prepared using MgO, $MgSO_4$, and H_2O in molar ratios of 10:1:20 and 15:1:20. These ratios are known to promote the formation of the 5:1:20 crystalline phase, known for its superior water resistance and strength [311], [312].

The following Table 7.3 provides a general overview of the the samples used and tested.

Table 7.3: Mix design samples and composition overview.

	CSA	MgO	$MgSO_4$	Water	GS	GS
	w/b ratio	g	g	g	wt%	g
CSA 0 GS	0.4	-	-	-	-	-
CSA 5 GS	0.4	-	-	-	5	-
CSA 10 GS	0.4	-	-	-	10	-
CSA 15 GS	0.4	-	-	-	15	-
CSA 20 GS	0.4	-	-	-	20	-
MOS 10	-	403	120	360.3	-	-
MOS 15	-	604.5	120	360.3	-	-
MOS 15 5 GS	-	604.5	120	360.3	5	36.2
MOS 15 10 GS	-	604.5	120	360.3	10	72.5
MOS 15 15 GS	-	604.5	120	360.3	15	108.7
MOS 15 20 GS	-	604.5	120	360.3	20	145

Mortar Mix Composition

Following BS EN 998-1/NHBC 2024 (6.1.14) guidelines, the mortar mix comprised 60% MOS cement and 40% fine aggregates by volume [313]. CSA cement was initially investigated but subsequently excluded. Preliminary experiments demonstrated that it was not possible to produce a stable coating with CSA that would maintain its integrity.

7.2.4 Pellet Preparation

Impregnation

The impregnated core was prepared using a 1:5 weight ratio of EV to GS. The procedure began by combining 50 g of EV, which had been previously dried overnight at 130°C, with 250 g of GS. This EV/GS mixture was then placed in a water bath and heated to 45°C. Once the GS had melted, 17 g of deionized water was added while the mixture was mechanically stirred until a homogeneous material was achieved. This added deionized water was included specifically to compensate for water loss due to evaporation during the heating and mixing process.After the material was fully integrated, it was cooled to room temperature. The cooled material was then sieved

to remove any clumps and subsequently allowed to stand for 24 hours to ensure full crystallization.

Pelletization

The coating process was conducted using an EIRICH TR04 cement pelletizer. Prior to pelletization, a 1:13 molar $MgSO_4$:H_2O solution was prepared one day in advance to serve as the wetting agent. The impregnated EV was added to the rotating drum, while MgO powder and water were alternately added to achieve a double coating while maintaining a consistent 15:1:20 ratio. The final MOS-to-material ratio was 1:6 (25 g MgO per 300 g of impregnated EV), with a w/b ratio of 0.4–0.6. The resulting pellets were cured in a humid environment (closed bucket with water source) for one month.

7.2.5 Thermal Testing

Thermal performance was evaluated using an ISOMET 2104 (Applied Precision) through transient heat flow analysis. Samples were cast into 3D-printed PLA cylinders (height = 2 cm, radius = 3 cm) containing 60 vol% pellets and 40 vol% MOS binder (15:1:20). The measurements yielded thermal conductivity (λ), volumetric heat capacity (c_ρ), and thermal diffusivity (α), following methods established for PCM–cement composites [314].

7.3 Results and Discussion

Understanding the long-term stability and potential detrimental effects of incorporating a PCM salt hydrate directly within a cementitious matrix is critical for successful implementation. Specifically, the experiments involving mixing GS with CSA and MOS pastes were designed to directly investigate the compatibility of the salt with these binders. The primary objective was to determine the potential risk of salt leakage and to assess any deleterious chemical reactions or physical changes that might compromise the cement paste's structural integrity over time. By simulating the direct contact environment, this research aims to predict if the presence of the salt would lead to long-term material detriment, such as surface degradation, reduced mechanical strength, or volume instability.

7.3.1 Isothermal-Calorimetry

Isothermal calorimetry was conducted to examine the impact of GS in the presence of CSA and MOS. As depicted in Figure 7.4, CSA reaction occur in the span of 24 hours with two noticeable peaks. Although the literature typically reports four peaks [294], these are not always individually visible, as two may overlap, resulting in only the dominant reactions being detected. The first peak (2-6 hours) is associated with the dissolution of ye'elemite, in the presence of gypsum, resulting in the formation of ettringite (Equation (7.1)):

$$Ca_4Al_6O_{12}SO_4 + 8\,CaSO_4 + 6\,Ca(OH)_2 + 80\,H_2O \longrightarrow 3\,Ca_6Al_2(SO_4)_3(OH)_{12}\cdot 26\,H_2O \quad (7.1)$$

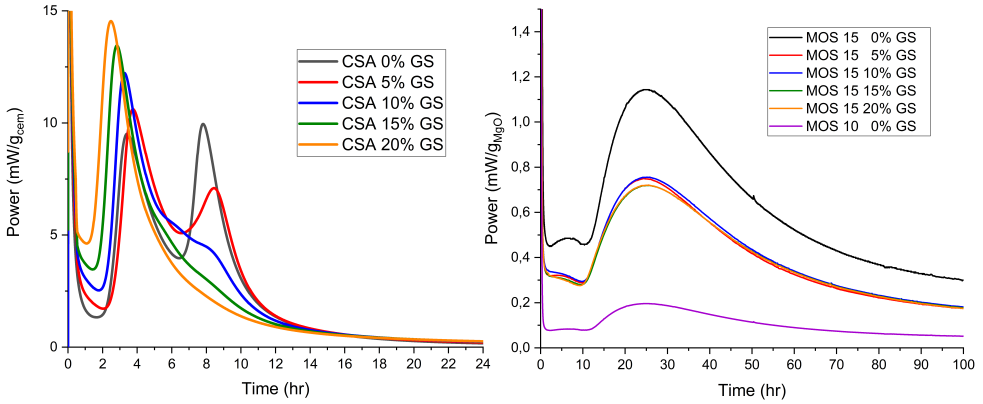

Figure 7.4: Iso-calorimetry of CSA (left) and MOS (right) with variations of additional GS percent.

The secondary peak (6-10 hours) in the calorimetry data marks the point of gypsum depletion and the subsequent conversion of ettringite to monosulfate, as illustrated by the reaction in Equation (7.2). When examining the CSA paste results, it is clear that increasing the addition of GS enhances the magnitude of the initial peak while concurrently diminishing the intensity of the secondary reaction.

$$Ca_6Al_2(SO_4)_3(OH)_{12} \cdot 26\,H_2O + 2\,Ca_3Al_2O_6 \longrightarrow 3\,(Ca_4Al_2O_6(SO_4) \cdot 12\,H_2O \tag{7.2}$$

Winter [315] suggests that as the sulfate content increases in the cementitious material it takes longer for sulfate depletion to occurand the effect diminishes. If the content is high enough aluminate becomes a limiting factor. The reaction involving GS, as described by Taylor [67], indicates that C_3S (Ca_3SiO_5) reacts with as little as 0.15 molar concentration of GS. Any additional GS also reacts with β-C_2S ($2CaO{\cdot}SiO_2$), presumably leading to the formation of gypsum. This reaction results in a decalcified C–S–H gel with a reduced Ca/Si ratio, ultimately decreasing the overall mechanical strength of the material.

Additionally demonstrated in Figure 7.4 is the reaction for MOS over a span of 100 hours with two broad peaks. No distinctions were observed in the isocalorimetry of the samples in both 10:1:20 and 15:1:20 ratios. Two distinct peaks were evident in the isocalorimetry reaction: the initial peak (0-10 hours) corresponding to the hydration of MOS cement components [298] (Equations (7.3) and (7.4)):

$$MgO + (x+1)\,H_2O \longrightarrow [Mg(H_2O)_x\,OH]^+ + OH^- \tag{7.3}$$

$$[Mg(H_2O)_x\,OH]^+ + OH^- \longrightarrow Mg(OH)_2 \cdot xH_2O \tag{7.4}$$

Followed by a large secondary peak (11-45 hours), [298] (Equation (7.5)):

$$Mg(OH)_2 \cdot xH_2O + {SO_4}^{-2} + y{Mg}^{2+} \longrightarrow yMg(OH)_2 \cdot MgSO_4 \cdot xH_2O \tag{7.5}$$

Analysis of the isothermal calorimetry data revealed that when the total heat release is normalized by the weight of MgO, the measurable energy decreases. This reduction in normalized heat release is consistent across all concentrations of GS added, indicating a primary control mechanism based on the MgO to sulfate ratio, rather than the absolute amount of GS. This observation is supported by the fact that the liquid volume remained constant while the sulfate content increased. Crucially, the addition of GS caused no observable delay in the initiation of the hydration reaction. Furthermore, the MOS 10 control mix exhibited a lower total heat release compared to the MOS 15 control mix, a difference that is maintained when comparing their respective GS-containing counterparts. These reaction result in various phases that will be discussed in following section.

7.3.2 Compressive Strength and Mineralogy

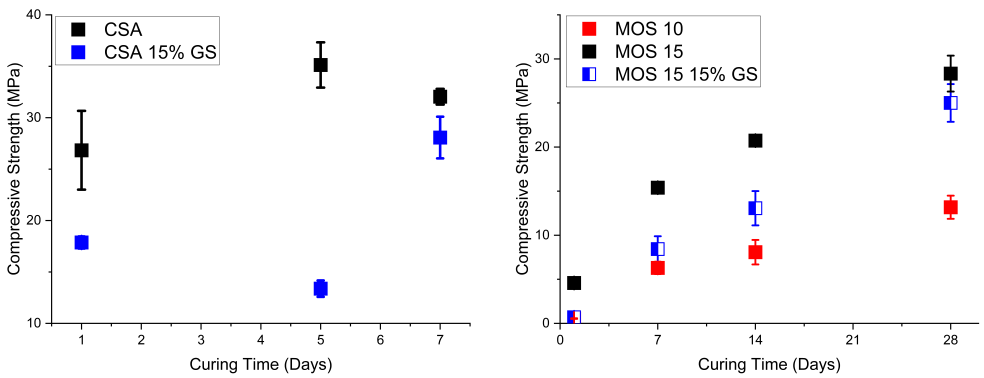

Figure 7.5: Compression Testing of CSA (left) and MOS (right).

Compressive strength test of the CSA and MOS cement were compared with and without the addition of 15% GS. As previously mentioned this is done to verify if the exposure to GS has any detrimental effects to the physical properties of the cementitious coating. The 15% concentration was chosen to represent the interphase between cementitious material and EV-GS matrix. TThe final curing ages tested were 7 days for CSA and 28 days for both MOS 10 and MOS 15. These periods reflect the maximum ages examined; however, samples were tested throughout the duration of curing at specified intervals. This difference in maximum curing age was necessary because CSA is known to cure rapidly within a span of 7 days, while the MOS mixes were cured to the standard 28 days as per ASTM C109 and C349 [316], [317].The resulting data is illustrated in Figure 7.5. Detailed numerical data is presented in Table 7.4.

The results presented in Figure 7.5 indicate that CSA-15 exhibits an average strength 54.5% lower than the CSA control. The strength of the control CSA paste strength aligns with early strength values reported in literature, which tipically range from 20-40 MPa [296]. Figure 7.6 provides a visual representation of the cross-sections of cement prisms. Notably, the CSA-15 sample displayed an increased amount of porosity within

Table 7.4: Compression test results of CSA and MOS.

	Compression (MPa)				
Day	1	5	7	14	28
CSA	26.83±3.83	35.13±2.21	32.04±0.76	-	-
CSA+15% GS	17.87±0.59	13.38±0.80	28.07±2.03	-	-
MOS 10	0.55±0.04	-	6.30±0.70	8.08±1.39	13.17±1.31
MOS 15	4.59±0.15	-	15.40±0.30	20.74±0.48	28.34±2.04
MOS 15 + 15% GS	0.69±0.02	-	8.43±1.45	13.07±1.95	25.01±2.14

the prism, which likely contributes significantly to the overall decrease in strength. The cause of this increased porosity is hypothesized to be the crystallization of sodium sulfate (derived from the GS addition), driven by the initial high reactivity of the cement paste, followed by the subsequent dissolution of the salt crystals as the cement cures. This mechanism of pore formation is consistent with literature findings which indicate that, at high salt concentrations, the CSA paste is prone to increasing its pore size [318]. Although the CSA system generally exhibits high heat release, the literature also notes that high salt concentrations can lead to slower overall hydration kinetics [318], [319], suggesting that the salt interferes with the long-term phase development while still triggering early, localized reactivity that drives the initial crystallization.

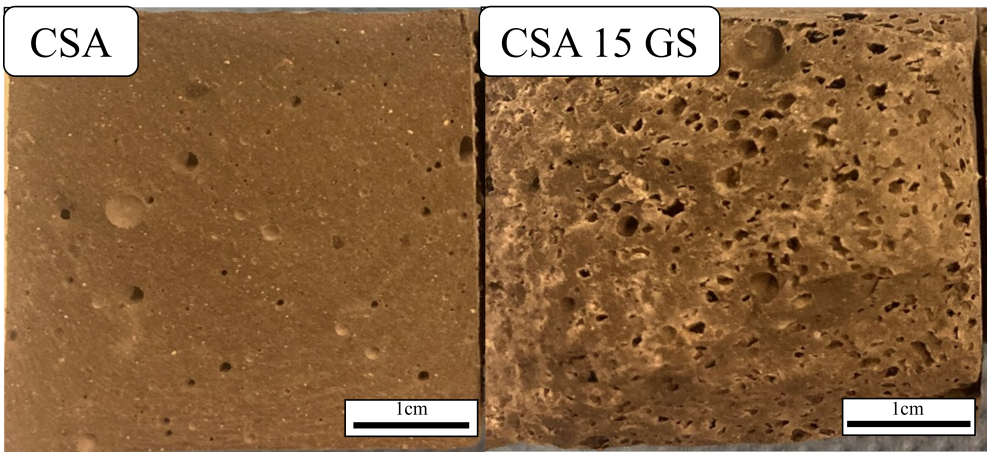

Figure 7.6: Visible comparison of effects of GS on CSA cement at 7 days. Formation of pores on right image as well as a noticeable discoloration.

Based on the quantitative X-ray diffraction (Q-XRD) analysis of the material's composition over time, as presented in Table 7.5, GS has profound effects on the CSA system. First, the presence of GS appears to increase the system's overall amorphous content. This increase may be attributed to the hydration water initially supplied by the GS, which subsequently dehydrates to its anhydrous form, thenardite [320]. When compared to the pure CSA system, the relative abundance of several crystalline phases—specifically ettringite, calcite, dolomite, gibbsite, and anhydrite—appears to decrease when exposed to GS. Furthermore, based on isothermal calorimetry, Q-XRD

results, and established literature [315], it is inferred that after the aluminate is fully reacted in the system, gypsum and anhydrite will be the primary products formed. The remaining sodium from the GS is plausibly adsorbed into the CSH gel. This disruption in phase composition, particularly the destabilization of the AFm and AFt phases by high sodium concentrations, could explain the subsequent low compression strength test results compared to pure CSA.

The observed unusual porous structure is attributed to a complex mechanism initiated by the GS addition. The workability of the material was no different from the regular CSA, and there were no crystals in the liquid added to the CSA. While the GS was pre-dissolved in the mixing water, the fast-setting nature of the CSA paste (evident from calorimetry) likely forced the premature crystallization of the GS. Subsequently, during the curing period, the continued hydration of the cement paste pulls the water necessary for its reaction, causing the GS crystals to dehydrate and partially dissolve. This dehydration and dissolution process leaves behind the observed pores within the cement paste as well as thernadite. This increased porosity, combined with the phase compositional changes, plays a significant role in the material's overall mechanical strength.

Table 7.5: Q-XRD of CSA and CSA GS 15% paste in 7-day ages (% by mass).

Phase Name	Composition	CSA -1	CSA -5	CSA -7	CSA GS-1	CSA GS-5	CSA GS-7
Anhydrite	$CaSO_4$	8.06±0.18	8.02±0.18	7.45±0.17	5.14±0.12	3.72±0.12	4.56±0.12
Bayerite	$Al(OH)_3$	1.17±0.33	1.44±0.25	1.27±0.26	1.17±0.24	0.99±0.24	0.85±0.25
Calcite	$CaCO_3$	3.58±0.17	4.17±0.22	3.84±0.16	2.68±0.13	2.63±0.18	2.83±0.13
Dolomite	$CaMg(CO_3)_2$	2.80±0.37	1.35±0.24	1.45±0.21	0.62±0.15	0.58±0.16	0.58±0.16
Ettringite	$Ca_6Al_2(SO_4)_3(OH)_{12} \cdot 26H_2O$	18.21±0.43	22.33±0.50	19.23±0.45	11.71±0.28	14.60±0.37	14.52±0.38
Gibbsite	$Al(OH)_3$	1.33±0.19	3.63±0.38	2.63±0.34	0.85±0.27	1.02±0.27	1.13±0.30
Kuzelite	$Ca_4Al_2(OH)_{12}SO_4 \cdot 6H_2O$	2.07±0.16	0.87±0.14	0.55±0.12	-	-	-
Larnite	Ca_2SiO_4	18.37±0.42	16.46±0.41	15.06±0.35	16.38±0.33	15.28±0.34	16.13±0.36
Magnetite	Fe_3O_4	-	1.65±0.14	1.67±0.12	2.45±0.15	1.51±0.10	1.59±0.11
Magnesite	$MgCO_3$	0.67±0.12	0.47±0.34	0.32±0.25	-	0.18±0.12	0.13±0.17
Perovskite	$CaTiO_3$	7.78±0.16	8.49±0.17	7.49±0.15	7.64±0.13	6.78±0.13	6.99±0.13
Quartz	SiO_2	0.54±0.10	4.20±0.12	8.08±0.14	0.50±0.14	4.95±0.10	8.34±0.13
Thenardite	Na_2SO_4	-	-	-	5.01±0.23	6.81±0.24	5.09±0.24
Yeelimite	$Ca_4(Al_6)SO_4$	1.59±0.14	3.79±0.17	3.92±0.16	3.48±0.13	1.99±0.13	2.57±0.13
Amorphous		33.84±1.10	23.14±1.25	27.06±1.10	42.38±0.88	38.87±0.96	34.69±1.00

Figure 7.5 presents the data for the strength test of MOS 15, MOS 10, and MOS 15 with 15% GS (MOS 15 15% GS). The results clearly highlight the superior strength performance of the MOS 15 mix compared to both MOS 10 and MOS 15 15% GS. The addition of GS caused a decrease in strength compared to MOS 15 without GS, resulting in a strength that was comparable to the MOS 10 mix, as depicted in the graph. The average strength based on literature varies depending on formulations; however, for highly reactive MgO, known values range from 25-60 MPa depending on curing conditions [321]. Nevertheless, this reduction did not significantly affect the general integrity or suitability of the material for coating applications. Visually, there was no distinction between MOS 10, MOS 15, or MOS 15 15% GS; all samples appeared as uniform white blocks with some inherent porosity, as depicted in fig. 7.7.

XRD analysis of the MOS material was conducted at curing ages of 1, 7, 14, and 28 days, correlating with the compression testing schedule. These samples were chemically

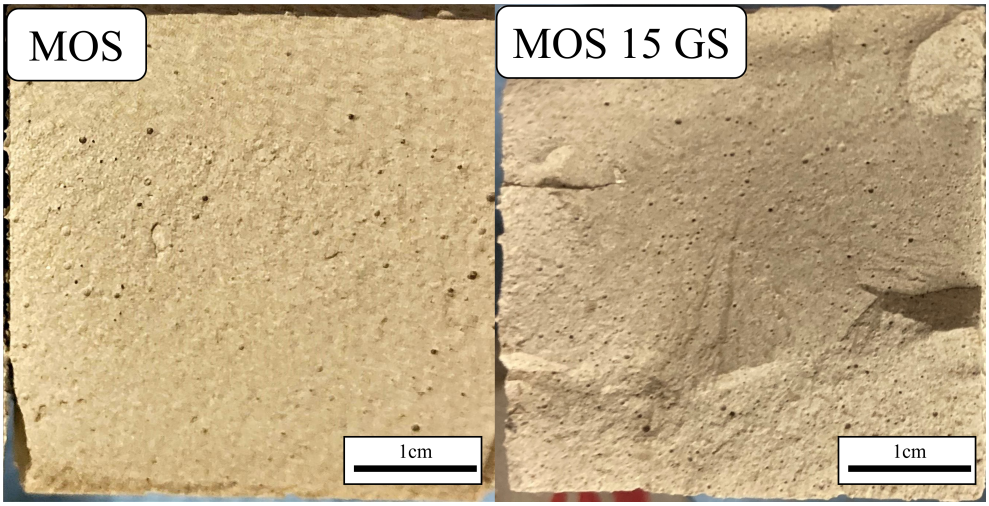

Figure 7.7: MOS Prism Cross-section at 28 days.

dried through solvent exchange to halt hydration for subsequent assessment of phase formation. On Day 1, samples exhibited no formation of crystalline MOS phases. Only the starting components were present: MgO (periclase) [P], magnesium sulfate hydrates ($MgSO_4 \cdot 7H_2O/6H_2O$) [S], and some $Mg(OH)_2$ (brucite) [B]. Further analysis revealed a consistent reduction in MgO (periclase) and a corresponding increase in $Mg(OH)_2$ (brucite) over time, indicating the slow progression of the hydration reaction. Gypsum was also identified in the graph (labeled with the letter [G]).

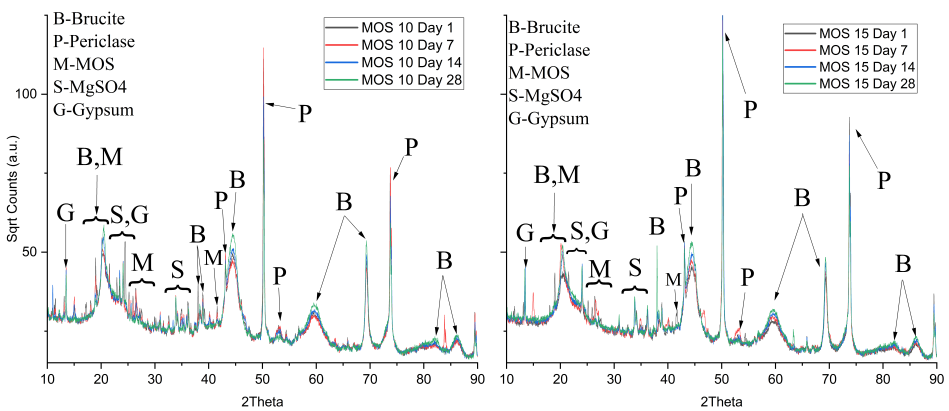

Figure 7.8: XRD of MOS phases in both MOS and MOS 15 cement mixes.

There are barely any differences between the MOS 10 and MOS 15 samples (Figure 7.8). The primary MOS peaks were generally identified by region under the moniker [M].

Because current databases lacked sufficient data for specific identification, literature comparisons were used to confirm the general MOS phase peaks [298], [322]. Noticeably the peaks at around 20 2θ are quite broad aligning with brucite, although this region is also associated with early MOS phases, including 5-1-3 and 3-1-8. When analyzing samples with GS (MOS 15 15% GS), minimal variation from this overall trend was noticed (Figure 7.9). The persistence of the MgO hydration to $Mg(OH)_2$ and the general formation of MOS phases suggest that the presence of GS has a minimal effect on the primary MOS crystal formation process. The only notable changes were the presence of bloedite ($Na_2Mg(SO_4)_2 \cdot 4H_2O$), identified with the letter [D], and the detection of small formations ($< 5\%$) of konyaite ($Na_2Mg(SO_4)_2 \cdot 5H_2O$) at $2\theta = 26.03°$ (Figure 7.9). Consistent with the calorimetry data, the hydration reaction remains consistent regardless of the amount of GS, confirming that the material's compression strength is primarily affected by the water content (w/b ratio) rather than the salt addition.

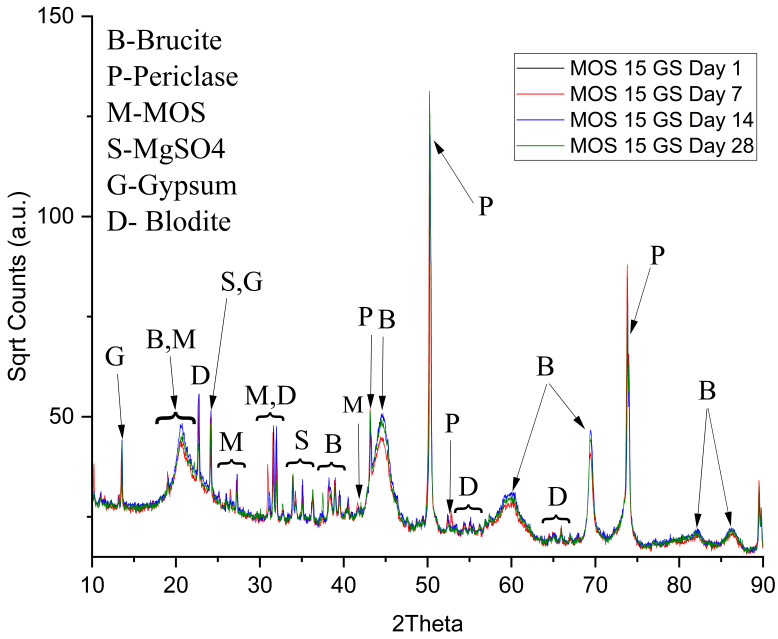

Figure 7.9: XRD phases on MOS 15 with 15% GS.

7.3.3 Pelletized Material

Pellets were tested with different starting size fractions of EV and those that provided the most consistent below 4 mm final size was the 1.4-2.0 mm. Initial tests were conducted using CSA, but the samples' overall integrity was not reliable for continued

use, as the coating would rub off easily. The tests pellets coated with MOS showed significantly better results with an even size distribution. As presented in the manual PSD, the majority of the pellet sizes remained consistent in the range of 2.0-4.0 mm diameter (Figure 7.10).

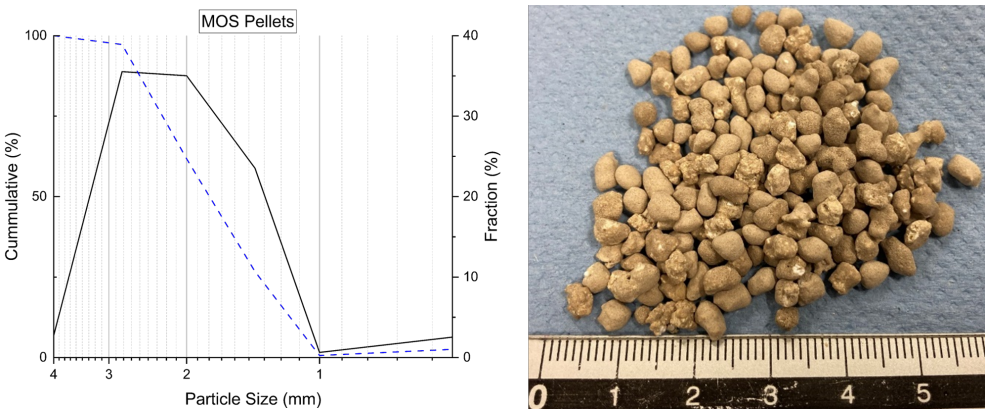

Figure 7.10: PSD (left) and visual result (right) of MOS pellets.

Density

Gas pycnometry was used to determine the density of EV. Additionally, manual pycnometry was performed to assess the absorption properties of the expanded vermiculite granules. The relevant data are summarized in Table 7.6, which shows that EV exhibits a porosity of 43–53% and an absorption capacity of up to four times its own weight. The absorption was measured using the manual pycnometry method as discussed in Chapter 2. The size fractions of 1.4-2.0 mm EV were used to make the EV-GS, which ultimately made up the pellets.

MOS-EV-GS pellets, with a size range of 1.0-4.0 mm, were initially assessed using gas pycnometry. Consequently, manual pycnometry was conducted on the largest sample pool (2.0-4.0 mm), yielding an average value of 1.18 g/mL.

Table 7.6: Pycnometry results overview of materials and pellets.

Pycnometry	Size Fraction (mm)	Skeletal Density	Bulk Density	Porosity (%)	Absorption (%)
EV	1.0-1.4	1.62±0.01	0.52±0.01	53.60	440.10
	1.4-2.0	1.78±0.01		43.07	402.04
EV-GS	1.0-2.8	1.39±0.003	1.88±0.005	-	-
CSA-EV-GS	1.0-1.4	1.63±0.002	1.65±0.1	-	-
	1.4-2.0	1.47±0.003		-	-
	2.0-2.8	1.45±0.003		-	-
MOS-EV-GS	2.0-4.0	1.96±0.001	1.18±0.4	-	-

Thermal Performance of Pelletized Material

To evaluate the thermal performance of the material, four sample types were prepared using a cylindrical 3D-printed PLA mold. The 15:1:20 MOS mixture was cast to

produce: (i) MOS – a pure MOS reference block, (ii) MOS (MOS-EV) – MOS containing empty EV pellets without PCM, (iii) MOS (EV-GS) – MOS containing uncoated EV–GS pellets, and (iv) MOS (MOS-EV-GS) – MOS containing coated EV–GS pellets. The PCM content in the MOS (MOS-EV-GS) sample was 26.4% by weight. After one week of curing, the molds containing the coated pellets expanded [MOS (MOS-EV) and MOS (MOS-EV-GS)], consistent with observations in literature [323], resulting in superficial cracking on one side. The thermal properties obtained are presented in Table 7.7, including the average values and corresponding standard deviations. The pure MOS reference exhibited the expected behaviour for a dense, compact material: relatively high thermal conductivity (λ), typical volumetric heat capacity (C_ρ), and high thermal diffusivity (α).

Table 7.7: Thermal properties of base materials and mortar MOS samples.

Material Sample	Thermal Conductivity (W/m·K)	Heat Capacity (10^6 J/m^3·K)	Thermal Diffusivity (10^{-6} m^2/s)	Apparent Density (g/ml)	Ref.
GS	1.00±0.02	1.62±0.14	-	-	[324]
EV	0.06	1.08	-	-	[325]
CSA	0.70	0.97	-	-	[326]
MOS	2.193±0.055	1.477±0.012	1.487±0.035	2.05	-
MOS (MOS-EV)	1.180±0.026	1.407±0.012	0.838±0.014	1.99	-
MOS (EV-GS)	1.123±0.032	1.433±0.006	0.826±0.025	1.82	-
MOS (MOS-EV-GS)	0.379±0.007	1.460±0.000	0.259±0.005	1.99	-

When introducing the coated blank pellets MOS (MOS-EV), a reduction in thermal conductivity was observed, attributable to the insulating effect of the vermiculite. A slight decrease in heat capacity was also measured, while thermal diffusivity showed a substantial reduction due to the presence of vermiculite alone. For the MOS (EV-GS) samples, both conductivity and diffusivity decreased further, while the heat capacity increased, indicating that the inclusion of PCM enhances the thermal buffering capability of the composite.

Finally, for the MOS (MOS-EV-GS) samples, despite the presence of superficial cracking, the coating thickness was sufficient to enable reliable measurements in areas without visible cracks. Although the recorded values may be partially affected by these defects, the observed increase in heat capacity combined with the continued reduction in thermal diffusivity and conductivity strongly supports the effectiveness of the encapsulated PCM pellets in achieving the targeted thermal regulation behaviour.

Compared with values reported in the literature, MOS exhibited a higher volumetric heat capacity of 1.477×10^6 J/m$^3 \cdot$ K, relative to the commonly reported 0.898×10^6 J/m$^3 \cdot$ K for MOS-based materials [308]. Within the context of this proof-of-concept study, the MOS (MOS-EV-GS) sample also demonstrated the lowest thermal diffusivity of all mixtures tested, which is a desirable characteristic for passive thermal regulation. Although no direct benchmark currently exists for cementitious coatings applied to salt-hydrate PCMs, an ideal thermally regulating material is expected to combine high heat capacity with low diffusivity to enhance thermal buffering and slow heat transfer [327]–[329]. As shown in Figure 7.11, the MOS (MOS-EV-GS) sample aligns with this expected behaviour and therefore presents a promising basis for further development

of coated salt-hydrate PCM systems.

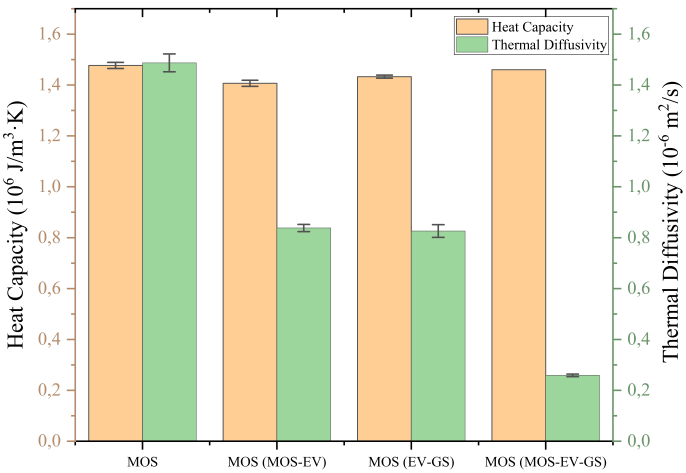

Figure 7.11: Graphical representation of thermal data of MOS concrete render mixes.

7.4 Discussion

This research project focused on developing a proof-of-concept for cement-coated PCM pellets for application in mortars/renders. The selected binders, Calcium Sulfoaluminate (CSA) and Magnesium Oxysulfate (MOS), were chosen for their potential compatibility with Glauber's Salt (GS), a widely studied PCM salt hydrate. Both CSA and MOS are commercially available and recognized for their sulfate resistance. This approach aimed to achieve the dual purpose of retaining PCM within pellets while imparting thermoregulation functionality to buildings [314], [330]–[332]. An expanded vermiculite (EV) matrix was employed to stabilize the PCM core, with the resulting EV-GS cores subsequently coated with the MOS cement via pelletization.

Experimental results revealed that GS exposure in CSA rendered the system unsuitable for development, as it rapidly dehydrates and crystallises beyond an upper threshold, forming a highly porous network rich in thenardite that resulted in an immediate loss of coating integrity. In contrast, the effect of GS on The effect of MOS 15 was primarily reflected in the isothermal calorimetry and mineralogical analysis. Regarding isothermal calorimetry, the addition of GS lowered the heat release, but that effect was largely independent of GS concentration in the measured range of 5 to 20%. Mineralogically, the formation of bloedite and konyaite occurred. However, after 28 days, the effect of GS on MOS 15 was negligible in terms of strength, and the material displayed comparable performance to the GS-free reference. Due to the absence of

standardised mix designs for MOS cements, two molar ratios (10:1:20 and 15:1:20) were evaluated, both of which demonstrated sufficient strength and resistance to adverse GS-related effects.

When incorporated into a render, the final composite material showed promising potential for thermal energy retention and storage. This was evident even at a PCM content of 26.4% in the coated pellet. Thermal testing of the renders indicated a 64% increase in heat capacity compared to solely GS, and a reduction in thermal diffusivity ranging from 20% to 75%.

The findings of this work hold significant relevance for sustainable construction. Improving the thermal behaviour of building materials can help reduce energy demand, lower carbon emissions, and support indoor comfort, particularly in climates with high heating or cooling needs. While CSA is typically expensive (two to three times higher than OPC), the thin 1 mm coating layer keeps overall material cost manageable, where the coating's primary function is to form a protective barrier around the salt-hydrate PCM to prevent sulfate leaching. MOS provides comparable benefits, including high strength, cost-effectiveness, and favourable chemical resistance, though its sensitivity to prolonged moisture exposure restricts its use to indoor applications.

This chapter provides a proof of concept for using niche cements to encapsulate salt hydrate PCM and establishes a basis for developing more durable and energy-efficient thermal storage solutions for building applications. Future work should investigate the optimisation of PCM-to-cement ratios and evaluate long-term performance under repeated thermal cycling, with emphasis on coating durability.

Chapter 8

Conclusions and Suggestions

> "I have come to the conclusion, after many years of sometimes bad experience, that you cannot come to any conclusion at all."
>
> —Vita Sackville-West, In Your Garden Again

This thesis has explored the potential of hydrated salt phase change materials (PCMs) as a sustainable solution for thermal energy storage. By investigating recycled salt hydrates derived from olivine waste, the research demonstrated that these materials exhibit a high latent heat of fusion and favorable thermal stability when appropriately stabilized. The comprehensive characterization—including DSC, TGA, XRD, and complementary techniques—has confirmed that salt hydrates can offer significant energy density advantages over conventional organic PCMs such as paraffins. Additionally, the research explored the effects of salt hydrates and solutions on cement chemistry, providing insights regarding the key effects and outcomes. The outcomes of this research are described in detail below.

8.1 Theoretical Thermodynamics and Melt Mechanics of Salt Hydrates

In Chapter 3, a comprehensive theoretical framework was established to explain the thermodynamics and melting mechanisms of salt hydrates. This chapter laid out the fundamental principles governing phase change phenomena, focusing on both sensible and latent heat storage. Detailed discussions on the role of water coordination, hydration dynamics, and the influence of kosmotropic versus chaotropic ions provided a deeper insight into the structural transformations that occur during melting and recrystallization. Additionally, thermodynamic models—such as the Glasser-Jenkins approach—were introduced to predict lattice energy, enthalpy, entropy, and heat capacity, thereby linking fundamental theory with the practical energy storage capacity of the materials.

The theoretical insights developed in this chapter form the backbone of the subsequent experimental investigations. By establishing a robust understanding of the physical processes underlying the behavior of salt hydrates, Chapter 3 sets the stage for evaluating and optimizing these materials for real-world thermal energy storage applications.

8.2 Epsomite from Olivine Waste

Chapter 4 shifted the focus to experimental investigations, where sulfate salt hydrates were extracted from an olivine nano-silica side stream. This chapter described the extraction, purification, and subsequent characterization of the salt hydrates using techniques such as XRF, XRD, and FT-IR. The experimental results highlighted the distinct phase change behavior of the extracted materials, including key parameters such as melting points, latent heat, and crystallization kinetics. The discussion emphasized both the potential advantages of utilizing waste-derived materials and the challenges involved in maintaining consistent phase change performance.

The outcomes of this chapter support the theoretical models presented earlier by demonstrating that the extracted salt hydrates exhibit promising thermal storage capabilities. These findings underscore the viability of repurposing industrial by-products for sustainable energy solutions and lay the groundwork for further stabilization studies.

8.3 Thermal Stability of Up-cycled Salt Hydrates

In Chapter 5, the long-term thermal stability of recycled salt hydrates was examined under conditions simulating seasonal thermal cycling. A series of thermal cycling experiments and calorimetric analyses were conducted to address the well-known problem of significant supercooling observed in the base salt hydrate. While additives—such as nucleating and thickening agents—can be a solution to this issue, identifying the optimal formulation remains challenging. The experimental work ultimately revealed that although the base material possesses a high latent heat storage capacity, its stability under repeated cycling can be significantly enhanced through optimized stabilization techniques.

These findings are critical for real-world applications, as they address practical concerns such as phase separation and supercooling. The insights gained from this chapter highlight the importance of material optimization to ensure that salt hydrate-based thermal batteries can maintain consistent performance over extended periods.

8.4 Effects of Marine Salts on Cementitious Materials

Chapter 6 explored an interdisciplinary application of cementitious materials in marine environments. By investigating the effects of seawater on the performance of various

cement formulations, the study evaluated their potential for use in artificial reefs. Through tests of compressive strength, leaching behavior, and microstructural analysis, the chapter demonstrated that seawater can both challenge and, when properly managed, enhance the durability of cement-based materials. Optimized mixes can support marine life while maintaining the necessary mechanical properties for structural applications.

This chapter not only contributes to environmental engineering but also reinforces the broader theme of sustainable material usage. The integration of natural resources with industrial by-products opens up new avenues for eco-friendly construction practices and offers valuable lessons for the development of composite systems in other applications.

8.5 Alternative Coatings for Salt Hydrates

In Chapter 7, a novel composite system was developed by encapsulating salt hydrates within a vermiculite matrix, further enhanced by a coating of non-traditional cementitious materials. Detailed experimental analyses, including particle size distribution, thermal diffusivity, and compressive strength measurements, demonstrated that this composite approach holds significant promise for incorporating PCMs into render. The results indicate that the cementitious coating successfully preserves the desirable thermal properties of the salt hydrates while facilitating their integration into building components for thermal regulation.

This innovative approach not only validates the concept of combining salt hydrates with alternative cements but also opens up promising pathways for future research into salt hydrate integration into buildings as passive thermo-regulating components. The successful development of this composite material underlines the potential for scalable, durable, and sustainable thermal management systems in modern construction.

8.6 Recommendations

While research on hydrated salt phase change materials (PCMs) has made significant progress, there still are some limitations and unresolved questions in this field:

1. Thermal Cycling Durability
    - Salt hydrates are subjected to repeated thermal cycling during energy storage and release, and ensuring their long-term stability and performance over thousands of cycles remains a significant challenge due to material degradation.
    - Future research should focus on investigating degradation mechanisms, developing robust encapsulation methods, and exploring novel composite materials capable of withstanding cyclic thermo-mechanical stress.
2. Compatibility and System Modeling Challenges

- Integrating salt hydrates into existing energy systems (e.g., solar thermal plants, district heating) requires high material compatibility and efficient heat exchanger design.
- A major limitation to system integration is the current lack of robust computational models capable of accurately predicting long-term performance and heat transfer dynamics at scale.
- Fundamental thermodynamic data, including the necessary parameters for accurate hydration/dehydration kinetics (e.g., phase transition speed, effects of particle size and additives), is often missing or incomplete.
- Researchers must focus on generating this essential data to develop models that effectively address issues related to material compatibility, heat exchanger design, and the complex system integration with other energy storage technologies (e.g., batteries, pumped hydro).

3. Cost-Effectiveness and Scalability
    - Achieving cost-effective production and scalability is critical for widespread adoption.
    - Research should focus on optimizing material synthesis, minimizing production costs, and streamlining manufacturing processes while balancing cost with performance for large-scale applications.
4. Environmental Impact and Sustainability
    - While salt hydrates are abundant and non-toxic, their environmental impact during production, use, and disposal needs assessment.
    - Sustainable sourcing of raw materials and recycling strategies are essential for long-term viability, and life cycle assessments can guide decisions toward environmentally friendly solutions.

Collectively, the research presented in this thesis underscores the potential of hydrated salt PCMs as sustainable alternatives for thermal energy storage. The theoretical and experimental investigations have shown that, with proper stabilization and integration into composite systems, salt hydrates can achieve high energy densities while reducing environmental impacts. Despite the challenges of phase separation and potentially reducing supercooling, the work has provided a robust framework for further optimization and application.

Future research should focus on refining stabilization techniques, scaling up synthesis and encapsulation processes, and integrating these materials into smart, energy-efficient systems. Interdisciplinary collaboration will be key to translating these laboratory-scale findings into real-world solutions that contribute to energy conservation and carbon emission reduction. Continued exploration in this area promises to pave the way toward more resilient and sustainable energy infrastructures.

References

[1] K. A. R. Ismail, F. Tima, A. M. Lino, M. Teggar, M. ¨. Slu ¨ M Arıcı, P. L. O. Machado, T. A. Alves, A. C. O. De Paula, and A. Benhorma, "A Comprehensive Review on Phase Change Materials and Applications in Buildings and Components; reuse license CC-BY 4.0," *ASME Open Journal of Engineering 2022*, vol. 1, pp. 11 049–11 050, 2022. DOI: 10.1115/1.4055185. [Online]. Available: http://asmedigitalcollection.asme.org/openengineering/article-pdf/doi/10.1115/1.4055185/6930510/aoje_1_011049.pdf.

[2] R.-A. Mitran, S. Ioniţă, D. Lincu, D. Berger, and C. Matei, "A Review of Composite Phase Change Materials Based on Porous Silica Nanomaterials for Latent Heat Storage Applications," *Molecules*, vol. 26, no. 1, p. 241, Jan. 2021, ISSN: 1420-3049. DOI: 10.3390/molecules26010241.

[3] S. Raoux, "Phase Change Materials," *Annual Review of Materials Research*, vol. 39, no. 1, pp. 25–48, Aug. 2009, ISSN: 1531-7331. DOI: 10.1146/annurev-matsci-082908-145405.

[4] C. Alpers, J. Jambor, and D. Nordstrom, "Sulfate Minerals," *Reviews in Mineralogy and Geochemistry*, vol. 40, no. 1, pp. iii–iii, Jan. 2000, ISSN: 1529-6466. DOI: 10.2138/rmg.2000.40.0. [Online]. Available: https://pubs.geoscienceworld.org/rimg/article/40/1/iii/140659.

[5] J. M. Delgado, J. C. Martinho, A. Vaz Sá, A. S. Guimarães, and V. Abrantes, *Thermal Energy Storage with Phase Change Materials, A Literature Review of Applications for Buildings Materials*, English. Cham: Springer, 2019, p. 73, ISBN: 9783319974989. DOI: 10.1007/978-3-319-97499-6. [Online]. Available: https://www.springer.com/us/book/9783319974989.

[6] J. Kośny, *PCM-Enhanced Building Components: An Application of Phase Change Materials in Building Envelopes and Internal Structures*. 2015, pp. 21–59, ISBN: 9783319142852. DOI: 10.1007/978-3-319-14286-9. [Online]. Available: http://link.springer.com/10.1007/978-3-319-14286-9%5Cnhttp://www.springer.com/series/4604.

[7] A. Sharma, V. V. Tyagi, C. R. Chen, and D. Buddhi, *Review on thermal energy storage with phase change materials and applications*, Feb. 2009. DOI: 10.1016/j.rser.2007.10.005.

[8] B. Zalba, J. M. Marin, L. F. Cabeza, and H. Mehling, "Review on thermal energy storage with phase change: materials, heat transfer analysis and applications," *Applied Thermal Engineering*, vol. 23, pp. 251–283, 2003, ISSN: 00221120.

[9] T. S. Yan, T. X. Li, J. X. Xu, and J. W. Chao, "Understanding the transition process of phase change and dehydration reaction of salt hydrate for thermal energy storage," *Applied Thermal Engineering*, vol. 166, Feb. 2020, ISSN: 13594311. DOI: 10.1016/j.applthermaleng.2019.114655.

[10] V. V. Tyagi, K. Chopra, R. K. Sharma, A. K. Pandey, S. K. Tyagi, M. S. Ahmad, A. Sarı, and R. Kothari, "A comprehensive review on phase change materials for heat storage applications: Development, characterization, thermal and chemical stability," *Solar Energy Materials and Solar Cells*, vol. 234, Jan. 2022, ISSN: 09270248. DOI: 10.1016/j.solmat.2021.111392.

[11] M. Saqib and R. Andrzejczyk, "A review of phase change materials and heat enhancement methodologies," *WIREs Energy and Environment*, vol. 12, no. 3, May 2023, ISSN: 2041-8396. DOI: 10.1002/wene.467.

[12] V. Kulish, N. Aslfattahi, M. Schmirler, and P. Sláma, "New library of phase-change materials with their selection by the Rényi entropy method," *Scientific Reports*, vol. 13, no. 1, p. 10 446, Jun. 2023, ISSN: 2045-2322. DOI: 10.1038/s41598-023-37701-0.

[13] B. Buonomo, M. Rita Golia, O. Manca, and S. Nardini, "A review on thermal energy storage with phase change materials enhanced by metal foams," *Thermal Science and Engineering Progress*, vol. 53, p. 102 732, Aug. 2024, ISSN: 24519049. DOI: 10.1016/j.tsep.2024.102732.

[14] L. F. Cabeza, A. Castell, C. Barreneche, A. De Gracia, and A. I. Fernández, "Materials used as PCM in thermal energy storage in buildings: A review," *Renewable and Sustainable Energy Reviews*, vol. 15, no. 3, pp. 1675–1695, 2011, ISSN: 13640321. DOI: 10.1016/j.rser.2010.11.018. [Online]. Available: http://dx.doi.org/10.1016/j.rser.2010.11.018.

[15] A. Efimova, S. Pinnau, M. Mischke, C. Breitkopf, M. Ruck, and P. Schmidt, "Development of salt hydrate eutectics as latent heat storage for air conditioning and cooling," *Thermochimica Acta*, vol. 575, no. October 2018, pp. 276–278, 2014, ISSN: 00406031. DOI: 10.1016/j.tca.2013.11.011. [Online]. Available: http://dx.doi.org/10.1016/j.tca.2013.11.011.

[16] H. Kanwischer, "Development of Media for Dynamic Latent Heat Storage in the Low Temperature Range," German Research, test institure for Air-, and Space Travel, Stuttgard, Tech. Rep., Dec. 1983, pp. 3–63.

[17] M. Kenisarin and K. Mahkamov, "Salt hydrates as latent heat storage materials:Thermophysical properties and costs," *Solar Energy Materials and Solar Cells*, vol. 145, pp. 255–286, 2016, ISSN: 09270248. DOI: 10.1016/j.solmat.2015.10.029. [Online]. Available: http://dx.doi.org/10.1016/j.solmat.2015.10.029.

[18] Z. Khan, Z. Khan, and A. Ghafoor, *A review of performance enhancement of PCM based latent heat storage system within the context of materials, thermal stability and compatibility*, May 2016. DOI: 10.1016/j.enconman.2016.02.045.

[19] V. Palomba, V. Brancato, and A. Frazzica, "Thermal performance of a latent thermal energy storage for exploitation of renewables and waste heat: An experimental investigation based on an asymmetric plate heat exchanger," *Energy Conversion and Management*, vol. 200, Nov. 2019, ISSN: 01968904. DOI: 10.1016/j.enconman.2019.112121.

[20] J. Houben, "Accelerating Thermochemical Energy Storage by Doping," Ph.D. dissertation, Eindhoven University of Technology, Eindhoven, Mar. 2023, pp. i–181, ISBN: 978-94-6469-248-8.

[21] P. Dixit, V. J. Reddy, S. Parvate, A. Balwani, J. Singh, T. K. Maiti, A. Dasari, and S. Chattopadhyay, *Salt hydrate phase change materials: Current state of art and the road ahead*, Jul. 2022. DOI: 10.1016/j.est.2022.104360.

[22] F. Raaijmakers and B. van der Meer, *How the Eindhoven heat battery can quickly make millions of homes gas-free*, Apr. 2022.

[23] N. Beaupere, U. Soupremanien, and L. Zalewski, *Nucleation triggering methods in supercooled phase change materials (PCM), a review*, Dec. 2018. DOI: 10.1016/j.tca.2018.10.009.

[24] H. Akeiber, P. Nejat, M. Z. A. Majid, M. A. Wahid, F. Jomehzadeh, I. Zeynali Famileh, J. K. Calautit, B. R. Hughes, and S. A. Zaki, "A review on phase change material (PCM) for sustainable passive cooling in building envelopes," *Renewable and Sustainable Energy Reviews*, vol. 60, no. September 2018, pp. 1470–1497, 2016, ISSN: 18790690. DOI: 10.1016/j.rser.2016.03.036. [Online]. Available: http://dx.doi.org/10.1016/j.rser.2016.03.036.

[25] U. I. Shaikh, S. Kale, A. Roy, and A. Sur, "PERFORMANCE ANALYSIS OF AN ENERGY-EFFICIENT PCM-BASED ROOM COOLING SYSTEM," *Front. Heat Mass Transf.*, vol. 20, Apr. 2023, ISSN: 2151-8629. DOI: 10.5098/hmt.20.28.

[26] B. Huang, Z. Zheng, G. Lu, and X. Zhai, "Design and experimental investigation of a PCM based cooling storage unit for emergency cooling in data center," *Energy and Buildings*, vol. 259, p. 111 871, Mar. 2022, ISSN: 03787788. DOI: 10.1016/j.enbuild.2022.111871.

[27] K. Faraj, M. Khaled, J. Faraj, F. Hachem, and C. Castelain, "Phase change material thermal energy storage systems for cooling applications in buildings: A review," *Renewable and Sustainable Energy Reviews*, vol. 119, Mar. 2020, ISSN: 18790690. DOI: 10.1016/j.rser.2019.109579.

[28] A. Bland, M. Khzouz, T. Statheros, and E. I. Gkanas, "PCMs for Residential Building Applications: A Short Review Focused on Disadvantages and Proposals for Future Development," *Buildings*, vol. 7, no. 4, Aug. 2017, ISSN: 2075-5309. DOI: 10.3390/buildings7030078. [Online]. Available: http://www.mdpi.com/2075-5309/7/3/78.

[29] Y. G. Gurevich and J. E. Velazquez-Perez, "Peltier Effect in Semiconductors," in *Wiley Encyclopedia of Electrical and Electronics Engineering*, John Wiley & Sons, Inc., Apr. 2014, pp. 1–21. DOI: 10.1002/047134608x.w8206.

[30] Y. Li, N. Nord, Q. Xiao, and T. Tereshchenko, "Building heating applications with phase change material: A comprehensive review," *Journal of Energy Storage*, vol. 31, no. March, 2020, ISSN: 2352152X. DOI: 10.1016/j.est.2020.101634.

[31] Enerdata, *Global Energy statistical Yearbook 2021: Average CO2 emission factor*, 2021. [Online]. Available: https://yearbook.enerdata.net/co2/toe-emissions-co2.html.

[32] European Environment Agency, *Greenhouse gas emissions from energy use in buildings in Europe*, Oct. 2021. [Online]. Available: https://www.eea.europa.eu/data-and-maps/daviz/greenhouse-gas-emissions-from-energy-2#tab-chart_1.

[33] IEA, *Unit converter and glossary*, Dec. 2016. [Online]. Available: https://www.iea.org/reports/unit-converter-and-glossary.

[34] P. Tatsidjodoung, N. Le Pierrès, and L. Luo, *A review of potential materials for thermal energy storage in building applications*, 2013. DOI: 10.1016/j.rser.2012.10.025.

[35] European Commission, *How many single-parent households are there in the EU?* Jan. 2021. [Online]. Available: https://ec.europa.eu/eurostat/web/products-eurostat-news/-/edn-20210601-2#:~:text=In%202020%2C%20there%20were%20195.4%20million%20households%20in,single%20parents%2C%20accounting%20for%204%25%20of%20total%20households..

[36] IEA, *Europe Region Profile*, 2020. [Online]. Available: https://www.iea.org/regions/europe.

[37] N. Xie, Z. Huang, Z. Luo, X. Gao, Y. Fang, and Z. Zhang, "Inorganic salt hydrate for thermal energy storage," *Applied Sciences (Switzerland)*, vol. 7, no. 12, Dec. 2017, ISSN: 20763417. DOI: 10.3390/app7121317.

[38] P. A. Donkers, L. C. Sögütoglu, H. P. Huinink, H. R. Fischer, and O. C. Adan, *A review of salt hydrates for seasonal heat storage in domestic applications*, 2017. DOI: 10.1016/j.apenergy.2017.04.080.

[39] J. Hirschey, K. R. Gluesenkamp, A. Mallow, and S. Graham, "Review of Inorganic Salt Hydrates with Phase Change Temperature in Range of 5°C to 60°C and Material Cost Comparison with Common Waxes," in *5th International High Performance Buildings Conference at Purdue*, 2018, pp. 1–10.

[40] N. H. Almousa, M. R. Alotaibi, M. Alsohybani, D. Radziszewski, S. M. AlNoman, B. M. Alotaibi, and M. M. Khayyat, "Paraffin Wax [As a Phase Changing Material (PCM)] Based Composites Containing Multi-Walled Carbon Nanotubes for Thermal Energy Storage (TES) Development," *Crystals*, vol. 11, no. 8, p. 951, Aug. 2021, ISSN: 2073-4352. DOI: 10.3390/cryst11080951.

[41] B. Koçak, A. I. Fernandez, and H. Paksoy, "Review on sensible thermal energy storage for industrial solar applications and sustainability aspects," *Solar Energy*, vol. 209, pp. 135–169, Oct. 2020, ISSN: 0038-092X. DOI: 10.1016/J.SOLENER.2020.08.081. [Online]. Available: https://www.sciencedirect.com/science/article/pii/S0038092X20309208.

[42] M. M. Farid, A. M. Khudhair, S. A. K. Razack, and S. Al-Hallaj, "A review on phase change energy storage: materials and applications," *Energy Conversion and Management*, vol. 45, no. 9-10, pp. 1597–1615, Jun. 2004, ISSN: 0196-8904. DOI: 10.1016/J.ENCONMAN.2003.09.015. [Online]. Available: https://www.sciencedirect.com/science/article/pii/S0196890403002668.

[43] K. Ucler, A. Kibar, H. Metin Ertunc, and K. S. Yigit, "Investigation of a heat storage system consisting of basalt stones, water and a phase change material," *Journal of Energy Storage*, vol. 50, p. 104 196, Jun. 2022, ISSN: 2352152X. DOI: 10.1016/j.est.2022.104196.

[44] European Commission, *Electricity price statistics TEN00117*, Oct. 2021. [Online]. Available: https://ec.europa.eu/eurostat/statistics-explained/index.php?title=Electricity_price_statistics.

[45] European Commission, *Electricity prices for household consumers - bi-annual data (from 2007 onwards)*, Dec. 2024.

[46] N. Meysenburg, *How Your Conversation with ChatGPT Contributes to Climate Change*, Apr. 2024. [Online]. Available: https://www.newamerica.org/the-thread/artificial-intelligence-climate-impact/.

[47] X. Yuan, X. Zhou, Y. Pan, R. Kosonen, H. Cai, Y. Gao, and Y. Wang, "Phase change cooling in data centers: A review," *Energy and Buildings*, vol. 236, p. 110 764, Apr. 2021, ISSN: 03787788. DOI: 10.1016/j.enbuild.2021.110764.

[48] T. Moore, *How Much Does It Cost to Cool a Data Center? Optimizing Data Center Cooling Costs*, Dec. 2023. [Online]. Available: https://blog.enconnex.com/data-center-cooling-costs-and-how-to-reduce-them#:~:text=Data%20centers%20would%20need%20supplemental,and%20%242%2C000%20per%20kW%20cooled..

[49] G. Kamiya and P. Bertoldi, "Energy Consumption in Data Centres and Broadband Communication Networks in the EU," Publications Office of the European Union, Luxembourg, Tech. Rep., Feb. 2024. DOI: 10.2760/706491.

[50] B. Gomes and K. E. Brant, "Google: Environmental Report 2023," Tech. Rep., 2023.

[51] J. Salgado Beceiro and O. Galteland, *Cooling AI: How Phase Change Materials Make a Difference*, Mar. 2025. [Online]. Available: https://blog.sintef.com/energy/cooling-ai-how-phase-change-materials-make-a-difference/#:~:text=In%20these%20settings%2C%20alternative%20solutions,flexible%20in%20their%20energy%20usage..

[52] H. Selvnes, *Cartesian: Data Centres*, English, 2025. [Online]. Available: https://cartesian.no/data-centres/.

[53] B. Smith and M. Nakagawa, "2022 Enviromental Sustainability Report," Microsoft, Tech. Rep., Jun. 2022.

[54] European Commission, *Electricity prices for household consumers - bi-annual data (from 2007 onwards)*, 2023. DOI: https://doi.org/10.2908/NRG{_}PC{_}204.

[55] European Commission Directorate-General for Energy Directorate C. 2, "Executive summary: Mapping and analyses of the current and future (2020 - 2030) heating/cooling fuel deployment (fossil/renewables)," European Commission, Tech. Rep., Mar. 2016, pp. 1–15.

[56] M. Telkes, "Thermal energy storage in salt hydrates," *Solar Energy Materials*, vol. 2, no. 4, pp. 381–393, Jul. 1980, ISSN: 0165-1633. DOI: 10.1016/0165-1633(80)90033-7.

[57] F. Bruno, M. Belusko, M. Liu, and N. H. Tay, *Using solid-liquid phase change materials (PCMs) in thermal energy storage systems*. Woodhead Publishing Limited, 2015, pp. 201–246, ISBN: 9781782420965. DOI: 10.1533/9781782420965.2.201. [Online]. Available: http://dx.doi.org/10.1533/9781782420965.2.201.

[58] R. Bharathiraja, T. Ramkumar, M. Selvakumar, and N. Radhika, "Thermal characteristics enhancement of Paraffin Wax Phase Change Material (PCM) for thermal storage applications," *Renewable Energy*, vol. 222, p. 119 986, Feb. 2024, ISSN: 09601481. DOI: 10.1016/j.renene.2024.119986.

[59] H. A. Nabwey and M. A. Tony, "Enhancing the performance of paraffin's phase change material through a hybrid scheme utilizing sand core matrix," *Scientific Reports*, vol. 14, no. 1, p. 20 755, Sep. 2024, ISSN: 2045-2322. DOI: 10.1038/s41598-024-71848-8.

[60] Y. Li, Z. Fu, M. Xue, Z. Shao, Y. Li, and Q. Zhu, "Experimental study on preparation and thermal storage properties of expanded graphite/paraffin wax as a shape-stabilized phase change material," *Energy Reports*, vol. 8, pp. 324–331, Nov. 2022, ISSN: 23524847. DOI: 10.1016/j.egyr.2022.09.149.

[61] P. Moreno, L. Miró, A. Solé, C. Barreneche, C. Solé, I. Martorell, and L. F. Cabeza, "Corrosion of metal and metal alloy containers in contact with phase change materials (PCM) for potential heating and cooling applications," *Applied Energy*, vol. 125, pp. 238–245, 2014, ISSN: 03062619. DOI: 10.1016/j.apenergy.2014.03.022. [Online]. Available: http://dx.doi.org/10.1016/j.apenergy.2014.03.022.

[62] C. Hu, L. Sha, C. Huang, W. Luo, B. Li, H. Huang, C. Xu, and K. Zhang, "Phase change materials in food: Phase change temperature, environmental friendliness, and systematization," *Trends in Food Science & Technology*, vol. 140, p. 104 167, Oct. 2023, ISSN: 09242244. DOI: 10.1016/j.tifs.2023.104167.

[63] A. Lázaro García, "Nano-silica production at low temperatures from the dissolution of olivine, PhD Thesis," Ph.D. dissertation, Eindhoven University of Technology, Eindhoven, Jun. 2014, pp. 1–252, ISBN: 9789038636405.

[64] Y. E. Milián, A. Gutiérrez, M. Grágeda, and S. Ushak, *A review on encapsulation techniques for inorganic phase change materials and the influence on their thermophysical properties*, 2017. DOI: 10.1016/j.rser.2017.01.159.

[65] Mircrotek Laboratories Inc., "MICROENCAPSULATION TEMPERATURE CONTROL IS AT THE CORE OF OUR EXPERTISE," [Online]. Available: https://www.microteklabs.com/microencapsulation-solutions/.

[66] P. Gimenez-Gavarrell and S. Fereres, "Glass encapsulated phase change materials for high temperature thermal energy storage," *Renewable Energy*, vol. 107, pp. 497–507, 2017, ISSN: 18790682. DOI: 10.1016/j.renene.2017.02.005.

[67] H. Taylor, *Cement Chemistry*, 2nd ed. London: Thomas Telford, 1997, ISBN: 0727725920.

[68] B. Climent, O. Torroba, R. González-Cinca, N. Ramachandran, and M. D. Griffin, "Heat storage and electricity generation in the Moon during the lunar night," *Acta Astronautica*, vol. 93, pp. 352–358, 2014, ISSN: 00945765. DOI: 10.1016/j.actaastro.2013.07.024. [Online]. Available: http://dx.doi.org/10.1016/j.actaastro.2013.07.024.

[69] T. M. Hoefen, R. N. Clark, J. L. Bandfield, M. D. Smith, J. C. Pearl, and P. R. Christensen, "Discovery of Olivine in the Nili Fossae Region of Mars," *Science*, vol. 302, no. 5645, pp. 627–630, 2003, ISSN: 00368075. DOI: 10.1126/science.1089647.

[70] L. M. V. Martel, "Pretty Green Mineral – Pretty Dry Mars?" *Planetary Science Research Discoveries*, vol. 1, p. 7, 2003.

[71] L. Ojha, M. B. Wilhelm, S. L. Murchie, A. S. Mcewen, J. J. Wray, J. Hanley, M. Massé, and M. Chojnacki, "Spectral evidence for hydrated salts in recurring slope lineae on Mars," *Nature Geoscience*, vol. 8, no. 11, pp. 829–832, 2015, ISSN: 17520908. DOI: 10.1038/ngeo2546.

[72] "ISO 11357-1: Plastics-Differential scanning calorimetry (DSC)-Part 1: General principles," Tech. Rep., 2016.

[73] ASTM International, "E793-06 Standard Test Method for Enthalpies of Fusion and Crystallization by Differential Scanning Calorimetry 1," Tech. Rep., 2018. DOI: 10.1520/E0793-06R18. [Online]. Available: http://www.ansi.org..

[74] ASTM International, "E794-01 Standard Test Method for Melting And Crystallization Temperatures By Thermal Analysis 1," Tech. Rep., 2017. [Online]. Available: www.astm.org.

[75] ASTM International, "C1679-08 Standard Practice for Measuring Hydration Kinetics of Hydraulic Cementitious Mixtures Using Isothermal Calorimetry 1," Tech. Rep., 2009. [Online]. Available: http://api-ec.api.org..

[76] ASTM International, "C1702-09a Standard Test Method for Measurement of Heat of Hydration of Hydraulic Cementitious Materials Using Isothermal Conduction Calorimetry," Tech. Rep., 2010. DOI: 10.1520/C1702-09a. [Online]. Available: www.astm.org,.

[77] ASTM International, "C128-01 Standard Test Method for Density, Relative Density (Specific Gravity), and Absorption of Fine Aggregate," Tech. Rep., 2001. [Online]. Available: www.astm.org.

[78] British Standards Institution, "EN 196-1 Methods of testing cement Part 1: Determination of strength," Tech. Rep., 2015. [Online]. Available: www.austrian-standards.at/webshop.

[79] R. Snellings, J. Chwast, Ö. Cizer, N. De Belie, Y. Dhandapani, P. Durdzinski, J. Elsen, J. Haufe, D. Hooton, C. Patapy, M. Santhanam, K. Scrivener, D. Snoeck, L. Steger, S. Tongbo, A. Vollpracht, F. Winnefeld, and B. Lothenbach, "RILEM TC-238 SCM recommendation on hydration stoppage by solvent exchange for the study of hydrate assemblages," *Materials and Structures/Materiaux et Constructions*, vol. 51, no. 6, Dec. 2018, ISSN: 13595997. DOI: 10.1617/s11527-018-1298-5.

[80] P. Marliacy, R. Solimando, M. Bouroukba, and L. Schuffenecker, "Thermodynamics of crystallization of sodium sulfate decahydrate in H 2 O-NaCl-Na 2 SO 4 : application to Na 2 SO 4 *10H 2 O-based latent heat storage materials," *Thermochimica Acta*, no. 344, pp. 85–94, Aug. 2000.

[81] M. M. Ghafurian, B. Elmegaard, P. Weinberger, and A. Arabkoohsar, *Salt hydrates in renewable energy systems: A thorough review*, Dec. 2024. DOI: 10.1016/j.energy.2024.133808.

[82] A. Sankar Deepa and A. Tewari, "Phase transition behaviour of hydrated Glauber's salt based phase change materials and the effect of ionic salt additives: A molecular dynamics study," *Computational Materials Science*, vol. 203, Feb. 2022, ISSN: 09270256. DOI: 10.1016/j.commatsci.2021.111112.

[83] N. W. Ashcroft, *Solid State Physics*, English, D. Garbose Crane, Ed. Harcourt College Publishers, 1976, ISBN: 0-03-083993-9.

[84] L. Glasser and H. D. B. Jenkins, "Predictive thermodynamics for ionic solids and liquids," *Physical Chemistry Chemical Physics*, vol. 18, no. 31, pp. 21 226–21 240, 2016, ISSN: 14639076. DOI: 10.1039/c6cp00235h.

[85] P. W. Atkins and J. De Paula, *Atkins' Physical chemistry*. W.H. Freeman, 2006, p. 1053, ISBN: 0716787598.

[86] W. D. Callister and D. G. Rethwisch, *Materials science and engineering : an introduction*. Wiley, 2014, p. 960, ISBN: 1118324579.

[87] A. F. Wells, *Structural Inorganic Chemistry 4th Edition*, 4th ed. London: Oxford University Press, 1975, ISBN: 0-19-855354-4.

[88] H.-H. Emons, "Structure and properties of molten salt hydrates," *Electrochimica Acta*, vol. 33, no. 9, pp. 1243–1250, Sep. 1988, ISSN: 00134686. DOI: 10.1016/0013-4686(88)80155-5.

[89] W. Voigt and D. Zeng, "Solid-liquid equilibria in mixtures of molten salt hydrates for the design of heat storage materials," in *Pure and Applied Chemistry*, vol. 74, Walter de Gruyter GmbH, Oct. 2002, pp. 1909–1920. DOI: 10.1351/pac200274101909.

[90] F. A. Caporuscio, H. Boukhalfa, M. C. Cheshire, A. B. Jordan, and M. Ding, "BRINE MIGRATION EXPERIMENTAL STUDIES FOR SALT REPOSITORIES," English, Los Alamos National Laboratory, Los Alamos, Tech. Rep., Sep. 2013, pp. 1–102.

[91] A. U. Rehman, Z. Maosheng, and A. Hayat, "Hydration performance and cycling stability of three TCM: MgSO4, ZnSO4 and FeSO4," *International Journal of Energy Research*, vol. 44, no. 8, pp. 6981–6990, Jun. 2020, ISSN: 1099114X. DOI: 10.1002/er.5470.

[92] R. J. Clark, G. Gholamibozanjani, J. Woods, S. Kaur, A. Odukomaiya, S. Al-Hallaj, and M. Farid, "Experimental screening of salt hydrates for thermochemical energy storage for building heating application," *Journal of Energy Storage*, vol. 51, Jul. 2022, ISSN: 2352152X. DOI: 10.1016/j.est.2022.104415.

[93] K. Heijmans, "Thermochemical storage materials: advances in molecular modeling and applications.," Ph.D. dissertation, Eindhoven University of Technology, Eindhoven, Dec. 2021, pp. 1–311, ISBN: 978-90-386-5415-7. [Online]. Available: www.tue.nl/taverne.

[94] M. Steiger, K. Linnow, H. Juling, G. Gülker, A. El Jarad, S. Brüggerhoff, and D. Kirchner, "Hydration of MgSO4 · H2O and generation of stress in porous materials," *Crystal Growth and Design*, vol. 8, no. 1, pp. 336–343, Jan. 2008, ISSN: 15287483. DOI: 10.1021/cg060688c.

[95] S. Katyal, "Experimental study of salt hydrates for thermochemical seasonal heat storage," Ph.D. dissertation, Eindhoven Technical University, 2020, ISBN: 9789038640532.

[96] S. J. Chipera and D. T. Vaniman, "Experimental stability of magnesium sulfate hydrates that may be present on Mars," *Geochimica et Cosmochimica Acta*, vol. 71, no. 1, pp. 241–250, 2007, ISSN: 00167037. DOI: 10.1016/j.gca.2006.07.044.

[97] R. Peterson, W. Nelson, B. Madu, and H. Shurvell, "Meridianiite: A new mineral species observed on Earth and predicted to exist on Mars," *American Mineralogist*, vol. 92, no. 10, pp. 1756–1759, Oct. 2007, ISSN: 0003-004X. DOI: 10.2138/am.2007.2668.

[98] D. T. Vaniman and S. J. Chipera, "Transformations of Mg- And Ca-sulfate hydrates in Mars regolith," *American Mineralogist*, vol. 91, no. 10, pp. 1628–1642, 2006, ISSN: 0003004X. DOI: 10.2138/am.2006.2092.

[99] The Editors of Encyclopaedia Britannica, *melting*, Dec. 2024. [Online]. Available: https://www.britannica.com/science/melting.

[100] U. Müller, *Inorganic Structural Chemistry*. Wiley, Oct. 2006, ISBN: 9780470018644. DOI: 10.1002/9780470057278.

[101] B. E. Douglas and S.-M. Ho, *Structure and Chemistry of Crystalline Solids*. New York, NY: Springer New York, 2006, ISBN: 978-0-387-26147-8. DOI: 10.1007/0-387-36687-3.

[102] L. C. Sögütoglu, M. Steiger, J. Houben, D. Biemans, H. R. Fischer, P. Donkers, H. Huinink, and O. C. Adan, "Understanding the Hydration Process of Salts: The Impact of a Nucleation Barrier," *Crystal Growth and Design*, vol. 19, no. 4, pp. 2279–2288, Apr. 2019, ISSN: 15287505. DOI: 10.1021/acs.cgd.8b01908.

[103] C. Desgranges and J. Delhommelle, "Deciphering the complexities of crystalline state(s) with molecular simulations," *Communications Chemistry*, vol. 8, no. 1, p. 281, Sep. 2025, ISSN: 2399-3669. DOI: 10.1038/s42004-025-01667-z.

[104] S. Mahajan and Y. Li, "Toward Molecular Simulation Guided Design of Next-Generation Membranes: Challenges and Opportunities," *Langmuir*, vol. 41, no. 20, pp. 12 388–12 402, May 2025, ISSN: 0743-7463. DOI: 10.1021/acs.langmuir.4c05181.

[105] C. Fang, X. Lu, W. Buijs, Z. Fan, F. E. Genceli Güner, M. A. van Huis, G. J. Witkamp, and T. J. Vlugt, "Crystal structure, stability, and electronic properties of hydrated metal sulfates MSO4(H2O)n (M=Ni, Mg; n=6, 7) and their mixed phases: A first principles study," *Chemical Engineering Science*, vol. 121, pp. 77–86, 2015, ISSN: 00092509. DOI: 10.1016/j.ces.2014.07.026. [Online]. Available: http://dx.doi.org/10.1016/j.ces.2014.07.026.

[106] S. A. Albdour, Z. Haddad, O. Z. Sharaf, A. Alazzam, and E. Abu-Nada, *Micro/nano-encapsulated phase-change materials (ePCMs) for solar photothermal absorption and storage: Fundamentals, recent advances, and future directions*, Nov. 2022. DOI: 10.1016/j.pecs.2022.101037.

[107] W. Samah, P. Clain, F. Rioual, L. Fournaison, and A. Delahaye, *Review on ice crystallization and adhesion to optimize ice slurry generators without moving components*, Mar. 2023. DOI: 10.1016/j.applthermaleng.2023.119974.

[108] M. H. Zahir, S. A. Mohamed, R. Saidur, and F. A. Al-Sulaiman, "Supercooling of phase-change materials and the techniques used to mitigate the phenomenon," *Applied Energy*, vol. 240, pp. 793–817, Apr. 2019, ISSN: 03062619. DOI: 10.1016/j.apenergy.2019.02.045.

[109] B. Hribar, N. T. Southall, V. Vlachy, and K. A. Dill, "How ions affect the structure of water," *Journal of the American Chemical Society*, vol. 124, no. 41, pp. 12 302–12 311, Oct. 2002, ISSN: 00027863. DOI: 10.1021/ja026014h.

[110] A. Casimiro, "Simply complex: discerning specific ion effects for soft materials," Ph.D. dissertation, Eindhoven University of Technology, Eindhoven, Feb. 2023, pp. 1–149, ISBN: 978-90-386-5645-8. [Online]. Available: www.tue.nl/taverne.

[111] U. T. Huynh, A. Lerbret, F. Neiers, O. Chambin, and A. Assifaoui, "Binding of Divalent Cations to Polygalacturonate: A Mechanism Driven by the Hydration Water," *Journal of Physical Chemistry B*, vol. 120, no. 5, pp. 1021–1032, Feb. 2016, ISSN: 15205207. DOI: 10.1021/acs.jpcb.5b11010.

[112] D. R. Lide, *CRC Handbook of Chemistry and Physics*, 85th ed. CRC Press, 2004, vol. 85, pp. 1–2712.

[113] E. R. Segnit, T. J. Stevens, and J. B. Jones, "The role of water in opal," *Journal of the Geological Society of Australia*, vol. 12, no. 2, pp. 211–226, Jan. 2007, ISSN: 0016-7614. DOI: 10.1080/00167616508728593. [Online]. Available: http://www.tandfonline.com/doi/abs/10.1080/00167616508728593.

[114] D. S. Banerjee, "Direct Calculation Of Madelung Constant Processes Used to Calculate Madelung Constant : Madelung Constant in One Dimension : Madelung Constant in Two dimensions : Madelung constant for three dimensions : Summery and Conclusion : Main FORTRAN codes used in," 2012.

[115] A. D. Baker and M. D. Baker, "Rapid calculation of individual ion Madelung constants and their convergence to bulk values," *American Journal of Physics*, vol. 78, no. 1, pp. 102–105, 2010, ISSN: 0002-9505. DOI: 10.1119/1.3243281.

[116] T. Berry, N. Ng, and T. M. McQueen, "Single Crystal Growth Tricks and Treats," English, *arXiv*, Sep. 2022. [Online]. Available: http://arxiv.org/abs/2209.09370.

[117] X. Wang and Y. Zhou, "Research on Single Crystal Preparation via Dynamic Liquid Phase Method," *Crystals*, vol. 13, no. 7, p. 1150, Jul. 2023, ISSN: 2073-4352. DOI: 10.3390/cryst13071150.

[118] J. Kosny, N. Shukla, and A. Fallahi, "Cost Analysis of Simple Phase Change Material-Enhanced Building Envelopes in Southern U.S. Climates," Tech. Rep., 2013. [Online]. Available: http://www.osti.gov/bridge.

[119] S. Zhang, X. Li, Y. Sun, J. Zeng, S. Zhu, W. Song, Y. Zhou, X. Ren, C. Hai, and Y. Shen, "Low-cost magnesium-based eutectic salt hydrate phase change material with enhanced thermal performance for energy storage," *Solar Energy Materials and Solar Cells*, vol. 238, p. 111 620, May 2022, ISSN: 09270248. DOI: 10.1016/j.solmat.2022.111620.

[120] B. Kalidasan, A. K. Pandey, R. Saidur, M. Samykano, and V. V. Tyagi, "Nano additive enhanced salt hydrate phase change materials for thermal energy storage," *International Materials Reviews*, vol. 68, no. 2, pp. 140–183, Feb. 2023, ISSN: 0950-6608. DOI: 10.1080/09506608.2022.2053774.

[121] D. S. Schmool, *Solid State Physics*. Mercury Learning and Information, 2014, p. 590, ISBN: 978-1-942270-77-5.

[122] H. P. Huinink, S. Sansotta, and D. Zahn, "Defect-driven water migration in MgCl2 tetra- and hexahydrates," *Journal of Solid State Chemistry*, vol. 277, pp. 221–228, Sep. 2019, ISSN: 00224596. DOI: 10.1016/j.jssc.2019.06.010.

[123] C. Rathgeber, H. Schmit, S. Hiebler, and P. Hoock, "Development of Phase Change Materials Based on Mixtures of Salt Hydrates Through Theoretical Prediction and Experimental Investigation," Tech. Rep., 2021.

[124] T. Barz, A. Bres, and J. Emhofer, "slPCMlib: A Modelica Library for the Prediction of Effective Thermal Material Properties of Solid/Liquid Phase Change Materials (PCM)," in *Proceedings of Asian Modelica Conference 2022, Tokyo, Japan, November 24-25, 2022*, vol. 193, Linköping University Electronic Press, Nov. 2022, pp. 63–74. DOI: 10.3384/ecp19363.

[125] W. Voigt, "Chemical Monthly Calculation of Salt Activities in Molten Salt Hydrates Applying the Modified BET Equation, h Binary Systems*," Tech. Rep., 1993, pp. 839–848.

[126] N. Mazur, "Boosting power of salt hydrates for heat storage," Ph.D. dissertation, Eindhoven University of Technology, Eindhoven, Jan. 2023, pp. 1–261, ISBN: 978-90-386-5648-9.

[127] O. Okogeri and V. N. Stathopoulos, *What about greener phase change materials? A review on biobased phase change materials for thermal energy storage applications*, May 2021. DOI: 10.1016/j.ijft.2021.100081.

[128] BePe, "Transitional Mining of Lithium in the High Andeans Lakes of Catamarca (In Spanish)," Tech. Rep., Oct. 2019, pp. 1–50.

[129] G. O. Ocholla, M. M. Bunyasi, G. W. Asoka, O. Pacha, H. K. Mbugua, P. Mbuthi, S. Mbiti, H. K. Wendo, and P. K. Kamau, "Environmental Issues and Socio-economic Problems Emanating from Salt Mining in Kenya; A Case Study of Magarini District," Tech. Rep. 3, 2013. [Online]. Available: www.ijhssnet.com.

[130] B. Cárdenas and N. León, *High temperature latent heat thermal energy storage: Phase change materials, design considerations and performance enhancement techniques*, 2013. DOI: 10.1016/j.rser.2013.07.028.

[131] H. Nazir, M. Batool, F. J. Bolivar, M. Isaza-ruiz, X. Xu, K. Vignarooban, P. Phelan, and A. M. Kannan, "Recent developments in phase change materials for energy storage applications : A review," *International Journal of Heat and Mass Transfer*, vol. 129, pp. 491–523, 2019, ISSN: 0017-9310. DOI: 10.1016/j.ijheatmasstransfer.2018.09.126. [Online]. Available: https://doi.org/10.1016/j.ijheatmasstransfer.2018.09.126.

[132] X. Wang, W. Li, Z. Luo, K. Wang, and S. P. Shah, *A critical review on phase change materials (PCM) for sustainable and energy efficient building: Design, characteristic, performance and application*, Apr. 2022. DOI: 10.1016/j.enbuild.2022.111923.

[133] V. M. van Essen, H. a. Zondag, R. Schuitema, W. G. J. van Helden, C. C. M. Rindt, V. M. V. Essen, H. a. Zondag, R. Schuitema, W. G. J. V. Helden, and C. C. M. Rindt, "Materials for thermochemical storage : characterization of magnesium sulfate," *Proceedings Eurosun*, no. October, pp. 4–9, 2008.

[134] A. U. Rehman, A. Hayat, A. Munis, T. Zhao, M. Israr, and M. Zheng, "Characterisation of magnesium, zinc and iron sulfates for thermochemical storage," *Proceedings of Institution of Civil Engineers: Energy*, vol. 173, no. 2, pp. 60–67, May 2020, ISSN: 17514231. DOI: 10.1680/jener.19.00018.

[135] N. Xie, J. Luo, Z. Li, Z. Huang, X. Gao, Y. Fang, and Z. Zhang, "Salt hydrate/expanded vermiculite composite as a form-stable phase change material for building energy storage," *Solar Energy Materials and Solar Cells*, vol. 189, pp. 33–42, Jan. 2019, ISSN: 09270248. DOI: 10.1016/j.solmat.2018.09.016.

[136] S. Gulati, Z. Tabassum, U. Schwingenschlogl, and E. Iype, "Molecular dynamics simulation of dehydration of salt hydrates (MgSO4 · 7H2O and ZnSO4 · 7H2O)," in *Materials Today: Proceedings*, vol. 28, Elsevier Ltd, 2019, pp. 1013–1017. DOI: 10.1016/j.matpr.2019.12.341.

[137] V. M. Gurevich, O. L. Kuskov, K. S. Gavrichev, and A. V. Tyurin, "Heat capacity and thermodynamic functions of epsomite MgSO4 · 7 H2O at 0-303 K," *Geochemistry International*, vol. 45, no. 2, pp. 206–209, Feb. 2007, ISSN: 00167029. DOI: 10.1134/S0016702907020103.

[138] M. Scheidema, "The reaction mechanism and operating window for the decomposition of hydrated magnesium sulfate under reducing conditions," Ph.D. dissertation, Aalto University, Helsinki, Oct. 2015, pp. 1–143, ISBN: 978-952-60-6347-8. [Online]. Available: www.aalto.fi.

[139] J. D. Harris and A. W. Rusch, "Identifying hydrated salts using simultaneous thermogravimetric analysis and differential scanning calorimetry," *Journal of Chemical Education*, vol. 90, no. 2, pp. 235–238, 2013, ISSN: 00219584. DOI: 10.1021/ed300222y.

[140] SUEZ Water Technologies & Solutions, *Handbook of Industrial Water Treatment, External Treatment, Chapter 04 - Aeration*, Nov. 2021. [Online]. Available: https://www.suezwatertechnologies.com/handbook/chapter-04-aeration.

[141] K. Schollbach, "Recycling waste solution from olivine nano-silica production," 2014.

[142] J. Denson, V. Chevrier, D. Sears, and D. M. Ivey, "Sulfate Reduction: A Model for Subsurface Martian Life Experimental and Modeling Investigation of the Diurnal Water Vapor Dynamics in Subsurface Martian Environments View project Sulfate Reduction: A Model for Subsurface Martian Life," Tech. Rep., 2007. [Online]. Available: http://rdcu.be/vzSGViewproject.

[143] D. Peak, R. G. Ford, and D. L. Sparks, "An in Situ ATR-FTIR Investigation of Sulfate Bonding Mechanisms on Goethite," *Journal Of Colloidal and Interface Science*, vol. 218, pp. 289–299, 1999. [Online]. Available: http://www.sciencedirect.com/science/article/pii/B9780123822192002490.

[144] D. Talla and M. Wildner, "Investigation of the kieserite-szomolnokite solid-solution series, (Mg,Fe)SO4 · HO, with relevance to Mars: Crystal chemistry, FTIR, and Raman spectroscopy under ambient and martian temperature conditions," *American Mineralogist*, vol. 104, no. 12, pp. 1732–1749, 2019, ISSN: 19453027. DOI: 10.2138/am-2019-6983.

[145] D. L. Bish, P. Sarrazin, D. Blake, D. Vaniman, and S. Chipera, "Sulfate Mineral Analysis by the CheMin XRD/XRF Instrument on MSL," Tech. Rep., 2006, p. 1.

[146] H. Ma, D. L. Bish, H. W. Wang, and S. J. Chipera, "Structure determination of the 2.5 hydrate MgSO4 phase by simulated annealing," *American Mineralogist*, vol. 94, no. 7, pp. 1071–1074, 2009, ISSN: 0003004X. DOI: 10.2138/am.2009.3221.

[147] A. Wang, J. J. Freeman, and B. L. Jolliff, "Phase transition pathways of the hydrates of magnesium sulfate in the temperature range 50°C to 5°C: Implication for sulfates on mars," *Journal of Geophysical Research E: Planets*, vol. 114, no. 4, Apr. 2009, ISSN: 01480227. DOI: 10.1029/2008JE003266.

[148] F. C. Hawthorne, L. A. Groat, and M. Raudsepp, "Kieserite, MgSO4(H2O), a Titanite-Group Mineral," *Neues Jahrbuch für Mineralogie*, 1987. [Online]. Available: https://www.researchgate.net/publication/270759690.

[149] C. S. Jamieson, E. Z. Noe Dobrea, J. B. Dalton, K. M. Pitman, and W. J. Abbey, "The spectral variability of kieserite (MgSO4 · H 2O) with temperature and grain size and its application to the Martian surface," *Journal of Geophysical Research E: Planets*, vol. 119, no. 6, pp. 1218–1237, 2014, ISSN: 21699100. DOI: 10.1002/2013JE004489.

[150] H. Zhang, E. Iype, S. V. Nedea, and C. C. Rindt, "Molecular dynamics study on thermal dehydration process of epsomite (MgSO4 · 7H2O)," *Molecular Simulation*, vol. 40, no. 14, pp. 1157–1166, Nov. 2014, ISSN: 10290435. DOI: 10.1080/08927022.2013.854891.

[151] N. Kanari, N. E. Menad, E. Ostrosi, S. Shallari, F. Diot, E. Allain, and J. Yvon, "Thermal behavior of hydrated iron sulfate in various atmospheres," *Metals*, vol. 8, no. 12, Dec. 2018, ISSN: 20754701. DOI: 10.3390/met8121084.

[152] E. Tomaszewicz and M. Kotfica, "Mechanism and Kinetics of Thermal Decomposition of Nickel(II) Sulfate(VI) Hexahydrate," *Journal of Thermal Analysis and Calorimetry*, vol. 77, pp. 25–31, 2004.

[153] M. Földvári, *Handbook of thermogravimetric system of minerals and its use in geological practice*. Budapest: Geological Institute of Hungary, 2011, vol. 213, ISBN: 978-963-671-288-4.

[154] L. Bai, X. Zhao, R. Y. Bao, Z. Y. Liu, M. B. Yang, and W. Yang, "Effect of temperature, crystallinity and molecular chain orientation on the thermal conductivity of polymers: a case study of PLLA," *Journal of Materials Science*, vol. 53, no. 14, pp. 10 543–10 553, Jul. 2018, ISSN: 15734803. DOI: 10.1007/s10853-018-2306-4.

[155] T. Honorio, B. Bary, and F. Benboudjema, "Thermal properties of cement-based materials: Multiscale estimations at early-age," *Cement and Concrete Composites*, vol. 87, pp. 205–219, Mar. 2018, ISSN: 09589465. DOI: 10.1016/j.cemconcomp.2018.01.003.

[156] K. S. Karunadasa, C. H. Manoratne, H. M. Pitawala, and R. M. Rajapakse, "Thermal decomposition of calcium carbonate (calcite polymorph) as examined by in-situ high-temperature X-ray powder diffraction," *Journal of Physics and Chemistry of Solids*, vol. 134, pp. 21–28, Nov. 2019, ISSN: 00223697. DOI: 10.1016/j.jpcs.2019.05.023.

[157] A. Safari, R. Saidur, F. A. Sulaiman, Y. Xu, and J. Dong, "A review on supercooling of Phase Change Materials in thermal energy storage systems," *Renewable and Sustainable Energy Reviews*, vol. 70, no. November 2016, pp. 905–919, 2017, ISSN: 18790690. DOI: 10.1016/j.rser.2016.11.272. [Online]. Available: http://dx.doi.org/10.1016/j.rser.2016.11.272.

[158] B. K. Purohit and V. S. Sistla, "Inorganic salt hydrate for thermal energy storage application: A review," *Energy Storage*, vol. 3, no. 2, Apr. 2021, ISSN: 2578-4862. DOI: 10.1002/est2.212.

[159] K. K. Alaneme and E. A. Okotete, *Recrystallization mechanisms and microstructure development in emerging metallic materials: A review*, Mar. 2019. DOI: 10.1016/j.jsamd.2018.12.007.

[160] Netzsch, *Post Crystallization (Cold Crystallization)*. [Online]. Available: https://analyzing-testing.netzsch.com/en/training-know-how/glossary/post-crystallization-cold-crystallization.

[161] H. Yang, C. Wang, L. Tong, S. Yin, L. Wang, and Y. Ding, "Salt Hydrate Adsorption Material-Based Thermochemical Energy Storage for Space Heating Application: A Review," *Energies*, vol. 16, no. 6, Mar. 2023, ISSN: 19961073. DOI: 10.3390/en16062875.

[162] L. Glasser, "Thermodynamics of inorganic hydration and of humidity control, with an extensive database of salt hydrate pairs," *Journal of Chemical and Engineering Data*, vol. 59, no. 2, pp. 526–530, 2014, ISSN: 00219568. DOI: 10.1021/je401077x.

[163] L. Luo, N. L. Pierre, and C. Outline, *Innovative Systems for Storage of Thermal Solar Energy in Buildings*. 2015, ISBN: 9780124095403. DOI: 10.1016/B978-0-12-409540-3.00003-7.

[164] B. C. Zhao and R. Z. Wang, "Perspectives for short-term thermal energy storage using salt hydrates for building heating," *Energy*, vol. 189, Dec. 2019, ISSN: 03605442. DOI: 10.1016/j.energy.2019.116139.

[165] J. Lizana, R. Chacartegui, A. Barrios-Padura, J. M. Valverde, and C. Ortiz, *Identification of best available thermal energy storage compounds for low-to-moderate temperature storage applications in buildings*, Jul. 2018. DOI: 10.3989/mc.2018.10517.

[166] P. Gadhave, F. Pathan, S. Kore, and C. Prabhune, "Comprehensive review of phase change material based latent heat thermal energy storage system," *International Journal of Ambient Energy*, vol. 43, no. 1, pp. 4181–4206, 2022, ISSN: 21628246. DOI: 10.1080/01430750.2021.1873848.

[167] A. M. Ramos Archibold, "Thermal Assessment of a Latent-Heat Energy Storage Module During Melting and Freezing for Solar Energy Applications," Ph.D. dissertation, University of South Florida, Tampa, Nov. 2014, pp. 1–107. [Online]. Available: https://digitalcommons.usf.edu/etd.

[168] S. Dutt Sharma, H. Kitano, and K. Sagara, "Phase Change Materials for Low Temperature Solar Thermal Applications," *Res. Rep. Fac. Eng. Mie Univ*, vol. 29, pp. 31–64, 2004.

[169] L. Yang, X. Jin, Y. Zhang, and K. Du, *Recent development on heat transfer and various applications of phase-change materials*, Mar. 2021. DOI: 10.1016/j.jclepro.2020.124432.

[170] C. Adkins, "Change of phase," in *Equilibrium Thermodynamics*, Cambridge University Press, Jul. 1983, pp. 180–212, ISBN: 9781139167703. DOI: 10.1017/CBO9781139167703.011. [Online]. Available: https://www.cambridge.org/core/product/identifier/CBO9781139167703A079/type/book_part.

[171] B. Duraković, M. Halilović, and H. M. Ali, "Phase change materials applications in buildings," in *Phase Change Materials for Heat Transfer*, Elsevier, 2023, pp. 225–248. DOI: 10.1016/B978-0-323-91905-0.00005-8. [Online]. Available: https://linkinghub.elsevier.com/retrieve/pii/B9780323919050000058.

[172] M. K. Rathod, J. R. Patel, and H. M. Ali, "Battery thermal management using phase change material," in *Phase Change Materials for Heat Transfer*, Elsevier, 2023, pp. 181–224. DOI: 10.1016/B978-0-323-91905-0.00008-3. [Online]. Available: https://linkinghub.elsevier.com/retrieve/pii/B9780323919050000083.

[173] R. A. Kuntze, "Phase Change and their Basic Properties," *Gypsum: Connecting Science and Technology*, pp. 23–23, 2010. DOI: 10.1520/mnl11584m.

[174] S. Sikiru, T. L. Oladosu, T. I. Amosa, S. Y. Kolawole, and H. Soleimani, "Recent advances and impact of phase change materials on solar energy: A comprehensive review," *Journal of Energy Storage*, vol. 53, Sep. 2022, ISSN: 2352152X. DOI: 10.1016/j.est.2022.105200.

[175] S. Ali and S. P. Deshmukh, "An overview: Applications of thermal energy storage using phase change materials," in *Materials Today: Proceedings*, vol. 26, Elsevier Ltd, 2019, pp. 1231–1237. DOI: 10.1016/j.matpr.2020.02.247.

[176] J. C. Kurnia, L. A. Haryoko, I. Taufiqurrahman, L. Chen, L. Jiang, and A. P. Sasmito, "Optimization of an innovative hybrid thermal energy storage with phase change material (PCM) wall insulator utilizing Taguchi method," *Journal of Energy Storage*, vol. 49, May 2022, ISSN: 2352152X. DOI: 10.1016/j.est.2022.104067.

[177] N. Kumar, J. Hirschey, T. J. LaClair, K. R. Gluesenkamp, and S. Graham, *Review of stability and thermal conductivity enhancements for salt hydrates*, Aug. 2019. DOI: 10.1016/j.est.2019.100794.

[178] J. Braunstein, "Thermodynamic Properties and Interactions of Salt Hydrates used as Phase Changed Materials," Oak Ridge National Laboratory, Oak Ridge, Tech. Rep., 1989, pp. 1–6.

[179] S. Furbo, "HEAT STORAGE WITH AN INCONGRUENTLY MELTING SALT HYDRATE AS STORAGE MEDIUM BASED ON THE EXTRA WATER PRINCIPLE," English, Technical University of Denmark, Tech. Rep., Dec. 1980, pp. 1–21.

[180] M. A. Bashir and A. Giovannelli, "Phase change materials (PCMs) applications in solar energy systems," in *Phase Change Materials for Heat Transfer*, Elsevier, 2023, pp. 129–153. DOI: 10.1016/B978-0-323-91905-0.00004-6. [Online]. Available: https://linkinghub.elsevier.com/retrieve/pii/B9780323919050000046.

[181] D. Lu, X. Xu, X. Zhang, W. Xie, and Y. Gao, "Study on Influencing Factors of Phase Transition Hysteresis in the Phase Change Energy Storage," *Materials*, vol. 15, no. 8, Apr. 2022, ISSN: 19961944. DOI: 10.3390/ma15082775.

[182] J. Thakkar, N. Bowen, A. C. Chang, P. Horwath, M. J. Sobkowicz, and J. Kośny, "Optimization of Preparation Method, Nucleating Agent, and Stabilizers for Synthesizing Calcium Chloride Hexahydrate (CaCl2.6H2O) Phase Change Material," *Buildings*, vol. 12, no. 10, Oct. 2022, ISSN: 20755309. DOI: 10.3390/buildings12101762.

[183] P. Tan, P. Lindberg, K. Eichler, P. Löveryd, P. Johansson, and A. S. Kalagasidis, "Effect of phase separation and supercooling on the storage capacity in a commercial latent heat thermal energy storage: Experimental cycling of a salt hydrate PCM," *Journal of Energy Storage*, vol. 29, Jun. 2020, ISSN: 2352152X. DOI: 10.1016/j.est.2020.101266.

[184] H. W. Ryu, S. W. Woo, B. C. Shin, and S. D. Kim, "Prevention of supercooling and stabilization of inorganic salt hydrates as latent heat storage materials," Tech. Rep., 1992, pp. 161–172.

[185] G. Wypych, *Handbook of Nucleating Agents*, 2nd. Ontario: ChemTec Publisher, 2021, pp. i–279, ISBN: 978-1-927885-81-9.

[186] Y. Zhang, X. Zhang, X. Xu, and M. Lu, "Derivation of thermal properties of phase change materials based on T-history method," *Journal of Energy Storage*, vol. 27, Feb. 2020, ISSN: 2352152X. DOI: 10.1016/j.est.2019.101062.

[187] M. Marion and J. S. Kargel, "STABILITY OF MAGNESIUM SULFATE MINERALS IN MARTIAN ENVIRONMENTS. G," Tech. Rep., 2005.

[188] C. Wesemann, K. Schollbach, and H. Brouwers, "Phase change behavior of sulfate salt hydrates extracted from olivine nano-silica side stream," *Journal of Energy Storage*, vol. 80, p. 110 730, Mar. 2024, ISSN: 2352152X. DOI: 10.1016/j.est.2024.110730. [Online]. Available: https://linkinghub.elsevier.com/retrieve/pii/S2352152X24003141.

[189] R. Sinaga, J. Darkwa, M. Worall, and W. Su, "The effect of nucleating agent on the multiphase change materials for energy storage in buildings," *Applied Thermal Engineering*, vol. 239, Feb. 2024, ISSN: 13594311. DOI: 10.1016/j.applthermaleng.2023.122153.

[190] A. Lazaro, H. J. Brouwers, G. Quercia, and J. W. Geus, "The properties of amorphous nano-silica synthesized by the dissolution of olivine," *Chemical Engineering Journal*, vol. 211-212, pp. 112–121, Nov. 2012, ISSN: 13858947. DOI: 10.1016/j.cej.2012.09.042.

[191] A. Lazaro, L. Benac-Vegas, H. J. Brouwers, J. W. Geus, and J. Bastida, "The kinetics of the olivine dissolution under the extreme conditions of nano-silica production," *Applied Geochemistry*, vol. 52, pp. 1–15, Jan. 2015, ISSN: 18729134. DOI: 10.1016/j.apgeochem.2014.10.015.

[192] K. Ishino, H. Shingai, Y. Hikita, I. Yoshikawa, H. Houjou, and K. Iwase, "Cold Crystallization and the Molecular Structure of Imidazolium-Based Ionic Liquid Crystals with a p -Nitroazobenzene Moiety," *ACS Omega*, vol. 6, no. 48, pp. 32 869–32 878, Dec. 2021, ISSN: 2470-1343. DOI: 10.1021/acsomega.1c04866.

[193] M. S. Rahman, M. S. Hasan, A. S. Nitai, S. Nam, A. K. Karmakar, M. S. Ahsan, M. J. Shiddiky, and M. B. Ahmed, *Recent developments of carboxymethyl cellulose*, Apr. 2021. DOI: 10.3390/polym13081345.

[194] G. Feng, X. Xu, N. He, H. Li, and K. Huang, "Testing research of energy storage system during Na2SO4 · 10H2O phase change," in *Materials Research Innovations*, vol. 19, Maney Publishing, May 2015, S5972–S5977. DOI: 10.1179/1432891714Z.0000000001232.

[195] A. Palacios, M. E. Navarro, C. Barreneche, and Y. Ding, "Hybridization of Salt Hydrates with Solid–Solid Phase Change Materials: A Novel Pathway to Sorption Thermochemical Materials Manufacturing," *Advanced Sustainable Systems*, vol. 7, no. 7, Jul. 2023, ISSN: 23667486. DOI: 10.1002/adsu.202200184.

[196] W. Voigt, "Chemistry of salts in aqueous solutions: Applications, experiments, and theory," *Pure and Applied Chemistry*, vol. 83, no. 5, pp. 1015–1030, 2011, ISSN: 00334545. DOI: 10.1351/PAC-CON-11-01-07.

[197] F. Fasulo, G. M. Piccini, A. B. Muñoz-García, M. Pavone, and M. Parrinello, "Dynamics of Water Dissociative Adsorption on TiO2 Anatase (101) at Monolayer Coverage and Below," *Journal of Physical Chemistry C*, 2022, ISSN: 19327455. DOI: 10.1021/acs.jpcc.2c03077.

[198] H. Zondag, M. Van Essen, Z. He, R. Schuitema, and W. Van Helden, "CHARACTERISATION OF MgSO 4 FOR THERMOCHEMICAL STORAGE," TNO, Petten, Tech. Rep., 2008, pp. 1–6.

[199] H. R. Lemoine, A. B. Paxton, S. C. Anisfeld, R. C. Rosemond, and C. H. Peterson, "Selecting the optimal artificial reefs to achieve fish habitat enhancement goals," *Biological Conservation*, vol. 238, p. 108 200, Oct. 2019, ISSN: 00063207. DOI: 10.1016/j.biocon.2019.108200.

[200] W. B. Gladfelter, "White-band Disease in Acropora Palmata: Implications for the Structure and Growth of Shallow Reefs," *Bulletin of Marine Science*, vol. 32, no. 2, pp. 639–643, Apr. 1982.

[201] R. B. Aronson and W. F. Precht, "White-band disease and the changing face of Caribbean coral reefs," in *The Ecology and Etiology of Newly Emerging Marine Diseases*, Dordrecht: Springer Netherlands, 2001, pp. 25–38. DOI: 10.1007/978-94-017-3284-0{_}2.

[202] J. Jackson, M. Donovan, K. Cramer, and V. Lam, "Status and Trends of Caribbean Coral Reefs: 1970-2012," Global Coral Reef Monitoring Network, IUCN, Gland, Tech. Rep., 2014, pp. 1–306.

[203] L. Carral, C. Camba Fabal, M. I. Lamas Galdo, M. J. Rodríguez-Guerreiro, and J. J. Cartelle Barros, "Assessment of the Materials Employed in Green Artificial Reefs for the Galician Estuaries in Terms of Circular Economy," *International Journal of Environmental Research and Public Health*, vol. 17, no. 23, p. 8850, Nov. 2020, ISSN: 1660-4601. DOI: 10.3390/ijerph17238850.

[204] L. Burke, K. Reytar, M. Spalding, and A. Perry, "Reefs at Risk," World Resources Institute, Washington, Tech. Rep., 2011, pp. 1–130. [Online]. Available: www.wri.org.

[205] L. Firth, A. M. Knights, D. Bridger, A. Evans, N. Mieszkowska, P. J. Moore, N. E. O'Connor, E. V. Sheehan, R. C. Thompson, and S. J. Hawkins, "Ocean sprawl: challenges and opportunities for biodiversity management in a changing world," *Oceanography and Marine Biology: An Annual Review*, vol. 54, pp. 193–269, 2016. [Online]. Available: https://www.researchgate.net/publication/310462801.

[206] A. E. Bates, R. D. Stuart-Smith, N. S. Barrett, and G. J. Edgar, "Biological interactions both facilitate and resist climate-related functional change in temperate reef communities," *Proceedings of the Royal Society B: Biological Sciences*, vol. 284, no. 1856, Jun. 2017, ISSN: 14712954. DOI: 10.1098/rspb.2017.0484.

[207] D. R. Bellwood, T. P. Hughes, C. Folke, and M. Nyström, "Confronting the coral reef crisis," *Nature*, vol. 429, pp. 827–833, Jun. 2004. [Online]. Available: www.nature.com/nature.

[208] A. Hylkema, Q. C. Hakkaart, C. B. Reid, R. Osinga, A. J. Murk, and A. O. Debrot, "Artificial reefs in the Caribbean: A need for comprehensive monitoring and integration into marine management plans," *Ocean & Coastal Management*, vol. 209, p. 105 672, Aug. 2021, ISSN: 09645691. DOI: 10.1016/j.ocecoaman.2021.105672.

[209] X. Huang, Z. Wang, Y. Liu, W. Hu, and W. Ni, "On the use of blast furnace slag and steel slag in the preparation of green artificial reef concrete," *Construction and Building Materials*, vol. 112, pp. 241–246, Jun. 2016, ISSN: 09500618. DOI: 10.1016/j.conbuildmat.2016.02.088.

[210] S. G. Sutton and S. L. Bushnell, "Socio-economic aspects of artificial reefs: Considerations for the Great Barrier Reef Marine Park," *Ocean & Coastal Management*, vol. 50, no. 10, pp. 829–846, Jan. 2007, ISSN: 09645691. DOI: 10.1016/j.ocecoaman.2007.01.003.

[211] WBCSD, "A Scoping Report I Corporate Ecosystem Valuation Business and Ecosystems," World Business Council for Sustainable Development, Tech. Rep., May 2009.

[212] M. Baine, "Artificial reefs: a review of their design, application, management and performance," *Ocean & Coastal Management*, vol. 44, pp. 241–259, 2001.

[213] L. AW Ramm, J. H. Florisson, S. L. Watts, A. Becker, and J. R. Tweedley, "Artificial reefs in the Anthropocene: A review of geographical and historical trends in their design, purpose, and monitoring," *Bulletin of Marine Science*, vol. 97, no. 4, pp. 699–728, Oct. 2021, ISSN: 15536955. DOI: 10.5343/bms.2020.0046.

[214] B. P. Guilbeau, F. P. Harry, R. P. Gambrell, F. C. Knopf, and K. M. Dooley, "Algae attachment on carbonated cements in fresh and brackish waters - Preliminary results," *Ecological Engineering*, vol. 20, no. 4, pp. 309–319, 2003, ISSN: 09258574. DOI: 10.1016/S0925-8574(03)00026-0.

[215] Q. Xu, T. Ji, Z. Yang, and Y. Ye, "Preliminary investigation of artificial reef concrete with sulphoaluminate cement, marine sand and sea water," *Construction and Building Materials*, vol. 211, pp. 837–846, Jun. 2019, ISSN: 09500618. DOI: 10.1016/j.conbuildmat.2019.03.272.

[216] C. Chen, T. Ji, Y. Zhuang, and X. Lin, "Workability, mechanical properties and affinity of artificial reef concrete," *Construction and Building Materials*, vol. 98, pp. 227–236, Nov. 2015, ISSN: 09500618. DOI: 10.1016/j.conbuildmat.2015.05.109.

[217] S. Herrando-Pérez and C. L. J. Frid, "The Cessation of Long-term Fly-ash Dumping: Effects on Macrobenthos and Sediments," Tech. Rep. 111, 1998, pp. 780–790.

[218] Q. Xu, T. Ji, Z. Yang, and Y. Ye, "Steel rebar corrosion in artificial reef concrete with sulphoaluminate cement, sea water and marine sand," *Construction and Building Materials*, vol. 227, p. 116 685, Dec. 2019, ISSN: 09500618. DOI: 10.1016/j.conbuildmat.2019.116685.

[219] K. M. Dooley, F. C. Knopf, and R. P. Gambrell, "pH-Neutral Concrete for Attached Microalgae and Enhanced Carbon Dioxide Fixation - Phase I," Department of Energy, Baton Rougue, Tech. Rep., May 1999, pp. 1–42.

[220] M. Fischetti, N. Bockelman, and W. V. Srubar, *Solving Cement's Massive Carbon Problem*, English, Feb. 2023. [Online]. Available: www.scientificamerican.com/article/solving-cements-massive-carbon-problem/.

[221] S. Prakasan, S. Palaniappan, and R. Gettu, "Study of Energy Use and CO2 Emissions in the Manufacturing of Clinker and Cement," *Journal of The Institution of Engineers (India): Series A*, vol. 101, no. 1, pp. 221–232, Mar. 2020, ISSN: 22502157. DOI: 10.1007/s40030-019-00409-4.

[222] C. Bracho-Villavicencio, H. Matthews-Cascon, and S. Rossi, "Artificial Reefs around the World: A Review of the State of the Art and a Meta-Analysis of Its Effectiveness for the Restoration of Marine Ecosystems," *Environments - MDPI*, vol. 10, no. 7, Jul. 2023, ISSN: 20763298. DOI: 10.3390/environments10070121.

[223] P. Duan, W. Chen, J. Ma, and Z. Shui, "Influence of layered double hydroxides on microstructure and carbonation resistance of sulphoaluminate cement concrete," *Construction and Building Materials*, vol. 48, pp. 601–609, Nov. 2013, ISSN: 09500618. DOI: 10.1016/j.conbuildmat.2013.07.049.

[224] G. Bernardo, A. Telesca, and G. L. Valenti, "A porosimetric study of calcium sulfoaluminate cement pastes cured at early ages," *Cement and Concrete Research*, vol. 36, no. 6, pp. 1042–1047, Jun. 2006, ISSN: 00088846. DOI: 10.1016/j.cemconres.2006.02.014.

[225] D. Zhang, D. Xu, X. Cheng, and W. Chen, "Carbonation resistance of sulphoaluminate cement-based high performance concrete," *Journal of Wuhan University of Technology-Mater. Sci. Ed.*, vol. 24, no. 4, pp. 663–666, Aug. 2009, ISSN: 1000-2413. DOI: 10.1007/s11595-009-4663-y.

[226] M. Antoun, F. Becquart, N. Gerges, and G. Aouad, "The use of calcium sulfoaluminate cement as an alternative to Portland Cement for the recycling of municipal solid waste incineration bottom ash in mortar," *Waste Management & Research*, vol. 38, no. 8, pp. 868–875, Aug. 2020, ISSN: 0734-242X. DOI: 10.1177/0734242X20925170.

[227] M. C. Juenger, F. Winnefeld, J. L. Provis, and J. H. Ideker, "Advances in alternative cementitious binders," *Cement and Concrete Research*, vol. 41, no. 12, pp. 1232–1243, 2011, ISSN: 00088846. DOI: 10.1016/j.cemconres.2010.11.012.

[228] J. Kong, G. Cong, S. Ni, J. Sun, C. Guo, M. Chen, and H. Quan, "Recycling of waste oyster shell and recycled aggregate in the porous ecological concrete used for artificial reefs," *Construction and Building Materials*, vol. 323, p. 126 447, Mar. 2022, ISSN: 09500618. DOI: 10.1016/j.conbuildmat.2022.126447.

[229] R. Polder, T. Nijland, and M. de Rooij, "Slag cement concrete-the Dutch experience: Etatsprogrammet Varige konstruksjoner 2012-2015 Nr 270," Statens vegvesen, Tech. Rep., Feb. 2014.

[230] O. Ly, A. I. Yoris-Nobile, N. Sebaibi, E. Blanco-Fernandez, M. Boutouil, D. Castro-Fresno, A. E. Hall, R. J. Herbert, W. Deboucha, B. Reis, J. N. Franco, M. Teresa Borges, I. Sousa-Pinto, P. van der Linden, and R. Stafford, "Optimisation of 3D printed concrete for artificial reefs: Biofouling and mechanical analysis," *Construction and Building Materials*, vol. 272, p. 121 649, Feb. 2021, ISSN: 09500618. DOI: 10.1016/j.conbuildmat.2020.121649.

[231] M. Florea and H. Brouwers, "Properties of various size fractions of crushed concrete related to process conditions and re-use," *Cement and Concrete Research*, vol. 52, pp. 11–21, Oct. 2013, ISSN: 00088846. DOI: 10.1016/j.cemconres.2013.05.005.

[232] M. Florea, Z. Ning, and H. Brouwers, "Activation of liberated concrete fines and their application in mortars," *Construction and Building Materials*, vol. 50, pp. 1–12, Jan. 2014, ISSN: 09500618. DOI: 10.1016/j.conbuildmat.2013.09.012.

[233] P. Shafigh, S. Yousuf, J. C. Lee, and Z. Ibrahim, "The effect of cement mortar composition on the pH value," in *IOP Conference Series: Materials Science and Engineering*, vol. 770, Institute of Physics Publishing, Mar. 2020. DOI: 10.1088/1757-899X/770/1/012026.

[234] B. Mos, S. A. Dworjanyn, L. T. Mamo, and B. P. Kelaher, "Building global change resilience: Concrete has the potential to ameliorate the negative effects of climate-driven ocean change on a newly-settled calcifying invertebrate," *Science of The Total Environment*, vol. 646, pp. 1349–1358, Jan. 2019, ISSN: 00489697. DOI: 10.1016/j.scitotenv.2018.07.379.

[235] B. Mos, M. Byrne, and S. A. Dworjanyn, "Effects of low and high pH on sea urchin settlement, implications for the use of alkali to counter the impacts of acidification," *Aquaculture*, vol. 528, p. 735 618, Nov. 2020, ISSN: 00448486. DOI: 10.1016/j.aquaculture.2020.735618.

[236] J. R. Bone, R. Stafford, A. E. Hall, and R. J. Herbert, "The intrinsic primary bioreceptivity of concrete in the coastal environment – A review," *Developments in the Built Environment*, vol. 10, p. 100 078, May 2022, ISSN: 26661659. DOI: 10.1016/j.dibe.2022.100078.

[237] S. Kashef-Haghighi, Y. Shao, and S. Ghoshal, "Mathematical modeling of CO2 uptake by concrete during accelerated carbonation curing," *Cement and Concrete Research*, vol. 67, pp. 1–10, 2015, ISSN: 00088846. DOI: 10.1016/j.cemconres.2014.07.020.

[238] B. Šavija and M. Luković, "Carbonation of cement paste: Understanding, challenges, and opportunities," *Construction and Building Materials*, vol. 117, pp. 285–301, Aug. 2016, ISSN: 09500618. DOI: 10.1016/j.conbuildmat.2016.04.138.

[239] S. Steiner, B. Lothenbach, T. Proske, A. Borgschulte, and F. Winnefeld, "Effect of relative humidity on the carbonation rate of portlandite, calcium silicate hydrates and ettringite," *Cement and Concrete Research*, vol. 135, p. 106 116, Sep. 2020, ISSN: 00088846. DOI: 10.1016/j.cemconres.2020.106116.

[240] S. Schmidlin, C. Parcerisas, J. Hubert, M. S. Watson, J. Mees, D. Botteldooren, P. Devos, E. Debusschere, and P. I. Hablützel, "Comparison of the effects of reef and anthropogenic soundscapes on oyster larvae settlement," *Scientific Reports*, vol. 14, no. 1, Dec. 2024, ISSN: 20452322. DOI: 10.1038/s41598-024-63322-2.

[241] J. Petersen, J. Titschack, J. Groeneveld, A. Wehrmann, D. Hebbeln, and A. Freiwald, "Reef-building Pacific oysters record seasonal variations in water mass-properties of tidal basins from the Central Wadden Sea (North Sea)," *Palaeogeography, Palaeoclimatology, Palaeoecology*, vol. 577, Sep. 2021, ISSN: 00310182. DOI: 10.1016/j.palaeo.2021.110534.

[242] R. Lenth, "Population marginal means in the linear model: An alternative to least squares means," R Package version 1.7.2, Tech. Rep. 4, 2022, pp. 1–102. DOI: 10.1080/00031305.1980.10483031.

[243] M. M. Islam, S. Islam, and M. Al-Amin, "Suitability of Sea Water on Curing and Compressive Strength of Structural Concrete," English, *Journal of Civil Engineering(IEB)*, vol. 40, no. 1, pp. 37–45, May 2012. [Online]. Available: https://www.researchgate.net/publication/360218866.

[244] S. V. Vavrenyuk, Y. V. Efimenko, and V. G. Vavrenyuk, "On Standard Requirements to Cement for Concrete Used in Marine Environment," in *IOP Conference Series: Materials Science and Engineering*, vol. 753, Institute of Physics Publishing, Mar. 2020. DOI: 10.1088/1757-899X/753/2/022040.

[245] t. E. Department of Climate Change Energy and Water, "National Artificial Reef Guidelines v1.0," Australian Government, Canberra, Tech. Rep., 2023, pp. 1–106.

[246] London Convention and Protocol/UNEP, *Guidelines for the Placement of Artificial Reefs*. London: International Maritime Organization (IMO) / United Nations Environment Programme (UNEP), 2009, vol. 187, pp. 1–103, ISBN: 9789280730227.

[247] R. R. Lukens and C. Selberg, "Guidelines for Marine Artificial Reef Materials 2ed," Atlantic and Gulf States Marine Fisheries Commissions, Tech. Rep., Jan. 2004, pp. 1–205.

[248] W. Vogelsberger, A. Seidel, and G. Rudakoff, "Solubility of silica gel in water," *Journal of the Chemical Society, Faraday Transactions*, vol. 88, no. 3, pp. 473–476, 1992, ISSN: 09565000. DOI: 10.1039/FT9928800473.

[249] V. Shah, K. Scrivener, B. Bhattacharjee, and S. Bishnoi, "Changes in microstructure characteristics of cement paste on carbonation," *Cement and Concrete Research*, vol. 109, pp. 184–197, Jul. 2018, ISSN: 00088846. DOI: 10.1016/j.cemconres.2018.04.016.

[250] I. E. Teune, K. Schollbach, M. V. Florea, and H. J. Brouwers, "Carbonation of hydrated cement: The impact of carbonation conditions on CO2 sequestration, phase formation, and reactivity," *Journal of Building Engineering*, vol. 79, p. 107 785, Nov. 2023, ISSN: 2352-7102. DOI: 10.1016/J.JOBE.2023.107785.

[251] C. W. Hargis, B. Lothenbach, C. J. Müller, and F. Winnefeld, "Carbonation of calcium sulfoaluminate mortars," *Cement and Concrete Composites*, vol. 80, pp. 123–134, Jul. 2017, ISSN: 09589465. DOI: 10.1016/j.cemconcomp.2017.03.003.

[252] B. Mather, "Effects of Seawater on Concrete," ARMY ENGINEER WATERWAYS EXPERIMENT STATION VICKSBURG MS, Vicksburg, Tech. Rep., Dec. 1964, pp. 33–42.

[253] W. Kunther, B. Lothenbach, and K. L. Scrivener, "Deterioration of mortar bars immersed in magnesium containing sulfate solutions," *Materials and Structures/Materiaux et Constructions*, vol. 46, no. 12, pp. 2003–2011, Dec. 2013, ISSN: 13595997. DOI: 10.1617/s11527-013-0032-6.

[254] D. Lowke and C. Gehlen, "The zeta potential of cement and additions in cementitious suspensions with high solid fraction," *Cement and Concrete Research*, vol. 95, pp. 195–204, May 2017, ISSN: 00088846. DOI: 10.1016/j.cemconres.2017.02.016.

[255] V. Afroughsabet, L. Biolzi, P. J. Monteiro, and M. M. Gastaldi, "Investigation of the mechanical and durability properties of sustainable high performance concrete based on calcium sulfoaluminate cement," *Journal of Building Engineering*, vol. 43, p. 102 656, Nov. 2021, ISSN: 23527102. DOI: 10.1016/j.jobe.2021.102656.

[256] S. Park, "Simulating the carbonation of calcium sulfoaluminate cement blended with supplementary cementitious materials," *Journal of CO2 Utilization*, vol. 41, p. 101 286, Oct. 2020, ISSN: 22129820. DOI: 10.1016/j.jcou.2020.101286.

[257] Y. Sumra, S. Payam, and I. Zainah, "The pH of Cement-based Materials: A Review," *Journal of Wuhan University of Technology-Mater. Sci. Ed.*, vol. 35, no. 5, pp. 908–924, Oct. 2020, ISSN: 1000-2413. DOI: 10.1007/s11595-020-2337-y.

[258] Y. Tao, A. Rahul, M. K. Mohan, G. De Schutter, and K. Van Tittelboom, "Recent progress and technical challenges in using calcium sulfoaluminate (CSA) cement," *Cement and Concrete Composites*, vol. 137, p. 104 908, Mar. 2023, ISSN: 09589465. DOI: 10.1016/j.cemconcomp.2022.104908.

[259] D. D. Akerele and F. Aguayo, "Evaluating the Impact of CO2 on Calcium SulphoAluminate (CSA) Concrete," *Buildings*, vol. 14, no. 8, p. 2462, Aug. 2024, ISSN: 2075-5309. DOI: 10.3390/buildings14082462.

[260] T. Nishikawa, K. Suzuki, S. Ito, K. Sato, and T. Takebe, "Decomposition of Synthesized Ettringite by Carbonation," *Cement and Concrete Research*, vol. 22, pp. 6–14, Mar. 1992.

[261] A. Cuesta, A. G. De la Torre, and M. A. Aranda, "X-ray total scattering study of phases formed from cement phases carbonation," *Minerals*, vol. 11, no. 5, 2021, ISSN: 2075163X. DOI: 10.3390/min11050519.

[262] C. Cau, D. Coumes, S. Courtois, D. Nectoux, S. Leclercq, and X. Bourbon, "Formulating a Low-Alkalinity, High-Resistance and Low-Heat Concrete for Radioactive Waste Repositories," *Cement and Concrete Research*, vol. 36, no. 12, pp. 2152–2163, 2006. DOI: 10.1016/j.cemconres.2006.10.005{\"{i}}. [Online]. Available: https://cea.hal.science/cea-02354116.

[263] X. Lin, "Effect of early age carbonation on strength and pH of concrete," Ph.D. dissertation, McGill University, Montreal, Jun. 2007, pp. 1–132, ISBN: 9780494384886.

[264] L. Irving, "The Precipitation of Calcium and Magnesium from Sea Water.," *Journal of Marine Biological Association*, vol. 14, no. 2, pp. 441–446, 1926.

[265] L. U. D. Tambara, J. C. Rocha, M. Cheriaf, A. Palomo, and A. Fernández-Jiménez, "EFFECT OF CHLORIDE SALTS ON SULFOALUMINATE CEMENT HYDRATION," in *4th International RILEM conference on Microstructure Related Durability of Cementitious Composite*, 2020.

[266] M. Kobayashi, "Study on the durability of cementitious materials under deep-sea condition," Ph.D. dissertation, Technische Universitat Bergakademie Freiberg, Frieberg, Dec. 2023, pp. 1–115.

[267] M. Kobayashi, K. Takahashi, Y. Kawabata, and T. A. Bier, "Physicochemical properties of Portland cement/calcium aluminate cement/calcium sulfate ternary binder exposed to long-term deep-sea conditions," *Materials and Structures/Materiaux et Constructions*, vol. 55, no. 7, Sep. 2022, ISSN: 13595997. DOI: 10.1617/s11527-022-02021-8.

[268] J. Huang and R. Zhang, "The Mineralization of Molluscan Shells: Some Unsolved Problems and Special Considerations," *Frontiers in Marine Science*, vol. 9, Jun. 2022, ISSN: 2296-7745. DOI: 10.3389/fmars.2022.874534.

[269] C. Wickramaratne, "Experimental Study of High-Temperature Range Latent Heat Thermal Energy Storage," Ph.D. dissertation, University of South Florida, Tampa, Nov. 2017, pp. 1–156. [Online]. Available: https://digitalcommons.usf.edu/etd.

[270] H. Yang, Y. Zou, and H. Cui, "Advancements and Challenges in Enhancing Salt Hydrate Phase Change Materials for Building Energy Storage: Optimization Methodologies and Mechanisms," *National Science Open*, Jan. 2024, ISSN: 2097-1168. DOI: 10.1360/nso/20230056.

[271] A. M. M. Irfeey, E. Jamei, H.-W. Chau, and B. Ramasubramanian, "Enhancing Occupants' Thermal Comfort in Buildings by Applying Solar-Powered Techniques," *Architecture*, vol. 3, no. 2, pp. 213–233, Apr. 2023. DOI: 10.3390/architecture3020013.

[272] A. Adesina, "Use of phase change materials in concrete: current challenges," *Renewable Energy and Environmental Sustainability*, vol. 4, p. 9, 2019. DOI: 10.1051/rees/2019006.

[273] B. Xu, H. Ma, Z. Lu, and Z. Li, "Paraffin/expanded vermiculite composite phase change material as aggregate for developing lightweight thermal energy storage cement-based composites," *Applied Energy*, vol. 160, pp. 358–367, Dec. 2015, ISSN: 03062619. DOI: 10.1016/j.apenergy.2015.09.069.

[274] T. S. Tie, K. H. Mo, U. J. Alengaram, S. K. Kaliyavaradhan, and T. C. Ling, "Study on the use of lightweight expanded perlite and vermiculite aggregates in blended cement mortars," *European Journal of Environmental and Civil Engineering*, vol. 26, no. 8, pp. 3612–3631, 2022, ISSN: 19648189. DOI: 10.1080/19648189.2020.1806934.

[275] A. Kounadis, E. Badogiannis, D. Karonis, A. Gaki, and M. Taxiarchou, "Incorporation of phase change materials in lightweight aggregate concrete," *WSEAS Transactions on Environment and Development*, vol. 16, pp. 105–118, 2020, ISSN: 22243496. DOI: 10.37394/232015.2020.16.11.

[276] D. Kramar and V. Bindiganavile, "Impact response of lightweight mortars containing expanded perlite," *Cement and Concrete Composites*, vol. 37, no. 1, pp. 205–214, Mar. 2013, ISSN: 09589465. DOI: 10.1016/j.cemconcomp.2012.10.004.

[277] J. K. Sharma and G. Polyzos, *METHOD OF ENCAPSULATING A PHASE CHANGE MATERIAL*, English, Sep. 2023.

[278] J. Sharma, "A new approach to encapsulate salt hydrate PCM FOA#2090-1591 Part 1," Oak Ridge National Lab (ORNL) and Phase Change Energy Solutions (PCES), Tech. Rep., Oct. 2021. [Online]. Available: https://www.energy.gov/eere/buildings/articles/new-approach-encapsulate-salt-hydrate-pcm.

[279] J. Sharma, "A New Approach to Encapsulate Salt Hydrate PCM FOA#2090-1591 Part 2," Oak Ridge National Lab (ORNL) and Phase Change Energy Solutions (PCES), Tech. Rep., 2023. [Online]. Available: https://www.energy.gov/eere/buildings/articles/new-approach-encapsulate-salt-hydrate-pcm.

[280] R. Nath, "Encapsulation of High Temperature Phase Change Materials for Thermal Energy Storage," Ph.D. dissertation, University of South Florida, Tampa, Jan. 2012, pp. 1–74. [Online]. Available: https://digitalcommons.usf.edu/etd.

[281] B. G. Van Ravensteijn, P. A. Donkers, R. C. Ruliaman, J. Eversdijk, H. R. Fischer, H. P. Huinink, and O. C. Adan, "Encapsulation of Salt Hydrates by Polymer Coatings for Low-Temperature Heat Storage Applications," *ACS Applied Polymer Materials*, vol. 3, no. 4, pp. 1712–1726, Apr. 2021, ISSN: 26376105. DOI: 10.1021/acsapm.0c01186.

[282] A. Shkatulov, R. Joosten, H. Fischer, and H. Huinink, "Core-Shell Encapsulation of Salt Hydrates into Mesoporous Silica Shells for Thermochemical Energy Storage," *ACS Applied Energy Materials*, vol. 3, no. 7, pp. 6860–6869, Jul. 2020, ISSN: 25740962. DOI: 10.1021/acsaem.0c00971.

[283] T. E. Alam, "Experimental Investigation of Encapsulated Phase Change Materials for Thermal Energy Storage," Ph.D. dissertation, University of South Florida, Tampa, Jan. 2015, pp. 1–126. [Online]. Available: https://digitalcommons.usf.edu/etd.

[284] S. Pendyala, "Macroencapsulation of Phase Change Materials for Thermal Energy Storage," Ph.D. dissertation, University of South Florida, Tampa, Jan. 2012, pp. 1–105. [Online]. Available: https://digitalcommons.usf.edu/etd.

[285] M. Frigione, M. Lettieri, and A. Sarcinella, "Phase change materials for energy efficiency in buildings and their use in mortars," *Materials*, vol. 12, no. 8, Apr. 2019, ISSN: 19961944. DOI: 10.3390/ma12081260.

[286] H. Umar, S. Rizal, M. Riza, and T. M. I. Mahlia, "Mechanical properties of concrete containing beeswax/dammar gum as phase change material for thermal energy storage," *AIMS Energy*, vol. 6, no. 3, pp. 521–529, 2018, ISSN: 23338334. DOI: 10.3934/ENERGY.2018.3.521.

[287] A. Sarı, G. Hekimoğlu, V. V. Tyagi, and R. K. Sharma, "Evaluation of pumice for development of low-cost and energy-efficient composite phase change materials and lab-scale thermoregulation performances of its cementitious plasters," *Energy*, vol. 207, Sep. 2020, ISSN: 03605442. DOI: 10.1016/j.energy.2020.118242.

[288] G. W. Bnrnorpv, P. E. Zn-Sxr, E. Cnerc, and M. Bbrure2, "Hydrobiotite, a regular 1:1 interstratification of biotite and vermiculite layers," Tech. Rep., 1983, p. 420 425.

[289] S. Song, J. Li, Z. Yang, and C. Wang, "Enhancement of Thermo-Physical Properties of Expanded Vermiculite-Based Organic Composite Phase Change Materials for Improving the Thermal Energy Storage Efficiency," *ACS Omega*, vol. 6, no. 5, pp. 3891–3899, Feb. 2021, ISSN: 24701343. DOI: 10.1021/acsomega.0c05739.

[290] G. Leng, G. Qiao, G. Xu, T. Vidal, and Y. Ding, "Erythritol-Vermiculite form-stable phase change materials for thermal energy storage," in *Energy Procedia*, vol. 142, Elsevier Ltd, 2017, pp. 3363–3368. DOI: 10.1016/j.egypro.2017.12.471.

[291] A. I. Shkatulov, J. Houben, H. Fischer, and H. P. Huinink, "Stabilization of K2CO3 in vermiculite for thermochemical energy storage," *Renewable Energy*, vol. 150, pp. 990–1000, May 2020, ISSN: 18790682. DOI: 10.1016/j.renene.2019.11.119.

[292] A. E. Burgos Castellanos, T. A. Ribeiro-Santos, and R. M. Lago, "Porous expanded vermiculite containing intercalated cetyltrimethylammonium: a versatile sorbent for the hormone ethinylestradiol from aqueous medium," *International Journal of Environmental Science and Technology*, vol. 16, no. 7, pp. 2877–2884, Jul. 2019, ISSN: 17352630. DOI: 10.1007/s13762-018-1901-x.

[293] G. Kastiukas, X. Zhou, and J. Castro-Gomes, "Development and optimisation of phase change material-impregnated lightweight aggregates for geopolymer composites made from aluminosilicate rich mud and milled glass powder," *Construction and Building Materials*, vol. 110, pp. 201–210, May 2016, ISSN: 09500618. DOI: 10.1016/j.conbuildmat.2016.02.029.

[294] M. Gołaszewska, B. Klemczak, and J. Gołaszewski, "Thermal properties of calcium sulphoaluminate cement as an alternative to ordinary portland cement," *Materials*, vol. 14, no. 22, Nov. 2021, ISSN: 19961944. DOI: 10.3390/ma14227011.

[295] J. Kaufmann and F. Winnefeld, "Seasonal heat storage in calcium sulfoaluminate based hardened cement pastes – experiences with different prototypes," *Journal of Energy Storage*, vol. 25, Oct. 2019, ISSN: 2352152X. DOI: 10.1016/j.est.2019.100850.

[296] J. Wang, Y. Wang, J. Yu, L. Xu, M. Li, J. Cheng, and Z. Li, "Effects of sodium sulfate and potassium sulfate on the properties of calcium sulfoaluminate (CSA) cement based grouting materials," *Construction and Building Materials*, vol. 353, Oct. 2022, ISSN: 09500618. DOI: 10.1016/j.conbuildmat.2022.129045.

[297] W. Zhang, S. Gong, and B. Kang, "Surface Corrosion and Microstructure Degradation of Calcium Sulfoaluminate Cement Subjected to Wet-Dry Cycles in Sulfate Solution," *Advances in Materials Science and Engineering*, vol. 2017, 2017, ISSN: 16878442. DOI: 10.1155/2017/1464619.

[298] H. Du, J. Li, W. Ni, C. Hou, and W. Liu, "The hydration mechanism of magnesium oxysulfate cement prepared by magnesium desulfurization byproducts," *Journal of Materials Research and Technology*, vol. 17, pp. 1211–1220, Mar. 2022, ISSN: 22387854. DOI: 10.1016/j.jmrt.2022.01.070.

[299] P. Cui, C. r. Wu, J. Chen, F. m. Luo, and S. c. Kou, "Preparation of magnesium oxysulfate cement as a 3D printing material," *Construction and Building Materials*, vol. 282, May 2021, ISSN: 09500618. DOI: 10.1016/j.conbuildmat.2021.122677.

[300] X. Zeng and H. Yu, "Research on technology of performance improvement of basic magnesium sulfate cement—BMS," *Structural Concrete*, 2020, ISSN: 17517648. DOI: 10.1002/suco.202000165.

[301] C. Wu, W. Chen, H. Zhang, H. Yu, W. Zhang, N. Jiang, and L. Liu, "The hydration mechanism and performance of Modified magnesium oxysulfate cement by tartaric acid," *Construction and Building Materials*, vol. 144, pp. 516–524, Jul. 2017, ISSN: 09500618. DOI: 10.1016/j.conbuildmat.2017.03.222.

[302] D. Li, D. Gao, Y. Dong, and W. Li, "Modeling of phase relations and thermodynamics in the Mg(OH)2 + MgSO4 + H2O system with implications on magnesium hydroxide sulfate cement," *Calphad: Computer Coupling of Phase Diagrams and Thermochemistry*, vol. 67, Dec. 2019, ISSN: 03645916. DOI: 10.1016/j.calphad.2019.101675.

[303] S. A. Walling and J. L. Provis, "Magnesia-Based Cements: A Journey of 150 Years, and Cements for the Future?" *Chemical Reviews*, vol. 116, no. 7, pp. 4170–4204, Apr. 2016, ISSN: 15206890. DOI: 10.1021/acs.chemrev.5b00463.

[304] A. Al-Tabbaa, "Reactive magnesia cement," in *Eco-Efficient Concrete*, Elsevier Ltd., 2013, pp. 523–543, ISBN: 9780857094247. DOI: 10.1533/9780857098993.4.523.

[305] D. K. Doran, *Construction Materials Reference Book*. Oxford: Butterworth-Heinemann, 1992, ISBN: 9780750610049.

[306] S. Eckhoff and M. Okos, "Solar Energy Heat Storage for Home, Farm and Small Business: Suggestions on Selecting and Using Thermal Storage Materials and Facilities," Purdue University, West Lafayette, Tech. Rep., Sep. 2015. [Online]. Available: https://docs.lib.purdue.edu/agext/1087.

[307] S. H. Kosmatka and M. L. (e. Wilson, *Design and control of concrete mixtures : the guide to applications, methods, and materials*, 15th ed. Skokie: Portland Cement Association, 2011, pp. 1–460, ISBN: 0893122726.

[308] A. Khalil, S. Sohn, and K. Celik, "Thermal properties and stability of reactive magnesia cement," *Construction and Building Materials*, vol. 308, Nov. 2021, ISSN: 09500618. DOI: 10.1016/j.conbuildmat.2021.125102.

[309] T. Ma, H. Sun, T. Peng, and Q. Zhang, "Transformation process from phlogopite to vermiculite under hydrothermal conditions," *Applied Clay Science*, vol. 208, Jul. 2021, ISSN: 01691317. DOI: 10.1016/j.clay.2021.106094.

[310] M. Valášková and G. S. Martynková, "Vermiculite: Structural Properties and Examples of the Use," in *Clay Minerals in Nature*, M. Valaškova and G. S. Martynkova, Eds., Rijeka: IntechOpen, 2012, ch. 11. DOI: 10.5772/51237. [Online]. Available: https://doi.org/10.5772/51237.

[311] M. A. Shand, "Magnesium oxysulfate cement," in *Magnesia Cements*, Elsevier, 2020, ch. 3, pp. 75–83. DOI: 10.1016/B978-0-12-391925-0.00010-8.

[312] E. Jin, J. Yu, T. Wen, C. Tian, Z. Liu, B. Ma, and L. Yuan, "The effect of the Mgo aggregate size on the densification of sintered MgO," *Ceramics - Silikaty*, vol. 64, no. 1, pp. 84–91, 2020, ISSN: 18045847. DOI: 10.13168/cs.2019.0052.

[313] H. Brouwers and H. Radix, "Self-compacting concrete: the role of the particle size distribution," in *First International Symposium on Design, Performance and Use of Self-Consolidation Concrete*, Changsha: Springer Nature, May 2005, pp. 109–118. DOI: 10.1617/2912143624.010.

[314] M. Theodoridou, L. Kyriakou, and I. Ioannou, "PCM-enhanced Lime Plasters for Vernacular and Contemporary Architecture," in *Energy Procedia*, vol. 97, Elsevier Ltd, 2016, pp. 539–545. DOI: 10.1016/j.egypro.2016.10.070.

[315] N. B. Winter, *Understanding Cement*. WHD Microanalysis Consultants Ltd., Dec. 2012, pp. 1–206, ISBN: 978-0-9571045-2-5.

[316] ASTM International, *C349-18 Test Method for Compressive Strength of Hydraulic-Cement Mortars (Using Portions of Prisms Broken in Flexure)*, West Conshohocken, PA, Dec. 2018. DOI: 10.1520/C0349-18.

[317] ASTM international, "C109/C109M-24 Test Method for Compressive Strength of Hydraulic Cement Mortars (Using 50mm [2 in.] Cube Specimens)," West Conshohocken, PA, Tech. Rep., Oct. 2024. DOI: 10.1520/C0109{_}C0109M-24.

[318] M. H. Aldayel Aldossary, S. Ahmad, and A. A. Bahraq, "Effect of total dissolved solids-contaminated water on the properties of concrete," *Journal of Building Engineering*, vol. 32, p. 101 496, Nov. 2020, ISSN: 23527102. DOI: 10.1016/j.jobe.2020.101496.

[319] L. Montanari, P. Suraneni, M. Tsui-Chang, M. Khatibmasjedi, U. Ebead, J. Weiss, and A. Nanni, "Hydration, Pore Solution, and Porosity of Cementitious Pastes Made with Seawater," *Journal of Materials in Civil Engineering*, vol. 31, no. 8, Aug. 2019, ISSN: 0899-1561. DOI: 10.1061/(ASCE)MT.1943-5533.0002818.

[320] V. Brito, T. A. Saidov, T. D. Gonçalves, and L. Pel, "Delamination of Ançã limestone due to sodium sulfate under different environmental conditions as studied by nuclear magnetic resonance," *Journal of Building Physics*, vol. 38, no. 5, pp. 465–482, Mar. 2015, ISSN: 1744-2591. DOI: 10.1177/1744259114543981.

[321] Y. Liu, Z.-Y. Zhang, Y. Zheng, X. Zhang, X. Wang, and X. Yin, "Comparison of magnesium oxysulfate (MOS) cement and reactive magnesia cement (RMC) under different curing conditions: Physical properties, mechanisms, and environmental impacts," *Construction and Building Materials*, vol. 405, p. 133 317, Nov. 2023, ISSN: 09500618. DOI: 10.1016/j.conbuildmat.2023.133317.

[322] N. Zhang, H. Yu, H. Ma, H. Ma, and M. Ba, "The phase composition of the MgO–MgSO4–H2O system and mechanisms of chemical additives," *Composites Part B: Engineering*, vol. 247, p. 110 328, Dec. 2022, ISSN: 1359-8368. DOI: 10.1016/J.COMPOSITESB.2022.110328. [Online]. Available: https://www.sciencedirect.com/science/article/abs/pii/S1359836822007016.

[323] K. Jin, C. Wu, Z. Xiong, D. Wang, X. Zhou, and X. Chen, "Impact of Cl- on the performance of magnesium oxysulfate (MOS) cement," *Construction and Building Materials*, vol. 430, p. 136 472, Jun. 2024, ISSN: 09500618. DOI: 10.1016/j.conbuildmat.2024.136472.

[324] X. Liu, J. Tie, Z. Wang, Y. Xia, C.-A. Wang, and S. Tie, "Improved thermal conductivity and stability of Na2SO4 10H2O PCMs system by incorporation of Al/C hybrid nanoparticles," *Journal of Materials Research and Technology*, vol. 12, pp. 982–988, May 2021, ISSN: 22387854. DOI: 10.1016/j.jmrt.2021.02.096.

[325] F. Köksal, M. A. Serrano-López, M. Şahin, O. Gencel, and C. López-Colina, "Combined effect of steel fibre and expanded vermiculite on properties of lightweight mortar at elevated temperatures," *Materials and Structures*, vol. 48, no. 7, pp. 2083–2092, Jul. 2015, ISSN: 1359-5997. DOI: 10.1617/s11527-014-0294-7.

[326] G. Huang, D. Pudasainee, R. Gupta, and W. V. Liu, "Thermal properties of calcium sulfoaluminate cement-based mortars incorporated with expanded perlite cured at cold temperatures," *Construction and Building Materials*, vol. 274, p. 122 082, Mar. 2021, ISSN: 09500618. DOI: 10.1016/j.conbuildmat.2020.122082.

[327] N. Jannat, A. Hussien, B. Abdullah, and A. Cotgrave, "A Comparative Simulation Study of the Thermal Performances of the Building Envelope Wall Materials in the Tropics," *Sustainability*, vol. 12, no. 12, p. 4892, Jun. 2020, ISSN: 2071-1050. DOI: 10.3390/su12124892.

[328] S. Fidan, H. Oktay, S. Polat, and S. Ozturk, "An Artificial Neural Network Model to Predict the Thermal Properties of Concrete Using Different Neurons and Activation Functions," *Advances in Materials Science and Engineering*, vol. 2019, pp. 1–13, Apr. 2019, ISSN: 1687-8434. DOI: 10.1155/2019/3831813.

[329] S. Verbeke and A. Audenaert, "Thermal inertia in buildings: A review of impacts across climate and building use," *Renewable and Sustainable Energy Reviews*, vol. 82, pp. 2300–2318, Feb. 2018, ISSN: 13640321. DOI: 10.1016/j.rser.2017.08.083.

[330] E. Y. Tuncel and B. Y. Pekmezci, "A sustainable cold bonded lightweight PCM aggregate production: Its effects on concrete properties," *Construction and Building Materials*, vol. 181, pp. 199–216, Aug. 2018, ISSN: 09500618. DOI: 10.1016/j.conbuildmat.2018.05.269.

[331] E. Mohseni, W. Tang, K. H. Khayat, and H. Cui, "Thermal performance and corrosion resistance of structural functional concrete made with inorganic PCM," *Construction and Building Materials*, vol. 249, Jul. 2020, ISSN: 09500618. DOI: 10.1016/j.conbuildmat.2020.118768.

[332] M. Kheradmand, J. Castro-Gomes, M. Azenha, P. D. Silva, J. L. De Aguiar, and S. E. Zoorob, "Assessing the feasibility of impregnating phase change materials in lightweight aggregate for development of thermal energy storage systems," *Construction and Building Materials*, vol. 89, pp. 48–59, Apr. 2015, ISSN: 09500618. DOI: 10.1016/j.conbuildmat.2015.04.031.

Summary

Salt Hydrate Phase Change Materials: Material Behaviour and Thermal Energy Storage Applications

This thesis has investigated the use of hydrated salt phase change materials (PCMs) for sustainable thermal energy storage. The research spanned theoretical foundations, extensive experimental characterization, and the development of practical composite systems, all aimed at addressing both energy efficiency and environmental sustainability.

In the early chapters, the fundamental principles of thermal energy storage were established. A clear distinction was drawn between sensible and latent heat, with an emphasis on the advantages of latent heat storage during phase transitions. Salt hydrates were introduced as promising candidates due to their high energy density and favorable melting behavior. The theoretical discussion provided the necessary background for understanding the thermodynamic and crystallographic factors that influence the performance of these materials.

The experimental work involved a suite of advanced characterization techniques. Differential scanning calorimetry (DSC), thermogravimetric analysis (TGA), and X-ray diffraction (XRD) were employed to evaluate the thermal stability, phase change behavior, and crystalline structure of the recycled salt hydrates. These methods yielded important insights into the melting mechanics, the role of water coordination, and the challenges posed by phase separation and corrosion. Despite these challenges, the overall performance of the salt hydrates confirmed their suitability as PCMs.

A significant portion of this work focused on the development of composite systems to enhance the practical application of salt hydrates. By incorporating the salt hydrates into cementitious and vermiculite matrices, the research demonstrated improved handling and stability of the materials. This integration not only maintained the essential thermal properties but also enabled compatibility with building materials—a key step toward real-world implementation.

Sustainability has been a core theme throughout this thesis. The use of recycled materials and the focus on reducing carbon emissions underscore the environmental benefits of adopting hydrated salt PCMs. While several technical challenges remain, the study has provided a robust framework for future efforts to optimize these materials. In

particular, the promising results suggest that with further research—especially in areas such as long-term performance testing and advanced stabilization techniques—salt hydrate-based thermal batteries could become an integral component of next-generation energy systems.

In conclusion, the work presented in this thesis demonstrates both the potential and the challenges of using hydrated salt PCMs for thermal energy storage. The findings contribute to a broader understanding of phase change materials and open up new possibilities for sustainable energy solutions. The insights gained here will serve as a valuable guide for future research and technological developments aimed at achieving efficient, durable, and environmentally friendly energy storage systems.

List of Publications

- **C.A. Wesemann**, K. Schollbach, and H.J.H. Brouwers, "Phase change behavior of sulfate salt hydrates extracted from olivine nano-silica side stream" J Energy Storage, vol. 80, p. 110730, Mar. 2024, doi: 10.1016/j.est.2024.110730.
- **C.A. Wesemann**, T. Junggeburth, and H.J.H. Brouwers, "Thermal performance evaluation of recycled salt hydrates through T-history." Case Studies in Thermal Engineering, vol. 68, p. 105961, Feb. 2025, doi: 10.1016/j.csite.2025.105961.
- **C.A. Wesemann**, M. Antoun, I. Teune, K. Schollbach, J. Rippen, A. Hylkema, B. Oosterhoff, & H. J. H. Brouwers, "Effect of Carbonation on Eco-Friendly Binders for Marine Infrastructures." Construction and Building Materials, vol. 477, p. 141293, May 2025, doi: 10.1016/j.conbuildmat.2025.141293.
- **C.A. Wesemann**, K. Schollbach, and H.J.H. Brouwers, (2026)."Novel encapsulation method for salt hydrates for building applications." (To be submitted)
- **C.A. Wesemann**, K. Schollbach, and H.J.H. Brouwers, "Review on the Melting Mechanics of Salt Hydrate PCM: From Fundamental Principles to Applications in Thermal Energy Storage" (In Preparation)

Conference Proceedings

- **C.A.Wesemann**, K. Schollbach, and H.J.H. Brouwers, "Magnesium Sulfate as Phase Change Material for Seasonal Thermal Storage", (Poster) 4th international Conference on the Chemistry of Construction Materials - ICCCM 2022 Karlsruhe, September 26-28, 2022
- **C.A. Wesemann**, T. Junggeburth, K. Schollbach, and H.J.H. Brouwers, "Thermostabilizing of Recycled Salt Hydrates for Thermal Energy Storage Applications", International Conference of Power Engineering - ICOPE 2023 Kyoto, May 21-26, 2023
- **C.A. Wesemann**, T. Junggeburth, K. Schollbach, and H.J.H. Brouwers, "Thermostabilizing of Recycled Salt Hydrates for Thermal Energy Storage Applications", 7th International Confernce Non-Traditional Cement & Concrete - NTCC 2023 Brno, June 25-28, 2023

Curriculum Vitae

Charles Alexander Wesemann Reoyo was born on March 28th, 1990, in Bremen, Germany. He completed his bachelor's degree in Cellular Molecular Biology in 2012 at the University of Puerto Rico - Rio Piedras campus in San Juan, Puerto Rico. Subsequently, he pursued a master's degree in Biobased Materials and Engineering at Maastricht University in Maastricht, Netherlands, where he graduated in 2019. His master's project, titled "Study of Porous 3D-printed PLLA Scaffold for Bone Tissue Engineering," showcased his early interest in materials science and engineering.

In 2020, he embarked on a Ph.D. project at Eindhoven Technical University in Eindhoven, Netherlands, where he delved deeper into research that culminates in this dissertation. In 2026, Charles completed his graduate studies with the Building Materials Group focusing on Phase Change Materials and Salt Hydrates. This experience laid the foundation for his continued exploration of innovative materials for sustainable applications.

Bouwstenen is een publicatiereeks
van de Faculteit Bouwkunde,
Technische Universiteit Eindhoven.
Zij presenteert resultaten van
onderzoek en andere activiteiten op
het vakgebied der Bouwkunde,
uitgevoerd in het kader van deze
Faculteit.

Bouwstenen en andere proefschriften van de
TU/e zijn online beschikbaar via:
https://research.tue.nl/

Reeds verschenen in de serie
Bouwstenen

nr 1
Elan: A Computer Model for Building Energy Design: Theory and Validation
Martin H. de Wit
H.H. Driessen
R.M.M. van der Velden

nr 2
Kwaliteit, Keuzevrijheid en Kosten: Evaluatie van Experiment Klarendal, Arnhem
J. Smeets
C. le Nobel
M. Broos
J. Frenken
A. v.d. Sanden

nr 3
Crooswijk: Van 'Bijzonder' naar 'Gewoon'
Vincent Smit
Kees Noort

nr 4
Staal in de Woningbouw
Edwin J.F. Delsing

nr 5
Mathematical Theory of Stressed Skin Action in Profiled Sheeting with Various Edge Conditions
Andre W.A.M.J. van den Bogaard

nr 6
Hoe Berekenbaar en Betrouwbaar is de Coëfficiënt k in x-ksigma en x-ks?
K.B. Lub
A.J. Bosch

nr 7
Het Typologisch Gereedschap: Een Verkennende Studie Omtrent Typologie en Omtrent de Aanpak van Typologisch Onderzoek
J.H. Luiten

nr 8
Informatievoorziening en Beheerprocessen
A. Nauta
Jos Smeets (red.)
Helga Fassbinder (projectleider)
Adrie Proveniers
J. v.d. Moosdijk

nr 9
Strukturering en Verwerking van Tijdgegevens voor de Uitvoering van Bouwwerken
ir. W.F. Schaefer
P.A. Erkelens

nr 10
Stedebouw en de Vorming van een Speciale Wetenschap
K. Doevendans

nr 11
Informatica en Ondersteuning van Ruimtelijke Besluitvorming
G.G. van der Meulen

nr 12
Staal in de Woningbouw, Korrosie-Bescherming van de Begane Grondvloer
Edwin J.F. Delsing

nr 13
Een Thermisch Model voor de Berekening van Staalplaatbetonvloeren onder Brandomstandigheden
A.F. Hamerlinck

nr 14
De Wijkgedachte in Nederland: Gemeenschapsstreven in een Stedebouwkundige Context
K. Doevendans
R. Stolzenburg

nr 15
Diaphragm Effect of Trapezoidally Profiled Steel Sheets: Experimental Research into the Influence of Force Application
Andre W.A.M.J. van den Bogaard

nr 16
Versterken met Spuit-Ferrocement: Het Mechanische Gedrag van met Spuit-Ferrocement Versterkte Gewapend Betonbalken
K.B. Lubir
M.C.G. van Wanroy

nr 17
De Tractaten van Jean Nicolas Louis Durand
G. van Zeyl

nr 18
Wonen onder een Plat Dak: Drie Opstellen over Enkele Vooronderstellingen van de Stedebouw
K. Doevendans

nr 19
Supporting Decision Making Processes: A Graphical and Interactive Analysis of Multivariate Data
W. Adams

nr 20
Self-Help Building Productivity: A Method for Improving House Building by Low-Income Groups Applied to Kenya 1990-2000
P. A. Erkelens

nr 21
De Verdeling van Woningen: Een Kwestie van Onderhandelen
Vincent Smit

nr 22
Flexibiliteit en Kosten in het Ontwerpproces: Een Besluitvormingondersteunend Model
M. Prins

nr 23
Spontane Nederzettingen Begeleid: Voorwaarden en Criteria in Sri Lanka
Po Hin Thung

nr 24
Fundamentals of the Design of Bamboo Structures
Oscar Arce-Villalobos

nr 25
Concepten van de Bouwkunde
M.F.Th. Bax (red.)
H.M.G.J. Trum (red.)

nr 26
Meaning of the Site
Xiaodong Li

nr 27
Het Woonmilieu op Begrip Gebracht: Een Speurtocht naar de Betekenis van het Begrip 'Woonmilieu'
Jaap Ketelaar

nr 28
Urban Environment in Developing Countries
editors: Peter A. Erkelens
George G. van der Meulen (red.)

nr 29
Stategische Plannen voor de Stad: Onderzoek en Planning in Drie Steden
prof.dr. H. Fassbinder (red.)
H. Rikhof (red.)

nr 30
Stedebouwkunde en Stadsbestuur
Piet Beekman

nr 31
De Architectuur van Djenné: Een Onderzoek naar de Historische Stad
P.C.M. Maas

nr 32
Conjoint Experiments and Retail Planning
Harmen Oppewal

nr 33
Strukturformen Indonesischer Bautechnik: Entwicklung Methodischer Grundlagen für eine 'Konstruktive Pattern Language' in Indonesien
Heinz Frick arch. SIA

nr 34
Styles of Architectural Designing: Empirical Research on Working Styles and Personality Dispositions
Anton P.M. van Bakel

nr 35
Conjoint Choice Models for Urban Tourism Planning and Marketing
Benedict Dellaert

nr 36
Stedelijke Planvorming als Co-Produktie
Helga Fassbinder (red.)

nr 37
Design Research in the Netherlands
editors: R.M. Oxman
M.F.Th. Bax
H.H. Achten

nr 38
Communication in the Building Industry
Bauke de Vries

nr 39
Optimaal Dimensioneren van Gelaste Plaatliggers
J.B.W. Stark
F. van Pelt
L.F.M. van Gorp
B.W.E.M. van Hove

nr 40
Huisvesting en Overwinning van Armoede
P.H. Thung
P. Beekman (red.)

nr 41
Urban Habitat: The Environment of Tomorrow
George G. van der Meulen
Peter A. Erkelens

nr 42
A Typology of Joints
John C.M. Olie

nr 43
Modeling Constraints-Based Choices for Leisure Mobility Planning
Marcus P. Stemerding

nr 44
Activity-Based Travel Demand Modeling
Dick Ettema

nr 45
Wind-Induced Pressure Fluctuations on Building Facades
Chris Geurts

nr 46
Generic Representations
Henri Achten

nr 47
Johann Santini Aichel: Architectuur en Ambiguiteit
Dirk De Meyer

nr 48
Concrete Behaviour in Multiaxial Compression
Erik van Geel

nr 49
Modelling Site Selection
Frank Witlox

nr 50
Ecolemma Model
Ferdinand Beetstra

nr 51
Conjoint Approaches to Developing Activity-Based Models
Donggen Wang

nr 52
On the Effectiveness of Ventilation
Ad Roos

nr 53
Conjoint Modeling Approaches for Residential Group preferences
Eric Molin

nr 54
Modelling Architectural Design Information by Features
Jos van Leeuwen

nr 55
A Spatial Decision Support System for the Planning of Retail and Service Facilities
Theo Arentze

nr 56
Integrated Lighting System Assistant
Ellie de Groot

nr 57
Ontwerpend Leren, Leren Ontwerpen
J.T. Boekholt

nr 58
Temporal Aspects of Theme Park Choice Behavior
Astrid Kemperman

nr 59
Ontwerp van een Geïndustrialiseerde Funderingswijze
Faas Moonen

nr 60
Merlin: A Decision Support System for Outdoor Leisure Planning
Manon van Middelkoop

nr 61
The Aura of Modernity
Jos Bosman

nr 62
Urban Form and Activity-Travel Patterns
Daniëlle Snellen

nr 63
Design Research in the Netherlands 2000
Henri Achten

nr 64
Computer Aided Dimensional Control in Building Construction
Rui Wu

nr 65
Beyond Sustainable Building
editors: Peter A. Erkelens
Sander de Jonge
August A.M. van Vliet
co-editor: Ruth J.G. Verhagen

nr 66
Das Globalrecyclingfähige Haus
Hans Löfflad

nr 67
Cool Schools for Hot Suburbs
René J. Dierkx

nr 68
A Bamboo Building Design Decision Support Tool
Fitri Mardjono

nr 69
Driving Rain on Building Envelopes
Fabien van Mook

nr 70
Heating Monumental Churches
Henk Schellen

nr 71
Van Woningverhuurder naar Aanbieder van Woongenot
Patrick Dogge

nr 72
Moisture Transfer Properties of Coated Gypsum
Emile Goossens

nr 73
Plybamboo Wall-Panels for Housing
Guillermo E. González-Beltrán

nr 74
The Future Site-Proceedings
Ger Maas
Frans van Gassel

nr 75
Radon transport in Autoclaved Aerated Concrete
Michel van der Pal

nr 76
The Reliability and Validity of Interactive Virtual Reality Computer Experiments
Amy Tan

nr 77
Measuring Housing Preferences Using Virtual Reality and Belief Networks
Maciej A. Orzechowski

nr 78
Computational Representations of Words and Associations in Architectural Design
Nicole Segers

nr 79
Measuring and Predicting Adaptation in Multidimensional Activity-Travel Patterns
Chang-Hyeon Joh

nr 80
Strategic Briefing
Fayez Al Hassan

nr 81
Well Being in Hospitals
Simona Di Cicco

nr 82
Solares Bauen: Implementierungs- und Umsetzungs-Aspekte in der Hochschulausbildung in Österreich
Gerhard Schuster

nr 83
Supporting Strategic Design of Workplace Environments with Case-Based Reasoning
Shauna Mallory-Hill

nr 84
ACCEL: A Tool for Supporting Concept Generation in the Early Design Phase
Maxim Ivashkov

nr 85
Brick-Mortar Interaction in Masonry under Compression
Ad Vermeltfoort

nr 86
Zelfredzaam Wonen
Guus van Vliet

nr 87
Een Ensemble met Grootstedelijke Allure
Jos Bosman
Hans Schippers

nr 88
On the Computation of Well-Structured Graphic Representations in Architectural Design
Henri Achten

nr 89
De Evolutie van een West-Afrikaanse Vernaculaire Architectuur
Wolf Schijns

nr 90
ROMBO Tactiek
Christoph Maria Ravesloot

nr 91
External Coupling between Building Energy Simulation and Computational Fluid Dynamics
Ery Djunaedy

nr 92
Design Research in the Netherlands 2005
editors: Henri Achten
Kees Dorst
Pieter Jan Stappers
Bauke de Vries

nr 93
Ein Modell zur Baulichen Transformation
Jalil H. Saber Zaimian

nr 94
Human Lighting Demands: Healthy Lighting in an Office Environment
Myriam Aries

nr 95
A Spatial Decision Support System for the Provision and Monitoring of Urban Greenspace
Claudia Pelizaro

nr 96
Leren Creëren
Adri Proveniers

nr 97
Simlandscape
Rob de Waard

nr 98
Design Team Communication
Ad den Otter

nr 99
Humaan-Ecologisch Georiënteerde Woningbouw
Juri Czabanowski

nr 100
Hambase
Martin de Wit

nr 101
Sound Transmission through Pipe Systems and into Building Structures
Susanne Bron-van der Jagt

nr 102
Het Bouwkundig Contrapunt
Jan Francis Boelen

nr 103
A Framework for a Multi-Agent Planning Support System
Dick Saarloos

nr 104
Bracing Steel Frames with Calcium Silicate Element Walls
Bright Mweene Ng'andu

nr 105
Naar een Nieuwe Houtskeletbouw
F.N.G. De Medts

nr 106 and 107
Niet gepubliceerd

nr 108
Geborgenheid
T.E.L. van Pinxteren

nr 109
Modelling Strategic Behaviour in Anticipation of Congestion
Qi Han

nr 110
Reflecties op het Woondomein
Fred Sanders

nr 111
On Assessment of Wind Comfort by Sand Erosion
Gábor Dezsö

nr 112
Bench Heating in Monumental Churches
Dionne Limpens-Neilen

nr 113
RE. Architecture
Ana Pereira Roders

nr 114
Toward Applicable Green Architecture
Usama El Fiky

nr 115
Knowledge Representation under Inherent Uncertainty in a Multi-Agent System for Land Use Planning
Liying Ma

nr 116
Integrated Heat Air and Moisture Modeling and Simulation
Jos van Schijndel

nr 117
Concrete Behaviour in Multiaxial Compression
J.P.W. Bongers

nr 118
The Image of the Urban Landscape
Ana Moya Pellitero

nr 119
The Self-Organizing City in Vietnam
Stephanie Geertman

nr 120
A Multi-Agent Planning Support System for Assessing Externalities of Urban Form Scenarios
Rachel Katoshevski-Cavari

nr 121
Den Schulbau Neu Denken, Fühlen und Wollen
Urs Christian Maurer-Dietrich

nr 122
Peter Eisenman Theories and Practices
Bernhard Kormoss

nr 123
User Simulation of Space Utilisation
Vincent Tabak

nr 125
In Search of a Complex System Model
Oswald Devisch

nr 126
Lighting at Work: Environmental Study of Direct Effects of Lighting Level and Spectrum on Psycho-Physiological Variables
Grazyna Górnicka

nr 127
Flanking Sound Transmission through Lightweight Framed Double Leaf Walls
Stefan Schoenwald

nr 128
Bounded Rationality and Spatio-Temporal Pedestrian Shopping Behavior
Wei Zhu

nr 129
Travel Information: Impact on Activity Travel Pattern
Zhongwei Sun

nr 130
Co-Simulation for Performance Prediction of Innovative Integrated Mechanical Energy Systems in Buildings
Marija Trčka

nr 131
Niet gepubliceerd

nr 132
Architectural Cue Model in Evacuation Simulation for Underground Space Design
Chengyu Sun

nr 133
Uncertainty and Sensitivity Analysis in Building Performance Simulation for Decision Support and Design Optimization
Christina Hopfe

nr 134
Facilitating Distributed Collaboration in the AEC/FM Sector Using Semantic Web Technologies
Jacob Beetz

nr 135
Circumferentially Adhesive Bonded Glass Panes for Bracing Steel Frame in Façades
Edwin Huveners

nr 136
Influence of Temperature on Concrete Beams Strengthened in Flexure with CFRP
Ernst-Lucas Klamer

nr 137
Sturen op Klantwaarde
Jos Smeets

nr 139
Lateral Behavior of Steel Frames with Discretely Connected Precast Concrete Infill Panels
Paul Teewen

nr 140
Integral Design Method in the Context of Sustainable Building Design
Perica Savanović

nr 141
Household Activity-Travel Behavior: Implementation of Within-Household Interactions
Renni Anggraini

nr 142
Design Research in the Netherlands 2010
Henri Achten

nr 143
Modelling Life Trajectories and Transport Mode Choice Using Bayesian Belief Networks
Marloes Verhoeven

nr 144
Assessing Construction Project Performance in Ghana
William Gyadu-Asiedu

nr 145
Empowering Seniors through Domotic Homes
Masi Mohammadi

nr 146
An Integral Design Concept for Ecological Self-Compacting Concrete
Martin Hunger

nr 147
Governing Multi-Actor Decision Processes in Dutch Industrial Area Redevelopment
Erik Blokhuis

nr 148
A Multifunctional Design Approach for Sustainable Concrete
Götz Hüsken

nr 149
Quality Monitoring in Infrastructural Design-Build Projects
Ruben Favié

nr 150
Assessment Matrix for Conservation of Valuable Timber Structures
Michael Abels

nr 151
Co-simulation of Building Energy Simulation and Computational Fluid Dynamics for Whole-Building Heat, Air and Moisture Engineering
Mohammad Mirsadeghi

nr 152
External Coupling of Building Energy Simulation and Building Element Heat, Air and Moisture Simulation
Daniel Cóstola

nr 153
Adaptive Decision Making In Multi-Stakeholder Retail Planning
Ingrid Janssen

nr 154
Landscape Generator
Kymo Slager

nr 155
Constraint Specification in Architecture
Remco Niemeijer

nr 156
A Need-Based Approach to Dynamic Activity Generation
Linda Nijland

nr 157
Modeling Office Firm Dynamics in an Agent-Based Micro Simulation Framework
Gustavo Garcia Manzato

nr 158
Lightweight Floor System for Vibration Comfort
Sander Zegers

nr 159
Aanpasbaarheid van de Draagstructuur
Roel Gijsbers

nr 160
'Village in the City' in Guangzhou, China
Yanliu Lin

nr 161
Climate Risk Assessment in Museums
Marco Martens

nr 162
Social Activity-Travel Patterns
Pauline van den Berg

nr 163
Sound Concentration Caused by Curved Surfaces
Martijn Vercammen

nr 164
Design of Environmentally Friendly Calcium Sulfate-Based Building Materials: Towards an Improved Indoor Air Quality
Qingliang Yu

nr 165
Beyond Uniform Thermal Comfort on the Effects of Non-Uniformity and Individual Physiology
Lisje Schellen

nr 166
Sustainable Residential Districts
Gaby Abdalla

nr 167
Towards a Performance Assessment Methodology using Computational Simulation for Air Distribution System Designs in Operating Rooms
Mônica do Amaral Melhado

nr 168
Strategic Decision Modeling in Brownfield Redevelopment
Brano Glumac

nr 169
Pamela: A Parking Analysis Model for Predicting Effects in Local Areas
Peter van der Waerden

nr 170
A Vision Driven Wayfinding Simulation-System Based on the Architectural Features Perceived in the Office Environment
Qunli Chen

nr 171
Measuring Mental Representations Underlying Activity-Travel Choices
Oliver Horeni

nr 172
Modelling the Effects of Social Networks on Activity and Travel Behaviour
Nicole Ronald

nr 173
Uncertainty Propagation and Sensitivity Analysis Techniques in Building Performance Simulation to Support Conceptual Building and System Design
Christian Struck

nr 174
Numerical Modeling of Micro-Scale Wind-Induced Pollutant Dispersion in the Built Environment
Pierre Gousseau

nr 175
Modeling Recreation Choices over the Family Lifecycle
Anna Beatriz Grigolon

nr 176
Experimental and Numerical Analysis of Mixing Ventilation at Laminar, Transitional and Turbulent Slot Reynolds Numbers
Twan van Hooff

nr 177
Collaborative Design Support: Workshops to Stimulate Interaction and Knowledge Exchange Between Practitioners
Emile M.C.J. Quanjel

nr 178
Future-Proof Platforms for Aging-in-Place
Michiel Brink

nr 179
Motivate: A Context-Aware Mobile Application for Physical Activity Promotion
Yuzhong Lin

nr 180
Experience the City: Analysis of Space-Time Behaviour and Spatial Learning
Anastasia Moiseeva

nr 181
Unbonded Post-Tensioned Shear Walls of Calcium Silicate Element Masonry
Lex van der Meer

nr 182
Construction and Demolition Waste Recycling into Innovative Building Materials for Sustainable Construction in Tanzania
Mwita M. Sabai

nr 183
Durability of Concrete with Emphasis on Chloride Migration
Przemysław Spiesz

nr 184
Computational Modeling of Urban Wind Flow and Natural Ventilation Potential of Buildings
Rubina Ramponi

nr 185
A Distributed Dynamic Simulation Mechanism for Buildings Automation and Control Systems
Azzedine Yahiaoui

nr 186
Modeling Cognitive Learning of Urban Networks in Daily Activity-Travel Behavior
Şehnaz Cenani Durmazoğlu

nr 187
Functionality and Adaptability of Design Solutions for Public Apartment Buildings in Ghana
Stephen Agyefi-Mensah

nr 188
A Construction Waste Generation Model for Developing Countries
Lilliana Abarca-Guerrero

nr 189
Synchronizing Networks: The Modeling of Supernetworks for Activity-Travel Behavior
Feixiong Liao

nr 190
Time and Money Allocation Decisions in Out-of-Home Leisure Activity Choices
Gamze Zeynep Dane

nr 191
How to Measure Added Value of CRE and Building Design
Rianne Appel-Meulenbroek

nr 192
Secondary Materials in Cement-Based Products: Treatment, Modeling and Environmental Interaction
Miruna Florea

nr 193
Concepts for the Robustness Improvement of Self-Compacting Concrete: Effects of Admixtures and Mixture Components on the Rheology and Early Hydration at Varying Temperatures
Wolfram Schmidt

nr 194
Modelling and Simulation of Virtual Natural Lighting Solutions in Buildings
Rizki A. Mangkuto

nr 195
Nano-Silica Production at Low Temperatures from the Dissolution of Olivine - Synthesis, Tailoring and Modelling
Alberto Lazaro Garcia

nr 196
Building Energy Simulation Based Assessment of Industrial Halls for Design Support
Bruno Lee

nr 197
Computational Performance Prediction of the Potential of Hybrid Adaptable Thermal Storage Concepts for Lightweight Low-Energy Houses
Pieter-Jan Hoes

nr 198
Application of Nano-Silica in Concrete
George Quercia Bianchi

nr 199
Dynamics of Social Networks and Activity Travel Behaviour
Fariya Sharmeen

nr 200
Building Structural Design Generation and Optimisation including Spatial Modification
Juan Manuel Davila Delgado

nr 201
Hydration and Thermal Decomposition of Cement/Calcium-Sulphate Based Materials
Ariën de Korte

nr 202
Republiek van Beelden:
De Politieke Werkingen van het Ontwerp in Regionale Planvorming
Bart de Zwart

nr 203
Effects of Energy Price Increases on Individual Activity-Travel Repertoires and Energy Consumption
Dujuan Yang

nr 204
Geometry and Ventilation:
Evaluation of the Leeward Sawtooth Roof Potential in the Natural Ventilation of Buildings
Jorge Isaac Perén Montero

nr 205
Computational Modelling of Evaporative Cooling as a Climate Change Adaptation Measure at the Spatial Scale of Buildings and Streets
Hamid Montazeri

nr 206
Local Buckling of Aluminium Beams in Fire Conditions
Ronald van der Meulen

nr 207
Historic Urban Landscapes:
Framing the Integration of Urban and Heritage Planning in Multilevel Governance
Loes Veldpaus

nr 208
Sustainable Transformation of the Cities:
Urban Design Pragmatics to Achieve a Sustainable City
Ernesto Antonio Zumelzu Scheel

nr 209
Development of Sustainable Protective Ultra-High Performance Fibre Reinforced Concrete (UHPFRC):
Design, Assessment and Modeling
Rui Yu

nr 210
Uncertainty in Modeling Activity-Travel Demand in Complex Uban Systems
Soora Rasouli

nr 211
Simulation-based Performance Assessment of Climate Adaptive Greenhouse Shells
Chul-sung Lee

nr 212
Green Cities:
Modelling the Spatial Transformation of the Urban Environment using Renewable Energy Technologies
Saleh Mohammadi

nr 213
A Bounded Rationality Model of Short and Long-Term Dynamics of Activity-Travel Behavior
Ifigeneia Psarra

nr 214
Effects of Pricing Strategies on Dynamic Repertoires of Activity-Travel Behaviour
Elaheh Khademi

nr 215
Handstorm Principles for Creative and Collaborative Working
Frans van Gassel

nr 216
Light Conditions in Nursing Homes: Visual Comfort and Visual Functioning of Residents
Marianne M. Sinoo

nr 217
Woonsporen: De Sociale en Ruimtelijke Biografie van een Stedelijk Bouwblok in de Amsterdamse Transvaalbuurt
Hüseyin Hüsnü Yegenoglu

nr 218
Studies on User Control in Ambient Intelligent Systems
Berent Willem Meerbeek

nr 219
Daily Livings in a Smart Home: Users' Living Preference Modeling of Smart Homes
Erfaneh Allameh

nr 220
Smart Home Design: Spatial Preference Modeling of Smart Homes
Mohammadali Heidari Jozam

nr 221
Wonen: Discoursen, Praktijken, Perspectieven
Jos Smeets

nr 222
Personal Control over Indoor Climate in Offices: Impact on Comfort, Health and Productivity
Atze Christiaan Boerstra

nr 223
Personalized Route Finding in Multimodal Transportation Networks
Jianwe Zhang

nr 224
The Design of an Adaptive Healing Room for Stroke Patients
Elke Daemen

nr 225
Experimental and Numerical Analysis of Climate Change Induced Risks to Historic Buildings and Collections
Zara Huijbregts

nr 226
Wind Flow Modeling in Urban Areas Through Experimental and Numerical Techniques
Alessio Ricci

nr 227
Clever Climate Control for Culture: Energy Efficient Indoor Climate Control Strategies for Museums Respecting Collection Preservation and Thermal Comfort of Visitors
Rick Kramer

nr 228
Fatigue Life Estimation of Metal Structures Based on Damage Modeling
Sarmediran Silitonga

nr 229
A multi-agents and occupancy based strategy for energy management and process control on the room-level
Timilehin Moses Labeodan

nr 230
Environmental assessment of Building Integrated Photovoltaics: Numerical and Experimental Carrying Capacity Based Approach
Michiel Ritzen

nr 231
Performance of Admixture and Secondary Minerals in Alkali Activated Concrete: Sustaining a Concrete Future
Arno Keulen

nr 232
World Heritage Cities and Sustainable Urban Development:
Bridging Global and Local Levels in Monitoring the Sustainable Urban Development of World Heritage Cities
Paloma C. Guzman Molina

nr 233
Stage Acoustics and Sound Exposure in Performance and Rehearsal Spaces for Orchestras:
Methods for Physical Measurements
Remy Wenmaekers

nr 234
Municipal Solid Waste Incineration (MSWI) Bottom Ash:
From Waste to Value Characterization, Treatments and Application
Pei Tang

nr 235
Large Eddy Simulations Applied to Wind Loading and Pollutant Dispersion
Mattia Ricci

nr 236
Alkali Activated Slag-Fly Ash Binders: Design, Modeling and Application
Xu Gao

nr 237
Sodium Carbonate Activated Slag: Reaction Analysis, Microstructural Modification & Engineering Application
Bo Yuan

nr 238
Shopping Behavior in Malls
Widiyani

nr 239
Smart Grid-Building Energy Interactions: Demand Side Power Flexibility in Office Buildings
Kennedy Otieno Aduda

nr 240
Modeling Taxis Dynamic Behavior in Uncertain Urban Environments
Zheng Zhong

nr 241
Gap-Theoretical Analyses of Residential Satisfaction and Intention to Move
Wen Jiang

nr 242
Travel Satisfaction and Subjective Well-Being: A Behavioral Modeling Perspective
Yanan Gao

nr 243
Building Energy Modelling to Support the Commissioning of Holistic Data Centre Operation
Vojtech Zavrel

nr 244
Regret-Based Travel Behavior Modeling: An Extended Framework
Sunghoon Jang

nr 245
Towards Robust Low-Energy Houses: A Computational Approach for Performance Robustness Assessment using Scenario Analysis
Rajesh Reddy Kotireddy

nr 246
Development of sustainable and functionalized inorganic binder-biofiber composites
Guillaume Doudart de la Grée

nr 247
A Multiscale Analysis of the Urban Heat Island Effect: From City Averaged Temperatures to the Energy Demand of Individual Buildings
Yasin Toparlar

nr 248
Design Method for Adaptive Daylight Systems for buildings covered by large (span) roofs
Florian Heinzelmann

nr 249
Hardening, high-temperature resistance and acid resistance of one-part geopolymers
Patrick Sturm

nr 250
Effects of the built environment on dynamic repertoires of activity-travel behaviour
Aida Pontes de Aquino

nr 251
Modeling for auralization of urban environments: Incorporation of directivity in sound propagation and analysis of a framework for auralizing a car pass-by
Fotis Georgiou

nr 252
Wind Loads on Heliostats and Photovoltaic Trackers
Andreas Pfahl

nr 253
Approaches for computational performance optimization of innovative adaptive façade concepts
Roel Loonen

nr 254
Multi-scale FEM-DEM Model for Granular Materials: Micro-scale boundary conditions, Statics, and Dynamics
Jiadun Liu

nr 255
Bending Moment - Shear Force Interaction of Rolled I-Shaped Steel Sections
Rianne Willie Adriana Dekker

nr 256
Paralympic tandem cycling and handcycling: Computational and wind tunnel analysis of aerodynamic performance
Paul Fionn Mannion

nr 257
Experimental characterization and numerical modelling of 3D printed concrete: Controlling structural behaviour in the fresh and hardened state
Robert Johannes Maria Wolfs

nr 258
Requirement checking in the building industry: Enabling modularized and extensible requirement checking systems based on semantic web technologies
Chi Zhang

nr 259
A Sustainable Industrial Site Redevelopment Planning Support System
Tong Wang

nr 260
Efficient storage and retrieval of detailed building models: Multi-disciplinary and long-term use of geometric and semantic construction information
Thomas Ferdinand Krijnen

nr 261
The users' value of business center concepts for knowledge sharing and networking behavior within and between organizations
Minou Weijs-Perrée

nr 262
Characterization and improvement of aerodynamic performance of vertical axis wind turbines using computational fluid dynamics (CFD)
Abdolrahim Rezaeiha

nr 263
In-situ characterization of the acoustic impedance of vegetated roofs
Chang Liu

nr 264
Occupancy-based lighting control: Developing an energy saving strategy that ensures office workers' comfort
Christel de Bakker

nr 265
Stakeholders-Oriented Spatial Decision Support System
Cahyono Susetyo

nr 266
Climate-induced damage in oak museum objects
Rianne Aleida Luimes

nr 267
Towards individual thermal comfort: Model predictive personalized control of heating systems
Katarina Katic

nr 268
Modelling and Measuring Quality of Urban Life: Housing, Neighborhood, Transport and Job
Lida Aminian

nr 269
Optimization of an aquifer thermal energy storage system through integrated modelling of aquifer, HVAC systems and building
Basar Bozkaya

nr 270
Numerical modeling for urban sound propagation: developments in wave-based and energy-based methods
Raúl Pagán Muñoz

nr 271
Lighting in multi-user office environments: improving employee wellbeing through personal control
Sanae van der Vleuten-Chraibi

nr 272
A strategy for fit-for-purpose occupant behavior modelling in building energy and comfort performance simulation
Isabella I. Gaetani dell'Aquila d'Aragona

nr 273
Een architectuurhistorische waardestelling van naoorlogse woonwijken in Nederland: Het voorbeeld van de Westelijke Tuinsteden in Amsterdam
Eleonore Henriette Marie Mens

nr 274
Job-Housing Co-Dependent Mobility Decisions in Life Trajectories
Jia Guo

nr 275
A user-oriented focus to create healthcare facilities: decision making on strategic values
Emilia Rosalia Catharina Maria Huisman

nr 276
Dynamics of plane impinging jets at moderate Reynolds numbers – with applications to air curtains
Adelya Khayrullina

nr 277
Valorization of Municipal Solid Waste Incineration Bottom Ash - Chemical Nature, Leachability and Treatments of Hazardous Elements
Qadeer Alam

nr 278
Treatments and valorization of MSWI bottom ash - application in cement-based materials
Veronica Caprai

nr 279
Personal lighting conditions of office workers - input for intelligent systems to optimize subjective alertness
Juliëtte van Duijnhoven

nr 280
Social influence effects in tourism travel: air trip itinerary and destination choices
Xiaofeng Pan

nr 281
Advancing Post-War Housing: Integrating Heritage Impact, Environmental Impact, Hygrothermal Risk and Costs in Renovation Design Decisions
Lisanne Claartje Havinga

nr 282
Impact resistant ultra-high performance fibre reinforced concrete: materials, components and properties
Peipeng Li

nr 283
Demand-driven Science Parks: The Perceived Benefits and Trade-offs of Tenant Firms with regard to Science Park Attributes
Wei Keat Benny Ng

nr 284
Raise the lantern; how light can help to maintain a healthy and safe hospital environment focusing on nurses
Maria Petronella Johanna Aarts

nr 285
Modelling Learning and Dynamic Route and Parking Choice Behaviour under Uncertainty
Elaine Cristina Schneider de Carvalho

nr 286
Identifying indoor local microclimates for safekeeping of cultural heritage
Karin Kompatscher

nr 287
Probabilistic modeling of fatigue resistance for welded and riveted bridge details. Resistance models and estimation of uncertainty.
Davide Leonetti

nr 288
Performance of Layered UHPFRC under Static and Dynamic Loads: Effects of steel fibers, coarse aggregates and layered structures
Yangyueye Cao

nr 289
Photocatalytic abatement of the nitrogen oxide pollution: synthesis, application and long-term evaluation of titania-silica composites
Yuri Hendrix

nr 290
Assessing knowledge adoption in post-disaster reconstruction: Understanding the impact of hazard-resistant construction knowledge on reconstruction processes of self-recovering communities in Nepal and the Philippines
Eefje Hendriks

nr 291
Locating electric vehicle charging stations: A multi-agent based dynamic simulation
Seheon Kim

nr 292
De invloed van Lean Management op de beheersing van het bouwproces
Wim van den Bouwhuijsen

nr 293
Neighborhood Environment and Physical Activity of Older Adults
Zhengying Liu

nr 294
Practical and continuous luminance distribution measurements for lighting quality
Thijs Willem Kruisselbrink

nr 295
Auditory Distraction in Open-Plan Study Environments in Higher Education
Pieternella Elizabeth Braat-Eggen

nr 296
Exploring the effect of the sound environment on nurses' task performance: an applied approach focusing on prospective memory
Jikke Reinten

nr 297
Design and performance of water resistant cementitious materials– Mechanisms, evaluation and applications
Zhengyao Qu

nr 298
Design Optimization of Seasonal Thermal Energy Storage Integrated District Heating and Cooling System: A Modeling and Simulation Approach
Luyi Xu

nr 299
Land use and transport: Integrated approaches for planning and management
Zhongqi Wang

nr 300
Multi-disciplinary optimization of building spatial designs: co-evolutionary design process simulations, evolutionary algorithms, hybrid approaches
Sjonnie Boonstra

nr 301
Modeling the spatial and temporal relation between urban land use, temperature, and energy demand
Hung-Chu Chen

nr 302
Seismic retrofitting of masonry walls with flexible deep mounted CFRP strips
Ömer Serhat Türkmen

nr 303
Coupled Aerostructural Shape and Topology Optimization of Horizontal-Axis Wind Turbine Rotor Blades
Zhijun Wang

nr 304
Valorization of Recycled Waste Glass and Converter Steel Slag as Ingredients for Building Materials: Hydration and Carbonation Studies
Gang Liu

nr 305
Low-Carbon City Development based on Land Use Planning
Gengzhe Wang

nr 306
Sustainable energy transition scenario analysis for buildings and neighborhoods - Data driven optimization
Shalika Saubhagya Wickramarachchi Walker

nr 307
In-between living and manufactured: an exploratory study on biobuilding components for building design
Berrak Kirbas Akyurek

nr 308
Development of alternative cementitious binders and functionalized materials: design, performance and durability
Anna Monika Kaja

nr 309
Development a morphological approach for interactive kinetic façade design: Improving multiple occupants' visual comfort
Seyed Morteza Hosseini

nr 310
PV in urban context: modeling and simulation strategies for analyzing the performance of shaded PV systems
Ádám Bognár

nr 311
Life Trajectory, Household Car Ownership Dynamics and Home Renewable Energy Equipment Adoption
Gaofeng Gu

nr 312
Impact of Street-Scale Built Environment on Walking/Cycling around Metro Stations
Yanan Liu

nr 313
Advances in Urban Traffic Network Equilibrium Models and Algorithms
Dong Wang

nr 314
Development of an uncertainty analysis framework for model-based consequential life cycle assessment: application to activity-based modelling and life cycle assessment of multimodal mobility
Paul Martin Baustert

nr 315
Variable stiffness and damping structural joints for semi-active vibration control
Qinyu Wang

nr 316
Understanding Carsharing-Facilitating Neighborhood Preferences
Juan Wang

nr 317
Dynamic alignment of Corporate Real Estate to business strategies: An empirical analysis using historical data and in-depth modelling of decision making
Howard Cooke

nr 318
Local People Matter: Towards participatory governance of cultural heritage in China
Ji Li

nr 319
Walkability and Walkable Healthy Neighborhoods
Bojing Liao

nr 320
Light directionality in design of healthy offices: exploration of two methods
Parisa Khademagha

nr 321
Room acoustic modeling with the time-domain discontinuous Galerkin method
Huiqing Wang

nr 322
Sustainable insulating lightweight materials for enhancing indoor building performance: miscanthus, aerogel and nano-silica
Yuxuan Chen

nr 323
Computational analysis of the impact of façade geometrical details on wind flow and pollutant dispersion
Xing Zheng

nr 324
Analysis of urban wind energy potential around high-rise buildings in close proximity using computational fluid dynamics
Yu-Hsuan Jang

nr 325
A new approach to automated energy performance and fault detection and diagnosis of HVAC systems: Development of the 4S3F method
Arie Taal

nr 326
Innovative Admixtures for Modifying Viscosity and Volume Change of Cement Composites
Hossein Karimi

nr 327
Towards houses with low grid dependency: A simulation-based design optimization approach
Zahra Mohammadi

nr 328
Activation of demand flexibility for heating systems in buildings: Real-life demonstration of optimal control for power-to-heat and thermal energy storage
Christian Finck

nr 329
A computational framework for analysis and optimisation of automated solar shading systems
Samuel B. de Vries

nr 330
Challenges and potential solutions for cultural heritage adaptive reuse: a comparative study employing the Historic Urban Landscape approach
Nadia Pintossi

nr 331
Shared control in office lighting systems
Tatiana Aleksandrovna Lashina

nr 332
Comfort in Urban Public Spaces
You Peng

nr 333
Numerical modelling of metal soap formation in historical oil paintings
Gerardus Johannes Anna Maria Eumelen

nr 334
A transdisciplinary decision-making approach to food-water-energy nexus: A guide towards sustainable development
Maryam Ghodsvali

nr 335
Numerical modelling of transient low-frequency sound propagation and vibration in buildings
Indra Sihar

nr 336
Characterization of impact sound from lightweight joist floors
Yi Qin

nr 337
Cities for Children: Supporting Children and Caregivers in Participatory Urban Planning
Özlemnur Ataol

nr 338
Engaging the unengaged: Exploring citizen participation in nature-based solutions in China
Li Dai

nr 339
Municipal Solid Waste Incineration Residues: analysis, treatments, and applications
Ekaterina Loginova

nr 340
Enhancing the Uptake of Nature-Based Solutions in Urban Settings: An Information Systems Approach
Shahryar Ershad Sarabi

nr 341
Work Schedule Arrangements in Two-Adult Households with Children
Bilin Han

nr 342
Increasing awareness of urban cultural heritage using digital technologies: empirical design and analysis of a new multi-media web platform
Benshuo Wang

nr 343
Mechanical and physical properties of fibre-cement composites using alternative natural fibres
Katerina Kochova

nr 344
Numerical and experimental investigation of urban microclimate in a real compact heterogeneous urban area
Nestoras Antoniou

nr 345
Examining in-class activities to facilitate academic achievement in higher education: A framework for optimal indoor environmental conditions
Henk W. Brink

nr 346
High-temperature resistant geopolymers: composition, microstructure and performance
Kinga Malgorzata Klima

nr 347
Individual and household decision-making in shared parking
Qianqian Yan

nr 348
In-situ formation of LDHs in Alkali activated binders
Tao Liu

nr 349
Condition assessment of concrete sewer pipes through an integrated experimental-numerical approach
Irene C. Scheperboer

nr 350
In situ PU-based characterization of sound absorbing materials for room acoustic modeling purposes
Baltazar Briere de La Hosseraye

nr 351
Uncertainty analysis and management in building energy data mining: A bottom-up approach considering the temporal and spatial aspect of data
Waqas Khan

nr 352
Personalized Heating Control Systems to improve thermal comfort and reduce energy consumption
Michal Veselý

nr 353
Restorative value of the urban greenscape: Urban residential streets as restorative environments
Robert P. van Dongen

nr 354
Urban ventilation and the compact Mediterranean city: numerical investigations of the dynamic relationships between density, morphology and wind flow
Olga Palusci

nr 355
Data science for buildings: a multi-scale approach bridging occupants to smart-city energy planning
Julien Leprince

nr 356
Class Association Rule Models for Predicting Transportation Mode Choice
Jiajia Zhang

nr 357
Acceptance and use of autonomous vehicles
Zhihui Tian

nr 358
Consumer Acceptance of Crowdshipping Services
Chenyu Wang

nr 359
Determinants of habitual participation in leisure-time physical activity and active travel in life trajectories
Xiaoyue Chen

nr 360
Analysis of Citizens' Motivation and Intention Using Modern Information Technology in Urban Planning Public Participation
Wenshu Li

nr 361
Linking smart and physical port cities. Port-city interface areas: from obsolete/isolated to smart environments.
Mercè de Miguel Capdevila

nr 362
Assessment and improvement of indoor thermal comfort and energy demand of Chinese heritage apartment buildings under climate change
Muxi Lei

nr 363
Indoor airflow and heat transfer in a cross-ventilated generic building: wind tunnel experiments and computational fluid dynamics analyses
Katarina Kosutova

nr 364
A Robotic Construction Simulation Platform for Light-weight Prefabricated Structures.
Aiyu Zhu

nr 365
Lifetime prediction of vertical-axis wind turbines based on CFD simulations and high-cycle fatigue modeling
Feiyu Geng

nr 366
Computational modeling of convective heat transfer at building surfaces
Samy Iousef

nr 367
Numerical simulation of the atmospheric boundary layer with application to natural ventilation
Raffaele Vasaturo

nr 368
Bouwen zonder scrupules. De Nederlandse bouwnijverheid tijdens de bezetting en de eerste jaren van wederopbouw (1940-1950)
Geert-Jan Mellink

nr 369
Factors Promoting a Positive Experienced Neighborhood Public Space--A Virtual Environment-based analysis.
Yuwen Zhao

nr 370
Place quality making in high-speed railway station areas: Devising place quality indicators for urban design, beyond the transport-land use divide
Jinglun Du

nr 371
Sustainable Bio-based Adsorptive Concrete for Phosphorus Removal
Fan Wu

nr 372
The physical workplace as a resource for mental health: A salutogenic approach to a mentally healthy workplace design at home and at the office
Lisanne Bergefurt

nr 373
High-end application of basic oxygen furnace steel slag as sustainable building materials
Muhammad Jawad Ahmed

nr 374
Energy-Efficient Urban Rail Transit Operations: Models, Algorithms, and Applications
Kang Huang

nr 375
Household Energy Efficiency Adoption: Influencing Factors and Diffusion Interventions
Hua Du

nr 376
High-temperature resistant geopolymer-based materials out of industrial residuals.
Yan Luo

nr 377
A Simulation Approach Exploring the Impacts of Land Use Variables on Travel Behavior.
Xiaoming Lyu

nr 378
Understanding and modelling individual preferences for Mobility as a Service
Valeria Caiati

nr 379
Linking the physical and digital built environment - Enabling occupant-centric decision-making using cross-domain semantic digital twins
Alex Donkers

nr 380
Indoor Air Quality in Daycare Centers: Assessing and Mitigating Indoor Exposure on Young Children
Hailin Zheng

nr 381
A Data-Driven Approach to Understanding Visitors' Behavior to Reduce the Negative Effects of Tourism in Historical Cities
Sezi Karayazi

nr 382
Wind effects on internal depressurization for asbestos abatement
Anjali Radhakrishnan Jayakumari

nr 383
Spatiotemporal Graph Convolutional Neural Network for Robust and Accurate Traffic Flow Prediction
Yutian Liu

nr 384
Photo-responsive functional aluminosilicate cementitious materials - Design, Performance and Durability
Daoru Liu

nr 385
High-end applications of basic oxygen furnace slag as a cementitious binder. Phase Assemblage, Mechanical & Chemical Activation, Composites Application
Winnie Franco Santos

nr 386
Towards improved performance modelling of distributed PV systems in the built environment
Bin Meng

nr 387
Development of sustainable insulation materials. Design, performance and applications
Alex Koh Chuen Hon

nr 388
Simulations of Sandwich Panel Systems under Fire: Two-Scale Methods for Connections, Pyrolysis for Insulation, Experimental Validations
Qingfeng Xu

nr 389
Long-term Mechanical Performance of the Flax Fiber Reinforced Polymer Composites Considering the Environmental Effects
Bowen Xu

nr 390
Quality engineering and control for digital fabrication with concrete
Derk Bos

nr 391
Structural Engineering of 3D Printed Strain Hardening Cementitious Composites. From micro-scale analysis to application
Karsten Nefs

nr 392
Children's Outdoor Play in the Digital Age; The Role of Digital Interventions in Stimulating Children's Outdoor Play Behavior
Avin Khalilollahi

nr 393
Biophilic design and integrating nature in architecture: Guidelines for three-dimensional green spaces to innovate architectural typologies and create impact for sustainability
Weijie Zhong

nr 394
Crafting Smart Homes: Innovative Design Strategies to Enhance Housing Quality for Ageing Well
Chuan Ma

nr 395
Valorization of Natural Fibers and Municipal Solid Waste Incineration (MSWI) Bottom Ash in Building Composite
Helong Song

nr 396
Digital Placemaking and Healthy Ageing. A user-centric approach for empowering senior citizens in inclusive decision-making of future healthy ageing neighbourhoods
Peyman Najafi

nr 397
Optimizing aerodynamic performance in cycling. - Analyses of drafting strategies and skinsuit design through computational simulations and wind tunnel experiments
Thijs Druenen

nr 398
A simulation-based analytical framework for heat battery in residential use cases.
Shuwei Wang

nr 399
Design and performance of alternative cementitious materials using industrial solid wastes - carbonation and chemical activation
Yanjie Tang

nr 400
Valorization of industrial solid wastes as ingredients for construction materials: Design, Performance and Durability
Xuan Ling

nr 401
Towards Healthy Neighborhoods for Children –Analysis of Parental Perception of Child Friendliness and Children's Physical Activity
Xiaoli Gong

nr 402
Simultaneous large-scale modeling of individual and household life events
Yajie Yang

nr 403
Helical reinforcement in 3D printed concrete: Development and characterization of a novel reinforcement technique
Lauri Hass

nr 404
Advancing Sustainable Built Environment: Insights from stakeholder perspectives and decision support models
Pei-Hsuan Lee

nr 405
Children and urban green infrastructure in the digital age: children's perception and desires, and parents' attitudes, towards digitally-enabled interactions with urban green infrastructure
Shengchen Yin

nr 406
Exhibition Entanglements. The Department of Architecture at the Museo de Arte Moderno de Bogotá, 1983-1995
Michael Forero Parra

nr 407
Outdoor-to-indoor sound propagation models for noise exposure studies
Michail Evangelos Terzakis

nr 408
Conceptualising the relationship between the psychosocial and the physical learning environment. Towards an overarching theory, methodology and exploration of practices in innovative physical learning environments at a university of applied sciences
Siebren Baars

nr 409
Nano TiO2 hydrosols-based photocatalytic self-cleaning cementitious materials: FUNCTIONAL PERFORMANCES AND APPLICATIONS
Zixiao Wang

nr 410
Multi-Physics and Multi-Scale Investigations of the Temperature-Induced Response of Flax Fiber Reinforced Sandwich Footbridges with laboratory and field monitoring validation
Marco Manconi

nr 411
Flax Fiber Polyester Resin in Bridge Construction: Design, Modeling, and Long-Term Performance
Ali Shahmirzaloo

nr 412
Children's Mental Health and the Environment
Examining the role of activity patterns and environmental noise
exposure
Maud Dohmen

nr 413
Heterogeneous Human Mobility Analysis using Big DataCFD modeling of air pollution in an urban street canyon by car traffic emissions - Sensitivity analyses and recommendations
Bin Zhang

nr 414
CFD modeling of air pollution in an urban street canyon by car traffic emissions - Sensitivity analyses and recommendations
Pen Qin

nr 415
The spatial planning of urban green space – an empirical analysis and land-use modeling approach
Jianfei Li

nr 416
3D-printed mortars with carbon nanotubes for self-sensing applications
Albanela Dulaj

nr 417
A Framework for Modeling and Simulating Pedestrians' Affective Experiences, Perceptions, and Activities in Public Spaces
Senqi Yang

nr 418
High-rise living - Stimulating social interaction in high-rise apartment buildings
Linh Nguyen

nr 419
Enhancing activity-based models: dynamic scheduling and trip chain modeling
Pim Labee

nr 420
Built Environment, Active Travel, and Location-Based Outdoor Activity: Spatial and Temporal Perspectives
Ting Zhou

nr 421
In the Interplay of Acceptance of Crowd-Sourced Delivery and Transportation Mode Choice within a MaaS Service
Qiang Qi

nr 422
Spatial-Temporal Effects of Land-use on Food-Water Energy Nexus: A Case Study of Beijing-Tian Urban Agglomeration
Ke Yang

nr 423
Engaging Youth with Cultural Heritage in the Digital Age An Integrated Framework for Youth Digital Participation in Cultural Heritage Management
Yingxin Zhang

nr 424
E-bikes and the Built Environment. Cross-Sectional and Longitudinal Explorations of the Determinants of E-Bike Ownership and Use in the Netherlands
Yushan Zhang

nr 425
The fault-free case of low delta-T syndrome
Alet van den Brink

nr 426
The role of viewing behavior in simulating personal light conditions
Myrta Gkaintatzi Masouti

nr 427
Multi-scale analysis of the hygro-mechanical behaviour of oak wood. A numerical and experimental study
Amin Livani

nr 428
Ceiling and attic ventilation to improve the indoor thermal environment of residential buildings in hot-humid climates
Mutmainnah

nr 429
A multiscale approach to sustainable silica aerogels. Optimizing synthesis, waste valorization, and environmental analysis
Marina Borzova

nr 430
Smart and Hybrid Workplaces from the Perspective of Municipal Employees: Preferences and Experiences in Office- and Home-Workplaces
Deniz Tuzcuoglu

nr 431
High-temperature resistant sprayed UHPC based on PC-CAC-C$ system
Jia He

nr 432
Semantics for Smart Building Systems: Towards Portable Demand Side Management Applications in Buildings
Rathnayaka Mudiyanselag